

Reactions of nitrogen-containing compounds with ozone: kinetics and mechanisms

Présentée le 10 février 2020

à la Faculté de l'environnement naturel, architectural et construit
Laboratoire pour le traitement et la qualité de l'eau
Programme doctoral en génie civil et environnement

pour l'obtention du grade de Docteur ès Sciences

par

Sung Eun LIM

Acceptée sur proposition du jury

Prof. A. J. Wüest, président du jury
Prof. U. von Gunten, Dr C. McArdell, directeurs de thèse
Prof. T. Ternes, rapporteur
Prof. Y. Lee, rapporteur
Prof. T. Kohn, rapporteuse

Cover page (temporary, back)

Acknowledgements

PhD work is often compared to a long journey. In my case, it has been a journey through a dark cave without enough preparation. In the beginning, I was equipped with nothing but a weak lamp, a little water, and very basic gears. Nevertheless, I have been able to finally reach my goal, thanks to much help and support from all the people I have met along this journey.

First of all, I would like to thank my supervisor, Urs von Gunten. I have learned not only research, but also many invaluable life lessons such as maintaining work-life balance and dealing with stressful situations in an appropriate manner. He also sparked my interest in society, politics, and history. Words are simply not enough to describe how grateful I am for having the opportunity to work with him. I would also like to thank my co-supervisor, Christa McArdell. Only with her advice on analytical approaches and detailed comments, was it possible to produce and interpret such interesting results. I would also like to thank the jury members, Thomas Ternes, Yunho Lee, Tamar Kohn, and Alfred Johny Wüest, who each spent time and effort to thoroughly examine my thesis and shared their valuable opinions to help improve it. Sincere gratitude goes to Agnes Tekle-Röttering and Holger Lutze as well, for their collaboration on the Azole study, especially for patiently waiting for the progress from my side.

Next, I would like to thank Elisabeth Salhi, for her full support in the laboratory. I have hugely benefited from working closely with her, discussing all kinds of issues I have encountered in the lab, and learning her creative approaches to solve the issues. Special thanks go to Uchem colleagues: Marc Bourgin, Philipp Longree, Jakov Bolotin, Rebekka Gulde, and Jennifer Schollee. They were patient in bearing all the troubles that I made with the instruments and generously shared their knowledge on MS analyses with me. I would like to express a great thank you to Peter Tentscher, for the introduction to the world of computational chemistry and for all interesting and fruitful discussions about my results. The scope of my thesis has profoundly expanded thanks to his input. I would like to thank Paul Erickson and Kristopher McNeill, for advising me on setting up the single oxygen detector. A very special thank you goes to Daniel Rentsch and Samuel Derrer for the helpful advice and interesting ideas coming from their sound knowledge of organic chemistry.

My warmest thank you goes to Joanna Houska for proofreading my thesis and leaving helpful and interesting comments, as well as for being so patient with my broken German every morning! Thank you very much to the current and past members of the UvG group and W+T: Andrea Betterle, Silvio Canonica, Urs Jans, Rolf Kipfer, Frank Leresche, Tony Merle, Stephanie Remke, Ursula Schönenberger, Fabian Soltermann, Nicolas Walpen, and Tessoria Young. Thank you for helping me to easily adapt to the new surroundings and to make my time at Eawag so special and enjoyable.

I would like to thank Kyuhwa Lee for accompanying me through my entire PhD path from the beginning. All the adventures we had together in the Alps definitely helped me understand myself better. Lastly, I would like to thank my mom and dad, Sookyeol Lee and Jungho Lim, two amazing people in my life, whose lives have always inspired me to embrace challenges and to pursue continuous, lifelong learning!

Abstract

Nitrogen-containing moieties are widespread in natural waters in dissolved organic nitrogen and micropollutants. They are often susceptible to an electrophilic attack by ozone because of the electron-rich nature of the neutral form of nitrogen in organic compounds. This indicates that reactions of nitrogen-containing compounds with ozone inevitably occur in water and wastewater treatment where ozonation is applied for disinfection or oxidation. Despite the relevance to ozone chemistry, the knowledge on reactions of ozone with some principal nitrogen-containing functional groups is limited. The aim of this thesis was to elucidate reaction mechanisms of nitrogen-containing compounds with ozone for common nitrogen-containing functional groups: aliphatic amines and azoles. The primary objectives were (1) to determine the second-order rate constants for the reactions of nitrogen-containing compounds with ozone (k_{03}), (2) to identify/quantify transformation products and reactive oxygen species, (3) to perform kinetic simulations and quantum chemical computations to supplement or corroborate empirical evidences. Reaction mechanisms were proposed by compiling the results from all aspects, providing a better understanding of nitrogen-ozone chemistry. The investigation of triethylamine, diethylamine, and ethylamine yielded k_{03} of the neutral form of amines ranging from $9.3 \times 10^4 \text{ M}^{-1} \text{ s}^{-1}$ to $2.2 \times 10^6 \text{ M}^{-1} \text{ s}^{-1}$. The apparent k_{03} at pH 7 for potential or identified transformation products were $6.8 \times 10^5 \text{ M}^{-1} \text{ s}^{-1}$ for *N,N*-diethylhydroxylamine, $\sim 10^5 \text{ M}^{-1} \text{ s}^{-1}$ for *N*-ethylhydroxylamine, $1.9 \times 10^3 \text{ M}^{-1} \text{ s}^{-1}$ for *N*-ethylethanamine oxide, and $3.4 \text{ M}^{-1} \text{ s}^{-1}$ for nitroethane. All amines predominantly underwent oxygen-transfer pathways to form major transformation products containing nitrogen-oxygen bonds: triethylamine *N*-oxide (88% per abated triethylamine) and nitroethane (69% per abated diethylamine and 100% per abate ethylamine). *N,N*-diethylhydroxylamine was a potential primary transformation product from the diethylamine-ozone reaction. Its formation was not confirmed due to its high ozone reactivity, but supported by measurements of reactive oxygen species, kinetic simulations, and quantum chemical computations. Pyrrole and imidazole reacted fast ($k_{03} > 10^3 \text{ M}^{-1} \text{ s}^{-1}$ at pH 1 – 12), whereas pyrazole reacted moderately fast with ozone ($k_{03} = 56 \text{ M}^{-1} \text{ s}^{-1}$ at pH 7). All studied azoles underwent an addition of ozone to the C-C double bond in the ring. Subsequent pathways after the initial ozone addition varied considerably among the azoles. Pyrrole reacted with ozone via a Criegee-type and an oxygen-addition mechanism. The major identified products (yield per abated pyrrole) were maleimide (34%), formamide (14%) and formate (54%). Imidazole predominantly reacted via a Criegee-type mechanism with ring cleavage and formation of three fragments, formamide, cyanate, and formate ($\sim 100\%$ yields, respectively), completely closing the mass balance. For pyrazole, only carbonous products were identified (126% formate and 34% glyoxal per abated pyrazole). Products containing hydroxypyrazole and hydrazide moieties were postulated, possibly formed via an oxygen addition and a Criegee-type mechanism, respectively. The nitrogenous transformation products identified during this study may have different environmental implications. Some of them (e.g., nitroalkanes, *N*-formyl compounds) require further efforts to understand their impact on the aquatic environment and human health.

Keywords

Ozone, aliphatic amines, azoles, reaction kinetics, reaction mechanisms

Zusammenfassung

Stickstoffhaltige Verbindungen findet man häufig in natürlichen Gewässern in Form von gelöstem organischem Stickstoff oder Spurenstoffen. Diese stickstoffhaltigen Verbindungen reagieren mit Ozon während der Ozonung von Trink- oder Abwasser. Die elektronenreichen Eigenschaften des neutralen Stickstoffs begünstigen eine elektrophile Addition von Ozon. Trotz der Relevanz für die Ozonchemie sind Reaktionen von Ozon mit stickstoffhaltigen funktionellen Gruppen noch wenig verstanden. Ziel dieser Dissertation war es, die Reaktionsmechanismen von stickstoffhaltigen Verbindungen mit Ozon am Beispiel von zwei verbreiteten funktionellen Gruppen, den aliphatischen Aminen und Azolen, zu ermitteln. Der Fokus lag dabei auf (1) der Ermittlung der Geschwindigkeitskonstanten 2. Ordnung der Reaktionen zwischen Ozon und stickstoffhaltigen Verbindungen (k_{O_3}), (2) der Identifizierung/Quantifizierung von Transformationsprodukten und reaktiven Sauerstoffspezies, (3) der Durchführung von kinetischen Simulationen und quantenchemischen Berechnungen um die Resultate zu erhärten. Die Untersuchung von Triethylamin, Diethylamin und Ethylamin ergaben k_{O_3} im Bereich von $9.3 \times 10^4 \text{ M}^{-1} \text{ s}^{-1}$ bis $2.2 \times 10^6 \text{ M}^{-1} \text{ s}^{-1}$ für die neutralen Amine. Die apparenten k_{O_3} (pH 7) für Transformationsprodukte waren $\sim 10^5 \text{ M}^{-1} \text{ s}^{-1}$ für *N,N*-Diethylhydroxylamin und *N*-Ethylhydroxylamin, $1.9 \times 10^3 \text{ M}^{-1} \text{ s}^{-1}$ für *N*-Ethylethaniminoxid, und $3.4 \text{ M}^{-1} \text{ s}^{-1}$ für Nitroethan. Alle Amine reagierten vorwiegend via Sauerstofftransfer, was zur Bildung von Transformationsprodukten mit N-O-Bindungen führte: Triethylamin-*N*-oxid (88% pro abgebautes Triethylamin) und Nitroethan (69% und 100% pro abgebautes Triethylamin und Ethylamin). Die Bildung von *N,N*-Diethylhydroxylamin, ein potentielles, primäres Transformationsprodukt aus der Ozonung von Ethylamin konnte aufgrund seiner hohen Reaktivität mit Ozon nur durch Messungen von reaktiven Sauerstoffspezies, kinetischen Simulationen und quantenchemischen Berechnungen bestätigt werden. Pyrrol und Imidazol haben eine hohe Reaktivität mit Ozon ($k_{O_3} > 10^3 \text{ M}^{-1} \text{ s}^{-1}$, pH 1 - 12), während Pyrazol nur reaktiv langsam reagiert ($k_{O_3} = 56 \text{ M}^{-1} \text{ s}^{-1}$ at pH 7). Die Reaktionsmechanismen unterschieden sich deutlich für die verschiedenen Azole. Pyrrol reagierte mit Ozon über einen Criegee Mechanismus, sowie über eine Sauerstoffaddition. Die hauptsächlich identifizierten Produkte (Ausbeute auf abgebautes Pyrrol normiert) waren Maleimid (34%), Formamid (14%) und Formiat (54%). Imidazol reagierte hauptsächlich über den Criegee Mechanismus mit einer Ringspaltung und der Bildung von drei Fragmenten, nämlich, Formamid, Cyanat und Ameisensäure (jeweils 100% Ausbeute) was einer vollständigen Massenbilanz entspricht. Für Pyrazol wurden nur kohlenstoffhaltige Produkte identifiziert (126% Formiat und 34% Glyoxal auf das abgebaute Pyrazol normiert). Produkte welche Hydroxypyrazol und Hydrazid-Gruppen beinhalteten, wurden wahrscheinlich jeweils durch eine Sauerstoffaddition und den Criegeemechanismus gebildet. Die anhand der Resultate in dieser Arbeit postulierten Reaktionsmechanismen tragen zu einem besseren Verständnis der Stickstoff-Ozon-Chemie bei. Die hierbei identifizierten, stickstoffhaltigen Transformationsprodukte haben unterschiedliches Umweltverhalten. Einige Transformationsprodukte (z.B. Nitroalkane, *N*-Formyl Verbindungen) benötigen weitere Untersuchungen um ihre Auswirkungen auf die aquatische Umwelt und die menschliche Gesundheit zu verstehen.

Schlagwörter

Ozon, aliphatische Amine, Azole, Reaktionskinetik, Reaktionsmechanismen

Contents

Acknowledgements	iii
Abstract	v
Zusammenfassung	vi
Contents	viii
List of Figures	ix
List of Tables	xi
Chapter 1 Introduction	1
1.1 Nitrogen-containing compounds in water and wastewater treatment	2
1.1.1 Dissolved organic nitrogen	2
1.1.2 Micropollutants containing nitrogen	3
1.2 Ozonation in water and wastewater treatment	3
1.3 Reactions of nitrogen-containing compounds with ozone	4
1.3.1 Aliphatic amines	6
1.3.2 Heterocyclic amines	9
1.3.3 Amides, sulfonamides, and sulfamides	12
1.3.4 Anilines	13
1.3.5 Hydrazines, hydrazides, semicarbazides	14
1.4 Thesis layout	16
1.5 References	17
Chapter 2 Reactions of aliphatic amines with ozone: Kinetics and mechanisms	21
2.1 Introduction	23
2.2 Materials and methods	24
2.3 Results and discussion	25
2.3.1 Ozone reaction kinetics	25
2.3.2 Product analyses and reaction mechanisms	27
2.3.3 Practical implications	42
2.4 Conclusion	43
2.5 References	44
Supporting Information for Chapter 2	49
Chapter 3 Reactions of pyrrole, imidazole, and pyrazole with ozone: Kinetics and mechanisms	75
3.1 Introduction	77
3.2 Material and methods	78
3.3 Results and discussion	80
3.3.1 Ozone reaction kinetics	80

3.3.2	Reactive oxygen species.....	81
3.3.3	Transformation products and reaction pathways	83
3.3.4	Implications	94
3.4	Conclusion	95
3.5	References	96
Supporting Information for Chapter 3.....		101
Chapter 4	Conclusions and Outlook.....	169
Curriculum Vitae		172

List of Figures

Figure 1.1. Distribution of nitrogen-containing functional groups found in nitrogen-containing micropollutants (466 compounds).....	5
Figure 1.2. Examples of micropollutants containing multiple types of nitrogen-containing functional groups. The category each micropollutant belongs to is shown in parentheses.....	5
Figure 1.3. Examples of pharmaceuticals containing aliphatic amine moieties (primary, secondary, and tertiary amines from left to right; marked in red).....	6
Figure 1.4. Proposed mechanisms for the reactions of tertiary amines with ozone from various sources. ^{38,44,50,52-54}	8
Figure 1.5. Proposed mechanisms for the reactions of (a) secondary amines and (b) primary amines with ozone based on the available literature. ⁵⁵⁻⁶²	8
Figure 1.6. Examples of pharmaceuticals containing (a) saturated and (b) unsaturated heterocyclic amines moieties (the names of the nitrogen-containing functional groups, marked in red, are given in parentheses).....	10
Figure 1.7. Proposed mechanisms for the reactions of piperidine and piperidine derivatives with ozone. ^{54,57}	10
Figure 1.8. The major pathway of the reaction of pyridine with ozone. ^{64,65}	11
Figure 1.9. Examples of pharmaceuticals containing amide, sulfonamide, and sulfamide moieties (from left to right; marked in red).....	12
Figure 1.10. Proposed mechanisms for the reaction of hydrochlorothiazide with ozone. ⁵⁴	13
Figure 1.11. Proposed mechanisms for the reaction of diethylsulfamide with ozone forming <i>N</i> -nitrosodimethylamine (NDMA). ^{20,74}	13
Figure 1.12. Examples of pharmaceuticals containing aniline moieties.....	14
Figure 1.13. Proposed mechanisms for the reaction of aniline with ozone. ⁷⁷	14
Figure 1.14. Examples of NDMA precursors containing a hydrazine, hydrazide, or semicarbazide moiety (moieties are marked in red and shown in parentheses). ^{21,22}	15
Figure 1.15. Proposed mechanisms for the reactions of hydrazine derivatives with ozone forming <i>N</i> -nitrosodimethylamine (NDMA). ²²	15
Figure 1.16. Selected nitrogen-containing model compounds for detailed kinetic and mechanistic studies.....	16
Figure 2.1. Evolution of the amine model compounds and transformation products as a function of the ozone doses for the reactions of ozone with (a) triethylamine, (b) diethylamine, (c) <i>N,N</i> -diethylhydroxylamine, and (d) ethylamine.....	28
Figure 2.2. Proposed mechanism for the reaction of triethylamine with ozone.....	30
Figure 2.3. Proposed mechanism for the reaction of diethylamine with ozone.....	32
Figure 2.4. Proposed mechanism for the reaction of <i>N,N</i> -diethylhydroxylamine and <i>N</i> -ethylethanamine oxide with ozone.....	36
Figure 2.5. Proposed mechanism for the reaction of ethylamine with ozone.....	40

Figure 2.6. Summary of the reactions of aliphatic primary, secondary, and tertiary amines with ozone in aqueous solution based on this and other studies	42
Figure 3.1. Azole model compounds investigated in this study: Structures of pyrrole, imidazole, and pyrazole.....	78
Figure 3.2. Relative abatement of pyrrole and the formation (and consumption) of transformation products as a function of the molar ratio of $[O_3]/[Pyrrole]_0$	84
Figure 3.3. Initial reaction pathways (A, B, and C) proposed for the reaction of pyrrole with ozone based on the identified transformation products (highlighted in blue) and reactive oxygen species (in red).	86
Figure 3.4. Detailed reaction mechanisms of the subsequent degradation of the zwitterion formed via C2-addition (pathway C in Figure 3.3) of the pyrrole-ozone reaction (pathways D – G).....	88
Figure 3.5. Relative abatement of imidazole and the formation of transformation products as a function of the molar ratio of $[O_3]/[Imidazole]_0$	89
Figure 3.6. Proposed mechanisms for the reaction of imidazole with ozone based on the identified transformation products (highlighted in blue)	90
Figure 3.7. Relative abatement of pyrazole and the formation of formate as a function of the molar ratio of $[O_3]/[Pyrazole]_0$	92
Figure 3.8. Proposed mechanisms for the reaction of 1-benzylpyrazole with ozone based on the identified (highlighted in blue) and the proposed products.	94

List of Tables

Table 1.1. Constituents of dissolved organic nitrogen in natural waters and wastewater effluents.	2
Table 1.2. Second-order rate constants for the reactions of neutral forms of selected aliphatic amines with ozone.....	7
Table 1.3. Second-order rate constants for the reactions of unsaturated heterocyclic amines with ozone.	11
Table 2.1. Species-specific and apparent second-order rate constants for the reactions of the selected amines with ozone and pK_a values of the amines.	26
Table 2.2. Yields of reactive oxygen species (1O_2 and $^{\bullet}OH$) per consumed ozone at an amine:ozone ratio of 1:1	29
Table 3.1. Species-specific second-order rate constants (k) and apparent second-order rate constants at pH 7 ($k_{app, pH7}$) for the reactions of ozone with pyrrole, imidazole, pyrazole, maleimide, and 4-hydroxypyrazole.....	81
Table 3.2. Reaction stoichiometry and product yields for the reactions of pyrrole, imidazole, 1-benzylimidazole, pyrazole, and 1-benzylpyrazole with ozone at pH 7.0 – 7.6 in presence of <i>t</i> -butanol.	82

Chapter 1 Introduction

A critical review on reactions of nitrogen-containing compounds with ozone: Kinetics and mechanisms

1.1 Nitrogen-containing compounds in water and wastewater treatment

Since the invention of the industrial production of ammonia in the early 1900s, nitrogen-containing compounds were extensively synthesized and applied in agriculture (as fertilizers) and numerous industrial applications (explosives, rocket repellents, dyes, drugs, etc.).¹ The extensive use of nitrogen compounds has increased the amount of nitrogen returning to the environment.² Increased nitrate concentrations have been observed in rivers and groundwaters worldwide,¹ raising potential health concerns in drinking water.³ Nitrate in groundwaters is mostly attributed to agricultural activities,⁴ but leaky sewer and solid waste disposals also contribute to the increased nitrate levels especially beneath urban areas.⁵ Recently, growing emphasis has been laid on organic nitrogen which has been also found in elevated concentrations in surface waters. Major sources are considered intensive farming⁶ and discharge of municipal wastewater.⁷

1.1.1 Dissolved organic nitrogen

Total dissolved nitrogen occurs in two forms: dissolved inorganic nitrogen such as nitrite, nitrate, and ammonia/ammonium, and dissolved organic nitrogen (DON) such as amino acids, peptides and nucleotides. Wastewater discharge and agricultural activities have been shown to increase DON levels in many surface waters.⁷⁻⁹ Typical DON concentrations range from 0.2 to 0.9 mg N L⁻¹ for surface waters with varying dominant land-uses (e.g., urban, agricultural, and natural sites).^{7,10-12} Because of population growth, higher water demand, and water scarcity, these impaired waters become more dominant drinking water sources worldwide. As a result, the impact of the high DON levels on drinking water quality has received increasing attention. DON contains potential precursors of nitrogenous disinfection byproducts (N-DBPs) formed during the reactions with disinfectants commonly applied in water treatment (e.g., chlorine, chloramine, and ozone). Many studies have identified N-DBPs including haloacetonitriles, haloacetamides, halonitromethanes and nitrosamines from low molecular weight DON (e.g., free amino acids and simple aliphatic amines) to larger DON (e.g., algae or isolated organic material with high N contents).¹³ The majority of DON is still unidentified.¹⁴ The most common and identifiable DON components are combined amino acids (proteins and peptides) and free amino acids, which account for 7 – 50% of DON in natural waters and wastewater effluents (Table 1.1).^{7,9,11,14} Heterocyclic nitrogen compounds are considered to be the next dominant DON.⁹ They may be purines and pyrimidines, building blocks of RNA and DNA, but their proportions of DON in natural waters are largely unknown.¹⁵ Urea and simple aliphatic amines (e.g., methylamine) were also detected possibly as microbial degradation products.¹⁵

Table 1.1. Constituents of dissolved organic nitrogen in natural waters and wastewater effluents.

Compound	Percentage in DON	References
Total amino acids – the sum of the free and combined amino acids	7 – 50%	7,9,11,14
Free amino acids	1 – 5%	7,11
Urea	6%	11
Methylamines	< 1%	11
Nucleic acids (DNA and RNA), purines, and pyrimidines	NA ^a	15

^aGeneral proportion in DON is unknown, but a few measured concentrations in rivers and lakes are summarized in Jørgensen (2009)¹⁵ as 0.006 – 0.95 µM N for DNA, 0.25 – 9.30 µM N for RNA, and 0.06 µM N for purines.

1.1.2 Micropollutants containing nitrogen

Another important pool of nitrogen-containing compounds consists of micropollutants. Micropollutants include pharmaceuticals, pesticides, and personal care products that are not fully removed by conventional wastewater treatment plants and therefore are discharged to the aquatic environment.¹⁶ As they are often biologically active, micropollutants are of growing concern because of their possible adverse effects on the aquatic environment and human health. Many micropollutants contain nitrogen and some have shown to be transformed into toxic transformation products after oxidation processes in water and wastewater treatment.¹⁷ In reality, chemical oxidants applied for water treatment are mostly consumed by DON present in much higher quantity (0.01 – 0.15 mM as N)^{7,14} rather than by micropollutants ($< 0.1 \mu\text{M}$) in surface waters and wastewater effluents.¹⁸ However, certain micropollutants can produce toxic transformation products with high molar yields, which have gained particular attention: e.g., ranitidine transformed into *N*-nitrosodimethylamine (NDMA) by chloramine with $> 70\%$ yield,¹⁷ *N,N*-dimethylsulfamide into NDMA by ozone with $> 50\%$ yield,^{19,20} semicarbazide derivatives into NDMA by ozone with 10% and 27% yields,²¹ and daminozide into NDMA by ozone with 100% yield.²² Based on these high yields of toxic compounds, micropollutants may still contribute significantly to the overall oxidant-induced toxicity, even though they are present in much smaller concentrations than DON.

1.2 Ozonation in water and wastewater treatment

Ozone has been applied in water and wastewater treatment as a disinfectant and/or oxidant since the early 1900s.²³ As a disinfectant, ozone is considered as an alternative to chlorine disinfection, as it not only effectively kills bacteria, viruses, and protozoa, but also prevents the formation of trihalomethanes and haloacetic acids, the disinfection byproducts associated with chlorine. Ozone is also used as a powerful oxidant in conjunction with hydroxyl radical, a secondary oxidant produced from ozone decay in water. As an electrophile, ozone reacts preferentially with electron-rich compounds such as olefins, activated aromatic compounds, neutral amines and reduced sulfur compounds with second-order rate constants of $k_{\text{O}_3} = 10^3 \text{ M}^{-1} \text{ s}^{-1}$ to $10^9 \text{ M}^{-1} \text{ s}^{-1}$.²³ Hydroxyl radical oxidizes almost all organic and inorganic compounds including ozone-refractory compounds (e.g. saturated aliphatic hydrocarbons) with nearly diffusion-controlled second-order rate constants of $k_{\text{OH}} \geq 10^9 \text{ M}^{-1} \text{ s}^{-1}$.²⁴ Despite these advantages, ozonation has potential to form disinfection byproducts such as bromate,²⁵ quinones,²⁶ and low molecular weight oxygen-containing organic compounds.^{27,28} Most of the byproducts are biodegradable and easily removed by biological post-treatment implemented after ozonation.^{27,29} Bromate is hardly abated by conventional treatment processes, and therefore, minimizing its formation is an important mitigation strategy for ozonation.²⁵

Recently, ozonation has been considered a viable option for enhanced abatement of micropollutant loads in wastewater treatment plants.³⁰ It has been demonstrated to efficiently abate various micropollutants in laboratory-, pilot-, and full-scale systems.^{31–35} However, micropollutants are not fully mineralized with common ozone doses applied in treatment plants, but rather converted to transformation products whereof the structures, biological activities, or ecotoxicity aspects are largely unknown. Generally, overall toxicity after ozonation is decreased by selective reactions of ozone with the specific moieties responsible for biological activities.^{36–38} Even when transformation products exerting toxicity (e.g., assimilable organic carbon) are formed, biological post-treatment after ozonation usually effectively removes such compounds and ensures the quality of treated waters.^{27,39} However, some transformation products are more persistent than others during the biological post-

treatment (e.g., *N*-oxides)^{29,40} wherefore, the possibility of the presence of toxic products in treated waters cannot be entirely ruled out. To predict transformation products and assess their impact on the receiving waters, detailed knowledge is required on the kinetics and mechanisms of the reactions of micropollutants with ozone. Over the last few decades, a wealth of information has been collected regarding reactions of ozone with ozone-reactive compounds such as olefins and aromatic compounds and the relevant information has been well compiled.²³ Based on the kinetic/mechanistic information, computational tools have been developed to predict reaction kinetics and transformation products upon ozonation.^{41,42} Such tools highly depend on the underlying empirical information which should ideally include all ozone-reactive moieties. However, for nitrogen-containing compounds, previous studies have been focused on certain moieties (e.g., tertiary amines and anilines). In-depth understanding on the reactions of ozone with other principal nitrogen-containing functional groups is still missing.

1.3 Reactions of nitrogen-containing compounds with ozone

According to a comprehensive list including > 500 organic substances such as pharmaceuticals, pesticides, personal care products, food additives, industrial chemicals, and their metabolites (selected based on measurement campaigns in Swiss surface waters, chemical consumption data, and various international substances lists), about 85% of the selected substances have at least one nitrogen in their structures.^{29,43} These nitrogen-containing compounds contain a variety of nitrogen-containing functional groups including aliphatic amines, heterocyclic amines, amides, anilines, etc. Aliphatic amines (AA) including primary, secondary, or tertiary amines comprise 40% of the nitrogen-containing micropollutants as a single functional group or along with other functional groups (AA, AA mix, and AA+HA mix, Figure 1.1). Saturated heterocyclic amines containing secondary or tertiary amines are also classified as aliphatic amines as they behave similarly with regard to the reaction with ozone (see section 1.3.2). Another common functional groups are unsaturated heterocyclic amines (HA) accounting for 44% of the nitrogen-containing micropollutants (HA, HA mix, and AA+HA mix, Figure 1.1). The sum of the proportions of AA, HA, and their combinations is 70%; in other words, micropollutants containing neither AA nor HA functional groups account for only 30% of the nitrogen-containing micropollutants. Many micropollutants contain multiple types of nitrogen-containing functional groups within the structures (Figure 1.2). Amides (including sulfonamides, urea-based compounds, and sulfamides) and anilines are also common functional groups but usually present along with aliphatic amines or unsaturated heterocyclic amines in the micropollutants (incorporated in AA mix, HA mix, and AA+HA mix, Figure 1.1). Aliphatic amines and unsaturated heterocyclic amines are also commonly found together in the structures of micropollutants (AA+HA mix, Figure 1.1). As minor groups, carbamates, nitriles, imines, hydrazines, and nitro compounds are present (Others and Others mix, Figure 1.1). The classification shows clear prevalence of aliphatic amines and heterocyclic amines as structural units of micropollutants. The following section discusses key features for each nitrogen-containing functional group with regard to its reaction with ozone.

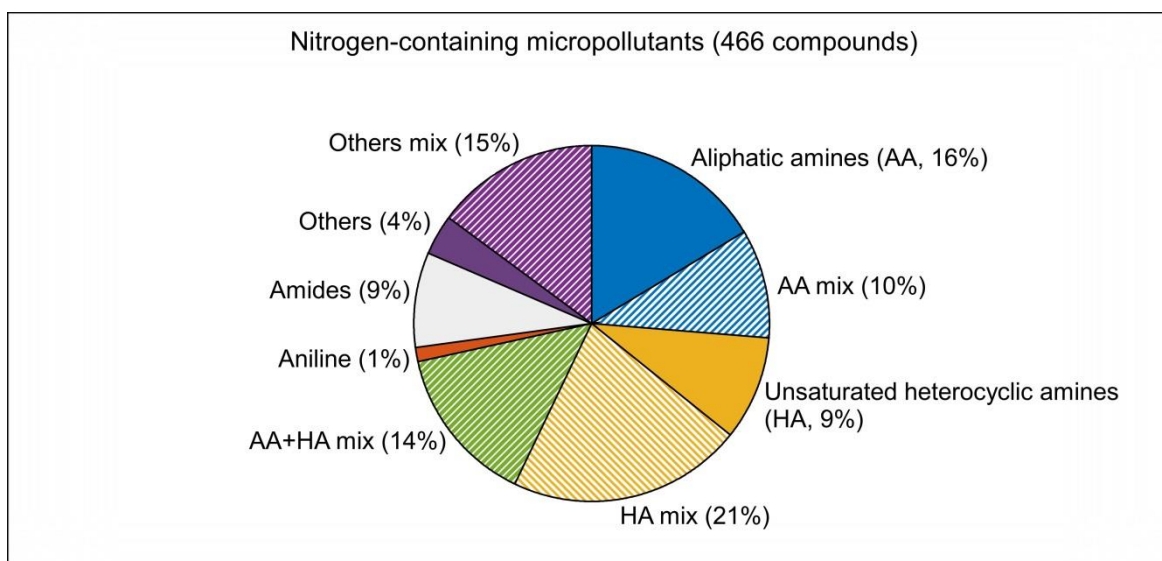


Figure 1.1. Distribution of nitrogen-containing functional groups found in nitrogen-containing micropollutants (466 compounds). The entire list of the micropollutants (from a total of 550 compounds as nitrogen and non-nitrogen compounds) is available in Bourgin et al. (2018).²⁹ Solid patterns indicate micropollutants containing only one type of functional group; dashed patterns indicate micropollutants containing multiple types of functional groups. The functional groups were classified as AA: aliphatic amines or saturated heterocyclic amines, containing primary, secondary, or tertiary amines; HA: unsaturated heterocyclic amines; Amides: amides, sulfonamides, urea-based compounds, and sulfamides; Anilines: substituted anilines; Others: unclassified functional groups including (in order of frequency) carbamates, nitriles, imines, hydrazines, nitro compounds, etc.; X mix: micropollutants containing Amides, Anilines, or Others in addition to the functional group X, where X indicates AA, HA, AA+HA, and Others.

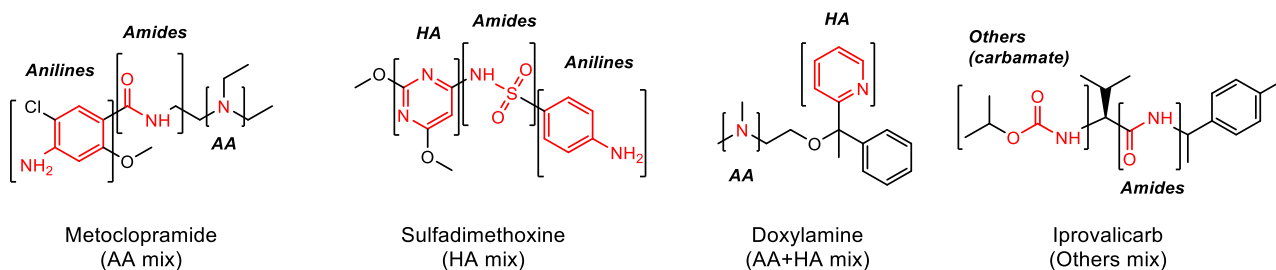


Figure 1.2. Examples of micropollutants containing multiple types of nitrogen-containing functional groups. The category to which each micropollutant belongs is shown in parentheses.

1.3.1 Aliphatic amines

Aliphatic amines are some of the most frequently found nitrogen-containing functional groups in micropollutants and also common moieties of DON. Aliphatic amines are derivatives of ammonia for which hydrogen atoms are substituted with one or more alkyl groups. Depending on the number of alkyl substituents, aliphatic amines can be categorized as primary, secondary, or tertiary amines as illustrated in Figure 1.3 for some examples. The nitrogen of aliphatic amines has a lone electron pair which can be easily attacked by ozone. If an amine is protonated, the electron pair is no longer available for an ozone attack, leading to a dramatic decrease in its reactivity with ozone. Therefore, the ozone reactivity of aliphatic amines is highly influenced by the speciation of amines determined by the pH of the solution. Examples of second-order rate constants for the reactions of aliphatic amines (as simple compounds and as micropollutants) with ozone are summarized in Table 1.2. Generally, aliphatic amines present in the neutral form react fast with ozone with k_{03} ranging from 10^3 to $10^8 \text{ M}^{-1} \text{ s}^{-1}$. The ozone reactivity of aliphatic amines tends to increase as the number of alkyl substituents increases (i.e., k_{03} = primary < secondary < tertiary), with the highest second-order rate constant k_{03} of $10^8 \text{ M}^{-1} \text{ s}^{-1}$ determined for micropollutants containing a tertiary amine moiety (tamoxifen and toremifene).⁴⁴ The tendency is likely related to the electron-donating nature of alkyl substituents, increasing the electron density leading to a higher reactivity of the nitrogen with the electrophilic ozone.

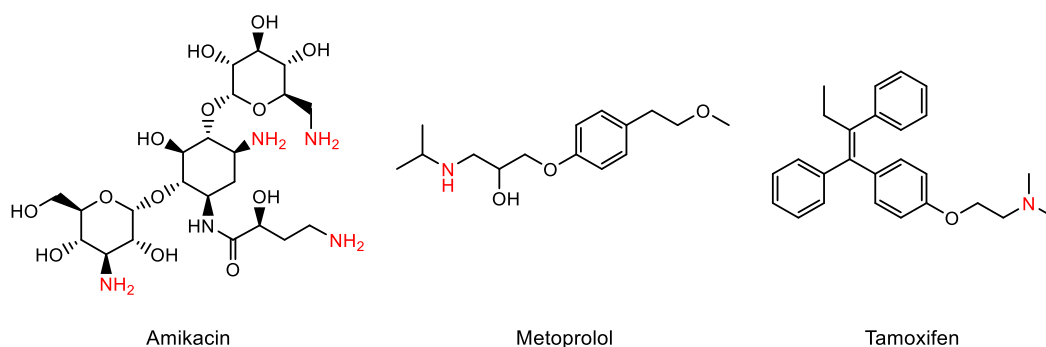


Figure 1.3. Examples of pharmaceuticals containing aliphatic amine moieties (primary, secondary, and tertiary amines from left to right; marked in red).

Table 1.2. Second-order rate constants for the reactions of neutral forms of selected aliphatic amines with ozone.

Compound	Amine type	pK _a	pH ^a	<i>k</i> ₀₃ , M ⁻¹ s ⁻¹ ^b	Reference
Simple aliphatic amines					
Ammonia	-	9.2		20	45
Alanine	primary	9.9		6.4 × 10 ⁴	45
Glycine	primary	9.8		1.3 × 10 ⁵	45
Methylamine	primary	10.6		< 1.4 × 10 ⁵	45
Dimethylamine	secondary	11.0		1.9 × 10 ⁷	45
Diethylamine	secondary	10.5		6.2 × 10 ⁵	46
Trimethylamine	tertiary	9.8		4.1 × 10 ⁶	45
Triethylamine	tertiary	11.0		2.1 × 10 ⁶	46
Micropollutants					
Amikacin	primary	6.7, 8.4	7	1.8 × 10 ^{3c}	47
Propranolol	secondary	9.5	7	~1 × 10 ^{5c}	48
Metoprolol	secondary	9.7		8.6 × 10 ⁵	48
Spectinomycin	secondary	6.8, 8.8		1.3 × 10 ⁶	49
Venlafaxine	tertiary	9.3	7	3.3 × 10 ^{4c}	50
Clarithromycin	tertiary	9.0	7	4.0 × 10 ^{4c}	38
Roxithromycin	tertiary	9.2		1.0 × 10 ⁷	35,51
Tylosin	tertiary	7.7		2.7 × 10 ⁶	51
Nitrilotriacetic acid (NTA)	tertiary	Multiple ^d		9.8 × 10 ⁵	52
Ethylenediaminetetraacetic acid (EDTA)	tertiary	Multiple ^d		3.2 × 10 ⁶	52
Tramadol	tertiary	9.4		1.0 × 10 ⁶	53
Tamoxifen	tertiary	9.5		3.2 × 10 ⁸	44
Toremifene	tertiary	9.6		1.5 × 10 ⁸	44

^ameasured pH for determining apparent second-order rate constants; ^bspecies-specific second-order rate constants of the neutral form of amines except amikacin, propranolol, venlafaxine, and clarithromycin; ^capparent second-order rate constants at pH 7. ^dpK_a values are 1.7, 2.9, 10.3 for NTA and 0.3, 1.0, 2.0, 2.7, 6.2, 10.2 for EDTA.

Mechanistic investigations of the reaction of aliphatic amines with ozone have mainly focused on tertiary amines^{38,44,50,52–54} and the findings are summarized in Figure 1.4. *N*-oxides and singlet oxygen were often identified as major products from tertiary amines upon ozonation. Accordingly, it has been suggested that ozone initially forms an adduct on the nitrogen (reaction 1), which is then further degraded to a *N*-oxide and singlet oxygen (reaction 2). In competition, the adduct can decompose into an amine radical cation and an ozonide radical anion (reaction 3), which can be also produced via an electron transfer pathway (reaction 5). The radicals can react again to form a *N*-oxide and oxygen in its triplet state (reaction 4) or react separately with dissolved oxygen (reaction 6) and water (reaction 7) to yield an *N*-dealkylated amine (a secondary amine) and hydroxyl radical.

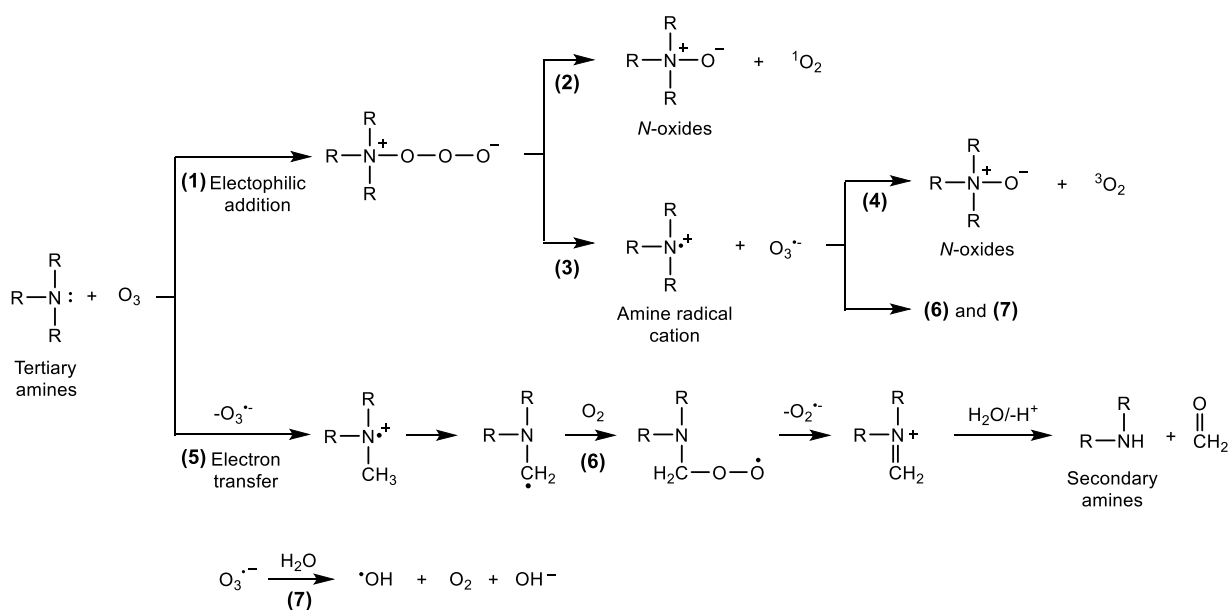


Figure 1.4. Proposed mechanisms for the reactions of tertiary amines with ozone from various sources.^{38,44,50,52-54}

The reactions of secondary and primary amines with ozone have been studied as well but to a lesser extent than tertiary amines. Hydroxylamines and primary amines were identified from secondary amines upon ozonation (Figure 1.5a).⁵⁵⁻⁵⁸ They are analogous to *N*-oxides and secondary amines from the reactions of tertiary amines with ozone. Ozone reaction studies for primary amines were performed for methylamine⁵⁹ and amino acids such as glycine^{60,61} and serine.⁶² Methylamine was transformed into nitromethane with an almost 100% yield by 12 molar equivalents of ozone.⁵⁹ Glycine and serine were transformed into nitrate with about 90% yields by 5 to 20 molar equivalents of ozone.⁶⁰⁻⁶² Only highly oxidized products (nitroalkanes and nitrates) were identified during the reactions of primary amines with ozone, due to the excessive ozonation conditions. Initial ozonation products of primary amines are still unknown.

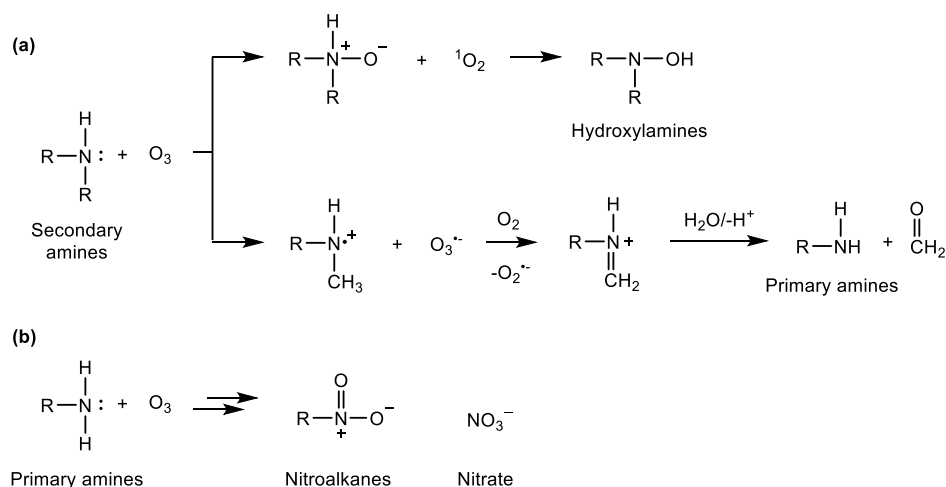


Figure 1.5. Proposed mechanisms for the reactions of (a) secondary amines and (b) primary amines with ozone based on the available literature.⁵⁵⁻⁶²

1.3.2 Heterocyclic amines

Heterocyclic amines form other principal nitrogen-containing functional groups as structural components of micropollutants as well as of DON. They are cyclic compounds containing at least two different elements including nitrogen in a ring structure. The heterocyclic amines found in micropollutants and DON usually consist of 5-membered, 6-membered or fused rings resulting from a combination of both. They are divided into two groups depending on the degree of saturation.

Saturated heterocyclic amines. Saturated heterocyclic amines (e.g., piperazine in cetirizine and piperidine in fexofenadine, Figure 1.6) are structurally close to aliphatic amines and behave similarly with regard to ozone reactions. According to a study on the reaction of cetirizine and fexofenadine with ozone, they are transformed into *N*-oxides as major products and dealkylated products as minor products in the same way as aliphatic tertiary amines (Figure 1.7).⁵⁴ They react fast with ozone with species-specific second-order rate constants k_{O_3} of $2.8 \times 10^5 \text{ M}^{-1} \text{ s}^{-1}$ (cetirizine) and $5.6 \times 10^5 \text{ M}^{-1} \text{ s}^{-1}$ (fexofenadine), within the range of the rate constants of micropollutants containing tertiary amine moieties (Table 1.2). Another recent study on secondary heterocyclic amines found a high yield of *N*-hydroxylamine from piperidine, similar to ozonation products of aliphatic secondary amines.⁵⁷

Unsaturated heterocyclic amines. The more interesting group of heterocyclic amines is unsaturated heterocycles (e.g. pyridine in sulfapyridine, imidazole in climbazole, and benzimidazole and tetrazole in candesartan, Figure 1.6). The second-order rate constants for the reactions of ozone with unsaturated heterocyclic amines available to date are summarized in Table 1.3. The ozone reactivity of unsaturated heterocyclic amines significantly varies with k_{O_3} ranging from $10^{-1} \text{ M}^{-1} \text{ s}^{-1}$ to $10^8 \text{ M}^{-1} \text{ s}^{-1}$. Six-membered heterocyclic amines like pyridine and pyrazine react very slowly with ozone, whereas compounds containing an imidazole moiety such as histidine and irbesartan exhibit very high ozone reactivity. This difference may be due to the effect of the nitrogen atom on the electronic distribution in the aromatic ring, which can induce or withdraw π electrons.⁶³ Six-membered heterocyclic amines, pyridine, pyridazine, and pyrazine, were thoroughly studied with regard to their reactions with ozone, and *N*-oxides were found as major transformation products (Figure 1.8).^{64,65} However, ozone reaction mechanisms of five-membered heterocyclic amines, expected to be much more reactive towards ozone, are largely unknown.

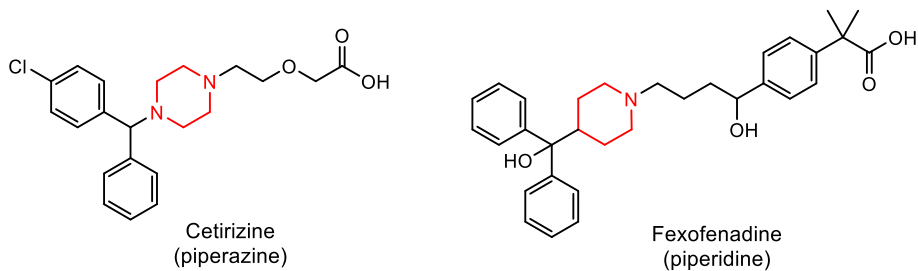
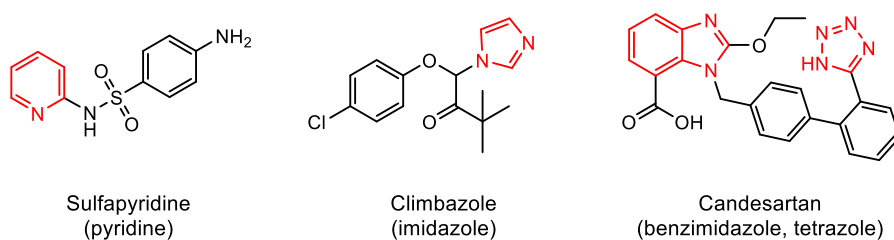
(a) Saturated heterocyclic amines**(b) Unsaturated heterocyclic amines**

Figure 1.6. Examples of pharmaceuticals containing (a) saturated and (b) unsaturated heterocyclic amines moieties (the names of the nitrogen-containing functional groups, marked in red, are given in parentheses).

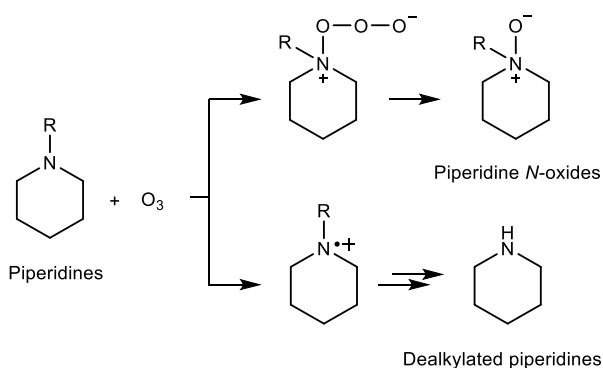
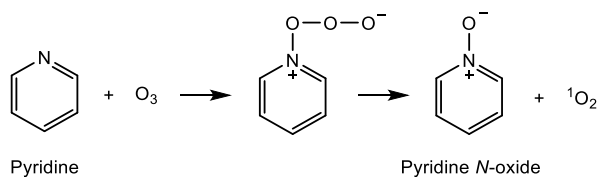


Figure 1.7. Proposed mechanisms for the reactions of piperidine and piperidine derivatives with ozone.^{54,57}

Table 1.3. Second-order rate constants for the reactions of unsaturated heterocyclic amines with ozone.

Compound	Substructure	pK _a	pH ^a	k ₀₃ , M ⁻¹ s ⁻¹ ^b	Reference
Simple heterocyclic amines					
3,5-Dimethylisoxazole	isoxazole	NA		5.4 × 10 ¹	51
4-Methylimidazole	imidazole	7.5		3.1 × 10 ⁶	46
5,6-Dimethylbenzotriazole	benzotriazole	~2		8.8 × 10 ²	23
5-Chlorobenzotriazole	benzotriazole	0, 7.5		1.3 × 10 ¹	23
5-Methylbenzotriazole	benzotriazole	~1.7, ~8.5		1.6 × 10 ²	23
Creatinine	imidazole + primary amine	12.3	6	~2 ^c	45
Histidine	imidazole + primary amine	6.0		2.1 × 10 ⁵	46
Imidazole	imidazole	7.0		2.4 × 10 ⁵	46
N-(4)-Acetylsulfamethoxazole	isoxazole	5.5		2.6 × 10 ²	51
N-a-Acetylhistidine	imidazole	7.3		8.4 × 10 ⁵	46
Quinoline	quinoline	4.9		5.1 × 10 ¹	66
Pyrazine	pyrazine	0.7		1.7 × 10 ⁻¹	65
Pyridazine	pyridazine	2.2		1.4	65
Pyridine	pyridine	5.2		3	45
Pyrimidine	pyrimidine	1.2		6.6 × 10 ⁻²	65
Micropollutants					
4-Dimethylaminoantipyrine	pyrazole + tertiary amine	5.1		1.7 × 10 ⁸	67
Atrazine	triazine + secondary amine	1.6	2	6.0 ^c	68
Benzotriazole	benzotriazole	1.6, 8.2		3.5 × 10 ¹	23
Candesartan	indazole + tetrazole	Multiple ^d	7	5.6 × 10 ² ^c	29
Diazepam	diazepine	3.4	7	7.5 × 10 ⁻¹ ^c	35
Irbesartan	imidazole + tetrazole	3.7, 4.4 ⁶⁹	7	2.4 × 10 ¹ ^c	29
Lamotrigine	triazine + primary amine	NA	6	~4 ^c	70
Losartan	imidazole + tetrazole	3.0, 4.3 ⁶⁹	7	2.1 × 10 ⁵ ^c	29
Prometon	triazine + secondary amine	4.3	7.5	< 1.2 × 10 ¹ ^c	71
Simazine	triazine + secondary amine	2.0		4.8	72
Telmisartan	indazole	NA	7	1.2 × 10 ⁵ ^c	29
Trimethoprim	pyrimidine + primary amine	3.2, 7.1		5.2 × 10 ⁵	51

^ameasured pH for determining apparent second-order rate constants; ^bspecies-specific second-order rate constants of the neutral form of amines except creatinine, atrazine, candesartan, diazepam, irbesartan, lamotrigine, losartan, prometon, and telmisartan; ^capparent second-order rate constants at the measured pH. ^dpK_a values are 2.1, 3.3, and 4.5.⁶⁹

Figure 1.8. The major pathway of the reaction of pyridine with ozone.^{64,65}

1.3.3 Amides, sulfonamides, and sulfamides

Amides and sulfonamides are common nitrogen-containing functional groups present in micropollutants (Figure 1.9). Due to the electron-withdrawing nature of the carbonyl and sulfonyl groups, the lone electron pair on nitrogen is delocalized into the neighboring atom and no longer available for the electrophilic attack of ozone. As a result, the second-order rate constants for the reactions of amides with ozone are low with $k_{03} < 10^2 \text{ M}^{-1} \text{ s}^{-1}$.^{46,73} However, if the electron-withdrawing effect of the neighboring group is strong enough, the nitrogen becomes acidic and a deprotonation may occur ($\text{R}_2\text{NH} \leftrightarrow \text{R}_2\text{N}^- + \text{H}^+$). The deprotonated species has a higher reactivity towards ozone due to the development of the negative charge on the nitrogen. This occurs in the nitrogen of the cyclic sulfonyl moiety of hydrochlorothiazide which reacts fast with ozone ($k_{03} > 10^5 \text{ M}^{-1} \text{ s}^{-1}$) at $\text{pH} > 8$ where the deprotonated cyclic sulfonyl moiety is expected.⁵⁴ The deprotonated hydrochlorothiazide reacts with ozone to form chlorothiazide as a major product with an almost 100% yield (Figure 1.10).⁵⁴ Electrophilic addition and electron transfer mechanisms were proposed (Figure 1.10), in analogy to the reactions of tertiary and secondary amines with ozone (Figure 1.4 and Figure 1.5).

Sulfamides are not as common moieties as amides or sulfonamides. However, they have potential to form *N*-nitrosodimethylamine (NDMA), a nitrogenous disinfection byproduct, upon ozonation under certain circumstances. Dimethylsulfamide, a degradant of the fungicide tolylfluanide, reacts slowly with ozone with the second-order rate constant k_{03} of $\sim 20 \text{ M}^{-1} \text{ s}^{-1}$, and the reaction does not lead to NDMA formation.²⁰ However, in presence of bromide (ubiquitous in all waters), dimethylsulfamide reacts fast with hypobromous acid formed by the reaction of bromide with ozone ($k_{\text{HOBr}} = 7.1 \times 10^8 \text{ M}^{-1} \text{ s}^{-1}$, for the deprotonated form of dimethylsulfamide), and further degrades into NDMA (Figure 1.11).^{20,74,75} During the reaction, bromide is released and reacts with ozone again, acting as a catalyst.^{20,74}

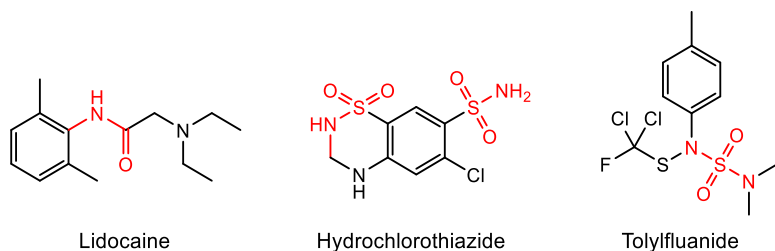


Figure 1.9. Examples of pharmaceuticals containing amide, sulfonamide, and sulfamide moieties (from left to right; marked in red).

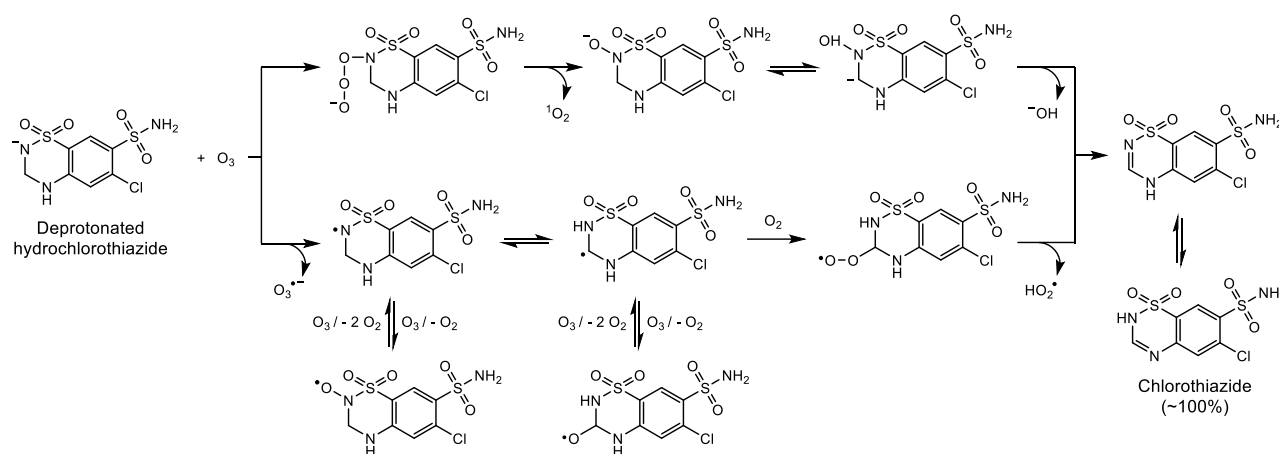


Figure 1.10. Proposed mechanisms for the reaction of hydrochlorothiazide with ozone.⁵⁴

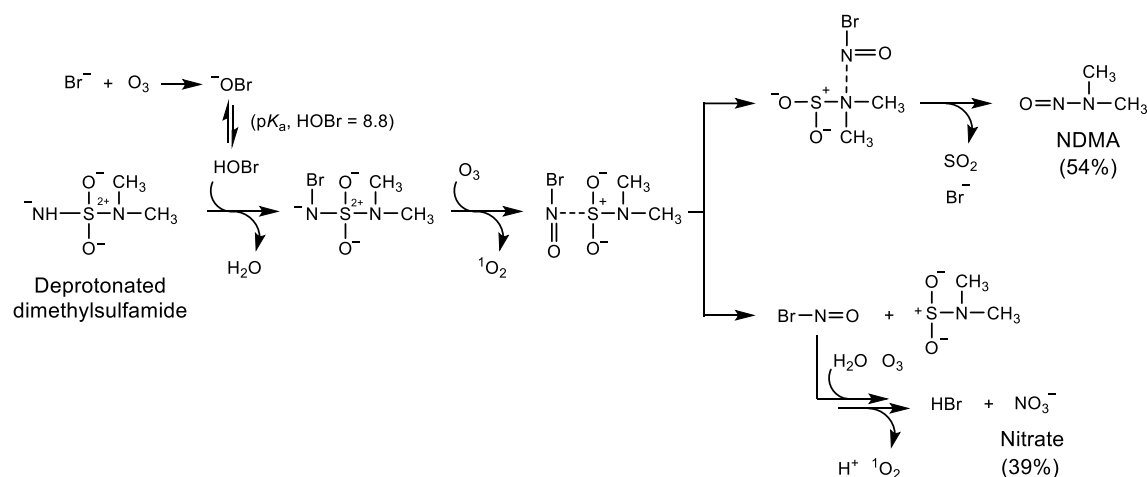


Figure 1.11. Proposed mechanisms for the reaction of diemethylsulfamide with ozone forming *N*-nitrosodimethylamine (NDMA).^{20,74}

1.3.4 Anilines

Anilines are often found in the structures of micropollutants with various substituents on the ring (Figure 1.12). Aniline itself reacts very fast with ozone ($k_{O_3} > 10^6 \text{ M}^{-1} \text{ s}^{-1}$).^{45,76,77} Substituted anilines show different reactivity depending on the effect of ring substituents on the benzene ring.^{76,77} The sites of ozone attack have been found to be both the nitrogen and the activated aromatic ring (Figure 1.13).⁷⁷ Nitrosobenzene, nitrobenzene, azobenzene and azoxybenzene were identified as the products from the addition of ozone to nitrogen (reaction 11),⁷⁷⁻⁷⁹ yet the reaction seems minor according to their low yields (< 8%).⁷⁷ The products with two additional aniline substituents were hypothesized (2-amino-5-anilino-benzochinon-anil and 2,5-dianilino-*p*-benzochinon-imin), likely formed from the aminyl radical form of aniline via an electron transfer pathway (reaction 10) and subsequent reactions with other products.⁷⁷ The major identifiable reaction pathways were the ozone additions on the aro-

matic ring which resulted in *p*-hydroxyaniline and *o*-hydroxyaniline with about 40% yield as a sum of the yields of all hydroxyanilines (reactions 8 and 9).

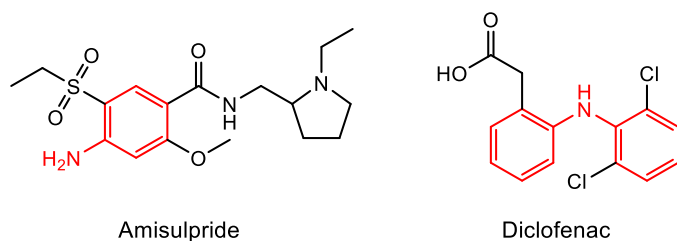


Figure 1.12. Examples of pharmaceuticals containing aniline moieties.

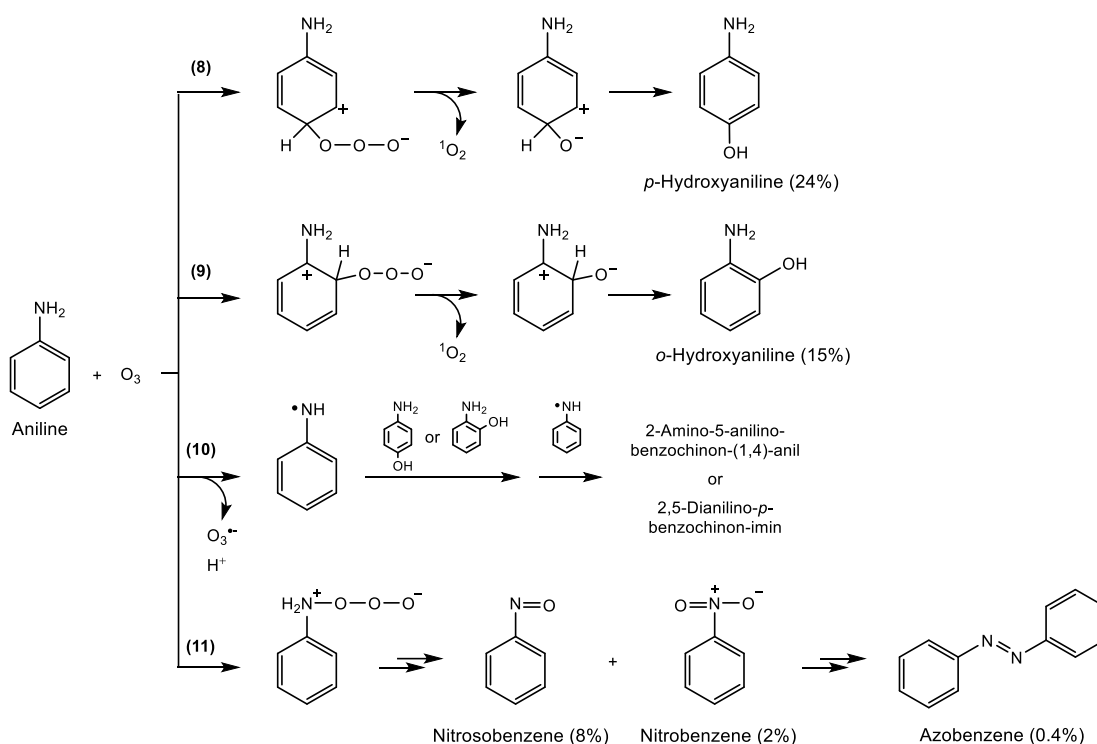


Figure 1.13. Proposed mechanisms for the reaction of aniline with ozone.⁷⁷

1.3.5 Hydrazines, hydrazides, semicarbazides

Hydrazine derivatives such as hydrazides and semicarbazides comprise a minor group in nitrogen-containing micropollutants. However, their occurrences in ozonation may be of great significance, as they can be transformed into NDMA with high yields, especially if substituted by a *N,N*-dimethylamino group (Figure 1.14). Industrial chemicals containing semicarbazide moieties were identified as NDMA precursors with molar NDMA formation yields of up to 140% upon ozonation.^{21,80} Daminozide, a pesticide containing a hydrazide moiety, yielded 100% NDMA by the reaction with ozone.²² They exhibit high reactivity to ozone with apparent second-order rate

constants at pH 7 higher than $10^5 \text{ M}^{-1} \text{ s}^{-1}$.²² Electrophilic addition and electron transfer were proposed as initial reaction pathways, followed by secondary ozone reactions to eventually form NDMA (Figure 1.15).²²

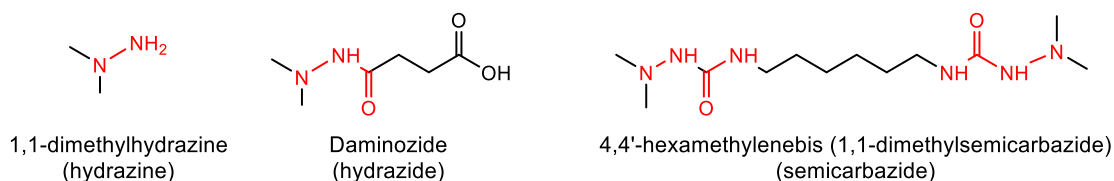


Figure 1.14. Examples of NDMA precursors containing a hydrazine, hydrazide, or semicarbazide moiety (moieties are marked in red and shown in parentheses).^{21,22}

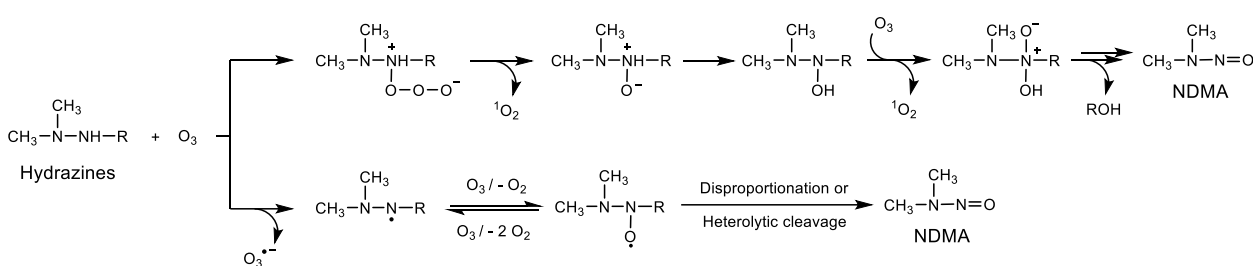


Figure 1.15. Proposed mechanisms for the reactions of hydrazine derivatives with ozone forming *N*-nitrosodimethylamine (NDMA).²²

Overall, nitrogen-containing compounds widely present as natural (DON) and artificial (micropollutants) substances react fast with ozone when they are in neutral forms, because of the electron-rich nature of nitrogen in its reduced form. This indicates that the reactions of nitrogen-containing compounds with ozone inevitably occur in water and wastewater treatment where ozonation is applied for disinfection or oxidation. Despite the great relevance of nitrogen-containing compounds to ozone chemistry, knowledge gaps still exist for some principal nitrogen-containing functional groups. Many studies were conducted on the reactions of aliphatic amines with ozone, but most focused on tertiary amine moieties. The reactions of primary/secondary amines with ozone were investigated to a lesser extent, and their mass balances and primary transformation products are relatively unknown. Unsaturated heterocyclic amines comprise a large percentage of the nitrogen-containing micropollutants, but only some specific subgroups (e.g., six-membered heterocycles) were studied with regard to their reactions with ozone. Moreover, previous mechanistic studies have focused mainly on micropollutants with complex structures and their results are often very specific. More information is needed on fundamental ozone reaction mechanisms by using simple model compounds representing structural units of complex nitrogen-containing compounds.

1.4 Thesis layout

The aim of this thesis was to elucidate reaction mechanisms of nitrogen-containing compounds with ozone based on principal nitrogen-containing functional groups. The nitrogen-containing functional groups were selected based on the following criteria: (1) common structural unit of DON and micropollutants, (2) high/moderate reactivity towards ozone, and (3) lack of understanding with regard to ozone reaction mechanisms. Based on these criteria, the nitrogen-containing functional groups selected were aliphatic amines and five-membered heterocyclic amines (Figure 1.16). A set of compounds was chosen for each functional group with a slight modification in their structures (e.g. ethylamine, diethylamine and triethylamine for the group of aliphatic amines) to facilitate systematic investigations of the reaction mechanisms.

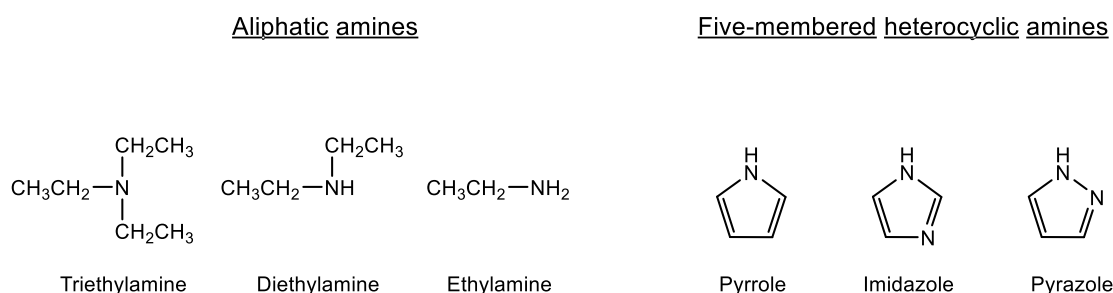


Figure 1.16. Selected nitrogen-containing model compounds for detailed kinetic and mechanistic studies in this thesis.

With the selection of nitrogen-containing compounds, the following objectives were set:

- 1) Determination of second-order rate constants for the reactions of the selected nitrogen-containing compounds with ozone,
- 2) Identification/quantification of transformation products and reactive oxygen species,
- 3) Kinetic simulations and quantum chemical computations to supplement empirical evidences.

The following chapters proceeded towards the goal of a better understanding of nitrogen-ozone chemistry while pursuing the three objectives.

Chapter 1 compiles the general background of nitrogen-containing compounds in the context of ozonation processes in water and wastewater treatment.

Chapter 2 presents the investigations of the reactions of ozone with the aliphatic amines, ethylamine, diethylamine, and triethylamine.

Chapter 3 presents the investigations of the reactions of ozone with the five-membered heterocyclic amines, pyrrole, imidazole, and pyrazole.

Chapter 4 provides general conclusions summarizing major findings of the thesis, their implications, and an outlook.

1.5 References

- (1) Smil, V.; Haber, F.; Bosch, C. *Enriching the Earth : Fritz Haber, Carl Bosch, and the Transformation of World Food Production*; MIT Press: Cambridge, Mass., 2001.
- (2) Galloway, J. N.; Dentener, F. J.; Capone, D. G.; Boyer, E. W.; Howarth, R. W.; Seitzinger, S. P.; Asner, G. P.; Cleveland, C. C.; Green, P. A.; Holland, E. A.; et al. Nitrogen Cycles: Past, Present, and Future. *Biogeochemistry* **2004**, *70* (2), 153–226. <https://doi.org/10.1007/s10533-004-0370-0>.
- (3) WHO. *Nitrate and Nitrite in Drinking-Water*; WHO/SDE/WSH/07.01/16/Rev/1; World Health Organization: Geneva, 2011.
- (4) van der Voet, E.; Kleijn, R.; Udo De Haes, H. A. Nitrogen Pollution in the European Union – Origins and Proposed Solutions. *Environmental Conservation* **1996**, *23* (2), 120–132. <https://doi.org/10.1017/S0376892900038509>.
- (5) Wakida, F. T.; Lerner, D. N. Non-Agricultural Sources of Groundwater Nitrate: A Review and Case Study. *Water Research* **2005**, *39* (1), 3–16. <https://doi.org/10.1016/j.watres.2004.07.026>.
- (6) Graeber, D.; Boëchat, I. G.; Encina-Montoya, F.; Esse, C.; Gelbrecht, J.; Goyenola, G.; Gücker, B.; Heinz, M.; Kronvang, B.; Meerhoff, M.; et al. Global Effects of Agriculture on Fluvial Dissolved Organic Matter. *Scientific Reports* **2015**, *5* (1). <https://doi.org/10.1038/srep16328>.
- (7) Westerhoff, P.; Mash, H. Dissolved Organic Nitrogen in Drinking Water Supplies: A Review. *Journal of Water Supply: Research and Technology-AQUA* **2002**, *51* (8), 415–448. <https://doi.org/10.2166/aqua.2002.0038>.
- (8) Pellerin, B. A.; Kaushal, S. S.; McDowell, W. H. Does Anthropogenic Nitrogen Enrichment Increase Organic Nitrogen Concentrations in Runoff from Forested and Human-Dominated Watersheds? *Ecosystems* **2006**, *9* (5), 852–864. <https://doi.org/10.1007/s10021-006-0076-3>.
- (9) Dotson, A.; Westerhoff, P. Occurrence and Removal of Amino Acids during Drinking Water Treatment. *Journal - American Water Works Association* **2009**, *101* (9), 101–115. <https://doi.org/10.1002/j.1551-8833.2009.tb09963.x>.
- (10) Lusk, M. G.; Toor, G. S. Dissolved Organic Nitrogen in Urban Streams: Biodegradability and Molecular Composition Studies. *Water Research* **2016**, *96*, 225–235. <https://doi.org/10.1016/j.watres.2016.03.060>.
- (11) Sipler, R. E.; Bronk, D. A. Chapter 4 - Dynamics of Dissolved Organic Nitrogen. In *Biogeochemistry of Marine Dissolved Organic Matter (Second Edition)*; Hansell, D. A., Carlson, C. A., Eds.; Academic Press: Boston, 2015; pp 127–232. <https://doi.org/10.1016/B978-0-12-405940-5.00004-2>.
- (12) Jani, J.; Toor, G. S. Composition, Sources, and Bioavailability of Nitrogen in a Longitudinal Gradient from Freshwater to Estuarine Waters. *Water Research* **2018**, *137*, 344–354. <https://doi.org/10.1016/j.watres.2018.02.042>.
- (13) Bond, T.; Templeton, M. R.; Graham, N. Precursors of Nitrogenous Disinfection By-Products in Drinking Water—A Critical Review and Analysis. *Journal of Hazardous Materials* **2012**, *235–236*, 1–16. <https://doi.org/10.1016/j.jhazmat.2012.07.017>.
- (14) Pehlivanoglu-Mantas, E.; Sedlak, D. L. Measurement of Dissolved Organic Nitrogen Forms in Wastewater Effluents: Concentrations, Size Distribution and NDMA Formation Potential. *Water Research* **2008**, *42* (14), 3890–3898. <https://doi.org/10.1016/j.watres.2008.05.017>.
- (15) Jørgensen, N. O. G. Organic Nitrogen. In *Encyclopedia of Inland Waters*; 2009; pp 832–851.
- (16) *Human Pharmaceuticals, Hormones and Fragrances - The Challenge of Micropollutants in Urban Water Management*; Ternes, T., Joss, A., Eds.; IWA Publishing, 2006.
- (17) Shen, R.; Andrews, S. A. Demonstration of 20 Pharmaceuticals and Personal Care Products (PPCPs) as Nitrosamine Precursors during Chloramine Disinfection. *Water Research* **2011**, *45* (2), 944–952. <https://doi.org/10.1016/j.watres.2010.09.036>.
- (18) von Gunten, U. Oxidation Processes in Water Treatment: Are We on Track? *Environmental Science & Technology* **2018**, *52* (9), 5062–5075. <https://doi.org/10.1021/acs.est.8b00586>.
- (19) Schmidt, C. K.; Brauch, H.-J. *N,N*-Dimethylsulfamide as Precursor for *N*-Nitrosodimethylamine (NDMA) Formation upon Ozonation and Its Fate During Drinking Water Treatment. *Environ. Sci. Technol.* **2008**, *42* (17), 6340–6346. <https://doi.org/10.1021/es7030467>.
- (20) von Gunten, U.; Salhi, E.; Schmidt, C. K.; Arnold, W. A. Kinetics and Mechanisms of *N*-Nitrosodimethylamine Formation upon Ozonation of *N,N*-Dimethylsulfamide-Containing Waters: Bromide Catalysis. *Environmental Science & Technology* **2010**, *44* (15), 5762–5768. <https://doi.org/10.1021/es1011862>.
- (21) Kosaka, K.; Asami, M.; Konno, Y.; Oya, M.; Kunikane, S. Identification of Antiyellowing Agents as Precursors of *N*-Nitrosodimethylamine Production on Ozonation from Sewage Treatment Plant Influent. *Environ. Sci. Technol.* **2009**, *43* (14), 5236–5241. <https://doi.org/10.1021/es900227g>.
- (22) Lim, S.; Lee, W.; Na, S.; Shin, J.; Lee, Y. *N*-Nitrosodimethylamine (NDMA) Formation during Ozonation of *N,N*-Dimethylhydrazine Compounds: Reaction Kinetics, Mechanisms, and Implications for NDMA Formation Control. *Water Res.* **2016**, *105*, 119–128. <https://doi.org/10.1016/j.watres.2016.08.054>.
- (23) von Sonntag, C.; von Gunten, U. *Chemistry of Ozone in Water and Wastewater Treatment*; IWA Publishing, 2012.
- (24) Buxton, G. V.; Greenstock, C. L.; Helman, W. P.; Ross, A. B. Critical Review of Rate Constants for Reactions of Hydrated Electrons, Hydrogen Atoms and Hydroxyl Radicals ($\cdot\text{OH}/\cdot\text{O}^-$ in Aqueous Solution. *Journal of Physical and Chemical Reference Data* **1988**, *17* (2), 513–886. <https://doi.org/10.1063/1.555805>.
- (25) von Gunten, U. Ozonation of Drinking Water: Part II. Disinfection and by-Product Formation in Presence of Bromide, Iodide or Chlorine. *Water Research* **2003**, *37* (7), 1469–1487. [https://doi.org/10.1016/S0043-1354\(02\)00458-X](https://doi.org/10.1016/S0043-1354(02)00458-X).
- (26) Tentscher, P. R.; Bourgin, M.; von Gunten, U. Ozonation of *Para*-Substituted Phenolic Compounds Yields *p*-Benzoquinones, Other Cyclic α,β -Unsaturated Ketones, and Substituted Catechols. *Environmental Science & Technology* **2018**,

- 52 (8), 4763–4773. <https://doi.org/10.1021/acs.est.8b00011>.
- (27) Hammes, F.; Salhi, E.; Köster, O.; Kaiser, H.-P.; Egli, T.; von Gunten, U. Mechanistic and Kinetic Evaluation of Organic Disinfection By-Product and Assimilable Organic Carbon (AOC) Formation during the Ozonation of Drinking Water. *Water Research* **2006**, *40* (12), 2275–2286. <https://doi.org/10.1016/j.watres.2006.04.029>.
- (28) Ramseier, M. K.; Peter, A.; Traber, J.; von Gunten, U. Formation of Assimilable Organic Carbon during Oxidation of Natural Waters with Ozone, Chlorine Dioxide, Chlorine, Permanganate, and Ferrate. *Water Research* **2011**, *45* (5), 2002–2010. <https://doi.org/10.1016/j.watres.2010.12.002>.
- (29) Bourgin, M.; Beck, B.; Boehler, M.; Borowska, E.; Fleiner, J.; Salhi, E.; Teichler, R.; von Gunten, U.; Siegrist, H.; McArdell, C. S. Evaluation of a Full-Scale Wastewater Treatment Plant Upgraded with Ozonation and Biological Post-Treatments: Abatement of Micropollutants, Formation of Transformation Products and Oxidation by-Products. *Water Research* **2018**, *129*, 486–498. <https://doi.org/10.1016/j.watres.2017.10.036>.
- (30) Eggen, R. I. L.; Hollender, J.; Joss, A.; Schärer, M.; Stamm, C. Reducing the Discharge of Micropollutants in the Aquatic Environment: The Benefits of Upgrading Wastewater Treatment Plants. *Environmental Science & Technology* **2014**, *48* (14), 7683–7689. <https://doi.org/10.1021/es500907n>.
- (31) Ternes, T. A.; Meisenheimer, M.; McDowell, D.; Sacher, F.; Brauch, H.-J.; Haist-Gulde, B.; Preuss, G.; Wilme, U.; Zulei-Seibert, N. Removal of Pharmaceuticals during Drinking Water Treatment. *Environmental Science & Technology* **2002**, *36* (17), 3855–3863. <https://doi.org/10.1021/es015757k>.
- (32) Hollender, J.; Zimmermann, S. G.; Koepke, S.; Krauss, M.; McArdell, C. S.; Ort, C.; Singer, H.; von Gunten, U.; Siegrist, H. Elimination of Organic Micropollutants in a Municipal Wastewater Treatment Plant Upgraded with a Full-Scale Post-Ozonation Followed by Sand Filtration. *Environmental Science & Technology* **2009**, *43* (20), 7862–7869. <https://doi.org/10.1021/es9014629>.
- (33) Zimmermann, S. G.; Wittenwiler, M.; Hollender, J.; Krauss, M.; Ort, C.; Siegrist, H.; von Gunten, U. Kinetic Assessment and Modeling of an Ozonation Step for Full-Scale Municipal Wastewater Treatment: Micropollutant Oxidation, by-Product Formation and Disinfection. *Water Research* **2011**, *45* (2), 605–617. <https://doi.org/10.1016/j.watres.2010.07.080>.
- (34) Margot, J.; Kienle, C.; Magnet, A.; Weil, M.; Rossi, L.; de Alencastro, L. F.; Abegglen, C.; Thonney, D.; Chèvre, N.; Schärer, M.; et al. Treatment of Micropollutants in Municipal Wastewater: Ozone or Powdered Activated Carbon? *Science of The Total Environment* **2013**, *461–462*, 480–498. <https://doi.org/10.1016/j.scitotenv.2013.05.034>.
- (35) Huber, M. M.; Canonica, S.; Park, G.-Y.; von Gunten, U. Oxidation of Pharmaceuticals during Ozonation and Advanced Oxidation Processes. *Environmental Science & Technology* **2003**, *37* (5), 1016–1024. <https://doi.org/10.1021/es025896h>.
- (36) Dodd, M. C.; Kohler, H.-P. E.; von Gunten, U. Oxidation of Antibacterial Compounds by Ozone and Hydroxyl Radical: Elimination of Biological Activity during Aqueous Ozonation Processes. *Environmental Science & Technology* **2009**, *43* (7), 2498–2504. <https://doi.org/10.1021/es8025424>.
- (37) Huber, M. M.; Ternes, T. A.; von Gunten, U. Removal of Estrogenic Activity and Formation of Oxidation Products during Ozonation of 17 α -Ethinylestradiol. *Environ. Sci. Technol.* **2004**, *38* (19), 5177–5186. <https://doi.org/10.1021/es035205x>.
- (38) Lange, F.; Cornelissen, S.; Kubac, D.; Sein, M. M.; von Sonntag, J.; Hannich, C. B.; Golloch, A.; Heipieper, H. J.; Möder, M.; von Sonntag, C. Degradation of Macrolide Antibiotics by Ozone: A Mechanistic Case Study with Clarithromycin. *Chemosphere* **2006**, *65* (1), 17–23. <https://doi.org/10.1016/j.chemosphere.2006.03.014>.
- (39) Stalter, D.; Magdeburg, A.; Oehlmann, J. Comparative Toxicity Assessment of Ozone and Activated Carbon Treated Sewage Effluents Using an in Vivo Test Battery. *Water Research* **2010**, *44* (8), 2610–2620. <https://doi.org/10.1016/j.watres.2010.01.023>.
- (40) Hübner, U.; von Gunten, U.; Jekel, M. Evaluation of the Persistence of Transformation Products from Ozonation of Trace Organic Compounds – A Critical Review. *Water Research* **2015**, *68*, 150–170. <https://doi.org/10.1016/j.watres.2014.09.051>.
- (41) Lee, Y.; von Gunten, U. Advances in Predicting Organic Contaminant Abatement during Ozonation of Municipal Wastewater Effluent: Reaction Kinetics, Transformation Products, and Changes of Biological Effects. *Environmental Science: Water Research & Technology* **2016**, *2* (3), 421–442. <https://doi.org/10.1039/C6EW00025H>.
- (42) Lee, M.; Blum, L. C.; Schmid, E.; Fenner, K.; von Gunten, U. A Computer-Based Prediction Platform for the Reaction of Ozone with Organic Compounds in Aqueous Solution: Kinetics and Mechanisms. *Environmental Science: Processes & Impacts* **2017**, *19* (3), 465–476. <https://doi.org/10.1039/C6EM00584E>.
- (43) Götz, C. W.; Hollender, J.; Kase, R. *Mikroverunreinigungen - Beurteilungskonzept für organische Spurenstoffe aus kommunalem Abwasser. Studie im Auftrag des Bundesamtes für Umwelt (BAFU); Eawag: Dübendorf*, 2010; p 108.
- (44) Knoop, O.; Hohrenk, L. L.; Lutze, H. V.; Schmidt, T. C. Ozonation of Tamoxifen and Toremifene – Reaction Kinetics and Transformation Products. *Environmental Science & Technology* **2018**, *52* (21), 12583–12591. <https://doi.org/10.1021/acs.est.8b00996>.
- (45) Hoigné, J.; Bader, H. Rate Constants of Reactions of Ozone with Organic and Inorganic Compounds in Water—II: Dissociating Organic Compounds. *Water Research* **1983**, *17* (2), 185–194.
- (46) Pryor, W. A.; Giamalva, D. H.; Church, D. F. Kinetics of Ozonation. 2. Amino Acids and Model Compounds in Water and Comparisons to Rates in Nonpolar Solvents. *Journal of the American Chemical Society* **1984**, *106* (23), 7094–7100. <https://doi.org/10.1021/ja00335a038>.
- (47) Dodd, M. C. Characterization of Ozone-Based Oxidative Treatment as a Means of Eliminating the Target-Specific Biological Activities of Municipal Wastewater-Borne Antibacterial Compounds. Doctoral Thesis, ETH Zurich, 2008. <https://doi.org/10.3929/ethz-a-005706450>.
- (48) Benner, J.; Salhi, E.; Ternes, T.; von Gunten, U. Ozonation of Reverse Osmosis Concentrate: Kinetics and Efficiency of

- Beta Blocker Oxidation. *Water Research* **2008**, *42* (12), 3003–3012. <https://doi.org/10.1016/j.watres.2008.04.002>.
- (49) Qiang, Z.; Adams, C.; Surampalli, R. Determination of Ozonation Rate Constants for Lincomycin and Spectinomycin. *Ozone: Science & Engineering* **2004**, *26* (6), 525–537. <https://doi.org/10.1080/01919510490885334>.
- (50) Lester, Y.; Mamane, H.; Zucker, I.; Avisar, D. Treating Wastewater from a Pharmaceutical Formulation Facility by Biological Process and Ozone. *Water Research* **2013**, *47* (13), 4349–4356. <https://doi.org/10.1016/j.watres.2013.04.059>.
- (51) Dodd, M. C.; Buffle, M.-O.; von Gunten, U. Oxidation of Antibacterial Molecules by Aqueous Ozone: Moiety-Specific Reaction Kinetics and Application to Ozone-Based Wastewater Treatment. *Environmental Science & Technology* **2006**, *40* (6), 1969–1977. <https://doi.org/10.1021/es051369x>.
- (52) Muñoz, F.; von Sonntag, C. The Reactions of Ozone with Tertiary Amines Including the Complexing Agents Nitrilotriacetic Acid (NTA) and Ethylenediaminetetraacetic Acid (EDTA) in Aqueous Solution. *Journal of the Chemical Society, Perkin Transactions 2* **2000**, No. 10, 2029–2033. <https://doi.org/10.1039/b004417m>.
- (53) Zimmermann, S. G.; Schmukat, A.; Schulz, M.; Benner, J.; von Gunten, U.; Ternes, T. A. Kinetic and Mechanistic Investigations of the Oxidation of Tramadol by Ferrate and Ozone. *Environmental Science & Technology* **2012**, *46* (2), 876–884. <https://doi.org/10.1021/es203348q>.
- (54) Borowska, E.; Bourgin, M.; Hollender, J.; Kienle, C.; McArdell, C. S.; von Gunten, U. Oxidation of Cetirizine, Fexofenadine and Hydrochlorothiazide during Ozonation: Kinetics and Formation of Transformation Products. *Water Research* **2016**, *94*, 350–362. <https://doi.org/10.1016/j.watres.2016.02.020>.
- (55) Benner, J.; Ternes, T. A. Ozonation of Propranolol: Formation of Oxidation Products. *Environmental Science & Technology* **2009**, *43* (13), 5086–5093. <https://doi.org/10.1021/es900282c>.
- (56) Benner, J.; Ternes, T. A. Ozonation of Metoprolol: Elucidation of Oxidation Pathways and Major Oxidation Products. *Environmental Science & Technology* **2009**, *43* (14), 5472–5480. <https://doi.org/10.1021/es900280e>.
- (57) Tekle-Röttering, A.; Jewell, K. S.; Reisz, E.; Lutze, H. V.; Ternes, T. A.; Schmidt, W.; Schmidt, T. C. Ozonation of Piperidine, Piperazine and Morpholine: Kinetics, Stoichiometry, Product Formation and Mechanistic Considerations. *Water Research* **2016**, *88*, 960–971. <https://doi.org/10.1016/j.watres.2015.11.027>.
- (58) von Gunten, U. Ozonation of Drinking Water: Part I. Oxidation Kinetics and Product Formation. *Water Research* **2003**, *37* (7), 1443–1467. [https://doi.org/10.1016/S0043-1354\(02\)00457-8](https://doi.org/10.1016/S0043-1354(02)00457-8).
- (59) McCurry, D. L.; Quay, A. N.; Mitch, W. A. Ozone Promotes Chloropicrin Formation by Oxidizing Amines to Nitro Compounds. *Environmental Science & Technology* **2016**, *50* (3), 1209–1217. <https://doi.org/10.1021/acs.est.5b04282>.
- (60) Berger, P.; Karpel Vel Leitner, N.; Doré, M.; Legube, B. Ozone and Hydroxyl Radicals Induced Oxidation of Glycine. *Water Research* **1999**, *33* (2), 433–441. [https://doi.org/10.1016/S0043-1354\(98\)00230-9](https://doi.org/10.1016/S0043-1354(98)00230-9).
- (61) de Vera, G. A.; Gernjak, W.; Weinberg, H.; Farré, M. J.; Keller, J.; von Gunten, U. Kinetics and Mechanisms of Nitrate and Ammonium Formation during Ozonation of Dissolved Organic Nitrogen. *Water Research* **2017**, *108*, 451–461. <https://doi.org/10.1016/j.watres.2016.10.021>.
- (62) Le Lacheur, R. M.; Glaze, W. H. Reactions of Ozone and Hydroxyl Radicals with Serine. *Environmental Science & Technology* **1996**, *30* (4), 1072–1080.
- (63) Albert, A. *Heterocyclic Chemistry: An Introduction*, 2nd ed.; Athlone Press: London, 1968.
- (64) Andreozzi, R.; Insola, A.; Caprio, V.; D'Amore, M. G. Ozonation of Pyridine in Aqueous Solution: Mechanistic and Kinetic Aspects. *Water research* **1991**, *25* (6), 655–659.
- (65) Tekle-Röttering, A.; Reisz, E.; Jewell, K. S.; Lutze, H. V.; Ternes, T. A.; Schmidt, W.; Schmidt, T. C. Ozonation of Pyridine and Other N-Heterocyclic Aromatic Compounds: Kinetics, Stoichiometry, Identification of Products and Elucidation of Pathways. *Water Research* **2016**, *102*, 582–593. <https://doi.org/10.1016/j.watres.2016.06.021>.
- (66) Wang, X.; Huang, X.; Zuo, C.; Hu, H. Kinetics of Quinoline Degradation by O₃/UV in Aqueous Phase. *Chemosphere* **2004**, *55* (5), 733–741. <https://doi.org/10.1016/j.chemosphere.2003.11.019>.
- (67) Lee, C.; Schmidt, C.; Yoon, J.; von Gunten, U. Oxidation of N-Nitrosodimethylamine (NDMA) Precursors with Ozone and Chlorine Dioxide: Kinetics and Effect on NDMA Formation Potential. *Environmental Science & Technology* **2007**, *41* (6), 2056–2063. <https://doi.org/10.1021/es062484q>.
- (68) Acero, J. L.; Stemmler, K.; von Gunten, U. Degradation Kinetics of Atrazine and Its Degradation Products with Ozone and OH Radicals: A Predictive Tool for Drinking Water Treatment. *Environmental Science & Technology* **2000**, *34* (4), 591–597. <https://doi.org/10.1021/es990724e>.
- (69) Tosco, P.; Rolando, B.; Fruttero, R.; Henchoz, Y.; Martel, S.; Carrupt, P.-A.; Gasco, A. Physicochemical Profiling of Sartans: A Detailed Study of Ionization Constants and Distribution Coefficients. *Helvetica Chimica Acta* **2008**, *91* (3), 468–482. <https://doi.org/10.1002/hlca.200890051>.
- (70) Keen, O. S.; Ferrer, I.; Michael Thurman, E.; Linden, K. G. Degradation Pathways of Lamotrigine under Advanced Treatment by Direct UV Photolysis, Hydroxyl Radicals, and Ozone. *Chemosphere* **2014**, *117*, 316–323. <https://doi.org/10.1016/j.chemosphere.2014.07.085>.
- (71) Chen, W. R.; Wu, C.; Elovitz, M. S.; Linden, K. G.; (Mel) Suffet, I. H. Reactions of Thiocarbamate, Triazine and Urea Herbicides, RDX and Benzenes on EPA Contaminant Candidate List with Ozone and with Hydroxyl Radicals. *Water Research* **2008**, *42* (1–2), 137–144. <https://doi.org/10.1016/j.watres.2007.07.037>.
- (72) Yao, C. C. D.; Haag, W. R. Rate Constants for Direct Reactions of Ozone with Several Drinking Water Contaminants. *Water Research* **1991**, *25* (7), 761–773. [https://doi.org/10.1016/0043-1354\(91\)90155-J](https://doi.org/10.1016/0043-1354(91)90155-J).
- (73) De Laat, J.; Maouala-Makata, P.; Dore, M. Constantes Cinétiques de Réaction de L'Ozone Moléculaire et Des Radicaux Hydroxyles Sur Quelques Phenyl-Ureés et Acétamides. Rate Constants for Reactions of Ozone and Hydroxyl Radicals with Several Phenyl-Ureas and Acetamides. *Environmental Technology* **1996**, *17* (7), 707–716. <https://doi.org/10.1080/09593330.1996.9618396>.

- (74) Trogolo, D.; Mishra, B. K.; Heeb, M. B.; von Gunten, U.; Arey, J. S. Molecular Mechanism of NDMA Formation from N,N-Dimethylsulfamide During Ozonation: Quantum Chemical Insights into a Bromide-Catalyzed Pathway. *Environmental Science & Technology* **2015**, *49* (7), 4163–4175. <https://doi.org/10.1021/es504407h>.
- (75) Heeb, M. B.; Kristiana, I.; Trogolo, D.; Arey, J. S.; von Gunten, U. Formation and Reactivity of Inorganic and Organic Chloramines and Bromamines during Oxidative Water Treatment. *Water Research* **2017**, *110*, 91–101. <https://doi.org/10.1016/j.watres.2016.11.065>.
- (76) Pierpoint, A. C.; Hapeman, C. J.; Torrents, A. Linear Free Energy Study of Ring-Substituted Aniline Ozonation for Developing Treatment of Aniline-Based Pesticide Wastes. *Journal of Agricultural and Food Chemistry* **2001**, *49* (8), 3827–3832. <https://doi.org/10.1021/jf010123i>.
- (77) Tekle-Röttering, A.; von Sonntag, C.; Reisz, E.; Eyser, C. vom; Lutze, H. V.; Türk, J.; Naumov, S.; Schmidt, W.; Schmidt, T. C. Ozonation of Anilines: Kinetics, Stoichiometry, Product Identification and Elucidation of Pathways. *Water Research* **2016**, *98*, 147–159. <https://doi.org/10.1016/j.watres.2016.04.001>.
- (78) Chan, W. F.; Larson, R. A. Formation of Mutagens from the Aqueous Reactions of Ozone and Anilines. *Water Research* **1991**, *25* (12), 1529–1538.
- (79) Sarasa, J.; Cortés, S.; Ormad, P.; Gracia, R.; Ovelheiro, J. L. Study of the Aromatic By-Products Formed from Ozonation of Anilines in Aqueous Solution. *Water Res.* **2002**, *36* (12), 3035–3044.
- (80) Kosaka, K.; Asami, M.; Ohkubo, K.; Iwamoto, T.; Tanaka, Y.; Koshino, H.; Echigo, S.; Akiba, M. Identification of a New *N*-Nitrosodimethylamine Precursor in Sewage Containing Industrial Effluents. *Environ. Sci. Technol.* **2014**, *48* (19), 11243–11250. <https://doi.org/10.1021/es502284t>.

Chapter 2 Reactions of aliphatic amines with ozone: Kinetics and mechanisms

S. Lim, C. S. McArdell, and U. von Gunten, *Water Research*, **2019**, 157, 514–528.

Sungeun Lim contributed to planning and conducting all experiments, performing quantum chemical computations and kinetic simulations, and writing the manuscript.

Abstract

Aliphatic amines are common constituents in micropollutants and dissolved organic matter and present in elevated concentrations in wastewater-impacted source waters. Due to high reactivity, reactions of aliphatic amines with ozone are likely to occur during ozonation in water and wastewater treatment. We investigated the kinetics and mechanisms of the reactions of ozone with ethylamine, diethylamine, and triethylamine as model nitrogenous compounds. Species-specific second-order rate constants for the neutral parent amines ranged from 9.3×10^4 to $2.2 \times 10^6 \text{ M}^{-1} \text{ s}^{-1}$ and the apparent second-order rate constants at pH 7 for potential or identified transformation products were $6.8 \times 10^5 \text{ M}^{-1} \text{ s}^{-1}$ for *N,N*-diethylhydroxylamine, $\sim 10^5 \text{ M}^{-1} \text{ s}^{-1}$ for *N*-ethylhydroxylamine, $1.9 \times 10^3 \text{ M}^{-1} \text{ s}^{-1}$ for *N*-ethylethanamine oxide, and $3.4 \text{ M}^{-1} \text{ s}^{-1}$ for nitroethane. Product analyses revealed that all amines were transformed to products containing a nitrogen-oxygen bond (e.g., triethylamine *N*-oxide and nitroethane) with high yields, i.e., 64 – 100 % with regard to the abated target amines. These findings could be confirmed by measurements of singlet oxygen and hydroxyl radical which are formed during the amine-ozone reactions. Based on the high yields of nitroethane from ethylamine and diethylamine, a significant formation of nitroalkanes can be expected during ozonation of waters containing high levels of dissolved organic nitrogen, as expected in wastewaters or wastewater-impaired source waters. This may pose adverse effects on the aquatic environment and human health.

2.1 Introduction

Ozone has been used as a disinfectant and/or oxidant in water and wastewater treatment since the early 20th century.¹ It has a significant potential for the abatement of micropollutants in drinking waters and also recently in wastewater effluents.²⁻⁵ In general, ozonation reduces the overall toxicity exerted by micropollutants by eliminating or altering the moieties responsible for biological activities.⁶⁻⁸ However, an increased toxicity has also been observed in ozone-treated waters.^{5,9,10} This resulted mainly from the reaction of ozone with dissolved organic matter (DOM), thereby forming byproducts such as quinones,³ low molecular weight organic carbon compounds,^{11,12} and compounds containing nitrogen-oxygen bonds.¹³ Micropollutants can also be transformed to toxic transformation products upon ozonation, but their contribution to the overall toxicity is expected to be smaller, as DOM is present in much higher concentrations than micropollutants in real water matrices and consumes by far the largest fraction of the oxidants.⁵ Toxic oxygen-containing products, whether they are byproducts from DOM or transformation products from micropollutants, are typically expected to be removed by biological post-treatment.¹¹ However, some products (e.g., *N*-oxides) are persistent even during a biological post-treatment step.^{14,15} To better understand the formation of persistent transformation products or byproducts, many studies have been conducted to reveal their formation pathways^{16,17} and to identify transformation products.^{1,15} Recently, computational tools have been developed based on the current kinetic/mechanistic knowledge to predict ozone exposure, reaction kinetics, and transformation products upon ozonation.^{18,19} A successful implementation of such prediction tools will depend on the quality of the underlying reaction mechanisms which ideally cover a comprehensive compilation of ozone-reactive moieties. A considerable wealth of information is available for the reactions of ozone with ozone-reactive moieties such as olefins, aromatic compounds, and sulfur-containing compounds, and the relevant information is also well documented.^{1,5} However, there is less information on the ozone-reactivity of nitrogenous compounds and a need for a more fundamental understanding of the corresponding reaction mechanisms.

Aliphatic amines, one of the simplest forms of nitrogen-containing compounds, are common constituents of dissolved organic nitrogen (DON).²⁰ Understanding the reactions of aliphatic amines with ozone has been important, because, due to water scarcity, water suppliers increasingly use impaired water resources with higher levels of DON. Such sources are surface waters impacted by wastewater discharge, agricultural activities, or algal blooms²⁰⁻²² and wastewater effluents treated for the purpose of direct potable reuse.²³ Aliphatic amines are also commonly found as functional groups in many organic micropollutants. From a list of 550 environmentally relevant substances,¹⁴ more than 80 % of micropollutants contain a nitrogen and about a quarter of the nitrogen-containing micropollutants are categorized as aliphatic amines. Aliphatic amines in their neutral forms react fast with ozone due to the lone electron pair on the nitrogen atom susceptible to an electrophilic attack by ozone with second-order rate constants $k_{O_3} = 10^3 - 10^7 \text{ M}^{-1} \text{ s}^{-1}$.¹ Certain primary and secondary amines have the potential to be transformed to harmful products such as *N*-nitrosodimethylamine with low yields of less than 0.02 % upon ozonation^{24,25} and chloropicrin with ~50 % yield upon ozonation followed by post-chlorination.¹³ These nitrogenous disinfection byproducts (e.g., *N*-nitrosamines, halonitroalkanes) are significantly more toxic than regulated disinfection byproducts (e.g., trihalomethanes, haloacetic acids), wherefore the formation of the nitrogenous disinfection byproducts has gained increasing attention recently.^{17,26,27} Despite the great relevance of aliphatic amines to the ozone chemistry in water and wastewater treatment (common moieties, high reactivity towards ozone, potential of harmful products), their reactions with ozone have not been entirely elucidated. In-depth investigations on ozone-amine reactions were reported by Bailey in 1960s - 1970s but most experiments were carried out in organic solvents.^{28,29} Current knowledge on amine-ozone reactions in aqueous solutions is mostly limited to tertiary amines. *N*-oxides have often been detected as major products during ozonation of mi-

cropollutants containing a tertiary amine moiety.^{30–35} Accordingly, the principal mechanism of the reaction of tertiary amines with ozone has been proposed as an oxygen transfer reaction where ozone initially attacks a tertiary amine nitrogen to form a $-N^+-O-O-O^-$ adduct which further dissociates into a *N*-oxide and singlet oxygen.¹ Alternatively, tertiary amines can react with ozone via an electron transfer pathway to yield an amine radical cation and an ozonide radical anion. The ensuing radicals further dissociate into a *N*-dealkylated amine and a hydroxyl radical, respectively.¹ For the reaction of secondary amines with ozone, hydroxylamines (an analogous product to *N*-oxides for tertiary amines) and primary amines were identified as products, but there is only limited molar yield information.^{36–39} For the reaction of primary amines with ozone, nitrate and ammonia were identified as final products,^{40–42} but the studies were conducted under ozone excess conditions and the initial ozonation products of primary amines are still unknown.

The aim of this study was to investigate the chemistry of the ozone-amine reactions for simple aliphatic amines such as ethylamine, diethylamine, and triethylamine. The second-order rate constants for the reactions of the model compounds with ozone, transformation products and reactive oxygen species (singlet oxygen and hydroxyl radical) were determined by various experimental approaches and analytical methods. In addition, kinetic experiments/simulations and quantum chemical computations were performed. Based on these results, reaction mechanisms for primary, secondary and tertiary amines were proposed, allowing a comprehensive assessment of the fate of these moieties during ozonation.

2.2 Materials and methods

Chemical reagents. Chemicals and suppliers are listed in Table S2.1 in the Supporting Information for Chapter 2. *N*-ethylethanamine oxide was synthesized at Eawag (Text S2.1) and UV-vis spectra of this compound were recorded as received ($\lambda_{\text{max}} = 224 \text{ nm}$). Working stocks of *N*-ethylethanamine oxide were freshly made every day and the concentrations were determined based on the absorbance at 224 nm (Figure S2.1).

Ozonation experiments. Ozone stock solutions were prepared by sparging ozone-containing oxygen through ultrapure water kept on ice.⁴³ The concentration of ozone in the stock solution (1.3 – 1.5 mM) was determined spectrophotometrically based on the molar absorption coefficient of ozone, $\epsilon = 3200 \text{ M}^{-1} \text{ cm}^{-1}$ at 260 nm.¹ An aliquot of the ozone stock solution was added to the solution containing the target amine compound to initiate the ozone reaction with doses ranging from 0 – 300 μM . The solutions of the model compounds (ethylamine, diethylamine, *N,N*-diethylhydroxylamine, *N*-ethylethanamine oxide, or triethylamine; initial concentrations $\sim 100 \mu\text{M}$) were prepared in 10 mM phosphate buffer at pH 7. 50 mM of *t*-butanol was present in the solutions as a hydroxyl radical scavenger to suppress unwanted side reactions associated with hydroxyl radical. The ozonated samples were typically allowed to react for 24 hours at room temperature to ensure a complete consumption of ozone and stored at 4°C for less than a week prior to further analyses.

Reaction kinetics. Second-order rate constants for the reactions of the model compounds and their transformation products with ozone in the pH range far below the pK_a of the amines were determined by a direct measurement of the ozone decrease with the indigo reagent (Text S2.2).⁴³ Under these conditions, the amines were predominantly present in the protonated form, which lowered the reaction kinetics sufficiently to allow measurements by a direct method. The species-specific second-order rate constants for the neutral amines were then obtained by extrapolating the determined apparent second-order rate constants to a higher pH.⁴⁴ Additionally, a competition kinetic method with cinnamic acid as a competitor⁴⁵ was used for determining apparent second-

order rate constants of *N,N*-diethylhydroxylamine at pH 5 – 8, which are too high to be determined by the direct method.

Analytical methods. Diethylamine, *N*-ethylethanamine oxide, triethylamine, triethylamine *N*-oxide were analyzed by liquid chromatography coupled with high resolution tandem mass spectrometry (LC-HRMS/MS) and nitroethane was analyzed by GC-MS. Ethylamine was derivatized with 9-fluorenylmethylchloroformate and the derivatized product was analyzed by HPLC-UV.⁴⁶ Nitrite and nitrate were determined by ion chromatography with conductivity detection. All chromatographic conditions and detection methods including the limits of quantification and the measuring ranges are provided in detail in Text S2.3 and Table S2.2. Singlet oxygen was quantified by a near-infrared photomultiplier tube which directly measured a characteristic phosphorescence of singlet oxygen emitted at 1270 nm. The setup and the reference reaction to calibrate the instrument were adapted from a previous study⁴⁷ and described in Text S2.4. Hydroxyl radicals were indirectly quantified by measuring the concentration of formaldehyde, a known product of the reaction of hydroxyl radicals with *t*-butanol.^{48,49} Formaldehyde was quantified by derivatization with 2,4-dinitrophenylhydrazine followed by HPLC-UV analysis (Text S2.5).⁵⁰ Hydrogen peroxide was indirectly quantified by measuring singlet oxygen formation after adding hypochlorous acid to the samples containing hydrogen peroxide (Text S2.6).³

Quantum chemical computations. All computations were conducted by the Gaussian 09 program (Revision D.01).⁵¹ Gas phase electronic energies of all molecules were computed by the CCSD(T) functional⁵² with the jul-cc-pVTZ basis set.⁵³ Aqueous Gibbs free energies were calculated by adding gas phase thermal corrections (computed by B3LYP/CBSB7)^{54,55} and solvation effects (by M062X/6-31G*)^{56–58} to the gas phase electronic energies. More details are provided in Text S2.8.

2.3 Results and discussion

The mechanisms for the reactions of ozone with aliphatic amines were elucidated as follows: (1) Determination of apparent and species-specific second-order rate constants for the reactions of the selected amines with ozone, (2) identification/quantification of transformation products and (3) reactive oxygen species ($^1\text{O}_2$ and $\cdot\text{OH}$) formed during the amine-ozone reactions, (4) quantum chemical computations, and (5) kinetic simulations. In the following these aspects are discussed and compiled to overall proposed reaction mechanisms.

2.3.1 Ozone reaction kinetics

Apparent second-order rate constants for the reactions of ethylamine, diethylamine, and triethylamine with ozone were determined in the pH range 3 – 7. Based on this, the species-specific second-order rate constants were calculated and are summarized in Table 2.1. The species-specific second-order rate constants for the reactions of ozone with the neutral amines are in the range of 9.3×10^4 – $2.2 \times 10^6 \text{ M}^{-1} \text{ s}^{-1}$. They are comparable to literature values within a factor of 2.6, an acceptable deviation commonly found among kinetic studies. At pH 7, the apparent second-order rate constants ($k_{\text{obs,pH7}}$) for the ozone reactions with all amines were 3 – 4 orders of magnitude lower because the protonated amines (pK_a values 10.5 – 11.0) which are dominant at pH 7, are practically unreactive with ozone. The second-order rate constants for the reactions of potential or identified transformation products were also determined. *N,N*-diethylhydroxylamine, a potential product from the diethylamine-ozone reaction, was very reactive at pH 7 due to its lower pK_a (5.4, see below) compared to other amines, which leads to an almost 100 % fraction of the neutral amine species at this pH. The pK_a of *N,N*-diethylhydroxylamine was estimated by fitting the apparent second-order rate constants determined in the pH

range 1.6 – 8.0 to an expression for the species-specific second-order rate constant. This includes the degree of dissociation of the amine at a given pH and the corresponding species-specific rate constants, i.e., $k = k_{\text{NH}^+}(1-\alpha) + k_{\text{N}}\alpha$ and $\alpha = 1/(1 + 10^{\text{pK}_a-\text{pH}})$, where k_{NH^+} and k_{N} are the species-specific second-order rate constants for the protonated and the neutral amines, respectively, and α is the fraction of the neutral amine. As a result of the fitting (shown in Figure S2.2), the estimated pK_a value is 5.4, similar to the predicted value of 5.7 determined by a commercial pK_a prediction software (ACD/Labs, V 11.02) (<https://www.acdlabs.com>). The species-specific second-order rate constant of *N,N*-diethylhydroxylamine was estimated as $7.0 \times 10^5 \text{ M}^{-1} \text{ s}^{-1}$. *N*-ethylhydroxylamine, a potential product from the ethylamine-ozone reaction, was also very reactive at pH 7. The estimated apparent second-order rate constant at pH 7 ($k_{\text{obs,pH7}}$) was $\sim 10^5 \text{ M}^{-1} \text{ s}^{-1}$, based on the measured apparent second-order rate constants at pH 2 and 4 and a predicted pK_a value of 6.2 (ACD/Labs, V 11.02). The $k_{\text{obs,pH7}}$ is only a rough estimate because only two pH conditions were applied. The reaction kinetics of *N*-ethylethanamine oxide, an identified product from the reactions of diethylamine and triethylamine with ozone, was determined with a fresh *N*-ethylethanamine oxide solution prepared *in situ* to minimize the impact of dimers on the reaction kinetics (Text S2.2). *N*-ethylethanamine oxide was moderately reactive to ozone at pH 7 with an apparent second-order rate constant at pH 7, $k_{\text{obs,pH7}} = 1.9 \times 10^3 \text{ M}^{-1} \text{ s}^{-1}$. Nitroethane, identified as a final product from all amine-ozone reactions, reacted slowly with ozone with an apparent second-order rate constant at pH 7, $k_{\text{obs,pH7}} = 3.4 \text{ M}^{-1} \text{ s}^{-1}$.

Table 2.1. Species-specific and apparent second-order rate constants for the reactions of the selected amines with ozone and pK_a values of the amines.

Compound	pK_a	Method ^c	pH ^d	$k, \text{M}^{-1} \text{s}^{-1}$	$k_{\text{obs,pH7}}, \text{M}^{-1} \text{s}^{-1}$	Reference
Ethylamine	10.6	Indigo	5.0 – 7.0	$(9.3 \pm 0.1) \times 10^4$ 2.4×10^5	21	This study 34
Diethylamine	10.5	Indigo	3.0 – 7.0	$(3.9 \pm 0.1) \times 10^5$ 6.2×10^5 9.1×10^5	1.3×10^2	This study 59 34
Triethylamine	11.0	Indigo	4.0 – 6.5	$(2.2 \pm 0.1) \times 10^6$ 2.1×10^6 4.1×10^6	2.2×10^2	This study 59 34
<i>N,N</i> -Diethylhydroxylamine	5.4 ^a	Indigo; CK	1.6 – 8.0	$(7.0 \pm 0.02) \times 10^5$	6.8×10^5	This study
<i>N</i> -Ethylhydroxylamine	6.2 ^b	Indigo	2 and 4	ND	$\sim 10^5$	This study
<i>N</i> -Ethylethanamine oxide	NA	Indigo	7.0 only	ND	$(1.9 \pm 0.04) \times 10^3$	This study
Nitroethane	NA	Indigo	7.0 only	ND	3.4 ± 0.1	This study

^a pK_a of *N,N*-diethylhydroxylamine was estimated from the apparent second-order rate constants measured at varying pH conditions (see the fitting equation and the result in Text S2.2 and Figure S2.2). ^b pK_a of *N*-ethylhydroxylamine was predicted by a commercial software (ACD/Labs, V11.02) (<https://www.acdlabs.com>). ^cReaction kinetics were determined by direct monitoring of the ozone decrease with the indigo method (indigo) or by competition kinetics with cinnamic acid (CK) as described in detail in Text S2.2. ^dExperimental pH range.

2.3.2 Product analyses and reaction mechanisms

2.3.2.1 Triethylamine-ozone reaction

Transformation products. The abatement of triethylamine and the evolution of transformation products as a function of the ozone doses were measured in presence of *t*-butanol as a hydroxyl radical scavenger (Figure 2.1a). All compounds presented in Figure 2.1 were quantified by various analytical methods with reference standards (Text S2.3). Triethylamine (94 μM initial concentration) gradually decreased for ozone doses of ≤ 100 μM and was completely abated for an ozone dose of ~ 110 μM , yielding a molar ozone:triethylamine reaction stoichiometry of about 1. The major product was triethylamine *N*-oxide, in agreement with previous findings from reactions of tertiary amines with ozone in laboratory- and full-scale studies.^{1,14,30–32,34,35} A minor product is nitroethane, which was formed in small concentrations but gradually built up with increasing ozone doses. Triethylamine *N*-oxide and nitroethane were final products with yields of 87 % and 9 %, respectively, based on the abated triethylamine at the highest applied ozone dose (300 μM). Diethylamine and *N*-ethylethanamine oxide were formed as transient products to a lesser extent (insert of Figure 2.1a) and were subsequently degraded at high ozone doses, likely concomitant with the formation of nitroethane (see the section 2.3.2.2). The sum of the concentrations of all nitrogen species is presented as a mass balance in Figure 2.1a. The mass balance was maintained at 89 – 110 % for all ozone doses. As this is a very reasonable mass balance for a product study, it can be concluded that no major transformation products are missing for the ozone-induced transformation of triethylamine.

Reactive oxygen species. The reaction of triethylamine with ozone exerted a high yield of $^1\text{O}_2$ (70 % of the consumed ozone, Table 2.2). In contrast, the $\cdot\text{OH}$ yield was only 6.4 %. These yields are roughly within the same range compared to previously reported values of 80 % for $^1\text{O}_2$ and 15 % for $\cdot\text{OH}$.^{47,48} The previously reported $^1\text{O}_2$ yields were determined without *t*-butanol. Nevertheless, the yields determined under amine-excess conditions (amine:ozone ≥ 10)⁴⁷ can be compared to our results because the effect of $\cdot\text{OH}$ on amine and ozone concentrations is minimal under these conditions despite the absence of an $\cdot\text{OH}$ scavenger. We also measured $^1\text{O}_2$ yields for conditions with the amine in excess without *t*-butanol and obtained comparable results (70 %, Table S2.3). The yields of $^1\text{O}_2$ and $\cdot\text{OH}$ correspond well to the product formation trend where triethylamine *N*-oxide (yielding $^1\text{O}_2$) was observed in much higher concentrations than the dealkylated amine, diethylamine (yielding $\cdot\text{OH}$) and its identified transformation products, nitroethane (see the section 2.3.2.2). Both results from the formation of transformation products and the detection of reactive oxygen species indicate that the reaction of triethylamine with ozone predominantly occurs via oxygen transfer forming triethylamine *N*-oxide and $^1\text{O}_2$ rather than via electron transfer forming diethylamine and $\cdot\text{OH}$.

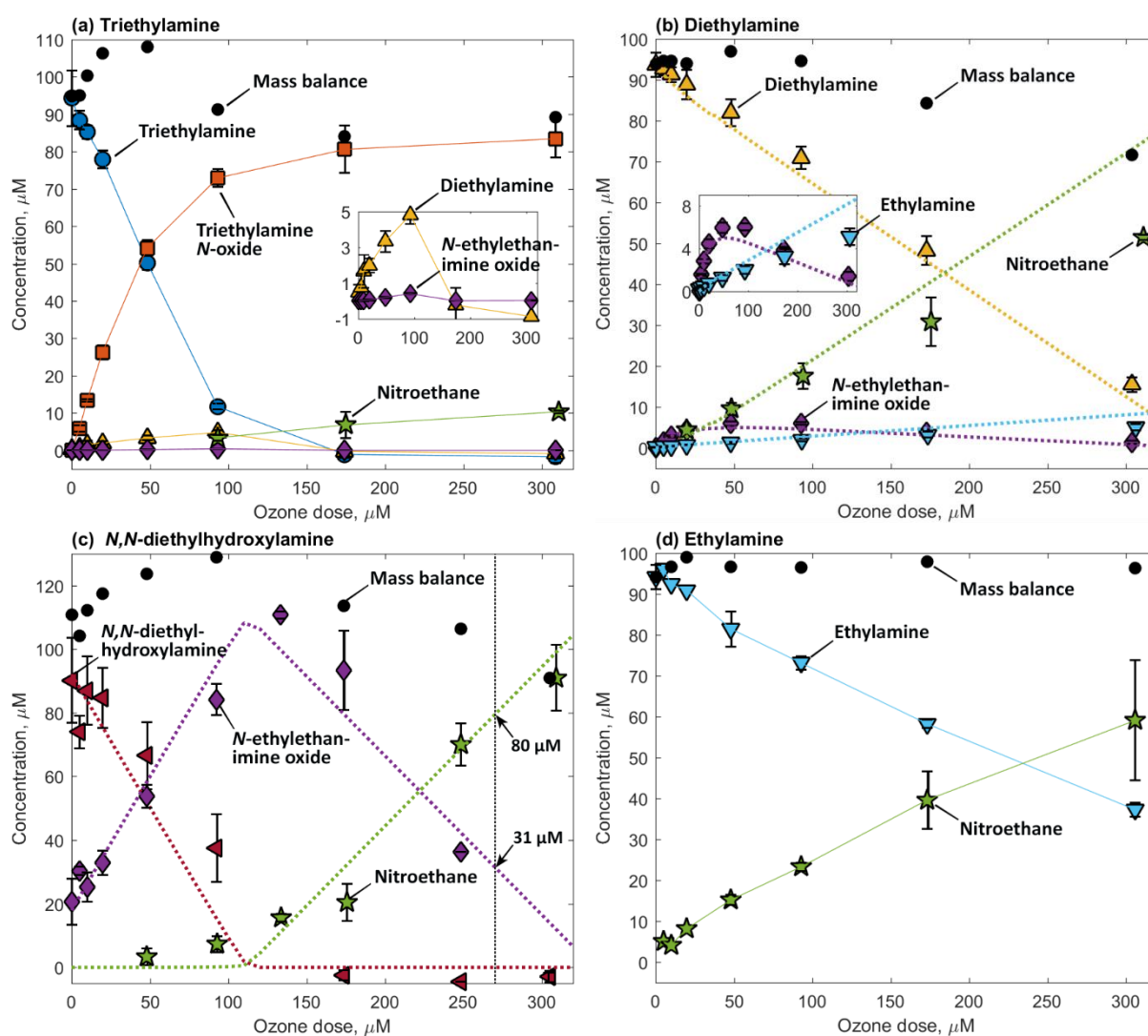


Figure 2.1. Evolution of the amine model compounds and transformation products as a function of the ozone doses for the reactions of ozone with (a) triethylamine, (b) diethylamine, (c) *N,N*-diethylhydroxylamine, and (d) ethylamine. Inserts in (a) and (b) have the same axis labels as the main plots. The symbols indicate measured concentrations (duplicate or triplicate) and the dotted lines in (b) and (c) indicate simulated concentrations based on the kinetic models described in Table S2.7 and Table S2.5, respectively. The vertical line in (c) is at an ozone dose of 270 μM . The errors were calculated as standard deviations. Experimental conditions: [amine]₀ \sim 100 μM , [ozone] = 0 – 300 μM , [*t*-butanol] = 50 mM, 10 mM phosphate buffer (pH 7), and reaction time = 24 h (triethylamine, diethylamine, and ethylamine) or 3 – 5 h (*N,N*-diethylhydroxylamine).

Table 2.2. Yields of reactive oxygen species ($^1\text{O}_2$ and $\cdot\text{OH}$) per consumed ozone at an amine:ozone ratio of 1:1 (yields for other ratios are given in Table S2.3 and Figure S2.12). Ozone concentrations were 0.1 or 0.4 – 0.5 mM for $^1\text{O}_2$ measurements and 0.09 mM for $\cdot\text{OH}$ measurements. All measurements were performed at pH 7, except for $^1\text{O}_2$ formation from ethylamine (pH 9). *t*-Butanol was added for all $^1\text{O}_2$ measurements carried out in this study. Yields were averaged for 5-9 replicates for $^1\text{O}_2$ and duplicates for $\cdot\text{OH}$ and standard deviations were within 10 % of the average values.

Compound	Type	$^1\text{O}_2/\text{O}_3$	Reference	$\cdot\text{OH}/\text{O}_3$	Reference
Triethylamine	Tertiary amine	0.70 0.80 ^a	This study ⁴⁷	0.064 0.15	This study ⁴⁸
Diethylamine	Secondary amine	0.46 0.20 ^b	This study ⁴⁷	0.26	This study
Piperidine		-		0.28	³⁸
Ethylamine	Primary amine	0.27 0.17 ^b	This study ⁴⁷	0.33	This study
Glycine		-		0.25	⁴¹
<i>N,N</i> -Diethylhydroxylamine	Hydroxylamine	0.38	This study	0.43	This study
<i>N</i> -Ethylethanamine oxide	Nitrone	0.43 ^c	This study	0.43 ^c	This study

^awithout *t*-butanol, pH 8, and molar amine:ozone = 100; ^bwithout *t*-butanol, pH 10.5, and molar amine:ozone = 10; ^cpossibly influenced by the presence of a dimer.

Reaction pathways. The experimental findings on the triethylamine-ozone reactions are described well by two pathways: The formation of triethylamine *N*-oxide and $^1\text{O}_2$ via an oxygen transfer and the formation of diethylamine and $\cdot\text{OH}$ via an electron transfer mechanism (Figure 2.2). The extent of oxygen transfer and electron transfer was further elucidated by calculating the yields of transformation products and reactive oxygen species. The concentrations of the products were divided by the concentrations of abated triethylamine determined at an ozone dose of 93 μM ($\Delta[\text{Triethylamine}] = 83 \mu\text{M}$) and expressed in percentage in Figure 2.2. For the reactive oxygen species, the yields determined with regard to consumed ozone in Table 2.2 were converted to the yields per abated triethylamine to be comparable with the transformation product yields (e.g., the converted $^1\text{O}_2$ yield = $(^1\text{O}_2/\text{O}_3) \times [\text{O}_3] / \Delta[\text{Triethylamine}] = 0.70 \times 93 \mu\text{M} / 83 \mu\text{M} = 78 \%$). In summary, of the abated 83 μM of triethylamine at 93 μM of ozone, $88 \pm 3 \%$ was transformed into triethylamine *N*-oxide and $5 \pm 1 \%$ into diethylamine. The yields of reactive oxygen species matched quite well the yields of the transformation product counterparts, namely $78 \pm 3 \%$ of $^1\text{O}_2$ and $7 \pm 0.3 \%$ of $\cdot\text{OH}$.

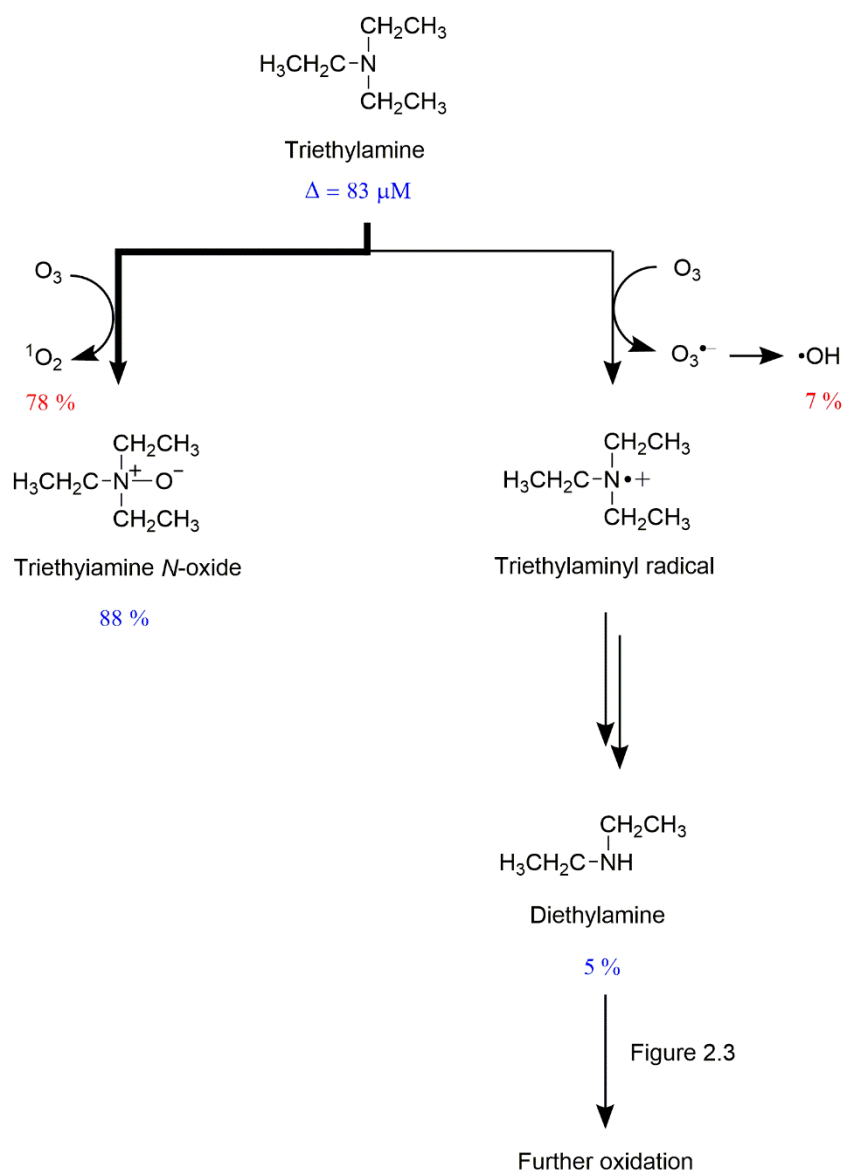


Figure 2.2. Proposed mechanism for the reaction of triethylamine with ozone. Product yields (in %) were calculated by dividing the measured concentrations of the transformation products and the reactive oxygen species by the abated triethylamine (83 μM) at an ozone dose of 93 μM . The yields of transformation products and reactive oxygen species are emphasized in blue and red, respectively. The bold arrow indicates the major pathway of the branched reaction.

2.3.2.2 Diethylamine-ozone reaction

Transformation products. Figure 2.1b shows the abatement of diethylamine and the corresponding product formation upon ozonation. In contrast to triethylamine, diethylamine required a much higher specific ozone dose with a molar stoichiometry ozone:diethylamine of about 4 for a complete abatement. Nitroethane, a highly oxidized form of nitrogen with an oxidation state of +3 (in comparison to -3 of diethylamine), was the major product with a 64 % yield based on the diethylamine abatement at 300 μM ozone. *N*-ethylethanamine oxide and ethylamine were additionally detected as minor products with yields of 2 % and 7 %, respectively, at 300 μM ozone (insert in Figure 2.1b). *N*-ethylethanamine oxide is a *N*-oxide of an imine derivative of diethylamine and belongs to the class of nitrones. *N*-ethylethanamine oxide was formed in small quantities for ozone doses ≤ 100 μM and was abated again for higher ozone doses. The decline in the *N*-ethylethanamine oxide concentrations is likely associated with the formation of nitroethane. Nitrones have been suggested as intermediates during the transformation of secondary amines into nitroalkanes upon ozonation.^{13,29} Ethylamine, the other minor product, gradually increased with increasing ozone doses, persisting as a final product along with nitroethane. The nitrogen mass balance was well maintained up to an ozone dose of 100 μM but fell short by 10 – 24 % for higher ozone doses, which is still reasonable compared to typical product studies. Attempts were made to identify *N,N*-diethylhydroxylamine as another possible transformation product by LC-MS/MS with the reference standard, but this compound was not detected (LOQ = 2.5 μM) at any ozone dose.

Reactive oxygen species. During the diethylamine-ozone reaction, 46 % of $^1\text{O}_2$ and 26 % of $\cdot\text{OH}$ were found relative to the consumed ozone (Table 2.2). The $^1\text{O}_2$ yield was higher than the reported value of 20 %.⁴⁷ However, a $^1\text{O}_2$ yield of 29 % (Table S2.3) determined under similar conditions to the previous study (i.e., amine excess and without *t*-butanol) was closer to the reported value. The $\cdot\text{OH}$ yield was similar to a reported value of 28 % for piperidine which contains a secondary amine moiety.³⁸ The relatively high $\cdot\text{OH}$ yield found in the reaction of diethylamine with ozone does not match to the low formation of the corresponding dealkylated product, ethylamine. There seems another reaction pathway responsible for the excess of $\cdot\text{OH}$ apart from the electron transfer pathway of diethylamine leading to ethylamine (see the section 2.3.2.3).

Reaction pathways. The diethylamine-ozone reaction can also be described by oxygen transfer and electron transfer pathways (Figure 2.3). However, it entailed secondary ozone reactions with the primary transformation products, which makes the elucidation of the reaction mechanism more complicated than in the case of triethylamine. The yields of the identified transformation products at an ozone dose of 93 μM was calculated in analogy to the triethylamine-ozone reaction (transformation product formed/diethylamine abated): 26 ± 1 % *N*-ethylethanamine oxide, 69 ± 13 % nitroethane, and 8 ± 1 % ethylamine. The total yield of the products with the oxygen addition (*N*-ethylethanamine oxide and nitroethane) was about 95 %, outweighing the yield of the dealkylated amine (ethylamine, 8%). This suggests that the diethylamine-ozone reaction also predominantly undergoes an oxygen transfer pathway (step (a), Figure 2.3). However, the reactive oxygen species yields were much higher than the yields of the corresponding transformation products: 186 % for $^1\text{O}_2$ and 105 % for $\cdot\text{OH}$ due to the little abatement of diethylamine ($\Delta[\text{Diethylamine}] = 23$ μM). These high yields of reactive oxygen species as well as the high ozone stoichiometry (4 mole equivalents of ozone, Figure 2.1b) and the highly oxidized product (nitroethane) imply secondary reactions of primary transformation products with ozone during the diethylamine-ozone reaction. It is hypothesized that *N,N*-diethylhydroxylamine might be a transient product. This is in analogy to *N*-oxides for the case of tertiary amines, as often suggested in other studies on the reaction of secondary amines with ozone.^{36,38,39} However, *N,N*-diethylhydroxylamine was not detected in our experiments. This contrasts a recent finding in the reaction of piperidine (a secondary amine) with ozone where a yield of 94 % *N*-hydroxypiperidine was reported.³⁸ The apparent disagreement can be explained by different pH conditions ap-

plied in the two studies. In the current study, the experiments were carried out at pH 7, where the apparent second-order rate constant for the reaction of *N,N*-diethylhydroxylamine with ozone is more than three orders of magnitude higher than the corresponding rate constant for diethylamine ($k_{\text{obs,pH7}}$, Table 2.1). Therefore, even if *N,N*-diethylhydroxylamine is formed as a primary transformation product during the diethylamine-ozone reaction, it would quickly react with ozone and be further oxidized, which would hinder its detection. In contrast, the experiment in the previous study was carried out at pH 11.5 where the kinetics for the reactions of ozone with piperidine and *N*-hydroxypiperidine only differ by a factor of two. Under these conditions and in excess of piperidine relative to ozone, *N*-hydroxypiperidine can be detected.

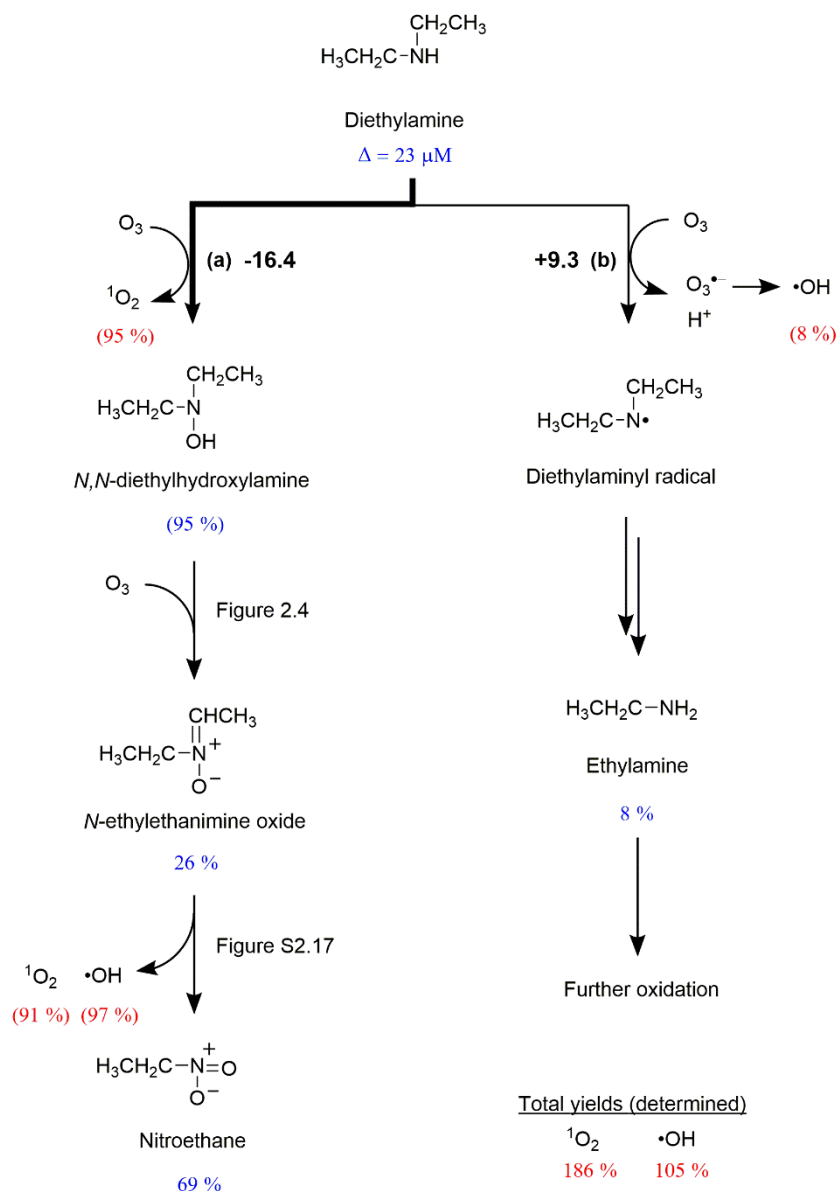


Figure 2.3. Proposed mechanism for the reaction of diethylamine with ozone. Product yields (in %) were calculated by dividing the measured concentrations of the transformation products and the reactive oxygen species by the abated diethylamine (23 μM) at an ozone dose of 93 μM . The yield of *N,N*-diethylhydroxylamine in parenthesis is a theoretical yield based on the sum of the *N*-ethylethanamine oxide and nitroethane yields. The $\text{}^1\text{O}_2$ and $\cdot\text{OH}$ yields in parentheses are also theoretical yields based on the yields of the corresponding transformation products and the total $\text{}^1\text{O}_2$ and $\cdot\text{OH}$ yields determined for the diethylamine-ozone reaction (186 % $\text{}^1\text{O}_2$ and 105 % $\cdot\text{OH}$). The yields of transformation products and reactive oxygen species are emphasized in blue and red, respectively. Bold numbers next to the reaction steps are calculated aqueous Gibbs free energies in kcal mol^{-1} . The bold arrow indicates the major pathway of the branched reaction.

Quantum chemical computations. Quantum chemical computations were performed to calculate aqueous Gibbs free energy of reaction ($\Delta G_{\text{aq,rxn}}$) for the oxygen transfer and electron transfer pathways of the diethylamine-ozone reaction by assuming *N,N*-diethylhydroxylamine as the primary product of the oxygen transfer pathway (steps (a) and (b) in Figure 2.3 and Reactions No. 1 and 2 in Table S2.4). The calculations were made for the initial reaction step of each pathway in which diethylamine and ozone react to form *N,N*-diethylhydroxylamine and $^1\text{O}_2$ via an oxygen transfer (step (a), Figure 2.3) or diethylaminyl radical ($(\text{CH}_3\text{CH}_2)\text{N}^\bullet$), proton (H^+), and ozonide radical anion ($\text{O}_3^{\bullet-}$) via electron transfer (step (b), Figure 2.3). The $\Delta G_{\text{aq,rxn}}$ was compared to estimated values based on more accurate gas-phase reactions for the oxygen transfer pathway⁶⁰ or to reported one-electron standard reduction potentials for the electron transfer pathway.^{61,62} The difference in $\Delta G_{\text{aq,rxn}}$ between the purely computed and the estimated values was $< 4 \text{ kcal mol}^{-1}$ (details are given in Text S2.8 and Table S2.4), and the uncertainty of calculation should be in the same range. The results clearly show that the oxygen transfer pathway ($\Delta G_{\text{aq,rxn}} = -16.4 \text{ kcal mol}^{-1}$) is thermodynamically more feasible than the electron transfer pathway ($\Delta G_{\text{aq,rxn}} = +9.3 \text{ kcal mol}^{-1}$). This is another strong indication suggesting a predominance of an oxygen transfer pathway over an electron transfer pathway during the initial phase of the diethylamine-ozone reaction shown in Figure 2.3.

2.3.2.3 *N,N*-Diethylhydroxylamine-ozone reaction

Transformation products. To further investigate whether *N,N*-diethylhydroxylamine can be an intermediate of the diethylamine-ozone reaction, *N,N*-diethylhydroxylamine was treated with ozone separately and its transformation products (Figure 2.1c) were compared with those of diethylamine (Figure 2.1b). *N,N*-diethylhydroxylamine was indeed transformed to *N*-ethylethanamine oxide and nitroethane, the identical products as formed in the diethylamine-ozone reaction. *N*-ethylethanamine oxide was detected even for the samples without ozone (i.e., at $0 \text{ }\mu\text{M}$ ozone), which was due to the spontaneous oxidation of hydroxylamines by oxygen to form nitrones.⁶³ Accordingly, the reaction time was reduced to 3 – 5 hours to minimize the autoxidation. *N*-ethylethanamine oxide reached the maximum formation at $150 \text{ }\mu\text{M}$ ozone where *N,N*-diethylhydroxylamine was completely abated, and decreased for higher ozone doses. The decrease in *N*-ethylethanamine oxide coincided with a gradual increase in nitroethane formation. Thus, the transformation reaction occurred in the sequence *N,N*-diethylhydroxylamine \rightarrow *N*-ethylethanamine oxide \rightarrow nitroethane. The mass balance of *N,N*-diethylhydroxylamine and the detected transformation products was within 82 – 116 % for the entire range of ozone doses.

Reactive oxygen species. Similar yields of $^1\text{O}_2$ and $\bullet\text{OH}$ were determined for the reaction of *N,N*-diethylhydroxylamine with ozone (38 % and 43 %, Table 2.2). The $^1\text{O}_2$ yield increased to 50 % at amine:ozone molar ratios > 1 (Table S2.3). Under these conditions with amine in excess, *N,N*-diethylhydroxylamine was transformed into *N*-ethylethanamine oxide with 100 % yield ($0 - 150 \text{ }\mu\text{M}$ ozone dose, Figure 2.1c). Therefore, the initial phase of the *N,N*-diethylhydroxylamine-ozone reaction can be characterized by two distinct pathways yielding $^1\text{O}_2$ and $\bullet\text{OH}$, which both led to the same product, *N*-ethylethanamine oxide. To investigate the secondary phase of the *N,N*-diethylhydroxylamine-ozone reaction where *N*-ethylethanamine oxide was transformed to nitroethane, we attempted to determine $^1\text{O}_2$ yields under ozone excess conditions (amine:ozone ≤ 1) and found the yields decreased as the specific ozone dose increased (Table S2.3). The low $^1\text{O}_2$ yields might be underestimated by the excess ozone which could quench $^1\text{O}_2$ formed during the *N,N*-diethylhydroxylamine-ozone reaction. The reaction of $^1\text{O}_2$ with ozone in the gas phase is known ($k = 2 \times 10^6 \text{ M}^{-1} \text{ s}^{-1}$).⁶⁴ However, currently little information is available for the quenching reaction in the aqueous phase.

*Comparison of reactive oxygen species yields for diethylamine- and *N,N*-diethylhydroxylamine-ozone reactions.* The reactive oxygen species yields of *N,N*-diethylhydroxylamine were compared to those of diethylamine to further examine the possibility of forming *N,N*-diethylhydroxylamine as a primary product of the diethylamine-ozone reaction. During the initial phase of the diethylamine-ozone reaction, 95 % $^1\text{O}_2$ and 8 % $\cdot\text{OH}$ would have been formed based on the yields of the corresponding transformation products, *N,N*-diethylhydroxylamine and ethylamine (steps (a) and (b), Figure 2.3). As mentioned above, the total $^1\text{O}_2$ and $\cdot\text{OH}$ yields determined for the diethylamine-ozone reaction were 186 % and 105 %, respectively, thus the remaining 91 % $^1\text{O}_2$ and 97 % $\cdot\text{OH}$ would have resulted from secondary reactions of a primary transformation product, e.g., *N,N*-diethylhydroxylamine. The hypothetical $^1\text{O}_2$ and $\cdot\text{OH}$ yields for the reaction of *N,N*-diethylhydroxylamine with ozone were estimated for the condition where *N*-ethylethanamine oxide and nitroethane were formed with 26 % and 69 % yields, respectively, as found in the diethylamine-ozone reaction. The ozone dose required for these specific product yields was approximately 270 μM (shown as a vertical line in Figure 2.1c) for *N,N*-diethylhydroxylamine with an initial concentration of $\sim 110 \mu\text{M}$. For this ozone dose, *N,N*-diethylhydroxylamine was transformed to 31 μM *N*-ethylethanamine oxide (29 % of the abated *N,N*-diethylhydroxylamine) and 80 μM nitroethane (72 %) based on the simulated concentrations of the products (dotted lines in Figure 2.1c; details on the simulation are discussed in the section 2.3.2.4). Converting the $^1\text{O}_2$ and $\cdot\text{OH}$ yields determined with regard to ozone (38 % and 43 %, Table 2.2) into the yields per abated *N,N*-diethylhydroxylamine with $[\text{O}_3] = 270 \mu\text{M}$ and $\Delta[\text{N,N-diethylhydroxylamine}] = 110 \mu\text{M}$ resulted in 93 % $^1\text{O}_2$ and 106 % $\cdot\text{OH}$. This agrees well with the aforementioned hypothetical yields, supporting *N,N*-diethylhydroxylamine as an intermediate of the diethylamine-ozone reaction.

Detailed reaction mechanisms. *N,N*-diethylhydroxylamine is a highly probable intermediate of the diethylamine-ozone reaction with a high theoretical yield of 95 %. Therefore, it is important to understand how *N,N*-diethylhydroxylamine reacts with ozone to obtain a complete picture of the diethylamine-ozone reaction. Clearly, our results show that *N,N*-diethylhydroxylamine was quantitatively transformed into *N*-ethylethanamine oxide upon ozonation during the initial phase of the reaction (Figure 2.1c). Based on the similarly high yields of $^1\text{O}_2$ and $\cdot\text{OH}$ from *N,N*-diethylhydroxylamine (38 % for $^1\text{O}_2$ and 43 % for $\cdot\text{OH}$, Table 2.2), both oxygen transfer and electron transfer seem to play an important role in the initial transformation of *N,N*-diethylhydroxylamine into *N*-ethylethanamine oxide. The oxygen transfer pathway would proceed via a $\text{N}^+-\text{O}-\text{O}-\text{O}^-$ adduct from an ozone attack on *N,N*-diethylhydroxylamine, which would then degrade into *N*-ethylethanamine oxide, $^1\text{O}_2$, and water (step (c), Figure 2.4). The formation of a $\text{N}^+-\text{O}-\text{O}-\text{O}^-$ adduct of a hydroxylamine was suggested by a study on the reaction of a primary amine with ozone in an organic solvent where a hydroxylamine was expected as a reaction intermediate, but with lack of experimental evidence.²⁸ In contrast, the electron transfer pathway would result in diethylnitroxide and ozonide radical anion ($\text{O}_3^{\cdot-}$) as primary products (step (d), Figure 2.4). Electron transfer pathways forming nitroxide compounds were often suggested by other studies to describe the oxidation of hydroxylamines, e.g., with ozone as an oxidant in the gas phase,⁶⁵ with molecular oxygen,⁶³ with $^1\text{O}_2$,⁶⁶ and during photooxidation.⁶⁷ The formation of diethylnitroxide during the photooxidation of *N,N*-diethylhydroxylamine was experimentally confirmed by detecting the characteristic EPR signal.⁶⁷ Nitroxides containing α -hydrogens are susceptible to an attack by other radicals to form nitrones.⁶⁸ Similarly, an α -hydrogen of diethylnitroxide can be abstracted by other radicals and transformed into *N*-ethylethanamine oxide (step (h), Figure 2.4). Such radicals can be diethylnitroxide itself inducing a bimolecular reaction forming *N*-ethylethanamine oxide and *N,N*-diethylhydroxylamine⁶⁹ or *t*-butanol derived peroxy radicals (e.g., $\text{C}(\text{CH}_3)_2(\text{OH})\text{CH}_2\text{OO}^\cdot$, hereafter referred to *t*-BuOO $^\cdot$)⁴⁸ likely present in the reaction system with high yields of $\cdot\text{OH}$. Alternatively, diethylnitroxide can further react with ozone to form an aminyl radical (R_2N^\cdot), which will likely further react with ozone and cause an ozone-consuming chain reaction (steps (e) and (f), Figure 2.4)^{1,70} or react also with *t*-BuOO $^\cdot$ to decompose to 2-Methyl-

1,2-propanediol and *N*-ethylethanamine oxide (step (i), Figure 2.4). The ozone reaction kinetics of diethylnitroxide have not been determined yet. A similar compound with a nitroxide group but with no α -hydrogen, TEMPO, has a very high second-order rate constant for its reaction with ozone ($k_{O_3} = 10^7 \text{ M}^{-1} \text{ s}^{-1}$).⁷¹ As the calculated $\Delta G_{\text{aq,rxn}}$ for the diethylnitroxide-ozone reaction (-16.7 kcal mol⁻¹, step (e) in Figure 2.4) is slightly energetically less favorable than the reported $\Delta G_{\text{aq,rxn}}$ for the TEMPO-ozone reaction (-23.2 kcal mol⁻¹),⁷² the kinetics of the diethylnitroxide-ozone reaction may be lower than $10^7 \text{ M}^{-1} \text{ s}^{-1}$. In contrast, the kinetics of the reaction of diethylnitroxide with radical species vary widely from $8.0 \times 10^2 \text{ M}^{-1} \text{ s}^{-1}$ (as the bimolecular reaction of diethylnitroxide)⁷³ to $2.8 \times 10^7 \text{ M}^{-1} \text{ s}^{-1}$ (as the reaction of TEMPO with *t*-BuOO \cdot).⁷⁴ Based on the available kinetic information, both reactions of diethylnitroxide with ozone and with radical seem probable, but we still propose that the radical reaction outcompetes the ozone reaction because of the following reasons: (1) Diethylaminyl radical resulted from the further ozone reaction would degrade into ethylamine via 1,2-H shift followed by a reaction with O₂ and hydrolysis (step (g), Figure 2.4),¹ which conflicts with the quantitative formation of *N*-ethylethanamine oxide as a primary product of the *N,N*-diethylhydroxylamine-ozone reaction (Figure 2.1c); (2) A catalytic ozone consumption accompanied with the further ozone reactions (steps (e) and (f)) is inconsistent with the relatively low stoichiometry of about 1.5 mole equivalents of ozone for the initial phase of the *N,N*-diethylhydroxylamine-ozone reaction (Figure 2.1c).

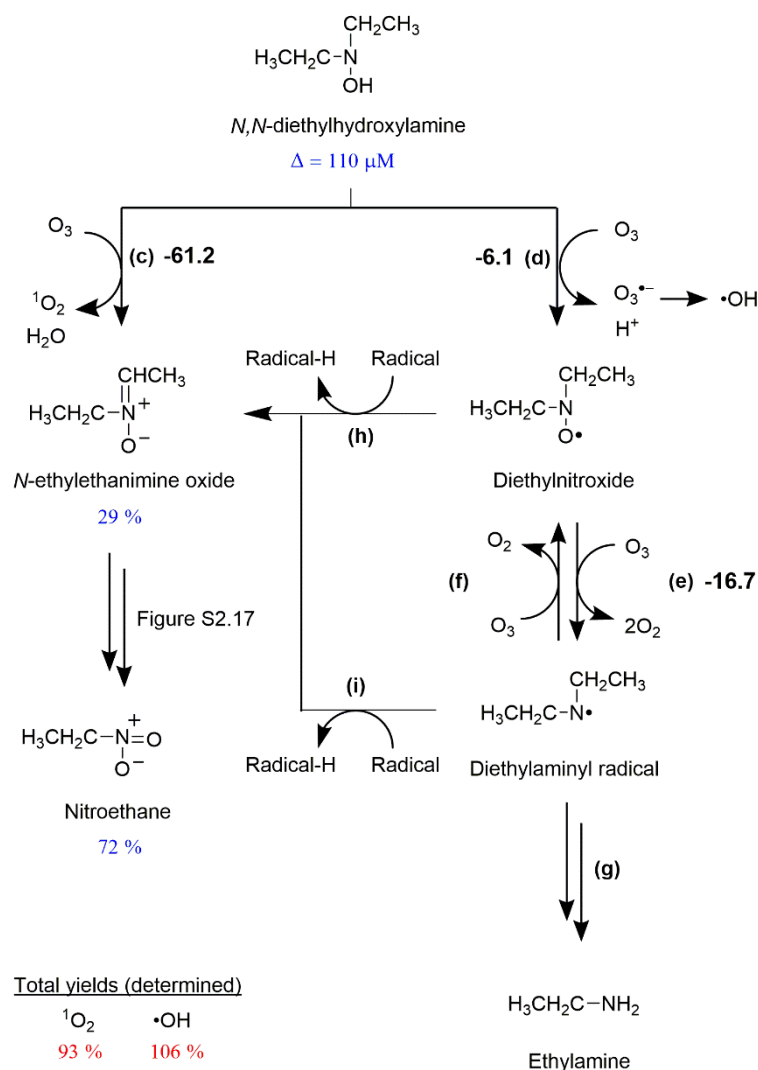


Figure 2.4. Proposed mechanism for the reaction of *N,N*-diethylhydroxylamine and *N*-ethylethanamine oxide with ozone. Product yields (in %) were calculated by dividing the simulated concentrations of the transformation products and the measured concentrations of reactive oxygen species by the abated *N,N*-diethylhydroxylamine (110 μM) at an ozone dose of 270 μM . The yields of transformation products and reactive oxygen species are emphasized in blue and red, respectively. Bold numbers next to the reaction steps are calculated aqueous Gibbs free energies in kcal mol^{-1} . For discussion of reactions (c) – (i) see text.

Quantum chemical computations. Quantum chemical computations of the $\Delta G_{\text{aq,rxn}}$ for the *N,N*-diethylhydroxylamine-ozone reaction were performed to test for an oxygen transfer or an electron transfer as the initial reaction step (steps (c) and (d) in Figure 2.4 and Reactions No. 3 and 4 in Table S2.4). The results showed that the oxygen transfer pathway is significantly and thermodynamically more favorable than the electron transfer pathway ($-61.2 \text{ kcal mol}^{-1}$ for the oxygen transfer, $-6.1 \text{ kcal mol}^{-1}$ for the electron transfer). However, it is worth to note that the electron transfer pathway is exergonic for the *N,N*-diethylhydroxylamine-ozone reaction, in contrast to the diethylamine-ozone reaction where the $\Delta G_{\text{aq,rxn}}$ of the electron transfer pathway is $+9.3 \text{ kcal mol}^{-1}$. This implies that *N,N*-diethylhydroxylamine-ozone reaction may have a higher probability to undergo an electron transfer pathway than the diethylamine-ozone reaction, which is confirmed by similar $^1\text{O}_2$ and $\bullet\text{OH}$ yields.

2.3.2.4 *N*-Ethylethanamine oxide-ozone reaction

Transformation products. The last piece of information needed to understand the diethylamine-ozone reaction is the transformation of *N*-ethylethanamine oxide to nitroethane. An ozonation experiment was carried out for *N*-ethylethanamine oxide using the synthesized stock described in Text S2.1 to investigate if it could be a transient product with a high yield of nitroethane. Nitroethane was indeed identified as a major product with a 73 % yield based on the abated *N*-ethylethanamine oxide at 300 μM ozone (Figure S2.13). However, there were a few distinguishing features observed in this separate ozonation experiment with *N*-ethylethanamine oxide as a starting material, compared to the *N,N*-diethylhydroxylamine-ozone reaction (Figure 2.1c) where *N*-ethylethanamine oxide was formed as an intermediate and further degraded. We assume the difference was caused by a spontaneous dimerization of *N*-ethylethanamine oxide,^{75,76} which contaminated the primary stock solution used in the separate ozonation experiment and affected the reaction of *N*-ethylethanamine oxide with ozone (Text S2.7). Therefore, for further discussions regarding *N*-ethylethanamine oxide, we rely on the result from the *N,N*-diethylhydroxylamine-ozone reaction at high ozone doses (100 – 300 μM). Under these conditions, *N*-ethylethanamine oxide is formed *in situ* and not affected by dimerization. Because of these experimental shortcomings, also the results of the reactive oxygen species in the experiments with *N*-ethylethanamine oxide should be interpreted cautiously by taking the presence of a dimer into account.

Kinetic simulation: *N,N*-diethylhydroxylamine- and *N*-ethylethanamine oxide-ozone reactions. Based on the information obtained so far, we performed kinetic simulations to describe the evolution of *N,N*-diethylhydroxylamine, *N*-ethylethanamine oxide, and nitroethane during the *N,N*-diethylhydroxylamine-ozone reaction by using the Kintecus software (www.kintecus.com)⁷⁷ (Table S2.5 and Figure 2.1c, dotted lines). The kinetic model contained the initial transformation reaction of *N,N*-diethylhydroxylamine to *N*-ethylethanamine oxide, diethylnitroxide, and an unknown radical species, X, via oxygen transfer and electron transfer pathways with a 1:1 branching ratio. X is a radical species (e.g., *t*-BuOO•) derived from the scavenging reaction of •OH with *t*-butanol, formed by the electron transfer reaction along with diethylnitroxide. The 1:1 ratio was selected based on the similar yields of ¹O₂ and •OH, the indicators of oxygen transfer and electron transfer, for the conditions where *N,N*-diethylhydroxylamine was in molar excess of ozone (i.e., amine:ozone > 1, Table S2.3 and Figure S2.12). The ensuing products of electron transfer, diethylnitroxide and X, react with each other and subsequently form *N*-ethylethanamine oxide. Additionally, the autooxidation of *N,N*-diethylhydroxylamine was included assuming oxygen saturation at 20 °C ([O₂ (aq)] ~ 9 mg/L). A bimolecular reaction of diethylnitroxide to form *N,N*-diethylhydroxylamine and *N*-ethylethanamine oxide was also included to describe the decay of diethylnitroxide under conditions without ozone (0 μM ozone). Lastly, two more reaction steps were added to describe the transformation of *N*-ethylethanamine oxide into nitroethane via an unknown intermediate, Y, which was assumed to react very fast with ozone (assumed $k_{\text{obs,pH7}} = 1 \times 10^6 \text{ M}^{-1} \text{ s}^{-1}$) to form nitroethane. The simulation results shown in Figure 2.1c (dotted lines) are in reasonable agreements with the experimental findings of the *N,N*-diethylhydroxylamine-ozone reaction which formed *N*-ethylethanamine oxide and nitroethane in a sequential order.

Detailed reaction mechanisms. Compounds containing C-N double bonds like nitrones and oximes typically form C-nitroso compounds upon ozonation according to the studies conducted in organic solvents.^{29,78,79} Similarly, *N*-ethylethanamine oxide could react with ozone to form nitrosoethane which would be further oxidized by ozone to form nitroethane (steps (j) and (k), Figure S2.17). However, as the nitroso moiety is a strong electron-withdrawing group, nitrosoethane cannot be the intermediate Y hypothesized to be highly reactive to ozone in the kinetic simulation. This was tested by a kinetic simulation substituting nitrosoethane for Y and using the same kinetic model but with a different $k_{\text{obs,pH7}}$ of the reaction No. 6 set at $1.0 \times 10^2 \text{ M}^{-1} \text{ s}^{-1}$ instead of $1.0 \times 10^6 \text{ M}^{-1}$.

s⁻¹ (Table S2.6). The new model with nitrosoethane as an intermediate did not perform as well as the previous one, featuring a lower ozone stoichiometry of the abatement of *N*-ethylethanimine oxide than the measured value (Figure S2.16b). Another possible mechanism of the *N*-ethylethanimine oxide-ozone reaction can be a Criegee-type mechanism forming an ozonide via a cycloaddition of ozone to the C-N double bond (step (l), Figure S2.17).^{80,81} The ozonide would dissociate into nitroethane and a peroxide intermediate. The latter would subsequently react with water to form acetaldehyde and hydrogen peroxide.^{80,82} To test this hypothesis, the formation of hydrogen peroxide was determined in ozonated *N*-ethylethanimine oxide samples. The *N*-ethylethanimine oxide solution was prepared *in situ* by oxidizing ~100 μ M *N,N*-diethylhydroxylamine with 180 μ M ozone to ensure all *N,N*-diethylhydroxylamine was converted to *N*-ethylethanimine oxide. Thereafter, 100 μ M ozone was added to the *N*-ethylethanimine oxide solution. The concentrations of hydrogen peroxide in the *N*-ethylethanimine oxide solution before and after the ozone addition remained the same (16 ± 4 μ M for both). This confirms that hydrogen peroxide was not formed during the reaction of *N*-ethylethanimine oxide with ozone and thus, makes the Criegee-type mechanism very unlikely. The other hypothesis is an electron transfer pathway forming a *N*-ethylethanimine oxide radical cation and an ozonide radical anion (step (m), Figure S2.17). This pathway can explain the possibly high \cdot OH yield of *N*-ethylethanimine oxide (43 %, Table 2.2). One-electron oxidation of nitrones has been postulated as an alternative spin trapping mechanism when nitrones were used as radical spin traps.^{83,84} The resulting nitron radical cations were detected experimentally.⁸⁴ However, little is known whether a similar pathway can be applied to the ozone reaction and how the radical cation further degrades into nitroethane.

Quantum chemical computations. The hypothesized mechanisms of the *N*-ethylethanimine oxide-ozone reaction (steps (j) and (l), Figure S2.17) were examined by calculating $\Delta G_{aq,rxn}$ of the reactions. The $\Delta G_{aq,rxn}$ of the reaction step (m) could not be calculated because of an unreliable result of the computation of the *N*-ethylethanimine oxide radical cation at the CCSD(T)/jul-cc-pVTZ level, resulting in T1 diagnostic > 0.03.⁸⁵ Besides the ozone reactions, the hydrolysis of *N*-ethylethanimine oxide forming *N*-ethylhydroxylamine and acetaldehyde (step (n), Figure S2.17), suggested by an earlier study,³⁹ was also examined because this could compete with the further reaction of *N*-ethylethanimine oxide with ozone. The calculations show that the further reactions with ozone are thermodynamically more feasible than the hydrolysis which is endergonic (-40.8 kcal mol⁻¹ and -70.8 kcal mol⁻¹ for the ozone reactions and $+8.4$ kcal mol⁻¹ for hydrolysis, steps (j), (l), and (n) in Figure S2.17 and Reaction No. 6 – 8 in Table S2.4). However, despite the thermodynamic feasibility of the reaction steps (j) and (l), neither of them were justified by the experimental findings as discussed above. This demonstrates that the results from quantum chemical computations must be interpreted cautiously and considered as supplementary information to experimental findings.

Kinetic simulation: diethylamine-ozone reaction. Finally, a kinetic simulation for the diethylamine-ozone reaction was carried out (Table S2.7 and Figure 2.1b, dotted lines). The kinetic model included the initial transformation reaction of diethylamine to *N,N*-diethylhydroxylamine and diethylaminy radical with a 9:1 branching ratio based on the product yields. The follow-up reaction steps were applied as in the model for the *N,N*-diethylhydroxylamine-ozone reaction (Table S2.5). The trends for the abatement of diethylamine and the evolution of the various transformation products were well described. However, the simulated concentrations of the final products (nitroethane and ethylamine) at 300 μ M ozone dose were about 50 % higher than the measured concentrations (Figure 2.1b). For such a complex reaction system, this is a reasonable outcome.

2.3.2.5 Ethylamine-ozone reaction

Transformation products. About 5.5 molar equivalents of ozone were required for a complete abatement of ethylamine (Figure 2.1d). Nitroethane was the major product with close to 100 % yields at all ozone doses, resulting in a very good mass balance. Therefore, only very limited additional products are expected from the ethylamine-ozone reaction. The high yield of nitroethane observed in the ethylamine-ozone reaction is in agreement with a recent study that found 100 % nitromethane from methylamine with a molar ozone:methylamine ratio of 12.¹³ However, these results disagree with previous studies, where nitrate was detected as a final product from the ozone reactions of ammonia⁸⁶ and amino acids containing a primary amine moiety.^{40–42} In the current study, only traces of nitrite and nitrate were detected from ethylamine over the entire range of ozone doses (< 1 %, not shown in Figure 2.1d). Additional ozonation experiments were carried out with ozone:ethylamine ratios of 20, but still only about 10 % nitrate was detected. This is far smaller than previously reported nitrate yields from amino acids (glycine and serine) of 85 - 90 % with molar ozone:model compound ratios of 5-20.^{40–42} The discrepancy may be due to the presence of a carboxylic group in the amino acids, which alters the reaction pathway to favor nitrate rather than nitroalkanes as final products (see the section “*primary amines vs amino acids*” below). Ammonia, a dealkylated product from ethylamine, is unlikely to be formed, because the nitrogen mass balance was completed by nitroethane alone. No ammonia formation was also reported in the oxidation of glycine by ozone in presence of a radical scavenger.⁴⁰

Reactive oxygen species. Similar yields of $^1\text{O}_2$ and $\cdot\text{OH}$ were determined for the ethylamine-ozone reaction (27 % and 33 % relative to the consumed ozone for $^1\text{O}_2$ and $\cdot\text{OH}$, respectively, Table 2.2). The $^1\text{O}_2$ yield was slightly higher than the previously reported value of 17 %.⁴⁷ The $\cdot\text{OH}$ yield was similar to the yield from glycine which contains a primary amine moiety.⁴¹ Similar to the diethylamine-ozone reaction, the significant yield of $\cdot\text{OH}$ seems to be a result of secondary ozone reactions of primary transformation products rather than from the initial phase of the ethylamine-ozone reaction.

Reaction pathways. The ethylamine-ozone reaction can be understood similarly to the diethylamine-ozone reaction as it was characterized by the same features: high ozone stoichiometry, the formation of a highly oxidized product (nitroethane), and high yields of reactive oxygen species per abated amine (Figure 2.5). The yields of nitroethane and reactive oxygen species ($^1\text{O}_2$ and $\cdot\text{OH}$) at 93 μM ozone are 100 %, 120 % and 146 %, respectively, where $\Delta[\text{Ethylamine}] = 21 \mu\text{M}$. The ethylamine-ozone reaction mainly underwent oxygen transfer reaction based on a 100 % yield of nitroethane. Accordingly, *N*-ethylhydroxylamine and $^1\text{O}_2$, the primary transformation product and the reactive oxygen species of the oxygen transfer pathway, would be formed with 100 % theoretical yields. The remaining $^1\text{O}_2$ and $\cdot\text{OH}$ yields (20 % and 146 %) should be associated with secondary reactions leading to nitroethane. However, considering the high ozone stoichiometry of 5.5 mole equivalents of ozone (or 550 % ozone in relation to abated ethylamine), the total reactive oxygen species yield (266 %) was too low. Thus, more reactive oxygen species (e.g., $^1\text{O}_2$ and $\cdot\text{OH}$ which might have been underestimated or superoxide radical and hydrogen peroxide which have not been determined) seems to be involved in the secondary reactions than what were actually measured.

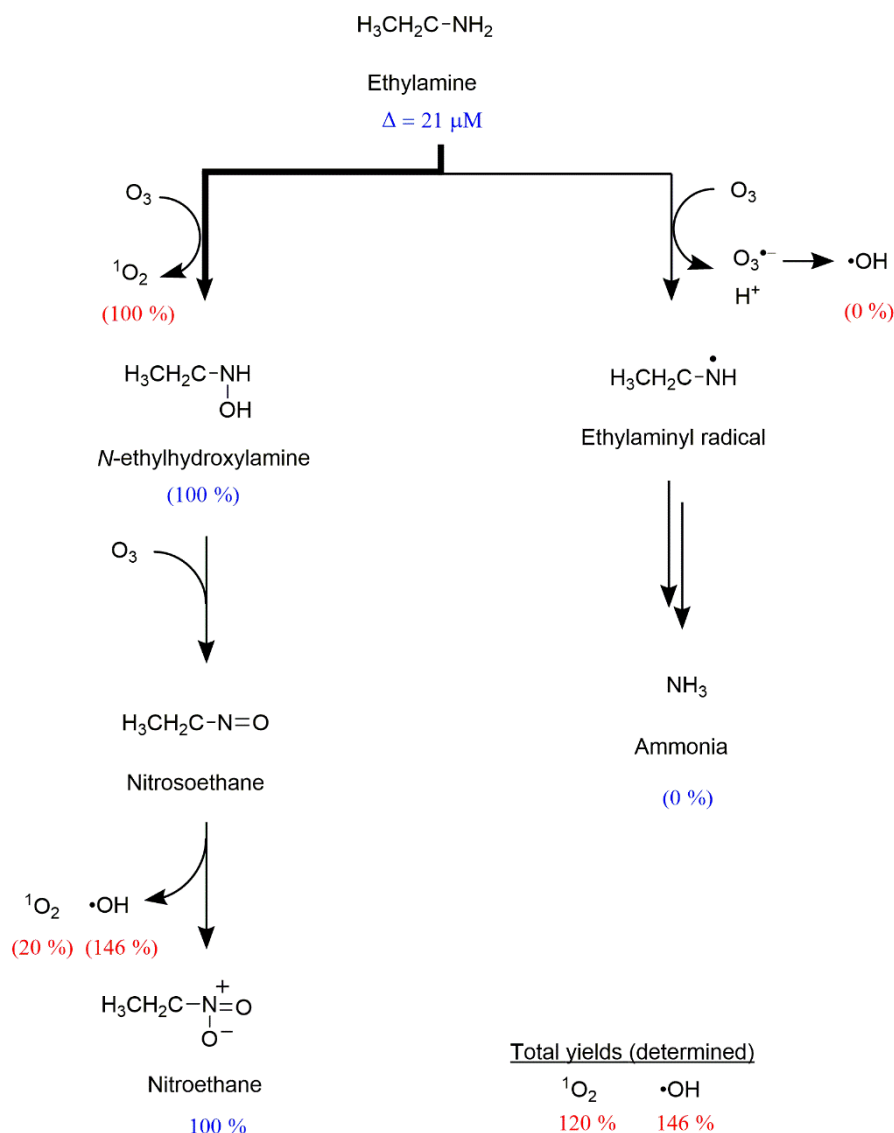


Figure 2.5. Proposed mechanism for the reaction of ethylamine with ozone. Product yields (in %) were calculated by dividing the measured concentrations of the transformation products and the reactive oxygen species by the abated ethylamine (21 μM) at an ozone dose of 93 μM . The yield of *N*-ethylhydroxylamine in parenthesis is a theoretical yield based on the nitroethane yield. The $^1\text{O}_2$ and $\cdot\text{OH}$ yields in parentheses are also theoretical yields based on the yields of the corresponding transformation products and the total $^1\text{O}_2$ and $\cdot\text{OH}$ yields determined for the ethylamine-ozone reaction (120 % $^1\text{O}_2$ and 146 % $\cdot\text{OH}$). The yields of transformation products and reactive oxygen species are emphasized in blue and red, respectively. The bold arrow indicates the major pathway of the branched reaction.

Detailed reaction mechanisms. *N*-ethylhydroxylamine is expected as a primary transformation product via oxygen transfer in analogy to *N,N*-diethylhydroxylamine of the diethylamine-ozone reaction. Similar to *N,N*-diethylhydroxylamine, *N*-ethylhydroxylamine ($k_{\text{obs,pH } 7} \sim 10^5 \text{ M}^{-1} \text{ s}^{-1}$, Table 2.1) reacts much faster with ozone than the parent amine, wherefore, it was not detectable and the formation of further oxidized products can be expected. During the further reaction of *N*-ethylhydroxylamine with ozone, a dihydroxylamine intermediate would be formed (Figure S2.18a), as suggested by studies on ozone reactions of primary amines in organic solvents.^{28,87} The dihydroxylamine intermediate would degrade to nitrosoethane or acetaldoxime by releasing water. Neither of these products were identified due to the lack of reference standards or an applicable analytical method. Nitroso compounds and oximes are tautomers of each other and oximes are known to be the more stable forms.⁸⁸ Although the tautomeric equilibrium would favor the formation of acetaldoxime, nitrosoethane still seems a

more probable product based on the predominant formation of nitroethane. If acetaldoxime was formed, the major product would have been nitrate, since acetaldoxime is hydrolyzed to hydroxylamine which can react fast with ozone ($k_{03} = 2.1 \times 10^4 \text{ M}^{-1} \text{ s}^{-1}$ for hydroxylamine)⁸⁹ to nitrate. Therefore, the high yield of nitroethane supports nitrosoethane as a precursor rather than acetaldoxime.

Primary amines vs amino acids. The different nitrate yields for primary amines and amino acids upon ozonation may be related to the secondary reaction pathways involving dihydroxylamines, nitroso compounds, or oximes as intermediates. Ethylamine and glycine, differing only by a substituent of the α -carbon (methyl for ethylamine and carboxyl for glycine), are compared in detail in Figure S2.18. The nitrate yields per abated amines under ozone-excess conditions (≥ 5 molar equivalent ozone) were 10 % for ethylamine (determined in this study) and 90 % for glycine.⁴⁰ To explain the high nitrate yield from glycine, we hypothesized that the nitroso intermediate of glycine can not only degrade into nitroacetic acid,¹³ but also produce nitrate as a final product similar to the oxime counterpart (Figure S2.18b). This is because the carboxyl group in the nitroso intermediate of glycine can decarboxylate, leaving formaldehyde oxime as the other product. The resulting formaldehyde oxime would be transformed into hydroxylamine and then nitrate in the same manner as the other oxime intermediates. The same decarboxylation mechanism was suggested for oxidation of amino acids by dimethyldioxirane, an electrophilic compound, for which the corresponding oximes and the carboxylic acids (resulted from further decomposition of the oximes) were found as major products.⁹⁰ In comparison, the reactions of primary amines with dimethyldioxirane produce nitro compounds with high yields.⁹¹ Alternatively, it can be hypothesized that the carboxyl group can withdraw electron density from the neighboring α -carbon and render the α -carbon more acidic and thus prone to lose a proton. As a result, the oxime intermediate may be formed more efficiently than the nitroso counterpart. The deprotonation of the α -carbon of amino acids has been accepted as a key step of the racemization of amino acids.⁹² The pK_a of the α -carbon of glycine in the zwitterion form was determined to be 29 in aqueous solution.⁹³ With the two additional hydroxyl groups, the α -carbon of the dihydroxylamine intermediate of glycine may be characterized by a much lower pK_a . Overall, the involvement of the oxime intermediates, either derived from dihydroxylamine intermediate or from nitroso intermediate, seems a decisive factor to explain the high nitrate yield from amino acids in comparison to primary amines.

2.3.2.6 Reaction mechanisms of aliphatic amines with ozone

Based on the findings of this study as well as available information in literature,^{28–30,34,35,37,38,40,41} the reactions of aliphatic primary, secondary, and tertiary amines with ozone are summarized in Figure 2.6. Our study revealed that all amines were predominantly transformed into products containing nitrogen-oxygen bonds, i.e., triethylamine *N*-oxide or nitroethane (64 – 100 % of the transformed parent amines at the highest applied ozone dose). Dealkylated products were formed only as small fractions of the transformed parent compounds (0 – 9 %).

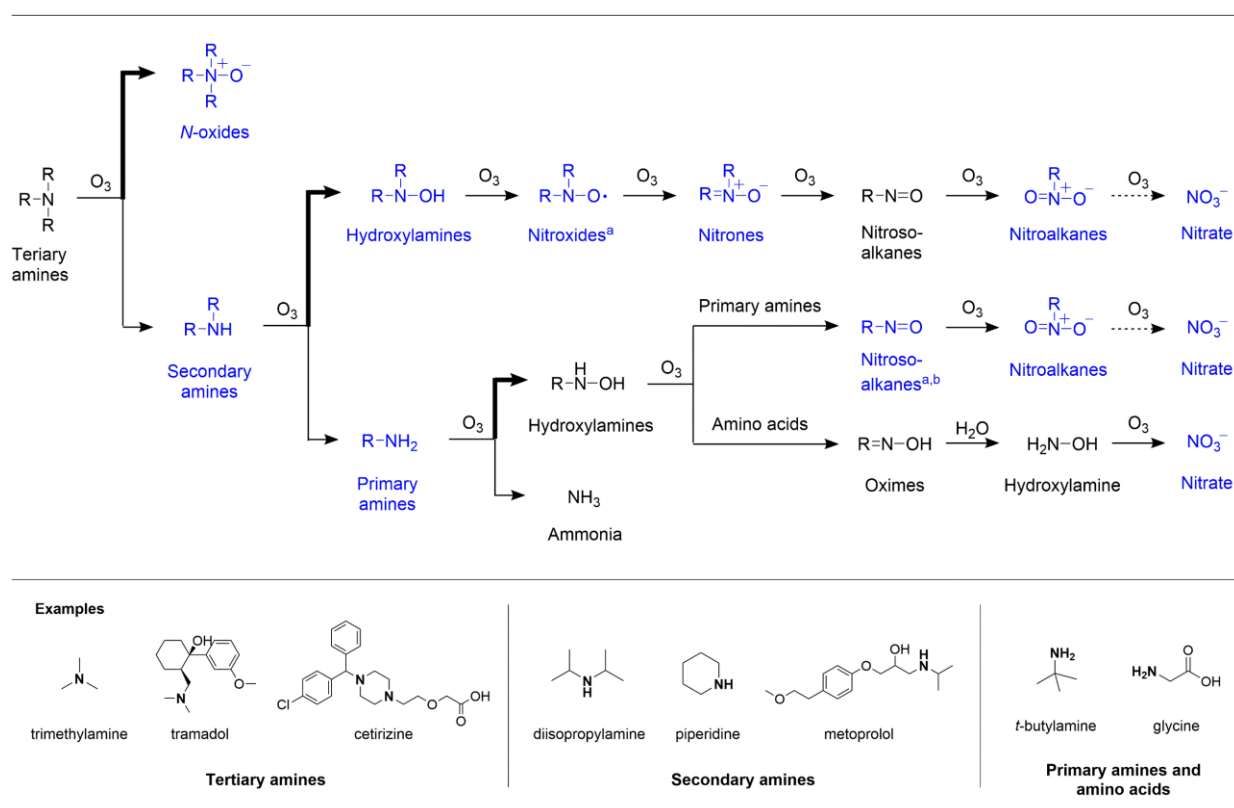


Figure 2.6. Summary of the reactions of aliphatic primary, secondary, and tertiary amines with ozone in aqueous solution based on this and other studies (both acyclic and saturated heterocyclic amines as shown in the examples).^{28–30,34,35,37,38,40,41} Bold arrows indicate the dominant pathway. Identified transformation products are highlighted in blue. ^aDetected only in organic solvent.²⁹ ^bIndirectly confirmed based on a change in color of the solution.²⁸

2.3.3 Practical implications

Nitroethane was detected as a final product in all tested amine-ozone reactions. The yield was considerable for almost all amines (> 60 % for diethylamine, ethylamine, *N,N*-diethylhydroxylamine, and *N*-ethylethanamine oxide) except for triethylamine (9 %). Short-chain aliphatic amines such as methylamine, dimethylamine, ethylamine, and diethylamine are typically present up to 0.1 μM in surface waters and up to 5 μM in wastewater effluents.^{94–98} Considering the amount of aliphatic amines formed as breakdown products from more complex organic compounds, the total concentration of the short-chain nitroalkanes derived from aliphatic amines can be higher than 5 μM after ozonation. The reactivity of nitroalkanes towards ozone is expected to be low based on the low second-order ozone rate constant of nitroethane determined in this study ($k = 3.4 \text{ M}^{-1} \text{ s}^{-1}$, Table 2.1). Thus, once formed, nitroalkanes would not be further transformed by ozone but persistent in water as they are not easily hydrolyzed nor biodegradable.⁹⁹ Moreover, the volatility of short-chain nitroalkanes is in the same range as trihalomethanes, known disinfection byproducts in chlorinated waters, based on the comparable Henry's constants ($2.9 \times 10^{-5} - 1.2 \times 10^{-4} \text{ atm m}^3 \text{ mol}^{-1}$ for nitroalkanes and $4.4 \times 10^{-4} - 7.8 \times 10^{-3} \text{ atm m}^3 \text{ mol}^{-1}$ for trihalomethanes).¹⁰⁰ Therefore, exposures to nitroalkanes could occur via inhalation or dermal adsorption during showering and bathing, similarly to trihalomethanes.¹⁰¹ The short-chain nitroalkanes such as nitromethane, nitroethane, 1-nitropropane, and 2-nitropropane are widely used as industrial solvents, building blocks for chemical syntheses, and fuels in combustion engines.¹⁰² Accordingly, studies on the toxicity of the nitroalkanes have mostly been conducted in the context of occupational exposures at workplaces where the nitroalkanes are used in high con-

centrations. Exposure to high levels of nitroalkanes causes acute and short-term toxicity (nitrite-induced methemoglobinemia) typically with little lingering effects. Such high levels of nitroalkanes are unlikely to be formed during water and wastewater treatment. Some nitroalkanes (nitromethane and 2-nitropropane) are reasonably anticipated to be human carcinogens¹⁰³ and effects of long-term exposure to them have been of great concern. Therefore, further information is needed on the occurrence of nitroalkanes during ozonation, especially in the context of wastewater-impacted source waters and water reuse systems, where relatively high concentrations of aliphatic amines are expected in the dissolved organic matter.

2.4 Conclusion

All amines predominantly underwent oxygen transfer reactions as initial ozone reaction pathways to form major products containing nitrogen-oxygen bonds, e.g., triethylamine *N*-oxide (triethylamine) or nitroethane (diethylamine and ethylamine). The yields of the major products were 69 – 100 % per abated amines with one molar equivalent of ozone (93 μ M). *N*-dealkylated products were additionally identified for triethylamine and diethylamine, but the yields were lower than 10 %. Good nitrogen mass balances were achieved for all amine-ozone reactions (> 70 %).

N,N-diethylhydroxylamine, a potential intermediate of the diethylamine-ozone reaction, escaped from our detection because of its high reactivity towards ozone in comparison to the ozone reactivity of diethylamine. However, the measurements of reactive oxygen species ($^1\text{O}_2$ and $\cdot\text{OH}$), quantum chemical computations, and kinetic simulations support the possibility of forming *N,N*-diethylhydroxylamine during the diethylamine-ozone reaction.

Different from the triethylamine-ozone reaction, the reactions of diethylamine and ethylamine with ozone were characterized by the high ozone molar stoichiometry (ozone:amine ≥ 4), which resulted in the formation of the highly oxidized product (nitroethane) and the excess formation of $^1\text{O}_2$ and $\cdot\text{OH}$.

The high yields of nitroethane from diethylamine- and ethylamine-ozone reactions determined in this study imply significant formation of nitroalkanes during ozonation especially for waters containing high levels of dissolved organic nitrogen (e.g., wastewater-impacted sources waters). Further efforts are required to understand the occurrence of nitroalkanes and their impact on the receiving aquatic environment and human health.

Acknowledgement

We thank Elisabeth Salhi for her support in the laboratory, Paul Erickson and Kris McNeill for their advice on the singlet oxygen measurement, Marc Bourgin, Philipp Longree and Jakov Bolotin for their support with MS measurements, Peter Tentscher for his help on quantum chemical computations, and Samuel Derrer for the synthesis of *N*-ethylethanamine oxide.

2.5 References

- (1) von Sonntag, C.; von Gunten, U. *Chemistry of Ozone in Water and Wastewater Treatment*; IWA Publishing, 2012.
- (2) Eggen, R. I. L.; Hollender, J.; Joss, A.; Schärer, M.; Stamm, C. Reducing the Discharge of Micropollutants in the Aquatic Environment: The Benefits of Upgrading Wastewater Treatment Plants. *Environmental Science & Technology* **2014**, *48* (14), 7683–7689. <https://doi.org/10.1021/es500907n>.
- (3) Tentscher, P. R.; Bourgin, M.; von Gunten, U. Ozonation of *Para* -Substituted Phenolic Compounds Yields *p* -Benzoquinones, Other Cyclic α,β -Unsaturated Ketones, and Substituted Catechols. *Environmental Science & Technology* **2018**, *52* (8), 4763–4773. <https://doi.org/10.1021/acs.est.8b00011>.
- (4) Ternes, T. A.; Stüber, J.; Herrmann, N.; McDowell, D.; Ried, A.; Kampmann, M.; Teiser, B. Ozonation: A Tool for Removal of Pharmaceuticals, Contrast Media and Musk Fragrances from Wastewater? *Water Research* **2003**, *37* (8), 1976–1982. [https://doi.org/10.1016/S0043-1354\(02\)00570-5](https://doi.org/10.1016/S0043-1354(02)00570-5).
- (5) von Gunten, U. Oxidation Processes in Water Treatment: Are We on Track? *Environmental Science & Technology* **2018**, *52* (9), 5062–5075. <https://doi.org/10.1021/acs.est.8b00586>.
- (6) Dodd, M. C.; Kohler, H.-P. E.; von Gunten, U. Oxidation of Antibacterial Compounds by Ozone and Hydroxyl Radical: Elimination of Biological Activity during Aqueous Ozonation Processes. *Environmental Science & Technology* **2009**, *43* (7), 2498–2504. <https://doi.org/10.1021/es8025424>.
- (7) Lee, Y.; Escher, B. I.; von Gunten, U. Efficient Removal of Estrogenic Activity during Oxidative Treatment of Waters Containing Steroid Estrogens. *Environ. Sci. Technol.* **2008**, *42* (17), 6333–6339. <https://doi.org/10.1021/es7023302>.
- (8) Mestankova, H.; Escher, B.; Schirmer, K.; von Gunten, U.; Canonica, S. Evolution of Algal Toxicity during (Photo)Oxidative Degradation of Diuron. *Aquatic Toxicology* **2011**, *101* (2), 466–473. <https://doi.org/10.1016/j.aquatox.2010.10.012>.
- (9) Magdeburg, A.; Stalter, D.; Schlüsener, M.; Ternes, T.; Oehlmann, J. Evaluating the Efficiency of Advanced Wastewater Treatment: Target Analysis of Organic Contaminants and (Geno-)Toxicity Assessment Tell a Different Story. *Water Research* **2014**, *50*, 35–47. <https://doi.org/10.1016/j.watres.2013.11.041>.
- (10) Stalter, D.; Magdeburg, A.; Weil, M.; Knacker, T.; Oehlmann, J. Toxication or Detoxication? In Vivo Toxicity Assessment of Ozonation as Advanced Wastewater Treatment with the Rainbow Trout. *Water Research* **2010**, *44* (2), 439–448. <https://doi.org/10.1016/j.watres.2009.07.025>.
- (11) Hammes, F.; Salhi, E.; Köster, O.; Kaiser, H.-P.; Egli, T.; von Gunten, U. Mechanistic and Kinetic Evaluation of Organic Disinfection By-Product and Assimilable Organic Carbon (AOC) Formation during the Ozonation of Drinking Water. *Water Research* **2006**, *40* (12), 2275–2286. <https://doi.org/10.1016/j.watres.2006.04.029>.
- (12) Ramseier, M. K.; Peter, A.; Traber, J.; von Gunten, U. Formation of Assimilable Organic Carbon during Oxidation of Natural Waters with Ozone, Chlorine Dioxide, Chlorine, Permanganate, and Ferrate. *Water Research* **2011**, *45* (5), 2002–2010. <https://doi.org/10.1016/j.watres.2010.12.002>.
- (13) McCurry, D. L.; Quay, A. N.; Mitch, W. A. Ozone Promotes Chloropicrin Formation by Oxidizing Amines to Nitro Compounds. *Environmental Science & Technology* **2016**, *50* (3), 1209–1217. <https://doi.org/10.1021/acs.est.5b04282>.
- (14) Bourgin, M.; Beck, B.; Boehler, M.; Borowska, E.; Fleiner, J.; Salhi, E.; Teichler, R.; von Gunten, U.; Siegrist, H.; McArdell, C. S. Evaluation of a Full-Scale Wastewater Treatment Plant Upgraded with Ozonation and Biological Post-Treatments: Abatement of Micropollutants, Formation of Transformation Products and Oxidation by-Products. *Water Research* **2018**, *129*, 486–498. <https://doi.org/10.1016/j.watres.2017.10.036>.
- (15) Hübner, U.; von Gunten, U.; Jekel, M. Evaluation of the Persistence of Transformation Products from Ozonation of Trace Organic Compounds – A Critical Review. *Water Research* **2015**, *68*, 150–170. <https://doi.org/10.1016/j.watres.2014.09.051>.
- (16) Krasner, S. W.; Mitch, W. A.; McCurry, D. L.; Hanigan, D.; Westerhoff, P. Formation, Precursors, Control, and Occurrence of Nitrosamines in Drinking Water: A Review. *Water Research* **2013**, *47* (13), 4433–4450. <https://doi.org/10.1016/j.watres.2013.04.050>.
- (17) Shah, A. D.; Mitch, W. A. Halonitroalkanes, Halonitriles, Haloamides, and N-Nitrosamines: A Critical Review of Nitrogenous Disinfection Byproduct Formation Pathways. *Environmental Science & Technology* **2012**, *46* (1), 119–131. <https://doi.org/10.1021/es203312s>.
- (18) Lee, M.; Blum, L. C.; Schmid, E.; Fenner, K.; von Gunten, U. A Computer-Based Prediction Platform for the Reaction of Ozone with Organic Compounds in Aqueous Solution: Kinetics and Mechanisms. *Environmental Science: Processes & Impacts* **2017**, *19* (3), 465–476. <https://doi.org/10.1039/C6EM00584E>.
- (19) Lee, Y.; von Gunten, U. Advances in Predicting Organic Contaminant Abatement during Ozonation of Municipal Wastewater Effluent: Reaction Kinetics, Transformation Products, and Changes of Biological Effects. *Environmental Science: Water Research & Technology* **2016**, *2* (3), 421–442. <https://doi.org/10.1039/C6EW00025H>.
- (20) Westerhoff, P.; Mash, H. Dissolved Organic Nitrogen in Drinking Water Supplies: A Review. *Journal of Water Supply: Research and Technology-AQUA* **2002**, *51* (8), 415–448. <https://doi.org/10.2166/aqua.2002.0038>.
- (21) Graeber, D.; Boëchat, I. G.; Encina-Montoya, F.; Esse, C.; Gelbrecht, J.; Goyenola, G.; Gucker, B.; Heinz, M.; Kronvang, B.; Meerhoff, M.; et al. Global Effects of Agriculture on Fluvial Dissolved Organic Matter. *Scientific Reports* **2015**, *5* (1). <https://doi.org/10.1038/srep16328>.
- (22) Pehlivanoglu-Mantas, E.; Sedlak, D. L. Wastewater-Derived Dissolved Organic Nitrogen: Analytical Methods, Characterization, and Effects—A Review. *Critical Reviews in Environmental Science and Technology* **2006**, *36* (3), 261–285. <https://doi.org/10.1080/10643380500542780>.

- (23) Leverenz, H. L.; Tchobanoglous, G.; Asano, T. Direct Potable Reuse: A Future Imperative. *Journal of Water Reuse and Desalination* **2011**, *1* (1), 2–10. <https://doi.org/10.2166/wrd.2011.000>.
- (24) Andrzejewski, P.; Kasprzyk-Hordern, B.; Nawrocki, J. N-Nitrosodimethylamine (NDMA) Formation during Ozonation of Dimethylamine-Containing Waters. *Water Research* **2008**, *42* (4–5), 863–870. <https://doi.org/10.1016/j.watres.2007.08.032>.
- (25) Yang, L.; Chen, Z.; Shen, J.; Xu, Z.; Liang, H.; Tian, J.; Ben, Y.; Zhai, X.; Shi, W.; Li, G. Reinvestigation of the Nitrosamine-Formation Mechanism during Ozonation. *Environmental Science & Technology* **2009**, *43* (14), 5481–5487. <https://doi.org/10.1021/es900319f>.
- (26) Bond, T.; Templeton, M. R.; Graham, N. Precursors of Nitrogenous Disinfection By-Products in Drinking Water—A Critical Review and Analysis. *Journal of Hazardous Materials* **2012**, *235–236*, 1–16. <https://doi.org/10.1016/j.jhazmat.2012.07.017>.
- (27) Bond, T.; Huang, J.; Templeton, M. R.; Graham, N. Occurrence and Control of Nitrogenous Disinfection By-Products in Drinking Water – A Review. *Water Research* **2011**, *45* (15), 4341–4354. <https://doi.org/10.1016/j.watres.2011.05.034>.
- (28) Bailey, P. S.; Keller, J. E. Ozonation of Amines. III. Tert-Butylamine. *The Journal of Organic Chemistry* **1968**, *33* (7), 2680–2684.
- (29) Bailey, P. S.; Southwick, L. M.; Carter Jr, T. P. Ozonation of Nucleophiles. 8. Secondary Amines. *The Journal of Organic Chemistry* **1978**, *43* (13), 2657–2662.
- (30) Borowska, E.; Bourgin, M.; Hollender, J.; Kienle, C.; McArdell, C. S.; von Gunten, U. Oxidation of Cetirizine, Fexofenadine and Hydrochlorothiazide during Ozonation: Kinetics and Formation of Transformation Products. *Water Research* **2016**, *94*, 350–362. <https://doi.org/10.1016/j.watres.2016.02.020>.
- (31) Knoop, O.; Hohrenk, L. L.; Lutze, H. V.; Schmidt, T. C. Ozonation of Tamoxifen and Toremifene – Reaction Kinetics and Transformation Products. *Environmental Science & Technology* **2018**, *52* (21), 12583–12591. <https://doi.org/10.1021/acs.est.8b00996>.
- (32) Lange, F.; Cornelissen, S.; Kubac, D.; Sein, M. M.; von Sonntag, J.; Hannich, C. B.; Golloch, A.; Heipieper, H. J.; Möder, M.; von Sonntag, C. Degradation of Macrolide Antibiotics by Ozone: A Mechanistic Case Study with Clarithromycin. *Chemosphere* **2006**, *65* (1), 17–23. <https://doi.org/10.1016/j.chemosphere.2006.03.014>.
- (33) Lester, Y.; Mamane, H.; Zucker, I.; Avisar, D. Treating Wastewater from a Pharmaceutical Formulation Facility by Biological Process and Ozone. *Water Research* **2013**, *47* (13), 4349–4356. <https://doi.org/10.1016/j.watres.2013.04.059>.
- (34) Muñoz, F.; von Sonntag, C. The Reactions of Ozone with Tertiary Amines Including the Complexing Agents Nitrilotriacetic Acid (NTA) and Ethylenediaminetetraacetic Acid (EDTA) in Aqueous Solution. *Journal of the Chemical Society, Perkin Transactions 2* **2000**, No. 10, 2029–2033. <https://doi.org/10.1039/b004417m>.
- (35) Zimmermann, S. G.; Schmukat, A.; Schulz, M.; Benner, J.; von Gunten, U.; Ternes, T. A. Kinetic and Mechanistic Investigations of the Oxidation of Tramadol by Ferrate and Ozone. *Environmental Science & Technology* **2012**, *46* (2), 876–884. <https://doi.org/10.1021/es203348q>.
- (36) Benner, J.; Ternes, T. A. Ozonation of Propranolol: Formation of Oxidation Products. *Environmental Science & Technology* **2009**, *43* (13), 5086–5093. <https://doi.org/10.1021/es900282c>.
- (37) Benner, J.; Ternes, T. A. Ozonation of Metoprolol: Elucidation of Oxidation Pathways and Major Oxidation Products. *Environmental Science & Technology* **2009**, *43* (14), 5472–5480. <https://doi.org/10.1021/es900280e>.
- (38) Tekle-Röttering, A.; Jewell, K. S.; Reisz, E.; Lutze, H. V.; Ternes, T. A.; Schmidt, W.; Schmidt, T. C. Ozonation of Piperidine, Piperazine and Morpholine: Kinetics, Stoichiometry, Product Formation and Mechanistic Considerations. *Water Research* **2016**, *88*, 960–971. <https://doi.org/10.1016/j.watres.2015.11.027>.
- (39) von Gunten, U. Ozonation of Drinking Water: Part I. Oxidation Kinetics and Product Formation. *Water Research* **2003**, *37* (7), 1443–1467. [https://doi.org/10.1016/S0043-1354\(02\)00457-8](https://doi.org/10.1016/S0043-1354(02)00457-8).
- (40) Berger, P.; Karpel Vel Leitner, N.; Doré, M.; Legube, B. Ozone and Hydroxyl Radicals Induced Oxidation of Glycine. *Water Research* **1999**, *33* (2), 433–441. [https://doi.org/10.1016/S0043-1354\(98\)00230-9](https://doi.org/10.1016/S0043-1354(98)00230-9).
- (41) de Vera, G. A.; Gernjak, W.; Weinberg, H.; Farré, M. J.; Keller, J.; von Gunten, U. Kinetics and Mechanisms of Nitrate and Ammonium Formation during Ozonation of Dissolved Organic Nitrogen. *Water Research* **2017**, *108*, 451–461. <https://doi.org/10.1016/j.watres.2016.10.021>.
- (42) Le Lacheur, R. M.; Glaze, W. H. Reactions of Ozone and Hydroxyl Radicals with Serine. *Environmental Science & Technology* **1996**, *30* (4), 1072–1080.
- (43) Bader, H.; Hoigné, J. Determination of Ozone in Water by the Indigo Method. *Water Research* **1981**, *15* (4), 449–456.
- (44) Hoigné, J.; Bader, H. Rate Constants of Reactions of Ozone with Organic and Inorganic Compounds in Water—II: Dissociating Organic Compounds. *Water Research* **1983**, *17* (2), 185–194.
- (45) Leitzke, A.; Reisz, E.; Flyunt, R.; von Sonntag, C. The Reactions of Ozone with Cinnamic Acids: Formation and Decay of 2-Hydroperoxy-2-Hydroxyacetic Acid. *Journal of the Chemical Society, Perkin Transactions 2* **2001**, No. 5, 793–797. <https://doi.org/10.1039/b009327k>.
- (46) Jámbo, A.; Molnár-Perl, I. Amino Acid Analysis by High-Performance Liquid Chromatography after Derivatization with 9-Fluorenylmethyloxycarbonyl Chloride. *Journal of Chromatography A* **2009**, *1216* (15), 3064–3077. <https://doi.org/10.1016/j.chroma.2009.01.068>.
- (47) Muñoz, F.; Mvula, E.; Braslavsky, S. E.; von Sonntag, C. Singlet Dioxygen Formation in Ozone Reactions in Aqueous Solution. *Journal of the Chemical Society, Perkin Transactions 2* **2001**, No. 7, 1109–1116. <https://doi.org/10.1039/b101230o>.

- (48) Flyunt, R.; Leitzke, A.; Mark, G.; Mvula, E.; Reisz, E.; Schick, R.; von Sonntag, C. Determination of $\bullet\text{OH}$, $\text{O}_2\bullet^-$, and Hydroperoxide Yields in Ozone Reactions in Aqueous Solution. *The Journal of Physical Chemistry B* **2003**, *107* (30), 7242–7253. <https://doi.org/10.1021/jp022455b>.
- (49) Nöthe, T.; Fahlenkamp, H.; von Sonntag, C. Ozonation of Wastewater: Rate of Ozone Consumption and Hydroxyl Radical Yield. *Environmental Science & Technology* **2009**, *43* (15), 5990–5995.
- (50) Lipari, F.; Swarin, S. J. Determination of Formaldehyde and Other Aldehydes in Automobile Exhaust with an Improved 2, 4-Dinitrophenylhydrazine Method. *Journal of Chromatography A* **1982**, *247* (2), 297–306.
- (51) Frisch, M. J.; Trucks, G. W.; Schlegel, H. B.; Scuseria, G. E.; Robb, M. A.; Cheeseman, J. R.; Scalmani, G.; Barone, V.; Petersson, G. A.; Nakatsuji, H.; et al. *Gaussian 09, Revision D.01*; Gaussian, Inc.: Wallingford CT, 2016.
- (52) Raghavachari, K.; Trucks, G. W.; Pople, J. A.; Head-Gordon, M. A Fifth-Order Perturbation Comparison of Electron Correlation Theories. *Chemical Physics Letters* **1989**, *157* (6), 479–483. [https://doi.org/10.1016/S0009-2614\(89\)87395-6](https://doi.org/10.1016/S0009-2614(89)87395-6).
- (53) Papajak, E.; Zheng, J.; Xu, X.; Leverentz, H. R.; Truhlar, D. G. Perspectives on Basis Sets Beautiful: Seasonal Plantings of Diffuse Basis Functions. *Journal of Chemical Theory and Computation* **2011**, *7* (10), 3027–3034. <https://doi.org/10.1021/ct200106a>.
- (54) Becke, A. D. Density-functional Thermochemistry. III. The Role of Exact Exchange. *The Journal of Chemical Physics* **1993**, *98* (7), 5648–5652. <https://doi.org/10.1063/1.464913>.
- (55) Montgomery, J. A.; Frisch, M. J.; Ochterski, J. W.; Petersson, G. A. A Complete Basis Set Model Chemistry. VI. Use of Density Functional Geometries and Frequencies. *The Journal of Chemical Physics* **1999**, *110* (6), 2822–2827. <https://doi.org/10.1063/1.477924>.
- (56) Hariharan, P. C.; Pople, J. A. The Influence of Polarization Functions on Molecular Orbital Hydrogenation Energies. *Theoretica Chimica Acta* **1973**, *28* (3), 213–222. <https://doi.org/10.1007/BF00533485>.
- (57) Marenich, A. V.; Cramer, C. J.; Truhlar, D. G. Universal Solvation Model Based on Solute Electron Density and on a Continuum Model of the Solvent Defined by the Bulk Dielectric Constant and Atomic Surface Tensions. *The Journal of Physical Chemistry B* **2009**, *113* (18), 6378–6396. <https://doi.org/10.1021/jp810292n>.
- (58) Zhao, Y.; Truhlar, D. G. The M06 Suite of Density Functionals for Main Group Thermochemistry, Thermochemical Kinetics, Noncovalent Interactions, Excited States, and Transition Elements: Two New Functionals and Systematic Testing of Four M06-Class Functionals and 12 Other Functionals. *Theoretical Chemistry Accounts* **2008**, *120* (1), 215–241. <https://doi.org/10.1007/s00214-007-0310-x>.
- (59) Pryor, W. A.; Giamalva, D. H.; Church, D. F. Kinetics of Ozonation. 2. Amino Acids and Model Compounds in Water and Comparisons to Rates in Nonpolar Solvents. *Journal of the American Chemical Society* **1984**, *106* (23), 7094–7100. <https://doi.org/10.1021/ja00335a038>.
- (60) Trogolo, D.; Arey, J. S.; Tentscher, P. R. Gas-Phase Ozone Reactions with a Structurally Diverse Set of Molecules: Barrier Heights and Reaction Energies Evaluated by Coupled Cluster and Density Functional Theory Calculations. *The Journal of Physical Chemistry A* **2019**. <https://doi.org/10.1021/acs.jpca.8b10323>.
- (61) Jonsson, M.; Wayner, D. D. M.; Luszyk, J. Redox and Acidity Properties of Alkyl- and Arylamine Radical Cations and the Corresponding Aminyl Radicals ¹. *The Journal of Physical Chemistry* **1996**, *100* (44), 17539–17543. <https://doi.org/10.1021/jp961286q>.
- (62) Wardman, P. Reduction Potentials of One-Electron Couples Involving Free Radicals in Aqueous Solution. *Journal of Physical and Chemical Reference Data* **1989**, *18* (4), 1637–1755. <https://doi.org/10.1063/1.555843>.
- (63) Johnson, D. H.; Rogers, M. A. T.; Trappe, G. 229. Aliphatic Hydroxylamines. Part II. Autoxidation. *Journal of the Chemical Society (Resumed)* **1956**, *0* (0), 1093–1103. <https://doi.org/10.1039/JR9560001093>.
- (64) Wayne, R. P.; Pitts, J. N. Rate Constant for the Reaction $\text{O}_2(1\Delta_g) + \text{O}_3 \rightarrow 2\text{O}_2 + \text{O}$. *The Journal of Chemical Physics* **1969**, *50* (8), 3644–3645. <https://doi.org/10.1063/1.1671606>.
- (65) Olszyna, K.; Heicklen, J. The Inhibition of Photochemical Smog VI. The Reaction of O_3 with Diethylhydroxylamine. *Science of The Total Environment* **1976**, *5* (3), 223–230. [https://doi.org/10.1016/0048-9697\(76\)90074-7](https://doi.org/10.1016/0048-9697(76)90074-7).
- (66) Encinas, M. V.; Lemp, E.; Lissi, E. A. Interaction of Singlet Oxygen [$\text{O}_2(1\Delta)$] with Aliphatic Amines and Hydroxylamines. *J. Chem. Soc., Perkin Trans. 2* **1987**, *0* (8), 1125–1127. <https://doi.org/10.1039/P29870001125>.
- (67) Bilski, P.; Motten, A. G.; Bilska, M.; Chignell, C. F. The Photooxidation of Diethylhydroxylamine by Rose Bengal in Micellar and Nonmicellar Aqueous Solutions. *Photochemistry and Photobiology* **1993**, *58* (1), 11–18. <https://doi.org/10.1111/j.1751-1097.1993.tb04896.x>.
- (68) Amar, M.; Bar, S.; Iron, M. A.; Toledo, H.; Tumanskii, B.; Shimon, L. J. W.; Botoshansky, M.; Fridman, N.; Szpilman, A. M. Design Concept for α -Hydrogen-Substituted Nitroxides. *Nature Communications* **2015**, *6*, 6070. <https://doi.org/10.1038/ncomms7070>.
- (69) Adamic, K.; Bowman, D. F.; Ingold, K. U. Self-Reaction of Diethylnitroxide Radicals. *Journal of the American Chemical Society* **1970**, *92* (4), 1093–1094. <https://doi.org/10.1021/ja00707a076>.
- (70) Sein, M. M.; Zedda, M.; Tuerk, J.; Schmidt, T. C.; Gollock, A.; Sonntag, C. von. Oxidation of Diclofenac with Ozone in Aqueous Solution. *Environmental Science & Technology* **2008**, *42* (17), 6656–6662. <https://doi.org/10.1021/es8008612>.
- (71) Muñoz, F.; von Sonntag, C. Determination of Fast Ozone Reactions in Aqueous Solution by Competition Kinetics. *Journal of the Chemical Society, Perkin Transactions 2* **2000**, No. 4, 661–664. <https://doi.org/10.1039/a909668j>.
- (72) Naumov, S.; von Sonntag, C. Standard Gibbs Free Energies of Reactions of Ozone with Free Radicals in Aqueous Solution: Quantum-Chemical Calculations. *Environmental Science & Technology* **2011**, *45* (21), 9195–9204. <https://doi.org/10.1021/es2018658>.

- (73) Ingold, K. U.; Adamic, K.; Bowman, D. F.; Gillan, T. Kinetic Applications of Electron Paramagnetic Resonance Spectroscopy. I. Self-Reactions of Diethyl Nitroxide Radicals. *Journal of the American Chemical Society* **1971**, *93* (4), 902–908. <https://doi.org/10.1021/ja00733a018>.
- (74) Goldstein, S.; Samuni, A. Kinetics and Mechanism of Peroxyl Radical Reactions with Nitroxides. *The Journal of Physical Chemistry A* **2007**, *111* (6), 1066–1072. <https://doi.org/10.1021/jp0655975>.
- (75) Ali, S. A.; AlSbaiee, A.; Wazeer, M. I. M. Conformational Analysis and Inversion Process in Some Perhydrodipyrido[1,2-b;1'2'-e]-1,4,2,5- Dioxadiazines. *Journal of Physical Organic Chemistry* **2010**, *23* (6), 488–496. <https://doi.org/10.1002/poc.1627>.
- (76) Roca-López, D.; Tejero, T.; Caramella, P.; Merino, P. $[2n2\pi + 2n2\pi]$ Cycloadditions: An Alternative to Forbidden $[4\pi + 4\pi]$ Processes. The Case of Nitron Dimerization. *Organic & Biomolecular Chemistry* **2014**, *12* (3), 517–525. <https://doi.org/10.1039/C3OB42014K>.
- (77) Ianni, J. C. *Kintecus*; 2017, Windows Version 6.01, www.kintecus.com.
- (78) Erickson, R. E.; Andrusis Jr, P. J.; Collins, J. C.; Lungle, M. L.; Mercer, G. D. Mechanism of Ozonation Reactions. IV. Carbon-Nitrogen Double Bonds. *The Journal of Organic Chemistry* **1969**, *34* (10), 2961–2966.
- (79) Riebel, A. H.; Erickson, R. E.; Abshire, C. J.; Bailey, P. S. Ozonation of Carbon-Nitrogen Double Bonds. I. Nucleophilic Attack of Ozone ¹. *Journal of the American Chemical Society* **1960**, *82* (7), 1801–1807. <https://doi.org/10.1021/ja01492a062>.
- (80) Criegee, R. Mechanism of Ozonolysis. *Angewandte Chemie International Edition* **1975**, *14* (11), 745–752. <https://doi.org/10.1002/anie.197507451>.
- (81) Dowideit, P.; von Sonntag, C. Reaction of Ozone with Ethene and Its Methyl- and Chlorine-Substituted Derivatives in Aqueous Solution. *Environmental Science & Technology* **1998**, *32* (8), 1112–1119.
- (82) Criegee, R.; Wenner, G. Die Ozonisierung des 9,10-Oktalins. *Justus Liebigs Annalen der Chemie* **1949**, *564* (1), 9–15. <https://doi.org/10.1002/jlac.19495640103>.
- (83) Ebersson, L. Inverted Spin Trapping. Part 111." Further Studies on the Chemical and Photochemical Oxidation of Spin Traps in the Presence of Nucleophiles. *Journal of the Chemical Society, Perkin Transactions 2* **1994**, *0*, 171–176.
- (84) Zubarev, V.; Brede, O. Direct Detection of the Cation Radical of the Spin Trap A-Phenyl-N-Tert-Butylnitron. *Journal of the Chemical Society, Perkin Transactions 2* **1994**, *0*, 1821–1828.
- (85) Lee, T. J.; Taylor, P. R. A Diagnostic for Determining the Quality of Single-Reference Electron Correlation Methods. *International Journal of Quantum Chemistry* **1989**, *36* (S23), 199–207. <https://doi.org/10.1002/qua.560360824>.
- (86) Hoigné, J.; Bader, H. Ozonation of Water: Kinetics of Oxidation of Ammonia by Ozone and Hydroxyl Radicals. *Environmental Science & Technology* **1978**, *12* (1), 79–84.
- (87) Bachman, G. B.; Strawn, K. G. Ozone Oxidation of Primary Amines to Nitroalkanes. *The Journal of Organic Chemistry* **1968**, *33* (1), 313–315. <https://doi.org/10.1021/jo01265a062>.
- (88) Long, J. A.; Harris, N. J.; Lammertsma, K. Formaldehyde Oxime \rightleftharpoons Nitrosomethane Tautomerism. *The Journal of Organic Chemistry* **2001**, *66* (20), 6762–6767. <https://doi.org/10.1021/jo010671v>.
- (89) Hoigné, J.; Bader, H.; Haag, W. R.; Staehelin, J. Rate Constants of Reactions of Ozone with Organic and Inorganic Compounds in Water—III. Inorganic Compounds and Radicals. *Water Research* **1985**, *19* (8), 993–1004. [https://doi.org/10.1016/0043-1354\(85\)90368-9](https://doi.org/10.1016/0043-1354(85)90368-9).
- (90) Paradkar, V. M.; Latham, T. B.; Demko, D. M. Oxidative Decarboxylation of α -Amino Acids with in Situ Generated Dimethyl Dioxirane. *Synlett* **1995**, No. 10, 1059–1060. <https://doi.org/10.1055/s-1995-5174>.
- (91) Murray, R. W.; Jeyaraman, R.; Mohan, L. A New Synthesis of Nitro Compounds Using Dimethyldioxirane. *Tetrahedron Letters* **1986**, *27* (21), 2335–2336.
- (92) Smith, G. G.; Sivakua, T. Mechanism of the Racemization of Amino Acids. Kinetics of Racemization of Arylglycines. *The Journal of Organic Chemistry* **1983**, *48* (5), 627–634. <https://doi.org/10.1021/jo00153a001>.
- (93) Rios, A.; Amyes, T. L.; Richard, J. P. Formation and Stability of Organic Zwitterions in Aqueous Solution: Enolates of the Amino Acid Glycine and Its Derivatives. *Journal of the American Chemical Society* **2000**, *122* (39), 9373–9385. <https://doi.org/10.1021/ja001749c>.
- (94) Ábalos, M.; Bayona, J. M.; Ventura, F. Development of a Solid-Phase Microextraction GC-NPD Procedure for the Determination of Free Volatile Amines in Wastewater and Sewage-Polluted Waters. *Analytical Chemistry* **1999**, *71* (16), 3531–3537. <https://doi.org/10.1021/ac990197h>.
- (95) Chen, G.; Liu, J.; Liu, M.; Li, G.; Sun, Z.; Zhang, S.; Song, C.; Wang, H.; Suo, Y.; You, J. Sensitive, Accurate and Rapid Detection of Trace Aliphatic Amines in Environmental Samples with Ultrasonic-Assisted Derivatization Microextraction Using a New Fluorescent Reagent for High Performance Liquid Chromatography. *Journal of Chromatography A* **2014**, *1352*, 8–19. <https://doi.org/10.1016/j.chroma.2014.05.061>.
- (96) Hwang, Y.; Matsuo, T.; Hanaki, K.; Suzuki, N. Identification and Quantification of Sulfur and Nitrogen Containing Odorous Compounds in Wastewater. *Water Research* **1995**, *29* (2), 711–718. [https://doi.org/10.1016/0043-1354\(94\)00145-W](https://doi.org/10.1016/0043-1354(94)00145-W).
- (97) Mitch, W. A.; Sedlak, D. L. Characterization and Fate of *N*-Nitrosodimethylamine Precursors in Municipal Wastewater Treatment Plants. *Environmental Science & Technology* **2004**, *38* (5), 1445–1454. <https://doi.org/10.1021/es035025n>.
- (98) Sacher, F.; Lenz, S.; Brauch, H.-J. Analysis of Primary and Secondary Aliphatic Amines in Waste Water and Surface Water by Gas Chromatography-Mass Spectrometry after Derivatization with 2,4-Dinitrofluorobenzene or Benzene-sulfonyl Chloride. *Journal of Chromatography A* **1997**, *764* (1), 85–93. [https://doi.org/10.1016/S0021-9673\(96\)00868-0](https://doi.org/10.1016/S0021-9673(96)00868-0).

- (99) USEPA. *Health and Environmental Effects Profile for Nitromethane*; EPA/600/X-85/116 (NTIS PB88180518); U.S. Environmental Protection Agency: Washington, D.C., 1985.
- (100) Sander, R. Compilation of Henry's Law Constants (Version 4.0) for Water as Solvent. *Atmospheric Chemistry and Physics* **2015**, *15*, 4399–4981.
- (101) WHO. Trihalomethanes in Drinking-Water. Background Document for Development of WHO Guidelines for Drinking-Water Quality; WHO/SDE/WSH/05.08/64; World Health Organization: Geneva, 2005.
- (102) Markofsky, S. B. Nitro Compounds, Aliphatic. In *Ullmann's Encyclopedia of Industrial Chemistry*; Wiley-VCH Verlag GmbH & Co. KGaA, Ed.; Wiley-VCH Verlag GmbH & Co. KGaA: Weinheim, Germany, 2011. https://doi.org/10.1002/14356007.a17_401.pub2.
- (103) National Toxicology Program. *Report on Carcinogens, Fourteenth Edition*; U.S. Department of Health and Human Services, Public Health Service: Research Triangle Park, NC, 2016.

Supporting Information for Chapter 2

Reactions of aliphatic amines with ozone: Kinetics and mechanisms

Text S2.1. Chemical reagents

The chemicals used in this study are listed in Table S2.1. *N*-ethylethanamine oxide was synthesized by the AuA laboratory at Eawag with *N,N*-diethylhydroxylamine as a starting material and mercury (II) oxide as an oxidant.^{1,2} The purity of the synthesized chemical was checked by comparing ¹H and ¹³C NMR signals of *N*-ethylethanamine oxide to those of the starting material, *N,N*-diethylhydroxylamine, which yielded > 98 % in mol/mol. The UV absorbance at $\lambda_{\text{max}} = 224$ nm was recorded with the synthesized product as received to obtain a calibration curve (Figure S2.1) which was used to determine the concentrations of the working stocks. The molar absorption coefficient was calculated to be $\epsilon = 6964 \text{ M}^{-1} \text{ cm}^{-1}$ at 224 nm with a 1 cm path length.

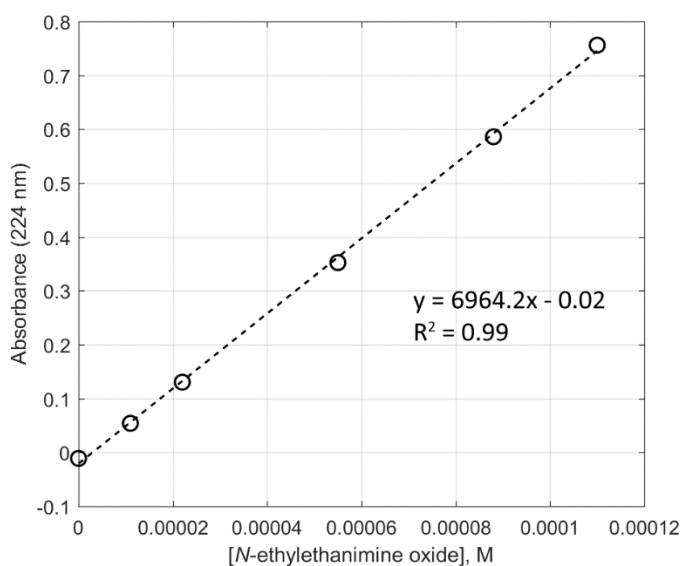


Figure S2.1. Calibration curve of *N*-ethylethanamine oxide standards at 224 nm (1 cm cell).

Table S2.1. List of chemicals used.

Chemicals	Suppliers	Product No.
Ethylamine hydrochloride, 98%	Sigma-Aldrich	232831
<i>N,N</i> -Diethylhydroxylamine, ≥ 98%	Sigma-Aldrich	471593
<i>N</i> -ethylhydroxylamine hydrochloride, 95%	Enamine	EN300-170097
Triethyl- <i>d</i> ₁₅ -amine, 99.2%	CDNisotopes	D-1221
Diethyl- <i>d</i> ₁₀ -amine HCl, 98.5%	CDNisotopes	D-5132
<i>N,N</i> -diethylethanamine oxide ("Triethylamine <i>N</i> -oxide"), ≥ 97%	SelectLab	SZ042
Nitroethane, 99%	Alfa Aesar	A10855
Diethylamine hydrochloride, 99%	Sigma-Aldrich	127744
<i>N</i> -Ethylacetamide, 99%	Alfa Aesar	L10300
Nitroethane- <i>d</i> ₅ , 99.1%	CDNisotopes	D-5262
Triethylamine hydrochloride, ≥ 99.0%	Fluka	90350
Acetaldoxime, syn + anti, 98%	Alfa Aesar	A10640
<i>tert</i> -Butanol, ≥ 99.7%	Sigma-Aldrich	19460
Sodium dihydrogen phosphate monohydrate, 99-102%	Merck	106346
di-Sodium hydrogen phosphate dihydrate, ≥ 99.5%	Merck	106580
Phosphoric acid, ≥ 85%	Sigma-Aldrich	30417

9-Fluorenylmethoxycarbonyl chloride, ≥99.0%	Sigma-Aldrich	23186
Amantadine hydrochloride, ≥ 98%	Sigma-Aldrich	A1260
Sodium hypochlorite solution, 6-14% active chlorine	Sigma-Aldrich	13440
Hydrogen peroxide solution, ≥35%	Sigma-Aldrich	95299
Sodium sulfate, ≥ 99.0%	Sigma-Aldrich	239313
<i>trans</i> -Cinnamic acid, ≥ 99%	Sigma-Aldrich	C80857
Benzaldehyde, ≥ 99.0%	Sigma-Aldrich	12010
2,4-Dinitrophenylhydrazine, ≥ 99.0%	Sigma-Aldrich	42210

Text S2.2. Reaction kinetics

Indigo method. Second-order rate constants for the reactions of the tested compounds (ethylamine, diethylamine, triethylamine, *N*-ethylhydroxylamine, *N*-ethylethanamine oxide, nitroethane, and *N,N*-diethylhydroxylamine (at pH ≤ 2 for *N,N*-diethylhydroxylamine)) with ozone were determined by a direct measurement of the ozone decrease as a function of time under pseudo first-order conditions where the molar [compound]₀ : [O₃]₀ ratio is ≥ 20. The decrease in the ozone concentration was determined by quenching the remaining ozone with the indigo reagent and measuring the decolorization of the indigo by a UV-vis spectrophotometer at 600 nm.³ For triethylamine, diethylamine, and ethylamine, the pH of the solutions was set far below the p*K*_a of the amines so that the amines were mostly present in the protonated forms and the reaction rates were low enough to be measured by the direct method. The second-order rate constants for the neutral form of the amines were obtained by extrapolating the measured apparent second-order rate constants to a higher pH.⁴ The plots for the determination of the pseudo first-order kinetics are summarized in Figure S2.3.

Competition kinetic method. The apparent second-order rate constants for the reaction of *N,N*-diethylhydroxylamine with ozone at pH 5 – 8 were determined by using a competition kinetic method with *trans*-cinnamic acid as a competitor. Benzaldehyde, a product of the reaction of *trans*-cinnamic acid with ozone, was quantified by HPLC⁵ at varying ratios of [*N,N*-diethylhydroxylamine]₀ to [*trans*-cinnamic acid]₀. The second-order rate constant of *N,N*-diethylhydroxylamine (*k*_{O₃, *N,N*-diethylhydroxylamine}) was deduced based on the following equation:⁶

$$\frac{[\text{Benzaldehyde}]_0}{[\text{Benzaldehyde}]} = 1 + \frac{k_{\text{O}_3, \text{N,N-diethylhydroxylamine}} [\text{N,N-diethylhydroxylamine}]}{k_{\text{O}_3, \text{trans-cinnamic acid}} [\text{trans-cinnamic acid}]}$$

*Estimating p*K*_a of *N,N*-diethylhydroxylamine based on *k*_{app}.* The p*K*_a of *N,N*-diethylhydroxylamine was estimated by fitting the determined apparent second-order rate constants for the reactions of *N,N*-diethylhydroxylamine with ozone in the pH range 1.6 to 8.0 (pH ≤ 2 by the direct method and 5 ≤ pH ≤ 8 by the competition kinetics method). The fitting was performed by the GraphPad software (version 5.02) based on the following equation: *k* = *k*_{NH⁺}(1-α) + *k*_Nα, where *k*_{NH⁺} and *k*_N are species-specific second-order rate constants for the protonated and neutral forms of *N,N*-diethylhydroxylamine and α is the fraction of the neutral form expressed as α = 1/(1 + 10^{p*K*_a-pH}). The fitting result as well as the measured rate constants are shown in Figure S2.2. The best-fit values with standard errors were (7.0 ± 0.02) × 10⁵ M⁻¹ s⁻¹ for *k*_N and 5.4 ± 0.01 for p*K*_a.

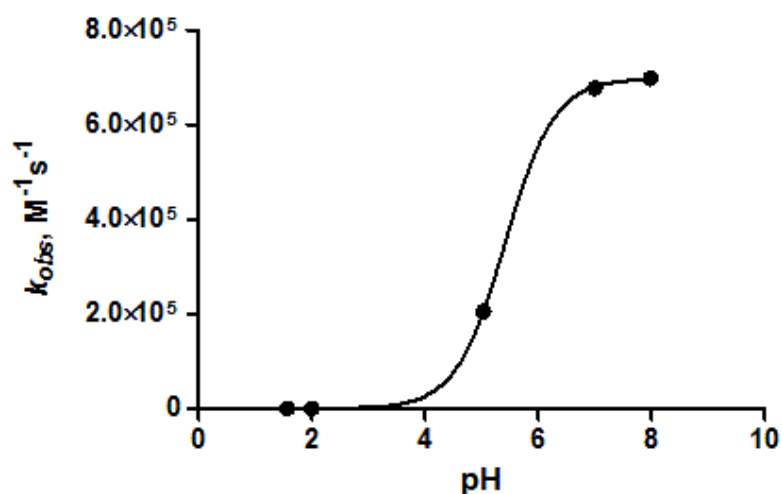
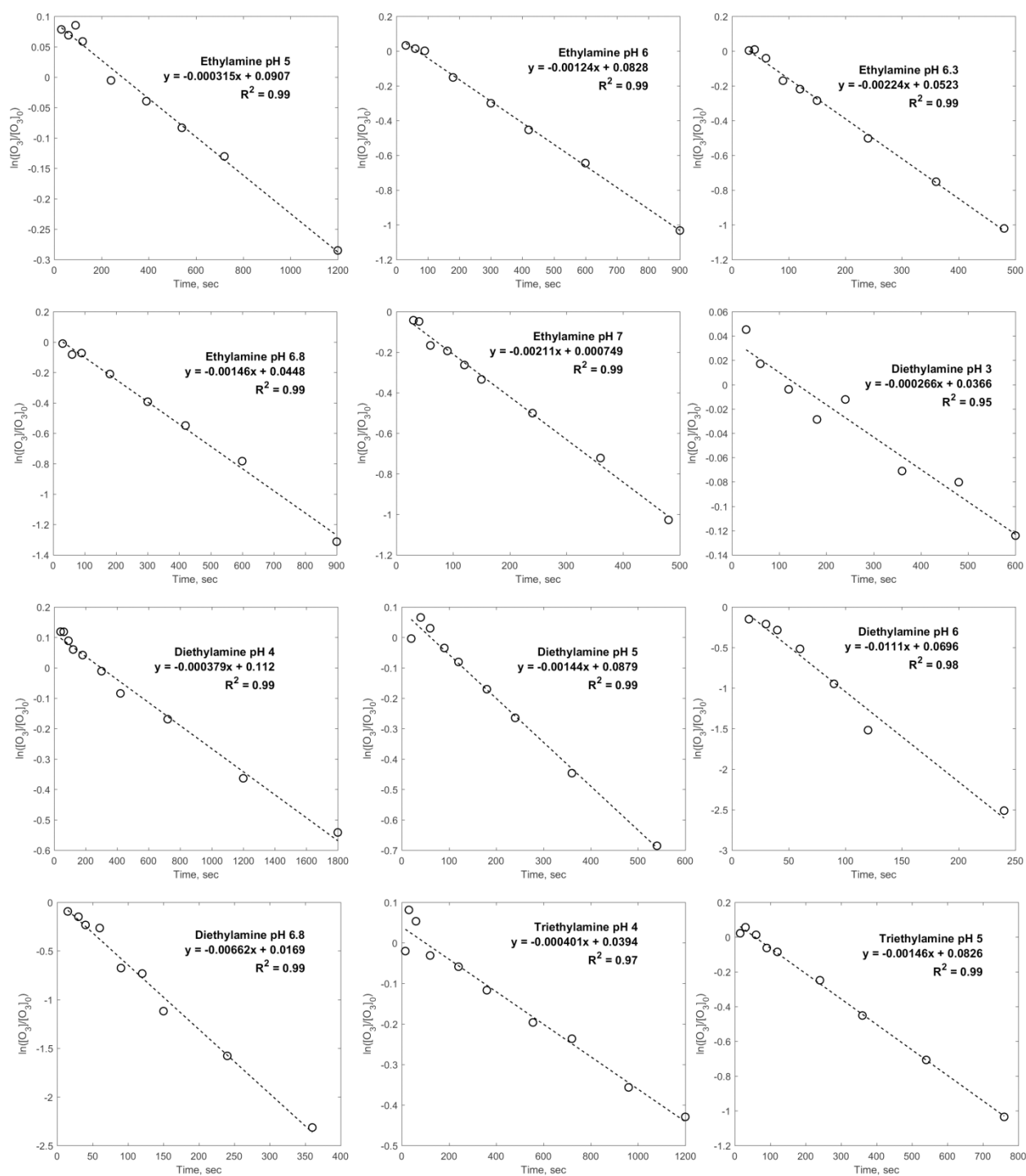


Figure S2.2. pH-dependent second-order rate constants for the reaction of *N,N*-diethylhydroxylamine with ozone. The symbols and the line indicate the measured and predicted data, respectively.

Determining ozone kinetics of N-ethylethanamine oxide. The synthesized *N*-ethylethanamine oxide stocks were suspected to contain a considerable amount of a dimer (Text S2.7), which hindered accurate determination of the reaction kinetics. For this reason, the *N*-ethylethanamine oxide solution was prepared *in situ* by oxidizing *N,N*-diethylhydroxylamine with a 1.5-fold stoichiometric excess of ozone, which yielded ~100 % *N*-ethylethanamine oxide (Figure 2.1c in main text), and kinetic experiments were carried out by the indigo method.



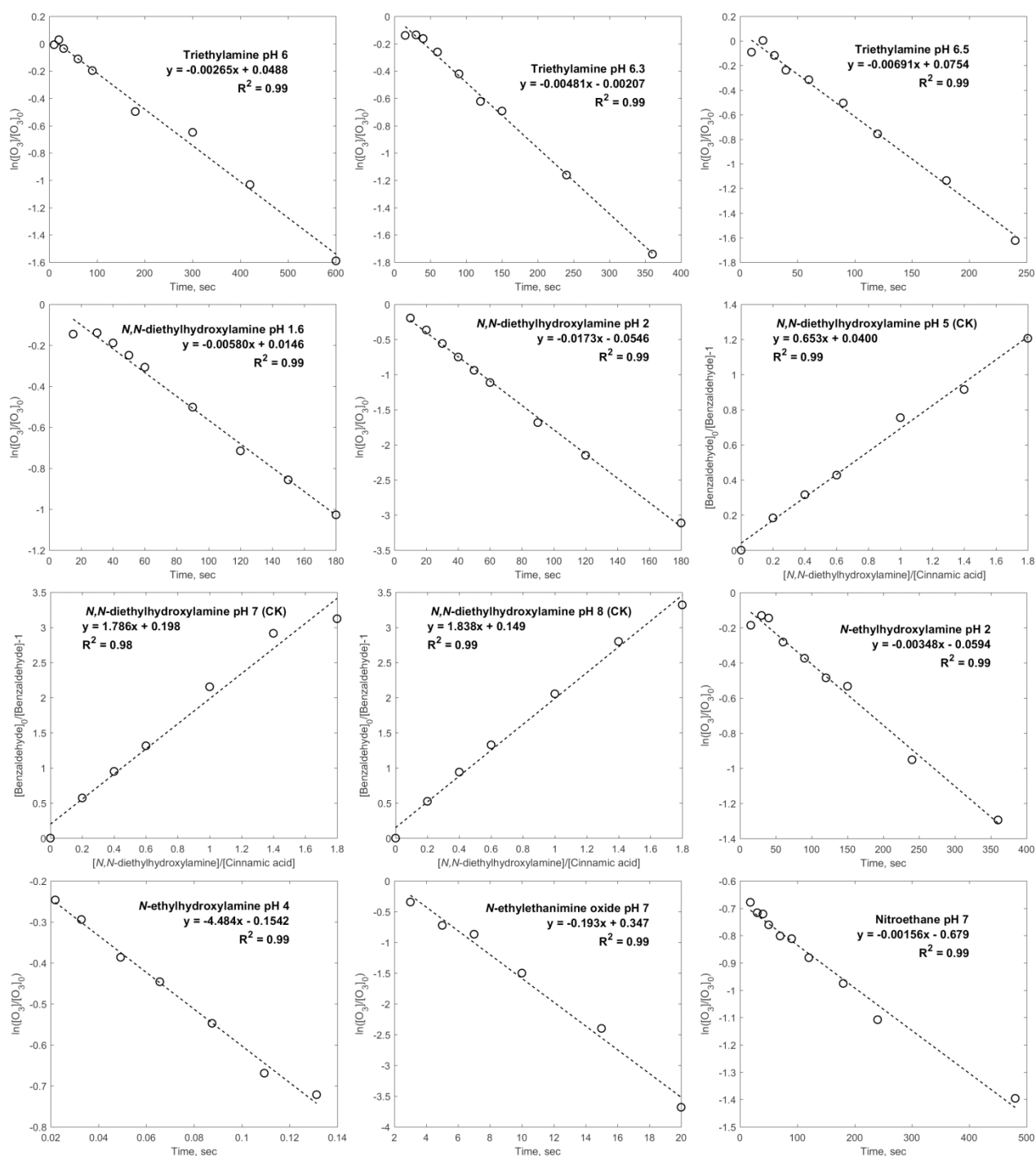


Figure S2.3. Pseudo-first-order kinetic plots for the reactions of ozone with ethylamine, diethylamine, triethylamine, *N,N*-diethylhydroxylamine, *N*-ethylhydroxylamine, *N*-ethylethanamine oxide, and nitroethane under varying pH conditions. The plots from competition kinetics (CK) are also presented for *N,N*-diethylhydroxylamine. Data points shown in the plots were from single measurements.

Text S2.3. Analyses of amines and their transformation products: LC-HRMS, GC-MS, IC, and HPLC methods

LC-HRMS for Diethylamine, N,N-diethylhydroxylamine, N-ethylethanamine oxide, Triethylamine, and Triethylamine N-oxide. Non-ozonated (ozone dose = 0 μM) and ozonated samples were diluted 10-fold in acetonitrile to achieve the composition of sample solvent (90 % acetonitrile and 10 % aqueous solution) suitable for hydrophilic interaction liquid chromatography (HILIC). A mixture of triethyl- d_{15} -amine and diethyl- d_{10} -amine (10 μM in each as final concentration) dissolved in acetonitrile were added as internal standards. Compounds in the diluted samples were separated on a HILIC column (XBridge™ BEH HILIC XP, 2.5 μM particle size, 3.0 \times 150 mm, Waters) at 30 °C with a flow of 400 $\mu\text{L}/\text{min}$ and ultrapure water and an acetonitrile mixture (95:3:2 of acetonitrile:methanol:ultrapure water) as eluents. 1 mM ammonium formate and 0.1 % formic acid were added to both eluents. The gradient started with 100 % of the acetonitrile mixture during the first 2 min, which linearly decreased to 5 % between 2 min and 12 min, maintained at 5 % until 17 min, increased to the initial conditions of 100 % acetonitrile mixture at 17.1 min, and maintained at 100 % until 37 min for column re-equilibration. After separation, compounds were detected by a Thermo Scientific Q-Exactive high-resolution mass spectrometer ($R = 70,000$) with electrospray ionization (ESI) in positive full scan mode with a spray voltage of 4000 V, a capillary temperature of 350 °C, a sheath gas flow rate of 40, and an auxiliary gas flow rate of 10. The limits of quantifications (LOQ) were estimated based on the slope of the calibration curve (s), the standard deviation of the y-intercept of the calibration curve (σ), and the equation of $\text{LOQ} = 10 \times \sigma/s$, and summarized in Table S2.2. The measuring range for *N,N*-diethylhydroxylamine was 3 μM – 10 μM and for the other compounds were 0.5 μM – 10 μM with linear correlation coefficients (R^2) above 0.99.

Table S2.2. List of compounds analyzed by LC-HRMS, their exact masses, and LOQ.

Compound	Molecular formula (M)	Exact mass as $[\text{M}+\text{H}]^+$	LOQ, μM
Triethylamine	$\text{C}_6\text{H}_{15}\text{N}$	102.1277	0.2
Triethylamine <i>N</i> -oxide	$\text{C}_6\text{H}_{15}\text{NO}$	118.1226	0.1
Diethylamine	$\text{C}_4\text{H}_{11}\text{N}$	74.0964	0.4
<i>N</i> -ethylethanamine oxide	$\text{C}_4\text{H}_9\text{NO}$	88.0757	0.4
<i>N,N</i> -diethylhydroxylamine	$\text{C}_4\text{H}_{11}\text{NO}$	90.0913	2.5

Liquid-liquid extraction + GC-MS for nitroethane. Nitroethane in ozonated samples was extracted from the aqueous phase by liquid-liquid extraction with methyl *tert*-butyl ether (MTBE). 2.5 mL of MTBE was added to 2.5 mL of a sample and the mixture was shaken for 5 min. After shaking, 1 mL of the organic phase was transferred to a GC sample vial via a Pasteur pipette filled with a cotton ball and a thin layer of sodium sulfate for drying. Nitroethane- d_5 was added as an internal standard (100 μM as final concentration). The extraction efficiencies tested for a low to high concentrations of nitroethane (10 μM , 50 μM , and 100 μM) were typically about 90 %. After extraction, analytes were separated on a Rtx-VMS column (60 m, 0.32 mm ID, 1.8 μm d_f , RESTEK) by injecting 1 μL in the splitless mode with an inlet temperature of 230 °C. The column oven was initially at 40 °C, ramped to 110 °C between 1 min and 15 min, ramped to 220 °C between 15 min and 18 min, and held at 220 °C until 23 min. After separation, nitroethane was detected by a Thermo Scientific DSQ II mass spectrometer with positive SIM mode. Quantification ions for nitroethane were m/z 27 and 29. LOQ \sim 5 μM was estimated based on a signal-to-noise ratio of 5 μM nitroethane standard solution greater than 10 (Figure S2.4). A signal-to-noise ratio of 10 is generally accepted for estimating LOQ.⁷ The measuring range was 3 μM – 100 μM .

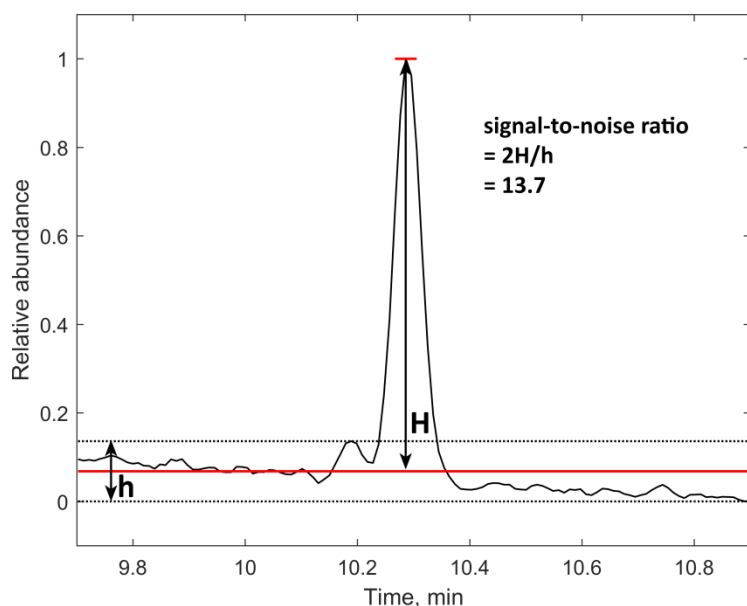


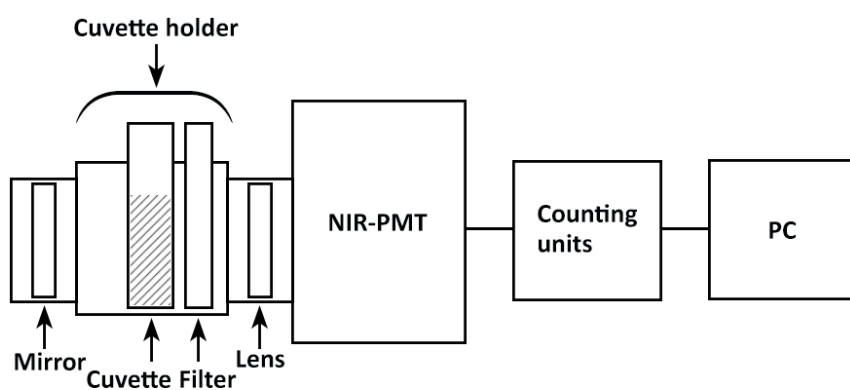
Figure S2.4 Example of chromatogram of 5 μM nitroethane standard solution in GC-MS, filtered with $m/z = 27$.

Fmoc chloride derivatization + HPLC-UV for ethylamine. Ethylamine was analyzed by a derivatization method using 9-Fluorenylmethoxycarbonyl chloride (Fmoc chloride)⁸ because of the low molecular weight (45 as average mass) that cannot be detected by the mass spectrometer of the LC-HRMS system. Derivatization was performed by mixing 150 μL of samples containing ethylamine with 150 μL of 0.4 M borate buffer (pH 9) and with 300 μL of 0.1 mM Fmoc chloride dissolved in acetonitrile. After 30 min, the reaction was stopped by adding 50 μL of 40 mM Amantadine. Derivatized analytes were then separated on a Cosmosil C18 column (5C18-MS-II, 3.0 \times 100 mm, NACALAI TESQUE, INC.) with a gradient (1 mL/min) of acetonitrile and ultrapure water. Both eluents were acidified by 0.1 % formic acid. The gradient started at 95 % ultrapure water during 5 min, which linearly decreased to 5 % between 5 min and 15 min, maintained at 5 % to 25 min, increased back to the initial condition of 95 % ultrapure water until 27 min, and maintained at the initial condition until 33 min. The derivatized product of ethylamine was analyzed by UV detection at 262 nm. LOQ calculated based on the calibration curve was 0.4 μM and the measuring range was 0.5 μM – 100 μM .

IC-conductivity detection for nitrite and nitrate. Ozonated samples were diluted 4-fold in ultrapure water to minimize a background peak of phosphate. The anions in the diluted samples were then separated on a capillary anion-exchange IC column (IonPac AS19-4 μM , 0.4 \times 250 mm, Dionex) with KOH as eluent with a flow rate of 0.01 mL/min. The eluent concentration was initially at 10 mM for 10 min, increased to 28.5 mM between 10 min and 15 min, increased to 120 mM between 15 min and 15.1 min, was maintained at 120 mM until 23 min, went back to the initial concentration of 10 mM between 23 min and 23.1 min, and held at 10 mM until 32 min. The anions were detected by suppressed conductivity (ACES 300 Capillary Electrolytic Suppressor, Dionex). LOQ and the measuring ranges calculated based on the calibration curves were 0.05 μM and 0.05 μM – 2 μM for nitrate and 1.4 μM and 1.4 μM – 20 μM for nitrite.

Text S2.4. Analysis of reactive oxygen species: Singlet oxygen

¹O₂ detector setup: A schematic diagram of the ¹O₂ detection setup is shown in Figure S2.5. A near-infrared photomultiplier tube (NIR-PMT, H10330B-45, Hamamatsu) was used to quantify ¹O₂ formation by detecting the characteristic phosphorescence emitted by ¹O₂ at 1270 nm. *In-situ* ¹O₂ formation was initiated by injecting an ozone solution (1 mL) to an amine solution (1 mL) placed in a cuvette (100-QS, 10 mm, Hellma). A cuvette holder (CVH100/M, Thorlabs) accommodating the cuvette was closely attached to NIR-PMT to minimize loss of photons (the distance between the cuvette holder and NIR-PMT was ~40 mm in our setup). A bandpass filter with 1270 ± 3 nm central wavelength (bk-1270-10-B, bk Interferenzoptik) was placed between the cuvette and the output port of the cuvette holder. A lens with an anti-reflective coating for near-infrared light (LA1951-C, Thorlabs) and a concave mirror with a protected gold coating (CM254-019-M01, Thorlabs) were installed in front of and behind the cuvette to enhance the efficiency of photon collection. The lens was housed in a lens tube with matching threads to the input window of NIR-PMT and the output port of the cuvette holder to ensure a light-tight setup. Output signals (multiplied photoelectrons) of NIR-PMT were counted by a following photon counting unit (C9744, Hamamatsu) with a predetermined threshold level (200 mV) and converted into digital signals. The digital signals were then counted by a pulse counting unit (C8805-01, Hamamatsu) equipped with a USB port to be connected to a PC. The final signals were expressed as counts per gate (with a typical gate time of 5 ms) and recorded by a sample software (Hamamatsu) provided together with the pulse counting unit. Experiments were carried out in a dark room with a LED lamp (3W, cool white) to protect the photocathode of NIR-PMT from excessive light and minimize background noise. The voltage of NIR-PMT was set as 800 V and the gate time was typically set as 5 ms unless mentioned otherwise.

Figure S2.5. Schematic diagram of a ¹O₂ detection setup.

Calibration: The ¹O₂ detection of NIR-PMT was calibrated by the reaction of hydrogen peroxide with hypochlorous acid ($\text{H}_2\text{O}_2 + \text{HOCl} \rightarrow {}^1\text{O}_2 + \text{H}_2\text{O} + \text{HCl}$) at pH 10. In a previous study on ¹O₂ formation during ozone reactions,⁹ the calibration reaction was performed at pH 7 where a 100 % yield of ¹O₂ can be expected. However, our setup detected somewhat greater ¹O₂ signals at pH 10 than at lower pH values (Figure S2.6). The seemingly marginal difference between pH 7 and 10 can give rise to different results in quantification. For this reason, in this study, the calibration reaction was performed at pH 10 where the highest ¹O₂ yield was observed. The reaction was initiated by injecting 1 mL of a 0.04 – 0.6 mM HOCl solution by a glass syringe to 1 mL of 10 mM H₂O₂ solution placed in a cuvette in the cuvette holder attached to NIR-PMT as in Figure S2.5. The measurements were repeated at least five times to reduce the deviations of the data which might be caused by incomplete mixing. The

concentrations of the HOCl and H₂O₂ solutions were determined spectrophotometrically ($\epsilon = 350 \text{ M}^{-1} \text{ cm}^{-1}$ at 290 nm for HOCl and $\epsilon = 40 \text{ M}^{-1} \text{ cm}^{-1}$ at 240 nm for H₂O₂). Considering the dilution factor of 2, the final ¹O₂ concentrations were expected to be 0.02 – 0.3 mM. A calibration curve was obtained by plotting integrated areas of the ¹O₂ signals as a function of the final ¹O₂ concentrations (Figure S2.7). LOQ ~ 3 μM was determined based on a signal-to-noise ratio greater than 10 for the calibration solution theoretically producing 3 μM ¹O₂ by the reaction of 10 mM H₂O₂ with 6 μM HOCl (Figure S2.8).

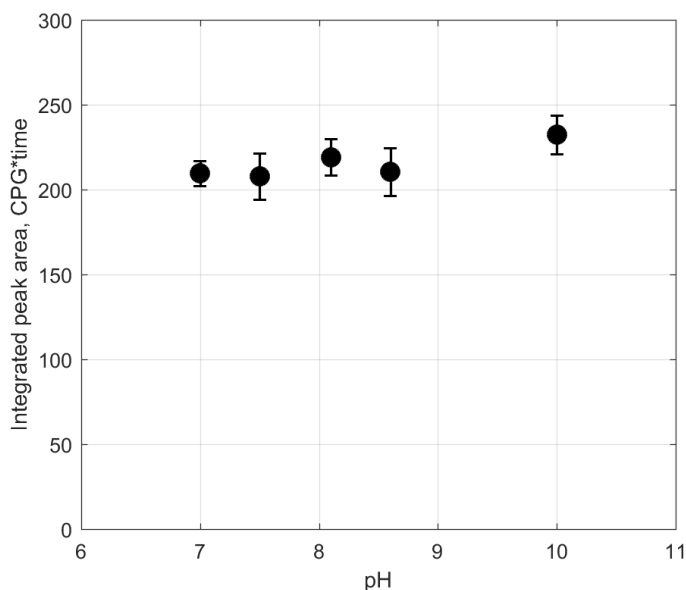


Figure S2.6. Integrated ¹O₂ signals formed during H₂O₂-HOCl reaction (5 mM H₂O₂ and 0.1 mM HOCl) under various pH conditions ranging from 7 to 10. Data points were averaged values over five repetitions.

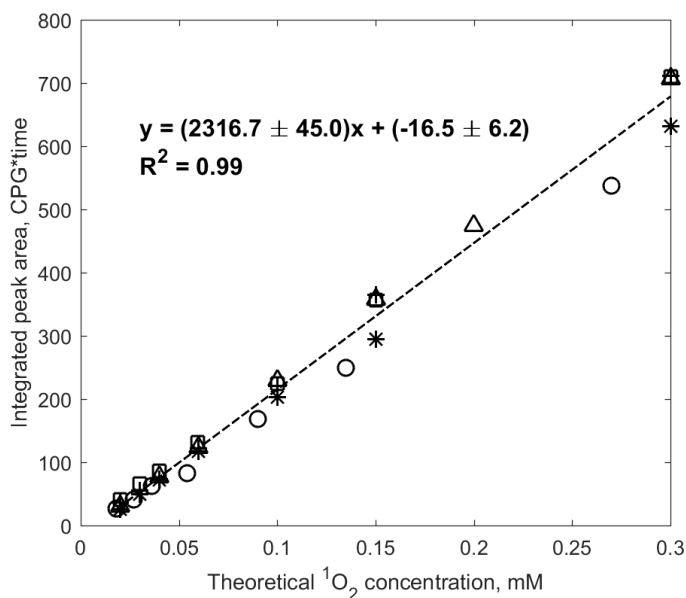


Figure S2.7. Integrated ¹O₂ signals as a function of theoretical concentrations of ¹O₂ formed during the reaction of hydrogen peroxide with hypochlorous acid, yielding a 100 % ¹O₂ yield at pH 10. Data from five individual experiments are shown with 10 mM H₂O₂ and 0.04 – 0.6 mM HOCl.

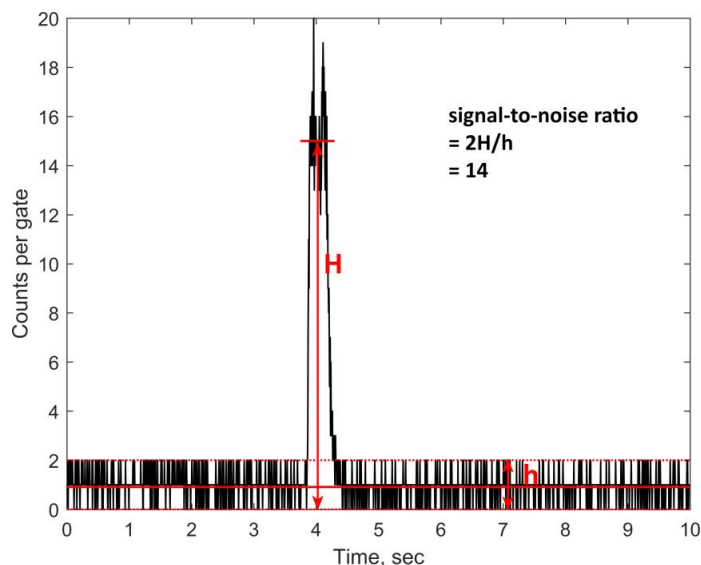


Figure S2.8. Example of a $^1\text{O}_2$ signal of a calibration solution (10 mM H_2O_2 and 6 μM HOCl), theoretically yielding 3 μM $^1\text{O}_2$.

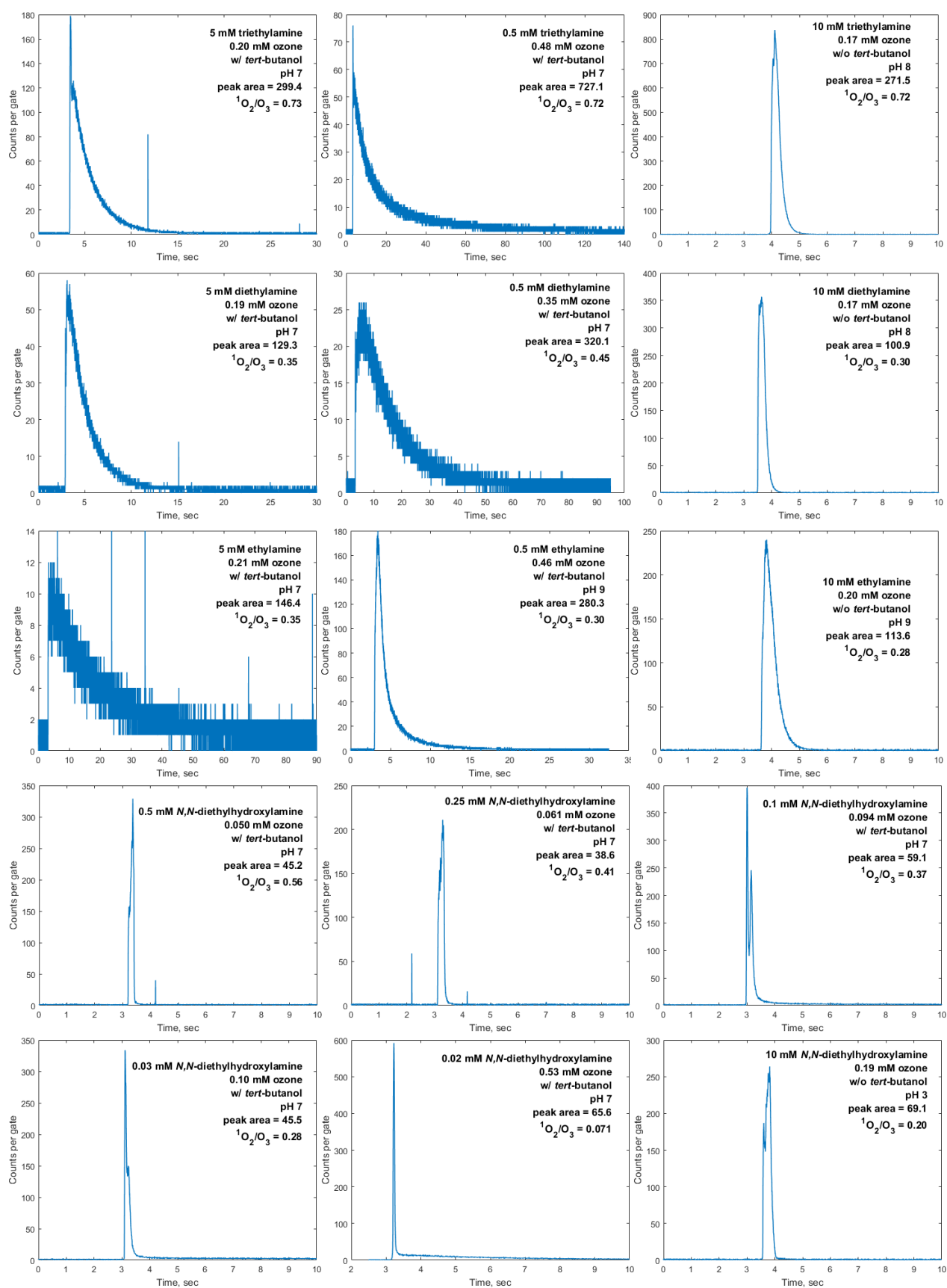
$^1\text{O}_2$ determination in ozone reactions: The formation of $^1\text{O}_2$ during various amine-ozone reactions was quantified by injecting 1 mL of 0.1 – 1 mM ozone solution by a glass syringe to 1 mL of 0.04 – 20 mM of amine solution placed in the cuvette attached to NIR-PMT. Ozone concentrations were determined in parallel for each measurement by using an indigo reagent³ and measuring decolorization of the indigo spectrophotometrically. Most experiments were performed in presence of *t*-butanol to scavenge $\cdot\text{OH}$ which could consume amines and ozone, but experiments without *t*-butanol were also carried out to compare the results to those from a previous study.⁹ The results and the full details of the experimental conditions are summarized in Table S2.3. Examples of $^1\text{O}_2$ signals corresponding to the results in Table S2.3 are shown in Figure S2.9.

Table S2.3. Measuring conditions and $^1\text{O}_2$ yields of various amine-ozone reactions. Each condition was repeated 5 – 9 times and the average values are shown in bold at the last row for each condition. The standard deviations were within 10 % of the average values. C and O_3 are final concentrations in the mixed solution by taking the dilution factor of 2 (1:1 mixing ratio) into account.

Compound (C)	$^1\text{O}_2$ Measuring conditions					Results		
	C, mM	O_3 , mM	O_3/C^a	t-BuOH ^b	pH	Area	$^1\text{O}_2$, mM	$^1\text{O}_2/\text{O}_3$
Triethylamine	5	0.20	0.04	Yes	7	299.38	0.15	0.73
		0.21				279.17	0.14	0.66
		0.20				255.17	0.13	0.63
		0.19				293.77	0.14	0.76
		0.21				266.84	0.13	0.63
		0.20				340.00	0.14	0.68
		0.20					0.14	0.68
	0.5	0.48	1	Yes	7	727.08	0.35	0.72
		0.47				700.16	0.33	0.71
		0.51				702.33	0.33	0.66
		0.46				701.55	0.33	0.73
		0.49				674.14	0.34	0.68
		0.48				678.72	0.34	0.70
		0.49					0.34	0.70
	10	0.17	0.02	No	8	271.52	0.12	0.72
		0.18				248.94	0.11	0.63
		0.17				292.21	0.13	0.75
		0.16				249.44	0.11	0.69
		0.16				250.36	0.11	0.71
		0.17					0.12	0.70
Diethylamine	5	0.19	0.04	Yes	7	129.29	0.067	0.35
		0.21				135.64	0.070	0.34
		0.21				127.97	0.067	0.32
		0.21				142.65	0.074	0.36
		0.20				123.07	0.064	0.32
		0.20				128.59	0.069	0.34
		0.20					0.069	0.34
	0.5	0.35	1	Yes	7	320.14	0.16	0.45
		0.35				328.62	0.16	0.45
		0.38				369.48	0.18	0.47
		0.35				338.81	0.17	0.48
		0.39				351.70	0.17	0.44
		0.36					0.17	0.46
	10	0.17	0.02	No	8	100.88	0.050	0.30
		0.17				82.19	0.043	0.25
		0.17				87.25	0.045	0.27
		0.16				93.62	0.047	0.29
		0.16				103.58	0.051	0.32
		0.17					0.047	0.29
Ethylamine	5	0.21	0.04	Yes	7	146.40	0.075	0.35
		0.21				135.64	0.070	0.34
		0.21				127.97	0.067	0.32
		0.21				142.65	0.074	0.36
		0.20				123.07	0.064	0.32
		0.19				129.29	0.067	0.35
		0.20				128.59	0.069	0.34
		0.20					0.069	0.35
	0.5	0.46	1	Yes	9	280.26	0.14	0.30
		0.46				273.43	0.13	0.29
		0.46				256.81	0.13	0.28
		0.46				246.22	0.12	0.26
		0.46				242.59	0.12	0.26
		0.45				234.59	0.12	0.26
		0.43				257.92	0.13	0.30
		0.45				235.58	0.12	0.26
		0.47				226.41	0.11	0.24
		0.46					0.12	0.27
	10	0.20	0.02	No	9	113.59	0.055	0.28
		0.21				107.79	0.053	0.26
		0.20				106.53	0.052	0.26
		0.19				113.09	0.055	0.28
		0.19				116.17	0.056	0.30
		0.20					0.054	0.28
N,N-diethyl-hydroxylamine	0.5	0.050	0.1	Yes	7	45.16	0.028	0.56
		0.055				47.54	0.029	0.53
		0.056				43.01	0.027	0.49
		0.046				48.11	0.030	0.64
		0.052				53.17	0.029	0.55
		0.052					0.029	0.55

	0.25	0.061 0.048 0.049 0.040 0.057 0.058		Yes	7	38.61 48.13 35.44 45.05 41.31 36.27	0.025 0.030 0.024 0.028 0.026 0.024	0.41 0.62 0.48 0.70 0.46 0.41
		0.052	0.2				0.026	0.52
	0.1	0.09 0.10 0.10 0.10 0.09 0.10		Yes	7	59.12 63.45 66.50 62.66 61.54 60.94	0.035 0.037 0.038 0.036 0.036 0.036	0.37 0.38 0.39 0.38 0.38 0.38
		0.10	1				0.036	0.38
	0.03	0.10 0.095 0.089 0.090 0.090 0.093		Yes	7	45.50 36.52 43.18 41.91 46.93 43.68	0.028 0.024 0.027 0.027 0.029 0.027	0.28 0.25 0.31 0.30 0.32 0.29
		0.093	3				0.027	0.29
	0.02	0.53 0.50 0.53 0.50 0.51 0.52		Yes	7	65.60 65.59 65.96 64.31 64.74 64.60	0.038 0.038 0.038 0.037 0.037 0.038	0.071 0.076 0.071 0.074 0.072 0.073
		0.52	26				0.038	0.073
	10	0.19 0.19 0.19 0.19 0.19		No	3	69.05 87.12 66.14 97.44 76.02	0.037 0.045 0.036 0.049 0.040	0.20 0.23 0.19 0.26 0.22
		0.19	0.02				0.041	0.22
	10	0.20 0.19 0.18 0.17 0.17		No	7	89.78 83.35 65.32 88.47 83.44	0.044 0.042 0.035 0.044 0.042	0.23 0.22 0.19 0.25 0.25
		0.18	0.02				0.041	0.23
N-ethylethan- imine oxide	0.5	0.054 0.052 0.051 0.047 0.043 0.045		Yes	7	29.95 32.59 30.90 30.63 29.22 28.59	0.021 0.022 0.022 0.021 0.021 0.020	0.39 0.43 0.42 0.46 0.48 0.46
		0.049	0.1				0.021	0.44
	0.1	0.081 0.076 0.086 0.089 0.092 0.085		Yes	7	60.75 65.37 63.08 64.53 58.29 56.89	0.035 0.038 0.037 0.037 0.034 0.036	0.44 0.50 0.42 0.42 0.37 0.43
		0.085	1				0.036	0.43
	0.03	0.10 0.092 0.082 0.083 0.084 0.088		Yes	7	37.88 40.24 38.90 36.42 36.98 38.60	0.025 0.026 0.025 0.024 0.024 0.025	0.25 0.28 0.31 0.29 0.29 0.28
		0.088	3				0.025	0.28
	10	0.17 0.16 0.16 0.15 0.15		No	7	75.35 47.26 57.46 63.94 54.86	0.040 0.028 0.033 0.035 0.032	0.23 0.17 0.21 0.23 0.22
		0.16	0.02				0.034	0.21

^a Molar ozone:compound ratio, ^b Yes = with *t*-butanol, No = without *t*-butanol.



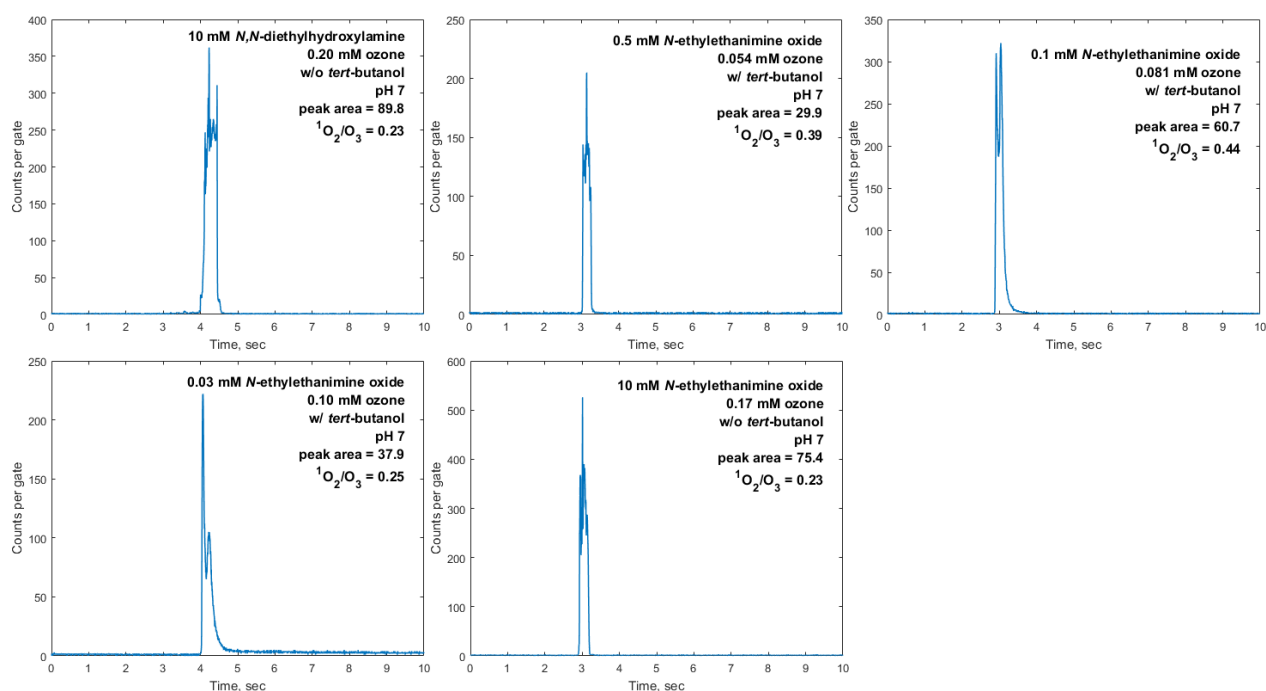


Figure S2.9. $^1\text{O}_2$ signals of triethylamine, diethylamine, ethylamine, *N,N*-diethylhydroxylamine, and *N*-ethylethanamine oxide, corresponding to the results in Table S2.3. Signals shown were from single measurements.

Effects of measuring conditions on $^1\text{O}_2$ signals: The shape of $^1\text{O}_2$ signals strongly depends on the kinetics of $^1\text{O}_2$ formation: as the reaction gets faster, the signal becomes sharper and narrower (Figure S2.10). Ideally, the integrated areas of the $^1\text{O}_2$ signals should be maintained regardless of the reaction kinetics. However, as previously mentioned by Muñoz et al. (2001)⁹ when the reaction is too fast, complete mixing of the solution is hardly achieved, leading to a higher error. In contrast, if the reaction is too slow, the $^1\text{O}_2$ signals can disappear in the noise, resulting in underestimation of the $^1\text{O}_2$ formation. In addition to the pH, the initial amine concentrations, which determined the molar amine: O_3 ratios also affect the reaction kinetics and thereby the shape of the $^1\text{O}_2$ signals. For example, the signals obtained for a molar amine: O_3 ratio of 118:1 (achieved by 10 mM triethylamine and 0.085 mM ozone) were sharper than the signals for an amine: O_3 ratio of 58:1 (by 5 mM triethylamine and 0.086 mM ozone) (Figure S2.11). This clearly becomes a drawback of this measurement such that the measuring conditions (e.g., pH of the solution and concentrations of amine and ozone solutions) should be always taken into account to interpret the data. Only the results obtained under similar conditions are comparable to each other.

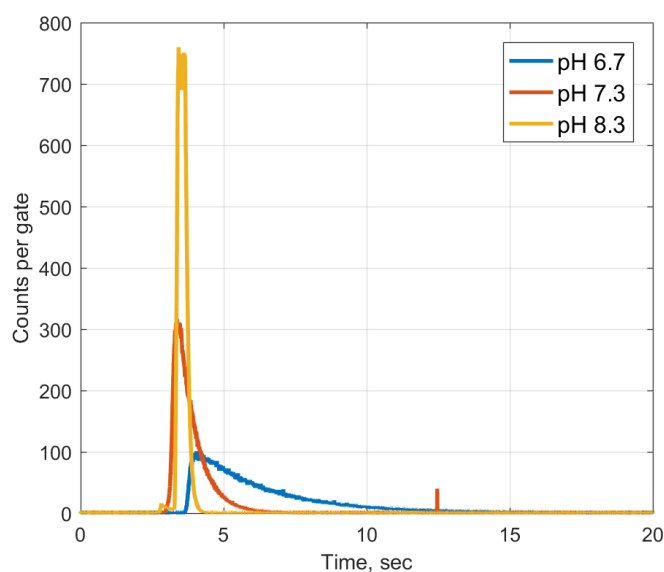


Figure S2.10. $^1\text{O}_2$ signals of the triethylamine-ozone reactions at pH 6.7, 7.3, and 8.3 where $k_{\text{O}_3, \text{TEA}} = 1.1 \times 10^2$, 4.3×10^2 , and $4.3 \times 10^3 \text{ M}^{-1}\text{s}^{-1}$, respectively. The concentrations of triethylamine and ozone were 5.0 mM and 0.18 mM, respectively, for all pH conditions. Gate time of PMT was 5 ms. The averages of the integrated $^1\text{O}_2$ signals (\pm standard deviation with $n = 5$) were 271 (± 7), 263 (± 7), and 300 (± 21) for pH 6.7, 7.4, and 8.3, respectively.

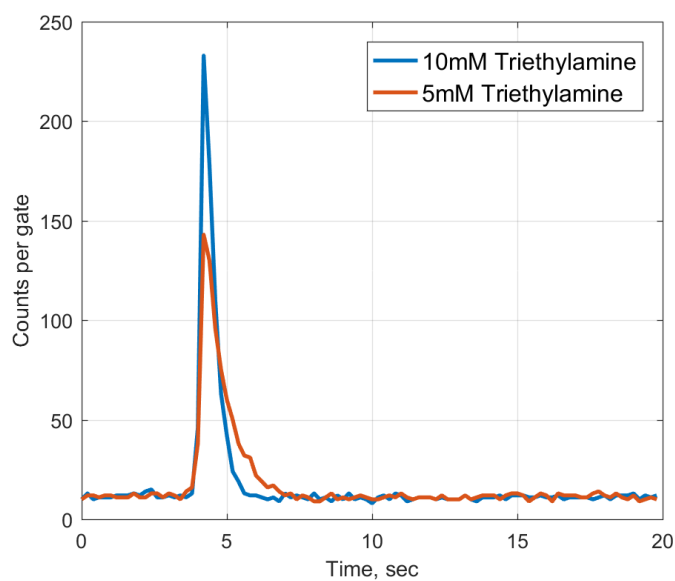


Figure S2.11. $^1\text{O}_2$ signals of triethylamine-ozone reaction at a triethylamine:ozone ratio of 118:1 (10 mM triethylamine and 0.085 mM ozone) and 58:1 (5 mM triethylamine and 0.086 mM ozone). The pH was maintained at pH 7.5 for both conditions. Gate time of PMT was 200 ms. The averages of the integrated $^1\text{O}_2$ signals (\pm standard deviation with $n = 4$ or 5) were 129 (± 8) and 128 (± 9) for 10 mM and 5 mM triethylamine, respectively.

Text S2.5. Analysis of reactive oxygen species: Hydroxyl radicals

The concentration of $\cdot\text{OH}$ was determined for varying ozone doses (0 – 300 μM) in the batch ozonation experiments by using an $\cdot\text{OH}$ scavenger, *t*-butanol (50 mM). After the batch experiments, formaldehyde, a product of the reaction of *t*-butanol with hydroxyl radicals, was quantified by a derivatization method with 2,4-dinitrophenylhydrazine.¹⁰ The $\cdot\text{OH}$ concentrations were estimated by doubling the determined formaldehyde concentrations based on the previously reported formaldehyde yield of $\sim 50\%$.¹¹ The derivatization was performed by adding 0.05 mL of 9 mM 2,4-dinitrophenylhydrazine prepared in acetonitrile and 0.05 mL of 1 M perchloric acid in acetonitrile to 0.9 mL of the sample solution.^{10,11} The mixture was allowed to stand for 45 min at room temperature. The derivatized product (2,4-dinitrophenylhydrazone) was analyzed by HPLC-UV using a Cosmosil C18 column (5C18-MS-II, 3.0×100 mm, NACALAI TESQUE, INC.), 50:50 acetonitrile:water as a mobile phase with a flow rate of 0.1 mL/min, and UV detection at 360 nm. The LOQ was ~ 4 μM . The determined $\cdot\text{OH}$ concentrations for all tested amine-ozone reactions as a function of the ozone dose are presented in Figure S2.12. The numbers next to the compound names indicate the $\cdot\text{OH}$ yields derived from the slopes of the linear regression of the determined $\cdot\text{OH}$ concentrations at low ozone doses (i.e., $\Delta[\cdot\text{OH}]/\Delta[\text{O}_3]$ at 0 – 100 μM ozone). We ignored the higher range of ozone doses (> 100 μM), because under these conditions most $\cdot\text{OH}$ was formed by self-decay of ozone or secondary oxidation reactions with other reaction intermediates than the target amine. The $\cdot\text{OH}$ yields derived from $\Delta[\cdot\text{OH}]/\Delta[\text{O}_3]$ are similar but differently determined yields compared with those presented in the main text (Table 2.2). The yields in the main text were derived from a single ozone dose (i.e., $[\cdot\text{OH}]/[\text{O}_3]$ at ~ 100 μM ozone) to be compared with the $^1\text{O}_2$ yields.

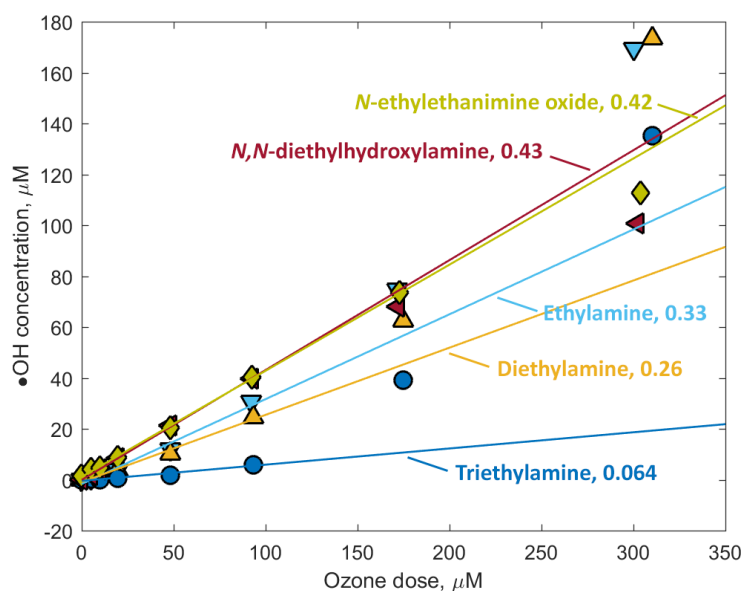


Figure S2.12. Hydroxyl radical ($\cdot\text{OH}$) formation during the reactions of ozone with ethylamine, diethylamine, triethylamine, *N,N*-diethylhydroxylamine, and *N*-ethylethanamine oxide (initial concentrations ~ 100 μM). Symbols indicate the determined $\cdot\text{OH}$ concentrations and lines are the linear regression of the data for ozone doses in the range of 0 – 100 μM . Numbers next to the compound names are the slopes of the linear regression. R-squared values for all regression were > 0.95 .

Text S2.6. Analysis of reactive oxygen species: Hydrogen peroxide

Hydrogen peroxide (H_2O_2) was indirectly quantified by adding hypochlorous acid (40 mM prepared in 100 mM phosphate buffer solution at pH 6.8) to samples or to H_2O_2 standard solutions (5 – 50 μM prepared in ultrapure water) and detecting $^1\text{O}_2$ formation by the $^1\text{O}_2$ detector.¹² The determined $^1\text{O}_2$ concentration was used to estimate the H_2O_2 concentration based on the reaction of $\text{H}_2\text{O}_2 + \text{HOCl} \rightarrow ^1\text{O}_2 + \text{H}_2\text{O} + \text{HCl}$.⁹

Text S2.7. *N*-ethylethanimine oxide-ozone reaction

An additional ozonation experiment was carried out with *N*-ethylethanimine oxide (Figure S2.13) to investigate if it is transformed to nitroethane with a high yield. The *N*-ethylethanimine oxide solution was prepared from the synthesized stock as described in Text S2.1. Nitroethane was indeed identified as a major product with a 73 % yield based on the abated *N*-ethylethanimine oxide at 300 μM ozone. However, some differences were found compared to the case of *N*-ethylethanimine oxide formation as an intermediate during the *N,N*-diethylhydroxylamine-ozone reaction. First, a high ozone stoichiometry (> 3 molar equivalents of ozone) was found, which suggests other compounds consuming more ozone were involved in the reaction. This is different from the almost direct formation of nitroethane from *N*-ethylethanimine oxide, which we observed during the *N,N*-diethylhydroxylamine-ozone reaction (between 150 – 300 μM ozone, Figure 2.1c in the main text). The over-stoichiometric feature can be attributed to a *N*-ethylethanimine oxide dimer present in the sample solution prior to ozonation. Dimerization of nitrones forming a six-membered heterocycle (e.g., Figure S2.14) has been experimentally and theoretically confirmed by NMR and quantum chemical computations for cyclic nitrones.^{13–16} Our LC-HRMS data also showed a considerable peak intensity with an exact mass of 175.1441 corresponding to the mass of the *N*-ethylethanimine oxide dimer as $[\text{M}+\text{H}]^+$ for the ozonated *N*-ethylethanimine oxide samples (Figure S2.15b). On the contrary, no significant peaks for 175.1441 were detected for the ozonated *N,N*-diethylhydroxylamine samples even at 100 – 200 μM ozone doses where the maximum formation of *N*-ethylethanimine oxide was observed (Figure S2.15a). This implies that our primary *N*-ethylethanimine oxide stock contained a significant amount of the dimer and thereby resulted in a different behavior upon ozonation compared with *N*-ethylethanimine oxide freshly formed during the *N,N*-diethylhydroxylamine-ozone reaction. Second, nitrite was detected along with nitroethane at high ozone doses (> 200 μM ozone) for the ozonation experiments with *N*-ethylethanimine oxide (Figure S2.13). This was not detected for any ozone doses during the *N,N*-diethylhydroxylamine-ozone reaction. If nitrite was formed during the ozone reaction, it would have been oxidized very efficiently to nitrate due to its high ozone reactivity ($k_{\text{O}_3} = 1.8 \times 10^5 \text{ M}^{-1} \text{ s}^{-1}$).¹⁷ However, only a few μM of nitrate was found at the highest ozone dose at which 25 μM of nitrite was detected. Thus, the nitrite detected at high ozone doses was assumedly derived from an unidentified transformation product which formed nitrite after the ozone was completely depleted.

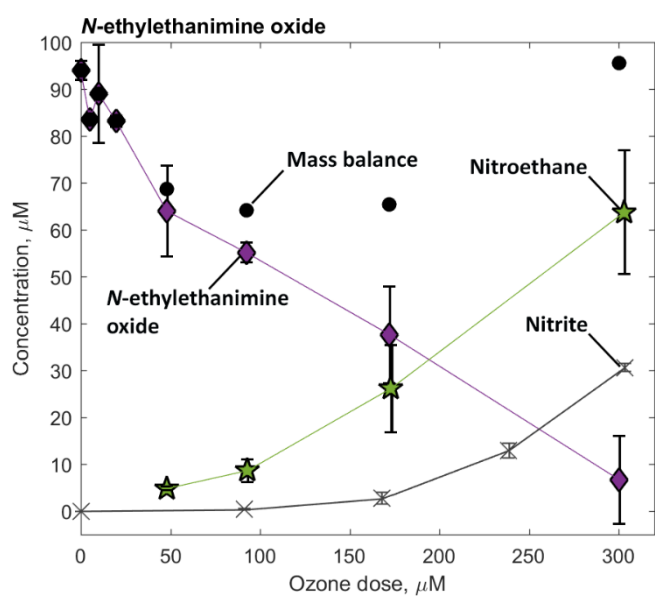


Figure S2.13. Evolution of transformation products as a function of the ozone dose for the reaction of *N*-ethylethanamine oxide with ozone. *N*-ethylethanamine oxide was prepared from the synthesized stock as described in Text S2.1.

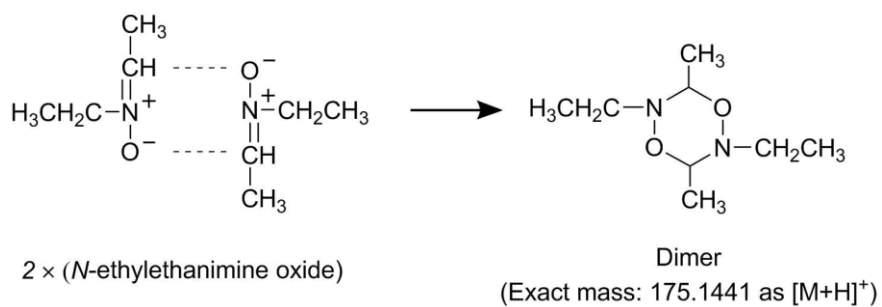


Figure S2.14. Dimerization of *N*-ethylethanamine oxide hypothesized based on the dimerization of cyclic nitrones observed experimentally^{13,14,16} and confirmed theoretically.¹⁵

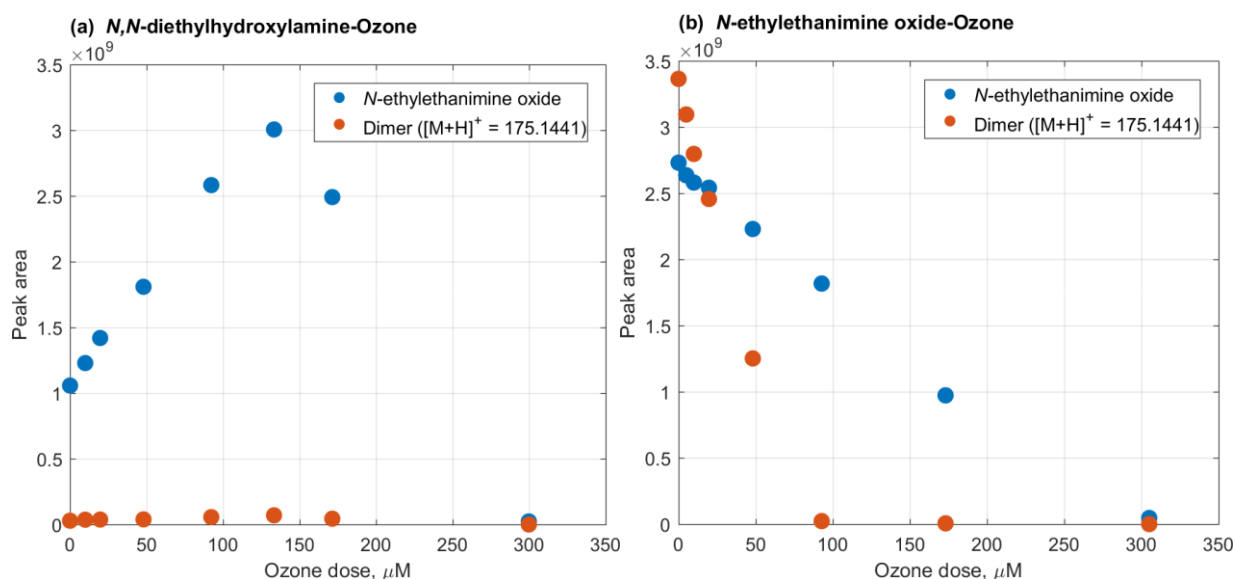


Figure S2.15. Integrated peak areas for *N*-ethylethanamine oxide and $[\text{M}+\text{H}]^+ = 175.1441$ as a function of ozone doses for (a) *N,N*-diethylhydroxylamine-ozone and (b) *N*-ethylethanamine oxide-ozone reactions.

Text S2.8. Quantum chemical computations

Methods. All computations were performed on the Gaussian 09 software package (Revision D.01).¹⁸ The structures of all molecules were first optimized at the B3LYP/CBSB7 level of theory.^{19,20} The optimized structures were then used to calculate the gas phase electronic energies (E_{gas}) at the CCSD(T)/jul-cc-pVTZ level of theory.^{21,22} For radical species (diethylnitroxide, diethylaminyl radical, and ozonide radical anion), the E_{gas} were computed based on both unrestricted and restricted Hartree-Fock wave functions (UHF and ROHF), which are known to perform well for small radicals.²³ The resulting E_{gas} differed by $< 0.1 \text{ kcal mol}^{-1}$ between UHF and ROHF, and the ROHF values were used to calculate the aqueous Gibbs free energy. The solvation energies (ΔG_{solv}) were calculated at the M062X/6-31G* level of theory^{24,25} with the SMD model²⁶ by using the same optimized structures (B3LYP/CBSB7) as initial inputs and re-optimizing them for both gas and solution phases. The ΔG_{solv} was obtained by subtracting the gas phase electronic energy from the solution phase electronic energy. Vibrational and rotational contributions were not included in the electronic energies. For the radical species, ΔG_{solv} were computed by an unrestricted Kohn-Sham method, and the spin contamination was insignificant in all results ($\langle S^2 \rangle < 0.76$). For the proton, the absolute aqueous solvation free energy was used as reported in literature ($\Delta G_{\text{solv}}(\text{H}^+) = -265.9 \text{ kcal mol}^{-1}$).²⁷ The thermal corrections to the electronic energies caused by rotation and vibration in gas phase (ΔG_{therm}) were taken from the B3LYP/CBSB7 computations. The total aqueous Gibbs free energy of a compound (G_{aq}) was then obtained by summing up E_{gas} , ΔG_{solv} , and ΔG_{therm} . Finally, the aqueous Gibbs free energy of a reaction ($\Delta G_{\text{aq,rxn}}$) was obtained by subtracting the sum of the total aqueous Gibbs free energies of reactants to the sum of the total aqueous Gibbs free energy of products: i.e., $\Delta G_{\text{aq,rxn}} = G_{\text{aq}}(\text{products}) - G_{\text{aq}}(\text{reactants})$.

Additional confirmation of $\Delta G_{\text{aq,rxn}}$ for ozone reactions. Ozone is a problematic molecule in quantum-chemical computations because of its diradical character which is considered as a multireference system.^{28,29} For this reason, the calculated $\Delta G_{\text{aq,rxn}}$ of the reactions associated with ozone were additionally confirmed by using previously calculated values based on more accurate computation methods³⁰ or by using reported one-electron standard reduction potentials^{31,32} which can deduce $\Delta G_{\text{aq,rxn}}$. For oxygen transfer pathways forming $^1\text{O}_2$ (step (a) in Figure 2.3, step (c) in Figure 2.4, and step (j) in Figure S2.17), the gas phase components (E_{gas}) of the $\Delta G_{\text{aq,rxn}}$ were esti-

mated based on the results obtained by higher levels of coupled-cluster theory.³⁰ To this end, the reactions were first divided into two parts: e.g., (1) $O_3 \rightarrow {}^1O_2 + {}^3O$ (3O : triplet oxygen atom) and (2) diethylamine + ${}^3O \rightarrow N,N$ -diethylhydroxylamine. The $\Delta G_{aq,rxn}$ of the sub-reaction (1) with the problematic species, O_3 , took the best estimate value calculated by Trogolo et al. (49.8 kcal mol⁻¹)³⁰ and the $\Delta G_{aq,rxn}$ of the sub-reaction (2) was calculated by our method as described above. The $\Delta G_{aq,rxn}$ of the overall reaction was obtained by summing up the $\Delta G_{aq,rxn}$ of the sub-reactions. The newly estimated $\Delta G_{aq,rxn}$ were -17.3, -62.1, and -41.8 kcal mol⁻¹ for step (a) in Figure 2.3, step (c) in Figure 2.4, and step (j) in Figure S2.17, respectively, ~1 kcal mol⁻¹ lower than our results (Table S2.4). For electron transfer pathways forming ozonide radical anions (step (b) in Figure 2.3 and step (d) in Figure 2.4), the aqueous Gibbs free energies were estimated from the reported one-electron standard reduction potential of ozone (1.01 V for $O_3/O_3^{\bullet-}$)³² and diethylamine (1.36 V for $(CH_3CH_2)_2NH^{\bullet+}/(CH_3CH_2)_2NH$).³¹ The ΔG of each reduction reaction was derived by the Nernst equation, $\Delta G = -nFE$ and used to calculate $\Delta G_{aq,rxn}$. The resulting $\Delta G_{aq,rxn}$ were +8.1 and -2.7 kcal mol⁻¹ for step (b) in Figure 2.3 and step (d) in Figure 2.4, differing by < 4 kcal mol⁻¹ to our results (Table S2.4).

Table S2.4. Summary of calculated and estimated^a Gibbs free energies of the possible primary and secondary reactions of the diethylamine- O_3 reaction.

No.	Reaction	Reaction index	$\Delta G_{aq,rxn}$, kcal mol ^{-1a}
1	Diethylamine + $O_3 \Rightarrow N,N$ -diethylhydroxylamine + 1O_2	Step (a), Figure 2.3	-16.4 (-17.3)
2	Diethylamine + $O_3 \Rightarrow$ Diethylaminy radical + $O_3^{\bullet-}$ + H^+	Step (b), Figure 2.3	+9.3 (+8.1)
3	N,N -diethylhydroxylamine + $O_3 \Rightarrow N$ -ethylethanamine oxide + 1O_2 + H_2O	Step (c), Figure 2.4	-61.2 (-62.1)
4	N,N -diethylhydroxylamine + $O_3 \Rightarrow$ Diethylnitroxide + $O_3^{\bullet-}$ + H^+	Step (d), Figure 2.4	-6.1 (-2.7)
5	Diethylnitroxide + $O_3 \Rightarrow$ Diethylaminy radical + $2O_2$	Step (e), Figure 2.4	-16.7
6	N -ethylethanamine oxide + $O_3 \Rightarrow$ Nitrosoethane + Acetaldehyde(CH_3CHO) + 1O_2	Step (j), Figure S2.17	-40.8 (-41.8)
7	N -ethylethanamine oxide + O_3 + $H_2O \Rightarrow$ Nitroethane + Acetaldehyde(CH_3CHO) + H_2O_2	Step (l), Figure S2.17	-70.8
8	N -ethylethanamine oxide + $H_2O \Rightarrow N$ -ethylhydroxylamine + Acetaldehyde(CH_3CHO)	Step (n), Figure S2.17	+8.4

^aThe values in parentheses were estimated from a more accurate gas-phase result (Reaction No. 1, 3, and 6)³⁰ or from reported one-electron standard reduction potentials (Reaction No. 2 and 4).^{31,32}

Text S2.9. Kinetic simulations

The evolution of *N,N*-diethylhydroxylamine and its transformation products as a function of ozone dose was simulated by a kinetic model described in Table S2.5. The predicted concentrations based on the model are presented in Figure 2.1c (dotted lines) in the main text. The evolution of diethylamine and its transformation products was also simulated based on a model described in Table S2.7 and the results are presented in Figure 2.1b (dotted lines) in the main text.

The reported second-order rate constants of the autoxidation of hydroxylamines are incoherent among previous studies:

0.06 M⁻¹ s⁻¹ *N,N*-diethylhydroxylamine at pH 12,³³

0.6 M⁻¹ s⁻¹ for *N,N*-diethylhydroxylamine at pH 7.2,³⁴

4.0 M⁻¹ s⁻¹ for *N,N*-diethylhydroxylamine at pH 10.1,³⁴ and

0.09 M⁻¹ s⁻¹ for hydroxylamine at pH 7.³⁵

We tested two rate constants, 0.06 M⁻¹ s⁻¹ and 0.6 M⁻¹ s⁻¹, for the kinetic simulation and confirmed the predicted initial concentrations of *N,N*-diethylhydroxylamine (at 0 μM O₃) were close to the measured concentration for simulation times of 1 hour for 0.6 M⁻¹ s⁻¹ and 6 hours for 0.06 M⁻¹ s⁻¹. When the simulation time was applied the same for both rate constants (e.g. 6 hours for 0.6 M⁻¹ s⁻¹ and 0.06 M⁻¹ s⁻¹), the predicted initial concentrations of *N,N*-diethylhydroxylamine differed by 66 % between the rate constants (*[N,N*-diethylhydroxylamine]₀ = 31 μM for 0.6 M⁻¹ s⁻¹ and 92 μM for 0.06 M⁻¹ s⁻¹). For further simulations, we used the autoxidation rate constant of 0.06 M⁻¹ s⁻¹ and the simulation time of 6 hours. The abatement trend of *N*-ethylethanamine oxide and the formation trend of nitroethane remained the same regardless of the second-order rate constant of the autoxidation and the simulation time.

Table S2.5. Kinetic model for the *N,N*-diethylhydroxylamine- and *N*-ethylethanamine oxide-ozone reactions performed by Kintecus.³⁶ The initial concentrations of *N,N*-diethylhydroxylamine, oxygen, and ozone were set as *[N,N*-diethylhydroxylamine] = 111 μM, [O₂] = 300 μM, and [O₃] = 0 – 350 μM (in 2 μM increments). Simulation time was set as 6 h.

No.	Reaction	Reaction index	<i>k</i> _{obs,pH7} , M ⁻¹ s ⁻¹	Reference
1	<i>N,N</i> -diethylhydroxylamine + O ₃ ==> 0.5* <i>N</i> -ethylethanamine oxide + 0.5*Diethylnitroxide + 0.5*X ^a	Step (c) and (d) with a 1:1 branching ratio, Figure 2.4 (main text)	6.8 × 10 ⁵	Table 2.1 of main text
2	diethylnitroxide + X ^a ==> <i>N</i> -ethylethanamine oxide	Step (h) with X ^a as an active radical species, Figure 2.4 (main text)	2.8 × 10 ⁷	estimated from the reaction of TEMPO with <i>t</i> -BuOO• ³⁷
3	<i>N,N</i> -diethylhydroxylamine + O ₂ ==> diethylnitroxide	Autoxidation	6.0 × 10 ^{-2c}	³³
4	2*diethylnitroxide + O ₃ ==> <i>N</i> -ethylethanamine oxide + <i>N,N</i> -diethylhydroxylamine	Step (h) as a bimolecular reaction, Figure 2.4 (main text)	8.0 × 10 ²	³⁸
5	<i>N</i> -ethylethanamine oxide + O ₃ ==> Y ^b	Step (j), (l), or (m) in Figure S2.17 or else	1.9 × 10 ³	Table 2.1 of main text
6	Y ^b + O ₃ ==> nitroethane	Not assigned	1.0 × 10 ⁶	assumed as a fast ozone-consuming reaction

^aX is a radical species formed during the •OH scavenging reaction by *t*-butanol, e.g., *t*-BuOO•. ^bY is an unknown product of the reaction of *N*-ethylethanamine oxide with ozone, which presumably reacts fast with ozone to form nitroethane. ^cSee the Text S2.9 for the result from another rate constant.

Table S2.6. Kinetic model for the *N,N*-diethylhydroxylamine- and *N*-ethylethanamine oxide-ozone reactions performed by Kintecus³⁶ by assuming nitrosoethane as the intermediate of *N*-ethylethanamine oxide-ozone reaction. The initial concentrations of *N,N*-diethylhydroxylamine, oxygen, and ozone were set as [*N,N*-diethylhydroxylamine] = 111 μM , [O_2] = 300 μM , and [O_3] = 0 – 350 μM (in 2 μM increments). Simulation time was set as 6 h.

No.	Reaction	Reaction index	$k_{\text{obs,pH7}}, \text{M}^{-1} \text{s}^{-1}$	Reference
1	<i>N,N</i> -diethylhydroxylamine + $\text{O}_3 \Rightarrow$ 0.5* <i>N</i> -ethylethanamine oxide + 0.5*Diethylnitroxide + 0.5*X ^a	Step (c) and (d) with a 1:1 branching ratio, Figure 2.4 (main text)	6.8×10^5	Table 2.1 of main text
2	diethylnitroxide + X ^a \Rightarrow <i>N</i> -ethylethanamine oxide	Step (h) with X ^a as an active radical species, Figure 2.4 (main text)	2.8×10^7	estimated from the reaction of TEMPO with <i>t</i> -BuOO• ³⁷
3	<i>N,N</i> -diethylhydroxylamine + $\text{O}_2 \Rightarrow$ diethylnitroxide	Autoxidation	6.0×10^{-2}	³³
4	2*diethylnitroxide + $\text{O}_3 \Rightarrow$ <i>N</i> -ethylethanamine oxide + <i>N,N</i> -diethylhydroxylamine	Step (h) as a bimolecular reaction, Figure 2.4 (main text)	8.0×10^2	³⁸
5	<i>N</i> -ethylethanamine oxide + $\text{O}_3 \Rightarrow$ nitrosoethane	Step (j), (l), or (m) in Figure S2.17 or else	1.9×10^3	Table 2.1 of main text
6	nitrosoethane + $\text{O}_3 \Rightarrow$ nitroethane	Step (j), Figure S2.17	1.0×10^2	assumed as a slow ozone-consuming reaction

^aX is a radical species formed during the •OH scavenging reaction by *t*-butanol, e.g., *t*-BuOO•.

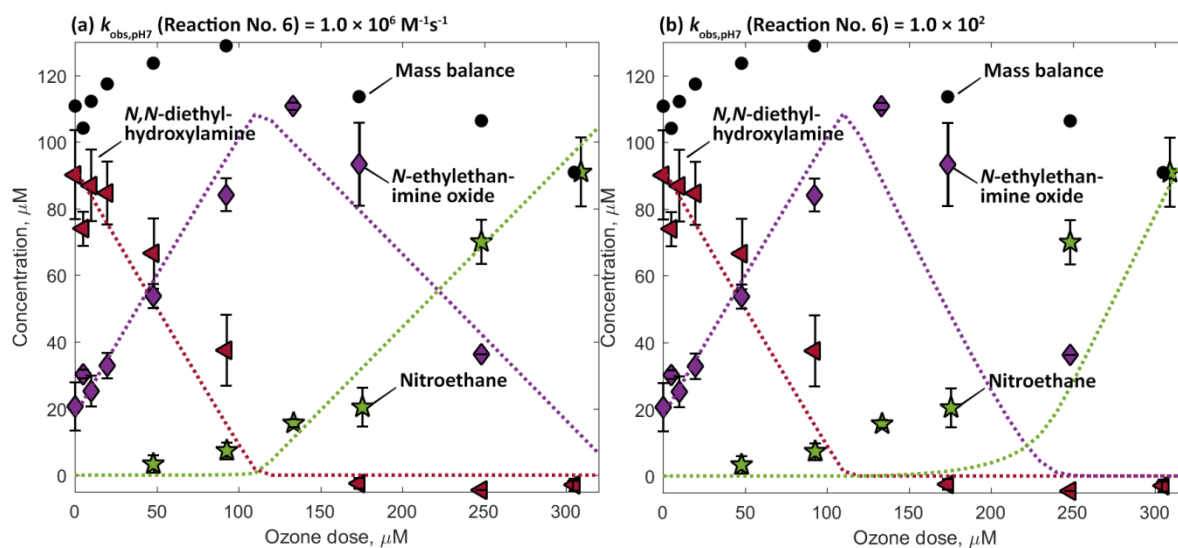


Figure S2.16. Kinetic simulation results of the *N,N*-diethylhydroxylamine-ozone reaction with two scenarios described as in (a) Table S2.5 and (b) Table S2.6. Figure S2.16a is same as Figure 2.1c in the main text and presented here again to be compared with Figure S2.16b.

Table S2.7. Kinetic model for the diethylamine-ozone reaction performed by Kintecus.³⁶ The initial concentrations of diethylamine, oxygen, and ozone were set as [diethylamine] = 94 μM , [O_2] = 300 μM , and [O_3] = 0 – 350 μM (in 2 μM increments). Simulation time was set as 24 h.

No.	Reaction	Reaction index	$k_{\text{obs,pH7}}, \text{M}^{-1} \text{s}^{-1}$	Reference
1	diethylamine + $\text{O}_3 \Rightarrow$ 0.9* <i>N,N</i> -diethylhydroxylamine + 0.1*Diethylaminyl radical	Step (a) and (b) with 9:1 branching ratio, Figure 2.3 (main text)	1.3×10^2	Table 2.1 of main text
2	Same as in Table S2.5			

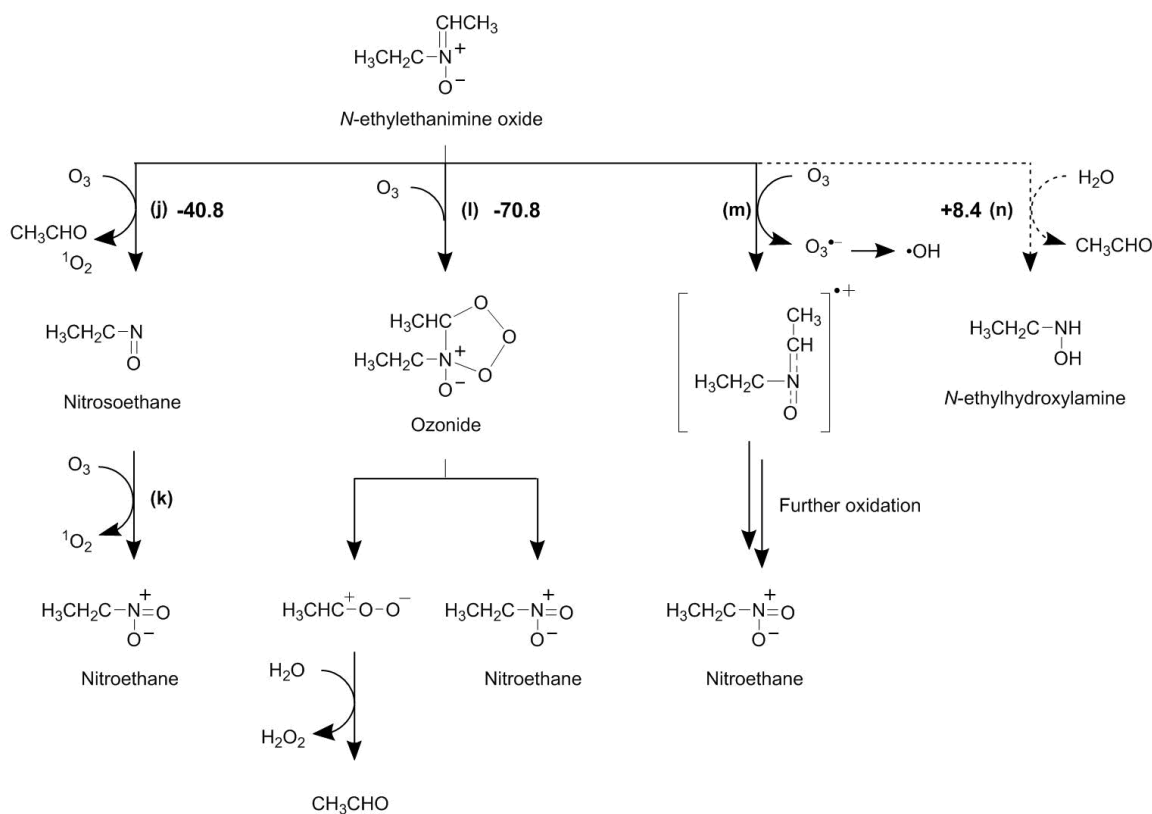


Figure S2.17. Possible mechanisms for the reactions of *N*-ethylethanamine oxide with ozone (solid lines, reaction steps (j) – (m)) and hydrolysis of *N*-ethylethanamine oxide (dashed line, reaction step (n)). Bold numbers next to the reaction steps are calculated aqueous Gibbs free energies in kcal mol⁻¹.

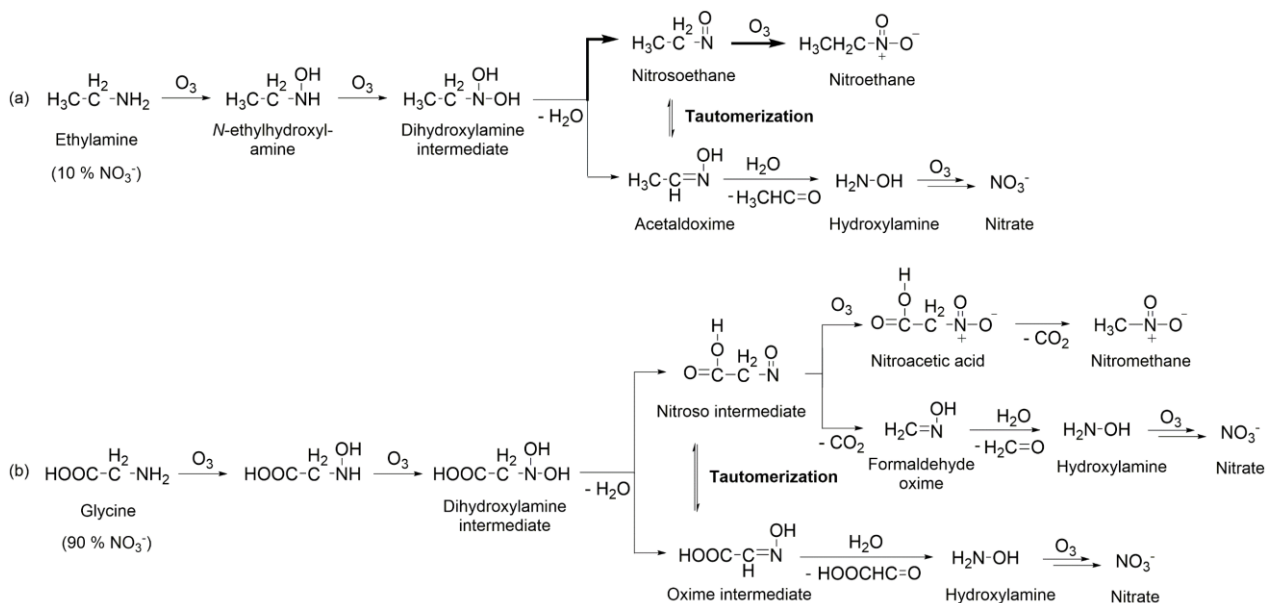


Figure S2.18. Comparison of ozone reaction mechanisms between (a) a primary amine, ethylamine, and (b) an amino acid, glycine. Nitrate yields in parenthesis were determined by this study (for ethylamine, under 20-fold ozone) and by Berger et al. (1999)³⁹ (for glycine, under 5-fold ozone). Bold arrows indicate a dominant pathway. The pathway of the formation of nitroacetic acid followed by nitromethane in the glycine-ozone reaction (b) was proposed by McCurry et al. (2016).⁴⁰

References

- (1) Cordero, F. M.; Machetti, F.; Sarlo, F. D.; Brandi, A. New Synthesis of (Methoxycarbonyl)-Indolizidin-7-one and -quinolizidin-2-one: An Access to B-Amino Acids with Indolizidine and Quinolizidine Backbone. *Gazzetta Chimica Italiana* **1997**, *127*, 25–29. <https://doi.org/10.1002/chin.199743213>.
- (2) Thesing, J.; Sirrenberg, W. Cyclische Nitrone, IV. Darstellung und Eigenschaften des Δ^1 -Pyrrolin-N-oxyds. *Chemische Berichte* **1959**, *92* (8), 1748–1755. <https://doi.org/10.1002/cber.19590920805>.
- (3) Bader, H.; Hoigné, J. Determination of Ozone in Water by the Indigo Method. *Water Research* **1981**, *15* (4), 449–456.
- (4) Hoigné, J.; Bader, H. Rate Constants of Reactions of Ozone with Organic and Inorganic Compounds in Water—II: Dissociating Organic Compounds. *Water Research* **1983**, *17* (2), 185–194.
- (5) Leitzke, A.; Reisz, E.; Flyunt, R.; von Sonntag, C. The Reactions of Ozone with Cinnamic Acids: Formation and Decay of 2-Hydroperoxy-2-Hydroxyacetic Acid. *Journal of the Chemical Society, Perkin Transactions 2* **2001**, No. 5, 793–797. <https://doi.org/10.1039/b009327k>.
- (6) Muñoz, F.; von Sonntag, C. Determination of Fast Ozone Reactions in Aqueous Solution by Competition Kinetics. *Journal of the Chemical Society, Perkin Transactions 2* **2000**, No. 4, 661–664. <https://doi.org/10.1039/a909668j>.
- (7) McCardell, C. S.; Alder, A. C.; Göbel, A.; Löffler, D.; Suter, M. J.-F.; Ternes, T. A. Analytical Methods. In *Human pharmaceuticals, hormones and fragrances. The challenge of micropollutants in urban water management*; 2006; pp 55–105.
- (8) Jámbo, A.; Molnár-Perl, I. Amino Acid Analysis by High-Performance Liquid Chromatography after Derivatization with 9-Fluorenylmethyloxycarbonyl Chloride. *Journal of Chromatography A* **2009**, *1216* (15), 3064–3077. <https://doi.org/10.1016/j.chroma.2009.01.068>.
- (9) Muñoz, F.; Mvula, E.; Braslavsky, S. E.; von Sonntag, C. Singlet Dioxygen Formation in Ozone Reactions in Aqueous Solution. *Journal of the Chemical Society, Perkin Transactions 2* **2001**, No. 7, 1109–1116. <https://doi.org/10.1039/b101230o>.
- (10) Lipari, F.; Swarin, S. J. Determination of Formaldehyde and Other Aldehydes in Automobile Exhaust with an Improved 2, 4-Dinitrophenylhydrazine Method. *Journal of Chromatography A* **1982**, *247* (2), 297–306.
- (11) Flyunt, R.; Leitzke, A.; Mark, G.; Mvula, E.; Reisz, E.; Schick, R.; von Sonntag, C. Determination of $\bullet\text{OH}$, $\text{O}_2\bullet^-$, and Hydroperoxide Yields in Ozone Reactions in Aqueous Solution. *The Journal of Physical Chemistry B* **2003**, *107* (30), 7242–7253. <https://doi.org/10.1021/jp022455b>.
- (12) Tentscher, P. R.; Bourgin, M.; von Gunten, U. Ozonation of *Para*-Substituted Phenolic Compounds Yields *p*-Benzoquinones, Other Cyclic α,β -Unsaturated Ketones, and Substituted Catechols. *Environmental Science & Technology* **2018**, *52* (8), 4763–4773. <https://doi.org/10.1021/acs.est.8b00011>.
- (13) Ali, S. A.; AlSbaiee, A.; Wazeer, M. I. M. Conformational Analysis and Inversion Process in Some Perhydrodipyrido[1,2-b;1'2'-e]-1,4,2,5-Dioxadiazines. *Journal of Physical Organic Chemistry* **2010**, *23* (6), 488–496. <https://doi.org/10.1002/poc.1627>.
- (14) Ali, S. A.; Wazeer, M. I. M. The Reactivities of Some Cyclic Nitrones in 1,3-Dipolar Cycloaddition Reactions. *J. CHEM. SOC. PERKIN TRANS. II* **1986**, 1789–1792.
- (15) Roca-López, D.; Tejero, T.; Caramella, P.; Merino, P. $[2n2\pi + 2n2\pi]$ Cycloadditions: An Alternative to Forbidden $[4\pi + 4\pi]$ Processes. The Case of Nitrone Dimerization. *Organic & Biomolecular Chemistry* **2014**, *12* (3), 517–525. <https://doi.org/10.1039/C3OB42014K>.
- (16) Thesing, J.; Mayer, H. Cyclische Nitrone I: Dimere 2.3.4.5-Tetrahydro-pyridin-N-oxyd. *Chemische Berichte* **1956**, *89* (9), 2159–2167. <https://doi.org/10.1002/cber.19560890919>.
- (17) Hoigné, J.; Bader, H.; Haag, W. R.; Staehelin, J. Rate Constants of Reactions of Ozone with Organic and Inorganic Compounds in Water—III. Inorganic Compounds and Radicals. *Water Research* **1985**, *19* (8), 993–1004. [https://doi.org/10.1016/0043-1354\(85\)90368-9](https://doi.org/10.1016/0043-1354(85)90368-9).
- (18) Frisch, M. J.; Trucks, G. W.; Schlegel, H. B.; Scuseria, G. E.; Robb, M. A.; Cheeseman, J. R.; Scalmani, G.; Barone, V.; Petersson, G. A.; Nakatsuji, H.; et al. *Gaussian 09, Revision D.01*; Gaussian, Inc.: Wallingford CT, 2016.
- (19) Becke, A. D. Density-functional Thermochemistry. III. The Role of Exact Exchange. *The Journal of Chemical Physics* **1993**, *98* (7), 5648–5652. <https://doi.org/10.1063/1.464913>.
- (20) Montgomery, J. A.; Frisch, M. J.; Ochterski, J. W.; Petersson, G. A. A Complete Basis Set Model Chemistry. VI. Use of Density Functional Geometries and Frequencies. *The Journal of Chemical Physics* **1999**, *110* (6), 2822–2827. <https://doi.org/10.1063/1.477924>.
- (21) Papajak, E.; Zheng, J.; Xu, X.; Leverentz, H. R.; Truhlar, D. G. Perspectives on Basis Sets Beautiful: Seasonal Plantings of Diffuse Basis Functions. *Journal of Chemical Theory and Computation* **2011**, *7* (10), 3027–3034. <https://doi.org/10.1021/ct200106a>.
- (22) Raghavachari, K.; Trucks, G. W.; Pople, J. A.; Replogle, E. Highly Correlated Systems: Structure, Binding Energy and Harmonic Vibrational Frequencies of Ozone. *Chemical Physics Letters* **1989**, *158* (3–4), 207–212. [https://doi.org/10.1016/0009-2614\(89\)87322-1](https://doi.org/10.1016/0009-2614(89)87322-1).
- (23) Tentscher, P. R.; Arey, J. S. Geometries and Vibrational Frequencies of Small Radicals: Performance of Coupled Cluster and More Approximate Methods. *Journal of Chemical Theory and Computation* **2012**, *8* (6), 2165–2179. <https://doi.org/10.1021/ct300194x>.
- (24) Hariharan, P. C.; Pople, J. A. The Influence of Polarization Functions on Molecular Orbital Hydrogenation Energies. *Theoretica Chimica Acta* **1973**, *28* (3), 213–222. <https://doi.org/10.1007/BF00533485>.

- (25) Zhao, Y.; Truhlar, D. G. The M06 Suite of Density Functionals for Main Group Thermochemistry, Thermochemical Kinetics, Noncovalent Interactions, Excited States, and Transition Elements: Two New Functionals and Systematic Testing of Four M06-Class Functionals and 12 Other Functionals. *Theoretical Chemistry Accounts* **2008**, *120* (1), 215–241. <https://doi.org/10.1007/s00214-007-0310-x>.
- (26) Marenich, A. V.; Cramer, C. J.; Truhlar, D. G. Universal Solvation Model Based on Solute Electron Density and on a Continuum Model of the Solvent Defined by the Bulk Dielectric Constant and Atomic Surface Tensions. *The Journal of Physical Chemistry B* **2009**, *113* (18), 6378–6396. <https://doi.org/10.1021/jp810292n>.
- (27) Kelly, C. P.; Cramer, C. J.; Truhlar, D. G. Aqueous Solvation Free Energies of Ions and Ion–Water Clusters Based on an Accurate Value for the Absolute Aqueous Solvation Free Energy of the Proton. *The Journal of Physical Chemistry B* **2006**, *110* (32), 16066–16081. <https://doi.org/10.1021/jp063552y>.
- (28) Wheeler, S. E.; Ess, D. H.; Houk, K. N. Thinking Out of the Black Box: Accurate Barrier Heights of 1,3-Dipolar Cycloadditions of Ozone with Acetylene and Ethylene. *The Journal of Physical Chemistry A* **2008**, *112* (8), 1798–1807. <https://doi.org/10.1021/jp710104d>.
- (29) Zhao, Y.; Tishchenko, O.; Gour, J. R.; Li, W.; Lutz, J. J.; Piecuch, P.; Truhlar, D. G. Thermochemical Kinetics for Multi-reference Systems: Addition Reactions of Ozone. *The Journal of Physical Chemistry A* **2009**, *113* (19), 5786–5799. <https://doi.org/10.1021/jp811054n>.
- (30) Trogolo, D.; Arey, J. S.; Tentscher, P. R. Gas-Phase Ozone Reactions with a Structurally Diverse Set of Molecules: Barrier Heights and Reaction Energies Evaluated by Coupled Cluster and Density Functional Theory Calculations. *The Journal of Physical Chemistry A* **2019**. <https://doi.org/10.1021/acs.jpca.8b10323>.
- (31) Jonsson, M.; Wayner, D. D. M.; Luszytk, J. Redox and Acidity Properties of Alkyl- and Arylamine Radical Cations and the Corresponding Aminyl Radicals ¹. *The Journal of Physical Chemistry* **1996**, *100* (44), 17539–17543. <https://doi.org/10.1021/jp961286q>.
- (32) Wardman, P. Reduction Potentials of One-Electron Couples Involving Free Radicals in Aqueous Solution. *Journal of Physical and Chemical Reference Data* **1989**, *18* (4), 1637–1755. <https://doi.org/10.1063/1.555843>.
- (33) Bilski, P.; Motten, A. G.; Bilski, M.; Chignell, C. F. The Photooxidation of Diethylhydroxylamine by Rose Bengal in Micellar and Nonmicellar Aqueous Solutions. *Photochemistry and Photobiology* **1993**, *58* (1), 11–18. <https://doi.org/10.1111/j.1751-1097.1993.tb04896.x>.
- (34) Shaffer, D.; Heicklen, J. Oxidation of Diethylhydroxylamine in Water Solution at 25–80.Degree. *The Journal of Physical Chemistry* **1986**, *90* (18), 4408–4413. <https://doi.org/10.1021/j100409a039>.
- (35) Tomat, R.; Rigo, A.; Salmaso, R. Kinetic Study on the Reaction between O₂ and Hydroxylamine. *Journal of Electroanalytical Chemistry and Interfacial Electrochemistry* **1975**, *59* (3), 255–260. [https://doi.org/10.1016/S0022-0728\(75\)80180-X](https://doi.org/10.1016/S0022-0728(75)80180-X).
- (36) Ianni, J. C. *Kintecus*; 2017, Windows Version 6.01, www.kintecus.com.
- (37) Goldstein, S.; Samuni, A. Kinetics and Mechanism of Peroxyl Radical Reactions with Nitroxides. *The Journal of Physical Chemistry A* **2007**, *111* (6), 1066–1072. <https://doi.org/10.1021/jp0655975>.
- (38) Ingold, K. U.; Adamic, K.; Bowman, D. F.; Gillan, T. Kinetic Applications of Electron Paramagnetic Resonance Spectroscopy. I. Self-Reactions of Diethyl Nitroxide Radicals. *Journal of the American Chemical Society* **1971**, *93* (4), 902–908. <https://doi.org/10.1021/ja00733a018>.
- (39) Berger, P.; Karpel Vel Leitner, N.; Doré, M.; Legube, B. Ozone and Hydroxyl Radicals Induced Oxidation of Glycine. *Water Research* **1999**, *33* (2), 433–441. [https://doi.org/10.1016/S0043-1354\(98\)00230-9](https://doi.org/10.1016/S0043-1354(98)00230-9).
- (40) McCurry, D. L.; Quay, A. N.; Mitch, W. A. Ozone Promotes Chloropicrin Formation by Oxidizing Amines to Nitro Compounds. *Environmental Science & Technology* **2016**, *50* (3), 1209–1217. <https://doi.org/10.1021/acs.est.5b04282>.

Chapter 3 Reactions of pyrrole, imidazole, and pyrazole with ozone: Kinetics and mechanisms

A. Tekle-Röttering,¹ S. Lim,¹ E. Reisz, H. V. Lutze, M. S. Abdighahroudi, S. Willach, W. Schmidt, P. R. Tentscher, D. Rentsch, C. S. McArdell, T. C. Schmidt, and U. von Gunten, In preparation for submission to *Environmental Science: Water Research & Technology*.

¹Co-primary authors equally contributed to this work

Sungeun Lim contributed to conducting kinetics experiments (except for pyrrole and imidazole), conducting ozonation experiments, identifying ozonation products with MS methods, quantifying singlet oxygen, compiling all data obtained by different laboratories, and writing the manuscript.

Abstract

Five-membered nitrogen-containing heterocyclic compounds (azoles) belong to potential moieties in complex structures where transformation occurs during ozonation. This study focused on the azole-ozone chemistry of pyrrole, imidazole, and pyrazole as model compounds. Reaction kinetics and ozonation products were determined by kinetic and analytical methods including NMR, LC-HRMS/MS, HPLC-UV, and IC-MS. Analyses of reactive oxygen species ($^1\text{O}_2$, $\cdot\text{OH}$, H_2O_2), quantum chemical computations (Gibbs energies), and kinetic simulations were used to further support the proposed reaction mechanisms. The species-specific second-order rate constants for the reactions of ozone with pyrrole and imidazole were $(1.4 \pm 1.1) \times 10^6 \text{ M}^{-1} \text{ s}^{-1}$ and $(2.3 \pm 0.1) \times 10^5 \text{ M}^{-1} \text{ s}^{-1}$, respectively. Pyrazole reacted more slowly with ozone at pH 7 ($k_{\text{app}} = (5.6 \pm 0.9) \times 10^1 \text{ M}^{-1} \text{ s}^{-1}$). Maleimide was an identified product of pyrrole, with a 34% yield per transformed pyrrole. Together with other products, formate, formamide, and glyoxal, C and N mass balances of $\sim 50\%$ were achieved. Imidazole reacted with ozone to cyanate, formamide, and formate ($\sim 100\%$ yields per transformed imidazole, respectively) with a closed mass balance. For pyrazole, a high ozone:pyrazole molar stoichiometry of 4.6 was found, suggesting the transformation products contributed to the over-stoichiometric consumption of ozone (e.g., hydroxypyrazoles). Glyoxal and formate were the only identified transformation products (C mass balance: 65%). Overall, the identified major products are suspected to hydrolyze and/or biodegraded and thereby abated by a biological post-treatment typically following ozonation. However, as subunits of more complex compounds (e.g., micropollutants), they might be more persistent during the post-treatment.

3.1 Introduction

Micropollutants are ubiquitously present in the aquatic environment.^{1,2} Although micropollutants are present in surface waters only in the $\mu\text{g L}^{-1}$ to ng L^{-1} range, they may be harmful to the aquatic ecosystem and/or pose a potential risk to human health through contamination of drinking water.³ Ozonation has been proven to successfully abate micropollutants in drinking waters and wastewater effluents.^{4–7} During ozonation, micropollutants are not mineralized but converted to transformation products. Often, biologically active micropollutants lose their effects upon transformation during ozonation,^{8–11} however in some cases, transformation products with higher toxicity than their parent compounds were formed.^{12–16} To predict the transformation products and assess their toxicities upon ozonation, a detailed knowledge of ozone reaction mechanisms is needed. To this end, several compilations of known reaction pathways are available,^{17,18} which recently resulted in an ozone pathway prediction tool.¹⁹ Many well-known ozone-reactive groups, such as phenols, olefins and nitrogen-containing moieties are commonly found as structural units of micropollutants. Several studies were carried out to understand ozone-nitrogen interactions for primary, secondary and tertiary amines and anilines.^{18,20,21} Information is also available for some heterocyclic amines such as *N*-heterocyclic aromatics, piperidine, piperazine, and morpholine.^{22–24} Nevertheless, there is still lack of information on the reactivity and/or transformation reactions of five-membered nitrogen-containing heterocyclic compounds (or azoles) such as pyrrole, imidazole, and pyrazole (Figure 3.1), which are commonly present in natural and synthetic organic compounds. Essential amino acids, histidine and tryptophan, contain an imidazole or a fused pyrrole moiety, respectively.²⁵ The nucleobases, adenine and guanine, contain a fused imidazole moiety, as part of the DNA.²⁵ Naturally occurring pigments, chlorophyll a (green pigments in plant) and heme (red pigments in blood) contain four pyrrole units which jointly form a larger ring system that complexes metal ions in the center.²⁵ Azoles are also of great significance as synthetic compounds. They have been widely used as core units of pharmaceuticals, pesticides, dyes, plastics, etc.^{26–28}

Because of their widespread occurrences and numerous applications in medical and material sciences, azoles are likely to be present in municipal and industrial wastewaters. Among more than 500 environmentally relevant micropollutants for municipal wastewaters,⁷ approximately 50% are heterocyclic compounds and about 20% of the heterocycles contain pyrrole, imidazole, or pyrazole moieties, based on our assessment. Ionic liquids, considered as promising replacements for traditional organic solvents, contain cationic head groups such as imidazolium. They have received an increasing attention as emerging contaminants in the aquatic environment because of their chemical and thermal stability and high solubility in water.^{29,30} Pyrazole has recently been detected in the rivers Meuse and Rhine with exceptionally high concentrations ($\sim 100 \mu\text{g L}^{-1}$).³¹ The source was identified to be industrial processes related to acrylonitrile synthesis which produces pyrazole as a by-product.

Recently, haloazoles, azoles substituted with one or more halogen atoms, have been identified as a new class of disinfection byproducts.³⁰ Tribromopyrroles were detected during chlorine disinfection of drinking water and wastewater containing high bromide levels.^{32,33} 2,3,5-tribromopyrrole was found to be a strong cytotoxin and genotoxin in mammalian cells.³² Tetrapyrroles, metabolites of the above-mentioned natural pigments, were suggested to be precursors.³³ Tri- and di-bromo-1-methylimidazoles were detected in swimming pool and spa waters treated by bromine.³⁴ Histidine introduced by urine, sweat, and personal care products containing an imidazole moiety was proposed as a possible precursor.

Despite the importance of understanding the fate of azoles in water and wastewater treatment, only limited information is available regarding the kinetics and mechanisms of their reactions with oxidants and in particular with ozone. Early investigations on the oxidation of azoles, which date back to the 1960s, were mostly carried out in organic solvents.^{35–38} More recently, six-membered heterocyclic amines, such as pyridine, pyridazine, pyrimidine and pyrazine were thoroughly investigated in terms of their reactions with ozone in aqueous solution.²³ They were found to react slowly with ozone with second-order rate constants $< 10^2 \text{ M}^{-1} \text{ s}^{-1}$.²³ On the contrary, imidazole and histidine showed very high reactivity towards ozone with second-order rate constants $> 10^5 \text{ M}^{-1} \text{ s}^{-1}$.³⁹ This implies that different reaction mechanisms are involved in the reactions of ozone with five-membered heterocyclic amines in comparison to the six-membered ones.

In this study the kinetics and mechanisms of the reactions of five-membered heterocycles, i.e., pyrrole, imidazole, and pyrazole with ozone were investigated (Figure 3.1). The second-order rate constants of the reactions of azoles with ozone were determined by competition kinetics with 3-buten-2-ol as a competitor or by direct monitoring of the ozone decrease. Transformation products formed during the azole-ozone reactions were identified by nuclear magnetic resonance (NMR), liquid chromatography coupled with high resolution tandem mass spectrometry (LC-HRMS/MS), ion chromatography coupled with conductivity detection (IC-CD) or mass spectrometry (IC-MS), and high performance liquid chromatography coupled with UV detection (HPLC-UV). Additionally, reactive oxygen species including singlet oxygen, hydroxyl radical, and hydrogen peroxide were quantified. Finally, kinetic simulations and quantum chemical computations were conducted to obtain additional mechanistic insights. The combination of the results of all these methods and approaches were used to derive reaction mechanisms of the azole-ozone reactions.

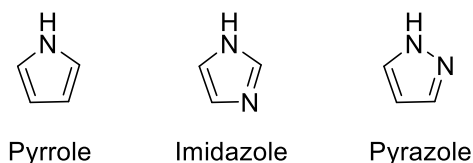


Figure 3.1. Azole model compounds investigated in this study: Chemical structures of pyrrole, imidazole, and pyrazole.

3.2 Material and methods

Chemical reagents. A list of water and chemicals used in this study is shown in Supporting Information (SI) for Chapter 3, Table S3.1.

Ozone reaction kinetics. All the applied kinetic methods are described in Text S3.1 and examples of competition kinetic and pseudo-first-order kinetic plots are shown in Figure S3.1. With the determined k_{app} , kinetic simulations were performed by the Kintecus software⁴⁰ based on the models described in Text S3.2. Apparent second-order rate constants (k_{app}) for the reactions of pyrrole and imidazole with ozone in the pH range 0.5 to 12 were determined by a competition kinetic method with 3-buten-2-ol as a competitor.⁴¹ k_{app} for the reaction of pyrazole with ozone at pH 7 was determined by following the pyrazole decrease by HPLC-UV under pseudo-first-order conditions of excess ozone. Additionally, k_{app} for the reactions of maleimide and 4-hydroxypyrazole (an identified and a suspected transformation product, respectively) with ozone at pH 7 were determined by following the ozone decrease by measurement with indigo-trisulfonate⁴² under pseudo-first-order conditions of excess sub-

strate. All kinetic experiments were carried out in presence of dimethylsulfoxide (DMSO) or *t*-butanol, as $\cdot\text{OH}$ scavengers.

Ozonation experiments for target compounds abatement and determination of transformation products. The required initial concentrations of azoles and ozone varied depending on subsequent analyses for product identification. Accordingly, various ozonation conditions were applied in this study and are described in detail in Text S3.3. For most analyses including LC-HRMS/MS and IC-CD, ozonation experiments were conducted by preparing approximately 100 μM of azole and 50 mM of *t*-butanol ($\cdot\text{OH}$ scavenger) in 10 mM phosphate buffer solution at pH 7 with a total volume of 10 mL. Ozone stock solutions were prepared by sparging ice-cooled water with ozone-containing oxygen.⁴² The concentrations of ozone (typically 1.4 mM – 1.6 mM) were determined spectrophotometrically with $\epsilon_{260\text{nm}} = 3200 \text{ M}^{-1} \text{ cm}^{-1}$.¹⁸ Aliquots of the ozone stock solution were added to the azole solutions under rapid stirring to initiate ozone reactions with ozone doses ranging from 0 to 200 μM . Ozonated solutions were left at room temperature for 4 – 6 hours to ensure complete consumption of ozone and stored at 4 °C prior to further analyses carried out within a week. For HPLC-UV quantifying formamide, higher concentrations of azoles and ozone were applied (Text S3.3(b)). For NMR identifying products from the pyrrole-ozone solution, ozone-containing oxygen-gas flow was directly sparged to the pyrrole solution (Text S3.3(d)). Some experiments were conducted in ultrapurified water without buffering agents (Texts S3.3(c) and S3.3(d)), which resulted in significant differences in pH before and after ozonation (differed by maximum 2 pH units). Under such conditions, ozone reactivity of azoles and their transformation products might change over the course of the reaction, especially for dissociating compounds, and thus the evolution of products might be different from the results obtained under buffered conditions.

Analytical methods. *N*-(3-oxo-1-propen-1-yl)formamide (TP1), 5-Hydroxy-1,5-dihydro-2H-pyrrol-2-one (TP2), and maleimide were identified by NMR. Pyrrole, imidazole, pyrazole, 1-benzylimidazole, 1-benzylpyrazole, maleimide, urea, and *N*-benzylformamide were analyzed by LC-HRMS/MS. Cyanate was analyzed by IC-CD as well as IC-MS. Formate was analyzed by IC-CD. Formamide was analyzed by HPLC-UV as well as GC-MS. Total *N*-nitrosamines were analyzed by a UV-photolysis-chemiluminescence system.⁴³ Glyoxal was analyzed by a derivatization method using *o*-phenyldiamine and the derivatized product, quinoxaline, was determined by HPLC-UV.⁴⁴ Singlet oxygen ($^1\text{O}_2$) was quantified by detecting the phosphorescence emitted by $^1\text{O}_2$ at 1270 nm by a near-infrared photomultiplier tube.²⁰ Hydroxyl radicals ($\cdot\text{OH}$) were quantified by using the $\cdot\text{OH}$ quencher *t*-butanol. Formaldehyde, a product of the reaction of *t*-butanol with $\cdot\text{OH}$ with a reported yield of ~50%,⁴⁵ was quantified by the Hantzsch method.⁴⁶ Formaldehyde formed during the reaction of pyrazole with ozone was taken into account for calculating its $\cdot\text{OH}$ yield. For pyrrole and imidazole, formaldehyde formation from the direct ozone reactions was minimal and thus disregarded. Hydrogen peroxide (H_2O_2) was quantified spectrophotometrically with Allen's reagent (molybdate-activated iodide).^{47,48} More details on the methods are provided in Texts S3.4 and S3.5, Figures S3.3 to S3.10, Tables S3.5 to S3.7. The limit of quantifications (LOQ) and precisions of the methods are summarized in Table S3.6.

Quantum chemical computations. All computations were performed with Gaussian09 vD.01.⁴⁹ The thermodynamic feasibility of the proposed reactions was tested with free energy calculations, along with the connectivity of intermediates on the potential energy surface.⁵⁰ The LC- ω PBE⁵¹ functional was chosen for the description of the initial ozone reactivity⁵² and for its generally sound description of the thermochemistry.⁵¹ The SMD implicit solvation model was used.⁵³ Free energy differences are reported with respect to the isolated molecules, ozone and an azole. Details are given in Text S3.6.

3.3 Results and discussion

3.3.1 Ozone reaction kinetics

Apparent second-order rate constants (k_{app}) for the reactions of ozone with pyrrole, imidazole, and pyrazole show that pyrrole and imidazole react fast with ozone with $k_{\text{app}} > 10^3 \text{ M}^{-1} \text{ s}^{-1}$ for pH 0.5 – 12 and pyrazole reacts moderately fast with $k_{\text{app}} = (5.6 \pm 0.9) \times 10^1 \text{ M}^{-1} \text{ s}^{-1}$ at pH 7 (Table 3.1, Table S3.2). k_{app} of pyrrole was hardly affected by pH (Figure S3.2), with averaged k_{app} of $(1.4 \pm 1.1) \times 10^6 \text{ M}^{-1} \text{ s}^{-1}$. k_{app} of imidazole changed over two orders of magnitude in the pH range 2 – 12. This is due to the acid-base speciation of imidazole with a $\text{p}K_{\text{a}}$ of 7.0, which lies in the investigated pH range where pyrrole is present as a neutral species⁵⁴ (note that generally deprotonated species react faster with ozone than protonated ones).¹⁸ The determined k_{app} values of imidazole were fitted by the expression $k_{\text{app}} = k_{\text{NH}^+}(1-\alpha) + k_{\text{N}}\alpha$ and $\alpha = 1/(1 + 10^{\text{p}K_{\text{a}}-\text{pH}})$ (Figure S3.2). k_{NH^+} and k_{N} are the species-specific second-order rate constants for the reactions of ozone with the protonated and the neutral imidazole, respectively, and α is the fraction of the neutral imidazole. Based on this approach, the species-specific second-order rate constant for the reaction of ozone with the neutral imidazole was determined to be $(2.3 \pm 0.1) \times 10^5 \text{ M}^{-1} \text{ s}^{-1}$ (Table 3.1), identical to the previously reported value of $2.4 \times 10^5 \text{ M}^{-1} \text{ s}^{-1}$.³⁹ The species-specific second-order rate constant for the protonated imidazole is $(1.5 \pm 0.1) \times 10^3 \text{ M}^{-1} \text{ s}^{-1}$ (Table 3.1). The k_{app} values determined in absence of an $\cdot\text{OH}$ scavenger were similar to those determined in presence of an $\cdot\text{OH}$ scavenger (Table S3.2). Maleimide, an identified product of the pyrrole-ozone reaction, reacts fast with ozone with $k_{\text{app}} = (4.2 \pm 0.2) \times 10^3 \text{ M}^{-1} \text{ s}^{-1}$ at pH 7. The moderate to high ozone reactivity of azoles is especially remarkable when compared to six-membered heterocyclic amines such as pyridine, pyrazine, and pyridazine with second-order rate constants for the reactions with ozone of $< 2 \text{ M}^{-1} \text{ s}^{-1}$.²³ The high ozone reactivity of pyrrole probably relates to the effect of the nitrogen atom in the π -aromatic system, which increases the electron density of the ring.²⁵ Consequently, ozone reacts faster with pyrrole than with typical, unsubstituted aromatic rings, e.g., benzene, of which $k_{\text{O}_3} = 2 \text{ M}^{-1} \text{ s}^{-1}$.⁵⁵ In contrast, the nitrogen in pyridine withdraws the electron density from the ring,²⁵ rendering the nitrogen more susceptible to the ozone attack, rather than the ring. This agrees with the high yield of pyridine *N*-oxide determined after ozonation.²³ Interestingly, these reactions show much lower kinetics than reactions of tertiary amines with ozone (typical $k_{\text{O}_3} \geq 10^6 \text{ M}^{-1} \text{ s}^{-1}$),^{20,56} which also form *N*-oxides as major products.

Table 3.1. Species-specific second-order rate constants (k) and apparent second-order rate constants at pH 7 ($k_{\text{app, pH7}}$) for the reactions of ozone with pyrrole, imidazole, pyrazole, maleimide, and 4-hydroxypyrazole. Reaction kinetics were determined in presence of $\cdot\text{OH}$ scavenger (DMSO or *t*-butanol) by competition kinetics with 3-buten-2-ol as a competitor or by direct monitoring of ozone or substrate decrease over time (Text S3.1).

Compound	pK _a ^a	pH ^b	k , M ⁻¹ s ⁻¹	$k_{\text{app, pH7}}$, M ⁻¹ s ⁻¹	Reference
Pyrrole	-3.8	0.5 – 12	$(1.4 \pm 1.1) \times 10^6$ ^c	$(8.6 \pm 0.7) \times 10^5$	This study
Imidazole	7.0	2 – 12	$(2.3 \pm 0.1) \times 10^5$ (as k_{N}) ^d	$(1.7 \pm 0.2) \times 10^5$	This study
			$(1.5 \pm 0.1) \times 10^3$ (as k_{NH^+}) ^d		This study
			2.4×10^5 (as k_{N})		39
			2.1×10^2 (as k_{NH^+})		39
Pyrazole	2.5	7	ND	$(5.6 \pm 0.9) \times 10^1$	This study
Maleimide	9.5	7	ND	$(4.2 \pm 0.2) \times 10^3$	This study
4-Hydroxypyrazole	NA	7	ND	$> 9 \times 10^4$ ^e	This study

^a pK_a values were from ⁵⁴ and ⁸⁴; ^b experimental pH range; ^c obtained by averaging k_{app} for the pH range 0.5 – 12 (Table S3.2); ^d obtained by fitting k_{app} for the pH range 2 – 12 with the expression $k_{\text{app}} = k_{\text{NH}^+}(1-\alpha) + k_{\text{N}}\alpha$ and $\alpha = 1/(1 + 10^{\text{pK}_a - \text{pH}})$ (dotted line in Figure S3.2). ^e See Text S3.1 for the estimation.

3.3.2 Reactive oxygen species

Reactive oxygen species (ROS) such as singlet oxygen ($^1\text{O}_2$), hydroxyl radical ($\cdot\text{OH}$), and hydrogen peroxide (H_2O_2) can be used to elucidate reaction mechanisms.¹⁸ In this study, they were quantified for the reactions of azoles with ozone with molar excess of azole relative to ozone ($[\text{azole}]_0/[\text{O}_3] > 1$) and the corresponding yields are summarized in Table 3.2. The ROS yields per consumed ozone ($\Delta[\text{ROS}]/\Delta[\text{O}_3]$) varied significantly for pyrrole, imidazole, and pyrazole. All measured data for $^1\text{O}_2$, $\cdot\text{OH}$, and H_2O_2 are summarized in Table S3.7, Figure S3.9, and Figure S3.10, respectively. Pyrrole produced mostly $^1\text{O}_2$ (11%) and H_2O_2 (7%) and only minor quantities of $\cdot\text{OH}$ (2%), whereas pyrazole produced mostly $\cdot\text{OH}$ (8%) and only traces of $^1\text{O}_2$ (2%) and H_2O_2 (2%). Imidazole showed almost no formation of any type of ROS (all $\leq 1\%$). The sum of all ROS yields per consumed ozone was only up to 20% for azoles, which is much smaller than 60% – 76%, the sum of the $^1\text{O}_2$ and $\cdot\text{OH}$ yields per consumed ozone determined for aliphatic amines.²⁰ The low ROS yields for the azole-ozone reactions are most likely due to reaction pathways, which do not form any ROS (see below). The ROS yields per consumed ozone were also multiplied by the ozone:azole molar stoichiometry to calculate the ROS yields per consumed azole ($\Delta[\text{ROS}]/\Delta[\text{Azole}]$) (Table 3.2). These yields will be compared with the yields of the formed transformation products below.

Table 3.2. Reaction stoichiometry, reactive oxygen species (ROS) yields, and transformation product yields for the reactions of pyrrole, imidazole, 1-benzylimidazole, pyrazole, and 1-benzylpyrazole with ozone at pH 7.0 – 7.6 in presence of *t*-butanol. The yields are expressed relative to the ozone consumption ($\Delta[X]/\Delta[O_3]$) or relative to the azole consumption ($\Delta[X]/\Delta[Azole]$). $\Delta[X]/\Delta[N]$ and $\Delta[X]/\Delta[C]$ are the yields per nitrogen and per carbon, respectively, obtained by comparing the numbers of nitrogen and carbon of the products with those of the parent azole compounds.

Azole	Product (X)	X type ^a	Ozone:azole molar stoichiometry ^b	$\Delta[X]/\Delta[O_3]^c$	$\Delta[X]/\Delta[Azole]^d$	$\Delta[X]/\Delta[N]^e$	$\Delta[X]/\Delta[C]^e$
Pyrrole	•OH	ROS	1.2	2%	2%	-	-
	H ₂ O ₂	ROS	1.2	7%	8%	-	-
	¹ O ₂	ROS	1.2	11%	13%	-	-
	Maleimide	TP_N	1.2	29%	34%	34%	34%
	Formamide	TP_N	1.2	12%	14%	14%	3.5%
	Formate	TP_C	1.2	46%	54%	0%	14%
	Glyoxal	TP_C	1.2	4%	5%	0%	2.5%
	Total^f					48%	54%
Imidazole	•OH	ROS	1.0	1%	1%	-	-
	H ₂ O ₂	ROS	1.0	0.2%	0.1%	-	-
	¹ O ₂	ROS	1.0	0.1%	0.1%	-	-
	Formamide	TP_N	1.0	105%	104%	52%	35%
	Cyanate	TP_N	1.0	114%	113%	57%	38%
	Formate	TP_C	1.0	98%	97%	0%	32%
	Glyoxal	TP_C	1.0	< LD	< LD	< LD	< LD
	Total^f					109%	105%
1-Benzylimidazole	<i>N</i> -Benzylformamide	TP_N	1.0	93%	91%	46%	30%
Pyrazole	•OH	ROS	4.6	8%	35%	-	-
	H ₂ O ₂	ROS	4.6	2%	7%	-	-
	¹ O ₂	ROS	4.6	2%	8%	-	-
	Formamide	TP_N	4.6	< LD	< LD	< LD	< LD
	Nitrosamines	TP_N	4.6	< LD	< LD	< LD	< LD
	Formate	TP_C	4.6	28%	126%	0%	42%
	Glyoxal	TP_C	4.6	7%	34%	0%	23%
	Total^f					0%	65%
1-Benzylpyrazole	<i>N</i> -Benzylformamide	TP_N	6.5	1%	9%	5%	3%

^a ROS, TP_N, and TP_C represent reactive oxygen species, nitrogenous transformation products, and carbonaceous transformation products, respectively, ^b Ozone:azole molar stoichiometry values were obtained by inverting the slopes from the linear regression of the measured concentrations and taking the absolute values (Figure S3.11); ^c For •OH, H₂O₂, maleimide, formate, glyoxal, cyanate, and *N*-benzylformamide, the yields per consumed ozone were determined by slopes from the linear regression of the measured concentrations at molar ratios of $[O_3]/[Azole]_0 \leq 1$. For ¹O₂, the yields were averaged for 6 replicates at a fixed molar ratio of $[O_3]/[Azole]_0 = 0.03 - 0.04$. For formamide, the yields were averaged for duplicate experiments at fixed molar ratios of $[O_3]/[Azole]_0 = 2.0$ for pyrrole-ozone reaction and at $[O_3]/[Azole] = 0.4$ and 0.8 for imidazole-ozone reaction; ^d Yields per consumed azoles were calculated by multiplying yields per ozone ($\Delta[X]/\Delta[O_3]$) by the ozone:azole molar stoichiometry. ^e Yields per nitrogen (or carbon) were calculated by multiplying the number of nitrogen (or carbon) of the product and dividing the number of nitrogen (or carbon) of the azole, with the yields per abated azole. ^f Total represents nitrogen or carbon mass balance.

3.3.3 Transformation products and reaction pathways

Reaction pathways of the azole-ozone reactions were investigated by identifying transformation products and taking into consideration the formation of ROS. Quantum chemical computations for Gibbs energies of reaction pathways were additionally performed to elucidate the plausibility of the proposed mechanisms.

3.3.3.1 Pyrrole-ozone reaction

Quantified products. To identify transformation products from the pyrrole-ozone reaction, pyrrole was oxidized by ozone in presence of *t*-butanol as a $\cdot\text{OH}$ scavenger mostly at pH 7 (10 mM phosphate buffer) except for the samples prepared for NMR analysis and for glyoxal determination (no buffer, Text S3.3). Figure 3.2 shows the abatement of pyrrole as a function of the molar ozone:pyrrole ratio (initial concentrations) ($[\text{O}_3]/[\text{Pyrrole}]_0$). The ozonated pyrrole samples were analyzed by various methods including NMR, LC-HRMS/MS, HPLC-UV, and IC-CD. Based on the combination of these analyses, the formation of six transformation products were confirmed: *N*-(3-oxo-1-propen-1-yl)formamide (TP1, hereafter), 5-hydroxy-1,5-dihydro-2H-pyrrol-2-one (TP2, hereafter), maleimide, formamide, formate, and glyoxal (for chemical structures see Figure 3.3). Maleimide, formamide, formate, and glyoxal for which reference standards are available, were quantified at varying ozone doses. The formation trends are shown in Figure 3.2 and the product yields are summarized in Table 3.2. Product concentrations in Figure 3.2 are expressed as pyrrole-normalized relative product concentrations, because the initial pyrrole concentrations were different for the various analytical methods. The stoichiometry for the reaction of ozone with pyrrole was calculated by the slope from a linear regression of the pyrrole concentrations measured with substoichiometric doses of ozone ($[\text{O}_3]/[\text{Pyrrole}]_0 < 1$). The fitting results for pyrrole as well as other azoles are shown in Figure S3.11. Pyrrole decreased with an ozone:pyrrole molar stoichiometry of 1.2, close to 1. Maleimide was gradually formed with a yield of 34% per consumed pyrrole up to about one molar equivalent of ozone ($[\text{O}_3]/[\text{Pyrrole}]_0 = 1$) and then decreased at higher molar ratios of $[\text{O}_3]/[\text{Pyrrole}]_0$. The concentrations of pyrrole and maleimide were predicted by a kinetic simulation by the Kintecus software,⁴⁰ with measured apparent second-order rate constants for the reactions with ozone at pH 7 ($8.6 \times 10^5 \text{ M}^{-1} \text{ s}^{-1}$ and $4.2 \times 10^3 \text{ M}^{-1} \text{ s}^{-1}$ for pyrrole and maleimide, respectively, Table 3.1). The model includes the stoichiometric coefficient for maleimide formation of 0.34, based on the measured maleimide yield (Table S3.3). The predicted concentrations are shown as lines in Figure 3.2 and agree well with the measured data. Formamide was formed with a yield of 14% per consumed pyrrole at a ratio of $[\text{O}_3]/[\text{Pyrrole}]_0 = 2$. It was not possible to quantify formamide at lower molar ratios of $[\text{O}_3]/[\text{Pyrrole}]_0$ of 1.1 and 0.8, because of an interference of neighboring peaks in the HPLC-UV method. Formate shows a gradual formation over the entire range of molar ratios of $[\text{O}_3]/[\text{Pyrrole}]_0$ with a yield of 54% per consumed pyrrole. Glyoxal was quantified as a minor product with a yield of 5% per consumed pyrrole. The product yields per consumed pyrrole can be further assessed in terms of nitrogen or carbon mass balances. For example, the yield of formamide was 14% per consumed pyrrole, which corresponds to 3.5% per carbon, as formamide contains only $\frac{1}{4}$ of carbons in comparison to pyrrole. The yields of other products were converted likewise, and the sum of the yields per nitrogen and per carbon for all products were 48% and 54%, respectively (Table 3.2). This means about half of nitrogen and carbon mass balances were completed based on the quantified products. Product yields determined under the different pH conditions (pH 2 and 11) are summarized in Figure S3.12 and Table S3.8. Maleimide was formed with similar yields at pH 2 and 7. Formate was formed with a higher yield at pH 11. This may indicate that the reaction proceeds differently at higher pH, but further investigations are needed to confirm this.

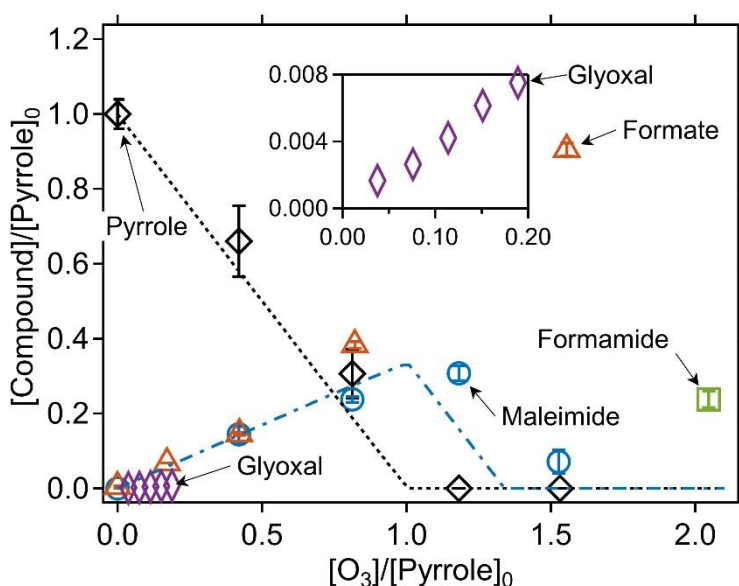


Figure 3.2. Relative abatement of pyrrole and the formation (and consumption) of transformation products as a function of the molar ratio of $[O_3]/[Pyrrole]_0$. The inset has the same axis labels as the main figure. The symbols indicate the measured concentrations (single measurement for glyoxal and duplicate/triplicate for everything else) and the lines indicate simulated concentrations based on the kinetic models described in Table S3.3. All measurements were carried out in presence of *t*-butanol (0.05 – 0.5 M). 10 mM phosphate buffer was used for all measurements but glyoxal. The initial pyrrole concentrations were around 110 μ M for determining pyrrole, maleimide, and formate, 0.8 mM – 2.0 mM for determining formamide, and 1 mM for determining glyoxal (Text S3.3).

Identified but not quantified products. The formation of TP1, TP2, and maleimide were qualitatively confirmed by NMR (Text S3.7). Assignments of 1H and ^{13}C NMR data of TP1, TP2, and maleimide are summarized in Table S3.9 and the recorded NMR spectra are shown in Figures S3.14 to S3.17. Because of the lack of reference standards, quantification of TP1 and TP2 was not possible. Moreover, the isolated solid from the ozonated pyrrole sample was not fully dissolvable in acetone- d_6 (NMR solvent), hindering an estimation of the relative quantities of TP1 and TP2 based on the comparison of 1H signal intensities (Text S3.8). The NMR sample containing TP1 and TP2 was also analyzed by LC-HRMS/MS to additionally support their presence and identification. Both TPs have an exact mass of $m/z = 100.0393$ as $[M+H]^+$ (molecular formula of $C_4H_5NO_2$) that showed up as two peaks at retention times of 4.2 min and 6.3 min ($C_4H_5NO_2_{4.2}$ and $C_4H_5NO_2_{6.3}$, Figure S3.18b) with distinct MS2 fragmentation patterns (Figure S3.19). $C_4H_5NO_2_{4.2}$ produced mostly a fragment ion of $m/z = 83.0125$, corresponding to $C_4H_2O_2$ (loss of NH_3), whereas $C_4H_5NO_2_{6.3}$ produced mostly $m/z = 72.0443$, corresponding to C_3H_5NO (loss of CO). TP1 with a carbonyl group at the end of the open-chain structure appears to be able to more readily release CO and form C_3H_5NO during fragmentation (Figure S3.20b) than TP2 with a cyclic structure (Figure S3.21b). In contrast, TP2 might more easily produce $C_4H_2O_2$ than TP1, because TP1 requires an intramolecular rearrangement to release NH_3 (Figure S3.21a for TP2 and Figures S3.20a for TP1). Examples of possible fragmentation pathways predicted by the mass spectra interpretation software (Mass Frontier™, Thermo Scientific) are illustrated in Figures S3.20 and S3.21. Based on the structural characteristics and the distinct MS2 fragmentation patterns, $C_4H_5NO_2_{4.2}$ and $C_4H_5NO_2_{6.3}$ are likely to correspond to TP2 and TP1, respectively.

The $C_4H_5NO_2_{4.2}$ and $C_4H_5NO_2_{6.3}$ peaks were not only observed in the sample prepared for NMR analysis but also in the samples with varying molar ratios of $[O_3]/[Pyrrole]_0$ during the pyrrole abatement and the maleimide formation (Figure 3.2). The integrated peak areas as a function of the molar ratios of $[O_3]/[Pyrrole]_0$ are plotted in Figure S3.22. Both peaks were gradually formed reaching a maximum formation at about one molar equivalent of ozone ($[O_3]/[Pyrrole]_0 = 1$) and decrease at higher ozone doses, similarly to maleimide (Figure 3.2). Con-

sidering the similar formation trends, TP1, TP2, and maleimide seem to be formed in parallel via different reaction pathways.

Unidentified products. A non-target screening with LC-HRMS/MS of the ozonated pyrrole samples revealed two additional peaks at retention times of 5.4 min and 7.0 min ($C_4H_5NO_{5.4}$ and $C_4H_5NO_{7.0}$, Figure S3.23a), which showed significant intensities for the ozonated pyrrole samples in comparison to the ozonated blank (no pyrrole) samples. Both peaks correspond to the exact mass of C_4H_5NO with a mass deviation of 3 ppm. 1,5-dihydropyrrole-one (see the structure in Figure S3.23b) was suspected, based on previous studies reporting it as an oxidation product of pyrrole.^{35,57} However, the reference standard, which is commercially available, resulted in too many peaks, probably due to the presence of impurities or isomers, which made it ambiguous to match the retention times (Figure S3.23b). The fragmentation patterns look similar for the ozonated pyrrole sample and the standard with the same fragment ion of $m/z = 56.0500$ (Figure S3.24).

The $C_4H_5NO_{5.4}$ and $C_4H_5NO_{7.0}$ peaks are plotted against the molar ratio of $[O_3]/[Pyrrole]_0$ (Figure S3.25). They were formed at a molar ratio of $[O_3]/[Pyrrole]_0$ of 0.5, followed by a gradual decrease, concurrent with the increase of $C_4H_5NO_2$ (Figure S3.26). This implies C_4H_5NO was formed at an earlier stage of the pyrrole-ozone reaction and could be a precursor of $C_4H_5NO_2$.

Initial reaction pathways. Based on the product identification, possible formation pathways for the transformation products formed during the reactions of pyrrole with ozone are proposed (Figure 3.3). Ozone initially attacks at a double bond of pyrrole via a Criegee-type mechanism (pathways A and B) or addition on C2-position (pathway C). Such concerted cycloadditions have been studied in depth for reactions of simple unsaturated hydrocarbons (e.g., ethene and ethyne) with ozone in aqueous phase by a recent quantum chemical study.⁵² The pyrrole-nitrogen is excluded as a possible attack site, because its lone electron pair is delocalized in the π -system of the ring. A recent study demonstrated that the addition of atomic oxygen on the pyrrole-N is very unlikely compared to the addition on C, based on quantum chemical computations of the energies of the corresponding products (+39 kcal mol⁻¹ for *N*-addition and -19 kcal mol⁻¹ for C2-addition).⁵⁸ Pathways A and B are cycloadditions of ozone to different positions of the ring. The ozone addition to the C2,C3-positions may lead to the ring-opened product, TP1, which could further degrade into formamide, formate, and glyoxal. In contrast, the addition to the C2,C5-positions could result in TP2 or maleimide. Besides cycloadditions, ozone can also attack at the C2 position to form a zwitterionic adduct (pathway C). The zwitterion can be rearranged to the C2,C3- or C2,C5-cycloadducts or follow other routes such as via cleavage of an O-O bond. The latter is discussed below in detail.

Addition of ozone to the C2,C5-positions of the five-membered ring was proposed for the reaction of furan with ozone.⁵⁹ Additionally, earlier studies which investigated the oxidation of substituted pyrroles with singlet oxygen suggested both C2,C3- and C2,C5-cycloadditions.^{60–62} These studies found the product with two oxygen atoms added to the C2,C5-positions (equivalent to TP2) and the ring-opened product (equivalent to TP1). Compounds containing a maleimide, formamide, or an epoxide moiety were also identified or hypothesized as minor products.^{61,62} The minor product containing a formamide moiety was presumably formed by subsequent degradation of the ring-opened product,⁶¹ which could also explain the formation of formamide as well as formate and glyoxal observed in our study.

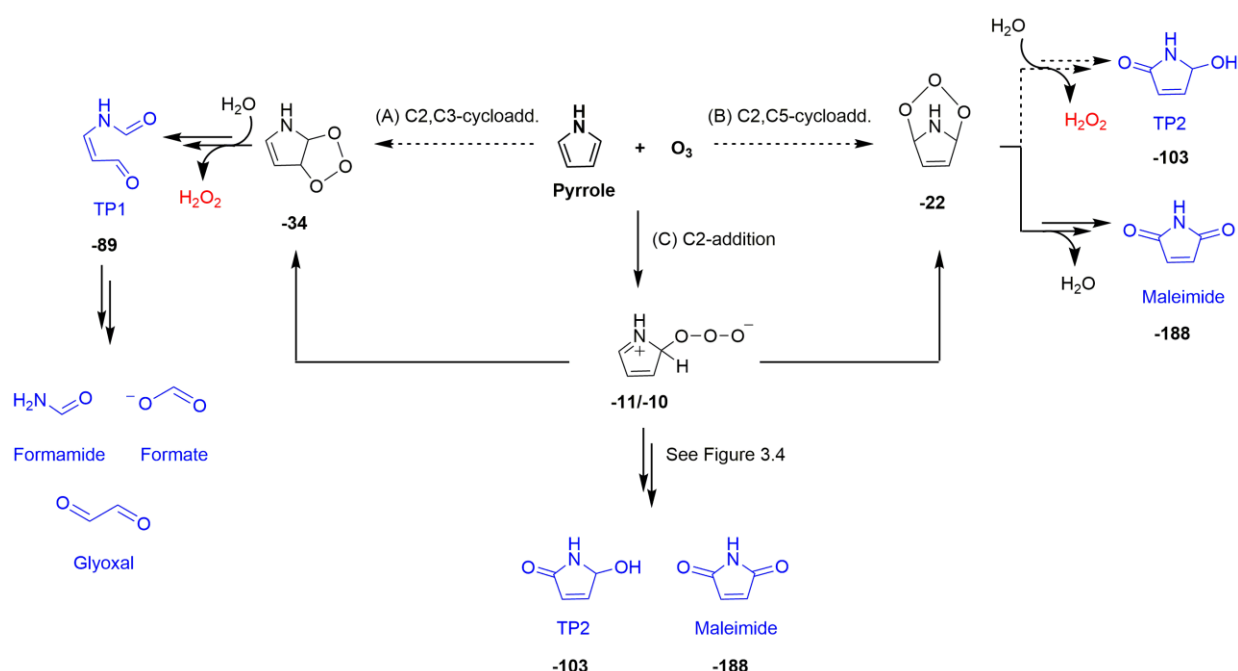


Figure 3.3. Initial reaction pathways (A, B, and C) proposed for the reaction of pyrrole with ozone based on the identified transformation products (highlighted in blue) and reactive oxygen species (in red). Bold numbers below the products and the intermediates are calculated Gibbs energies with respect to the initial reactants (pyrrole and ozone) in kcal mol⁻¹. Double arrows represent pathways involving more than one reaction step. Dashed arrows indicate that the transition structures have not been found or investigated during quantum chemical computations. The full descriptions of the initial reaction pathways including computed transition structures are shown in Figures S3.27, S3.28, and S3.29.

Quantum chemical computations. Additional evidences supporting the proposed pathways were obtained by quantum chemical computations of the energies of the products and their transition structures. All initial pathways (A, B, and C) are exergonic reactions with -10 to -34 kcal mol⁻¹ for the calculated energies of the products with respect to the initial reactants, pyrrole and ozone (Figure 3.3 and more details in Figures S3.27, S3.28, and S3.29). However, our calculations found transition structures only for pathway C, but not for pathways A nor B (presented as dashed arrows in Figure 3.3). Even though this implies pathway C as the only plausible reaction, we cannot exclude the possibility of pathways A and B, because ozone is typically considered as a difficult molecule to be treated by quantum chemical computations.^{50,63,64} If the cycloaddition pathways A and B occur, pathway A seems more likely than pathway B, because the ring strain of the C2,C5-cycloadduct is probably more pronounced than that of the C2,C3-cycloadduct (Text S3.10). For pathway C and the rearrangement to the cycloadducts, transition structures were found between the zwitterion and the C2,C3-cycloadduct and between the zwitterion and C2,C5-cycloadduct (Figure S3.27). Once the cycloadducts are formed, further reactions to the identified products, TP1 or maleimide, are exergonic with defined transition structures (Figures S3.28 and S3.29). The reaction of the C2,C5-cycloadduct to form TP2 could not be assessed, because of lack of details about the corresponding reaction mechanism. The full assessment of the proposed initial reaction pathways on the basis of the computation results are summarized in Texts S3.10, S3.11, and S3.12).

Subsequent reactions from pathway C. The zwitterion, the initial product of pathway C, can undergo diverse subsequent reactions, with a cleavage of an O-O bond and production of ¹O₂, hydrogen peroxide anion, or hydroperoxyl radical as transient oxygen species (Figure 3.4). The cleavage of the O-O bond to form ¹O₂ would produce 2H-pyrrole-2-ol, an isomer of 1,5-dihydro-pyrrole-one with the molecular formula of C₄H₅NO, which could further react with ozone to produce TP2 and another ¹O₂ (pathway D). The formation of 1,5-dihydro-pyrrole-one

was confirmed by other studies during the oxidation of pyrrole with hydrogen peroxide.^{35,57} Our analyses suggest the formation of 1,5-dihydro-pyrrole-one by the detection of its exact mass by LC-HRMS, but could not clearly identify it (Figure S3.23). Pathways E and F involve a cleavage of the O-O bond associated with H-transfer from the C2 position of the ring to form a hydrogen peroxide anion and a cationic form of 2*H*-pyrrole-2-one. The ensuing ions can be recombined by two ways. First, the hydrogen peroxide anion can abstract H⁺ from N-H of the cation to form H₂O₂ and 2*H*-pyrrole-2-one (pathway E). The latter can react with water to form TP2. Second, the hydrogen peroxide anion can also attack the C5 position of the ring to eventually form maleimide (pathway F). Such recombinations seem to occur as cage reactions based on the minimal free energy barrier (Figure S3.31). The cleavage of the O-O bond can also occur homolytically by forming the hydroperoxyl radical (pathway G). The radical further reacts with the ring at the C5 position to form maleimide. The maleimide formation pathways forming hydrogen peroxide anion or the hydroperoxyl radical followed by its subsequent attack on the C5 position of the ring (pathways F and G) do not produce any reactive oxygen species. These pathways can explain the low total ROS yields of 23% measured per consumed pyrrole as the sum of •OH, ¹O₂, and H₂O₂ (Table 3.2). All pathways depicted in Figure 3.4 are thermodynamically feasible based on quantum chemical computations and the corresponding Gibbs energies are shown in bold numbers underneath the chemical structures (kcal mol⁻¹). Detailed discussion and results including transition structures for each pathway are presented in Texts S3.13, S3.14, and S3.15.

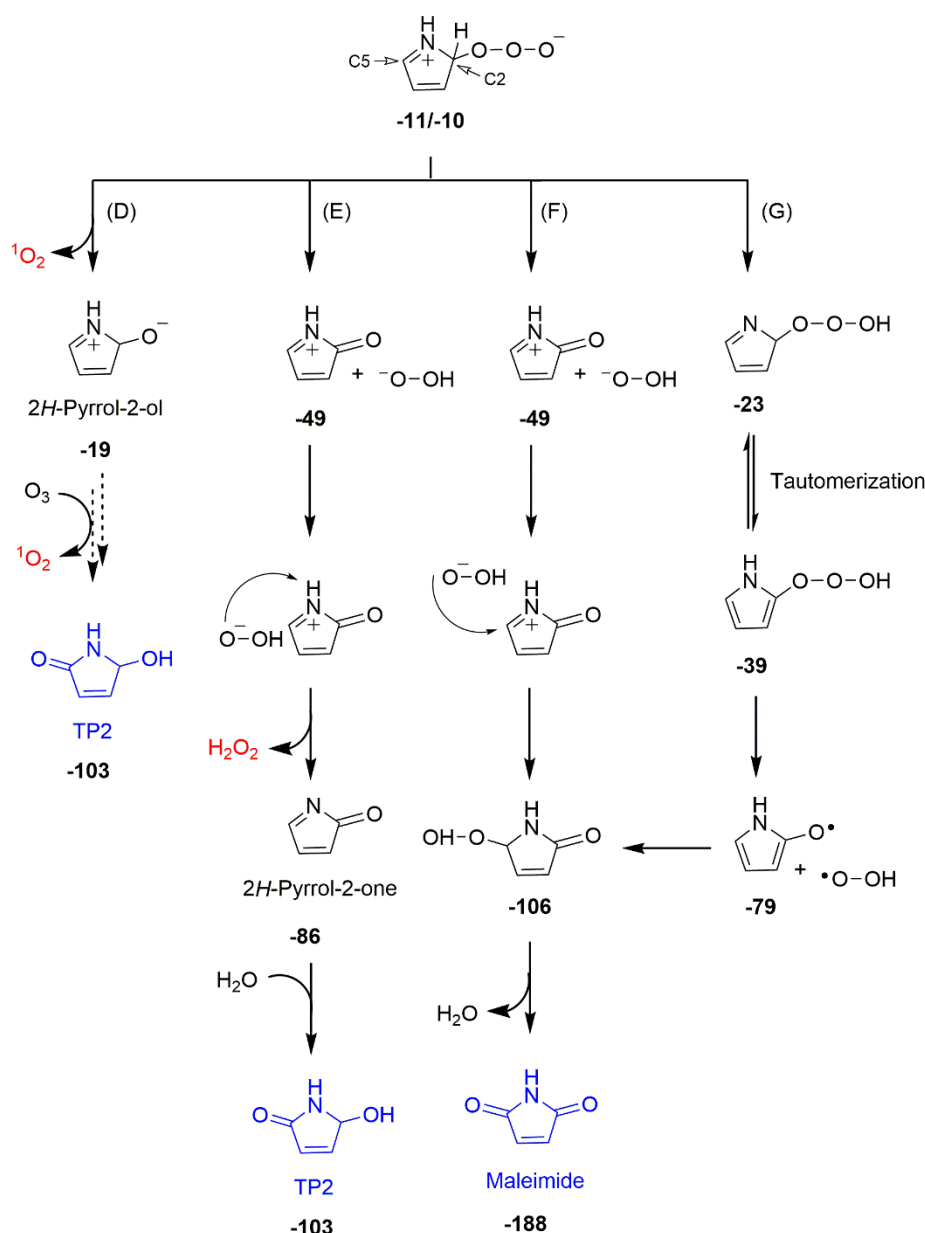


Figure 3.4. Detailed reaction mechanisms of the subsequent degradation of the zwitterion formed via C2-addition (pathway C in Figure 3.3) of the pyrrole-ozone reaction (pathways D – G). Bold numbers below the products and the intermediates are calculated Gibbs energies with respect to the initial reactants (pyrrole and ozone) in kcal mol⁻¹. Dashed arrows indicate that the corresponding reactions have not been investigated by quantum chemical computations. The full descriptions of the pathways including computed transition structures are shown in Figures S3.30, S3.31, and S3.32.

3.3.3.2 Imidazole-ozone reaction

Quantified products. The abatement of imidazole and the formation of the ozone-induced transformation products are shown in Figure 3.5. Imidazole reacts with ozone with an ozone:imidazole molar stoichiometry of 1 (Figure S3.11). Cyanate, formamide, and formate were identified as major products with high yields of (113 ± 5)%, (104 ± 5)%, and (97 ± 4)%, respectively, per consumed imidazole (Table 3.2). Urea was also detected as a minor product with a yield of less than 10% (Text S3.16 and Figure S3.33). The total yields of cyanate, formamide, and formate were (109 ± 4)% per nitrogen and (105 ± 3)% per carbon, resulting in almost perfect nitrogen

and carbon mass balances. The three products were formed concurrently, as all of them reached the maximum formation at one molar equivalent of ozone ($[\text{O}_3]/[\text{imidazole}]_0 = 1$). In addition, a kinetic simulation (lines in Figure 3.5) could well describe the evolution of imidazole and the products as a function of the ozone doses, based on the apparent second-order rate constants for the reactions of ozone with imidazole ($k = 1.7 \times 10^5 \text{ M}^{-1} \text{ s}^{-1}$ (Table 3.1)), cyanate ($k \leq 10^{-2} \text{ M}^{-1} \text{ s}^{-1}$),⁶⁵ formamide ($k \leq 10^{-2} \text{ M}^{-1} \text{ s}^{-1}$, estimated), and formate ($k = 46 \text{ M}^{-1} \text{ s}^{-1}$)⁶⁶ at neutral pH (Table S3.4). The second-order rate constant for the reaction of formamide with ozone was estimated to be small, considering its similar evolution as for cyanate. Under the condition where imidazole was completely consumed ($[\text{O}_3]/[\text{imidazole}]_0 > 1$), formate shows a gradual decrease because its ozone reactivity is much higher than for cyanate and formamide. At a high ozone dose ($[\text{O}_3]/[\text{imidazole}]_0 \sim 2$), the measured concentration of formate was higher than the predicted concentration, due to currently unknown reasons. The yield of formate decreased significantly at pH 2 (Figure S3.12), which suggests that the proposed mechanism may not be applicable to acidic conditions. However, more information (e.g., cyanate and formamide yields at low pH) is needed to confirm these findings.

The formation of formamide as a major product was also observed for another imidazole-containing compound (1-benzylimidazole) in this study. Similar to imidazole, 1-benzylimidazole was fully consumed at a 1:1 molar ratio of ozone to 1-benzylimidazole and transformed into *N*-benzylformamide with a 91% yield (Figure S3.35). This additionally supports the efficient conversion of imidazole to formamide upon ozonation and implies a similar reaction can also occur in more complex compounds.

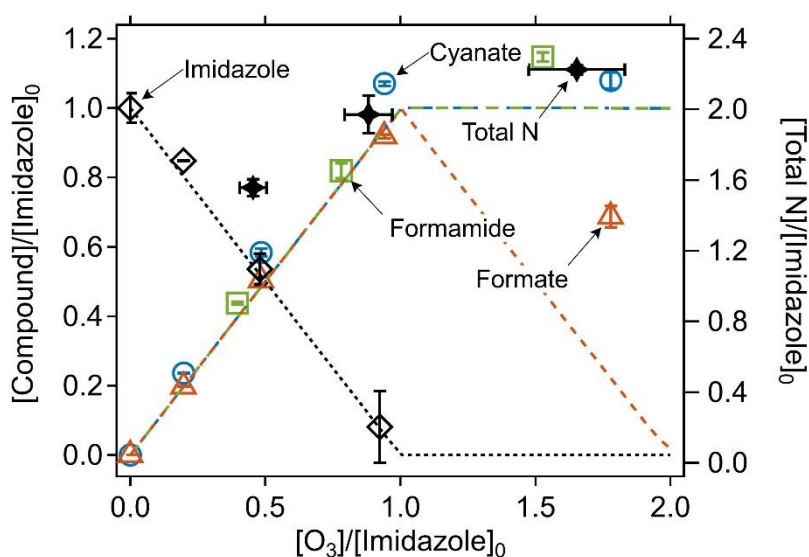


Figure 3.5. Relative abatement of imidazole and the formation of transformation products as a function of the molar ratio of $[\text{O}_3]/[\text{imidazole}]_0$. The symbols indicate the measured concentrations (duplicate or triplicate) and the lines indicate simulated concentrations based on the kinetic models described in Table S3.4. Total N indicates the sum of the concentrations of the nitrogen in the remaining imidazole and all nitrogen-containing transformation products. All measurements were carried out in presence of *t*-butanol at pH 7 (10 mM phosphate buffer). The initial imidazole concentration was around 100 μM for all experiments except for formamide determination where it was 1 mM – 4 mM (Text S3.3).

Reaction mechanisms. Three key findings can be summarized based on the product identification of the imidazole-ozone reaction: (1) Upon ozonation, imidazole was degraded into three compounds, namely cyanate, formamide, and formate; (2) the reaction was complete with one molar equivalent of ozone; (3) the reaction produced almost no reactive oxygen species. Based on these findings, a mechanism for the imidazole-ozone reaction is proposed in Figure 3.6. Ozone initially attacks at the C-C double bond of imidazole to form an ozonide intermediate, similarly to pathway A in the pyrrole-ozone reaction. However, different from the pyrrole case, the zwitterion derived from the ozonide intermediate is rearranged into a 3H-1,2,4-dioxazole ring to form a dioxazole intermediate, as hypothesized in Figure 3.6. The dioxazole intermediate then further decomposes to formamide and formyl isocyanate with the aid of a base and a proton. The resulting formyl isocyanate further hydrolyzes into formate and cyanate. Based on this mechanism, all oxygen atoms in ozone are transferred to the products, with no reactive oxygen species being formed.

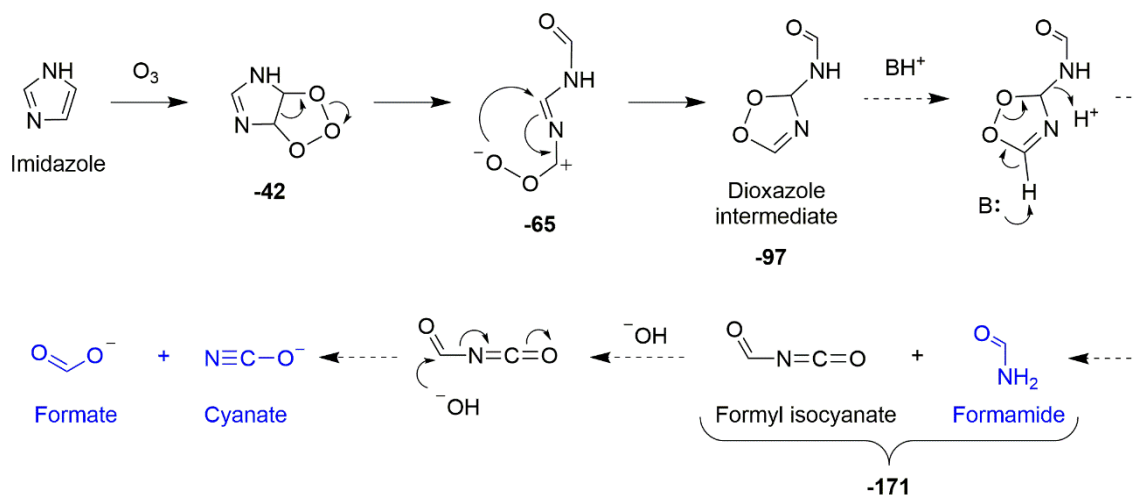


Figure 3.6. Proposed mechanisms for the reaction of imidazole with ozone based on the identified transformation products (highlighted in blue). Bold numbers below the products and the intermediates are calculated Gibbs energies with respect to the initial reactants (imidazole and ozone) in kcal mol^{-1} . Dashed arrows indicate that the corresponding reactions have not been investigated by quantum chemical computations. The full description of the pathway including computed transition structures is shown in Figure S3.36.

Quantum chemical computations. The proposed reaction mechanisms were partially investigated by quantum chemical computations. The cycloaddition on the C-C double bond, the ring cleavage, and the rearrangement of the zwitterion to the hypothesized dioxazole intermediate are exergonic reactions with -42, -65, and -97 kcal mol^{-1} , respectively, for the calculated energies with respect to the initial reactants, imidazole and ozone (Figure 3.6). The corresponding transition structures to the investigated reaction steps were found by the computations and are presented in Figure S3.36. The subsequent reactions from the dioxazole intermediate were not investigated in detail, but expected to be exergonic (Text S3.17).

Information on oxidation products of imidazole is not easily available. A few studies investigated the oxidation of histidine, an amino acid containing an imidazole moiety, but no mechanistic consensus has been obtained.^{67–70} The carbon between the two nitrogens in the imidazole ring was suggested as a main attack site of the oxidation of histidine in metal-catalyzed systems^{69,70} and by ozone.⁶⁷ This led to the formation of 2-oxohistidine as a final product. However, a product with three oxygens added to histidine was also reported during the oxidation of histidine with ozone,⁶⁸ which could be formed by an ozone attack⁶⁸ on the C-C double bond of the imidazole ring.

However, the previous ozonation experiments^{67,68} were performed without $\bullet\text{OH}$ scavenger, and thus it is unclear whether the products were formed by the reaction with ozone or with $\bullet\text{OH}$. Our findings strongly suggest the ozone attack at the double bond of the ring rather than at the carbon between the two nitrogens, according to the concomitant formation of the three major products by one molar equivalent of ozone, as discussed above.

3.3.3.3 Pyrazole-ozone reaction

Quantified products. The abatement of pyrazole as a function of the molar ratio of $[\text{O}_3]/[\text{Pyrazole}]_0$ is shown in Figure 3.7. Pyrazole required about 5 molar equivalents of ozone for its full abatement (Figure S3.11), which is much higher than for the pyrrole- and imidazole-ozone reactions. The $\bullet\text{OH}$ yield was also particularly high (35% per consumed pyrazole, Table 3.2) in comparison to the other azole-ozone reactions. The $\bullet\text{OH}$ yield was even higher at pH 11 (87%, Figure S3.12 and Table S3.8). The ozone reactivity of hydroxide ion ($k = 70 \text{ M}^{-1} \text{ s}^{-1}$)⁷¹ is similar to that of pyrazole. Therefore, at high pH where hydroxide ions are predominantly present, the reaction of hydroxide ion with ozone can outcompete the pyrazole-ozone reaction and result in forming excess $\bullet\text{OH}$. Formate and glyoxal were the only quantifiable transformation products, with yields of 126% and 34% per consumed pyrazole, respectively. The total yield of formate and glyoxal achieved 65% of the carbon mass balance. Formate yields remained similarly high for pH 2, 7, and 11 (Figure S3.12). No nitrogen-containing products were identified. Formamide was not detected (LOQ = $1.6 \mu\text{M}$) even for high molar $[\text{O}_3]/[\text{Pyrazole}]_0$ ratio of 5, for which pyrazole should be completely abated according to the ozone:pyrazole molar stoichiometry. *N*-nitroso compounds were suspected because of the N-N bond present in pyrazole, but they were not detected for any molar $[\text{O}_3]/[\text{Pyrazole}]_0$ ratios by the analysis of the total concentrations of *N*-nitroso compounds (LOQ = $0.7 \mu\text{M}$).⁴³ A non-target screening using LC-HRMS/MS resulted in three exact masses of interest, showing increases in the peak intensities with increasing ozone doses (Figures S3.37 and S3.38). However, molecular formulas assigned for these masses are not reasonable (e.g., containing five nitrogens for $m/z = 201.1009$, Table S3.13). Moreover, MS2 spectra were not measurable, probably due to the low intensity, which hindered obtaining further structural evidence. It seems that the products formed during the pyrazole-ozone reactions were not retained well on the applied LC column, poorly ionized by ESI-MS, or of the masses under the scan range of the MS detector ($m/z = 50$ as the lower limit), since pyrazole itself has only a mass of 68.

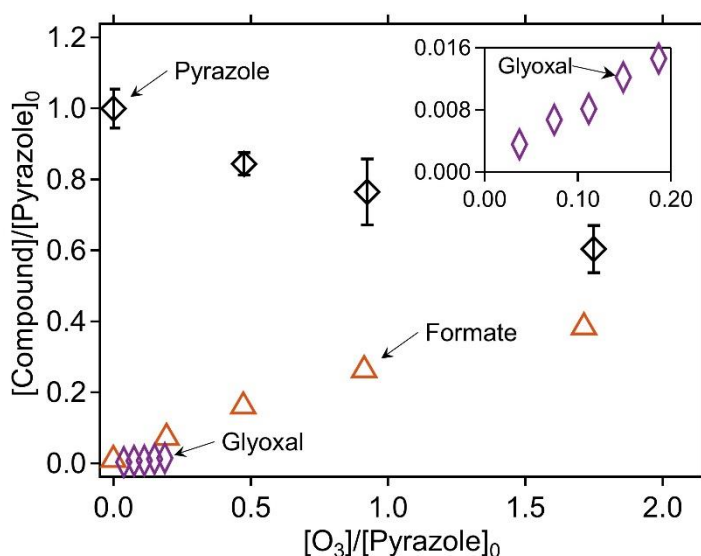


Figure 3.7. Relative abatement of pyrazole and the formation of formate as a function of the molar ratio of $[O_3]/[Pyrazole]_0$. The inset has the same axis labels as the main figure. The symbols indicate the measured concentrations (triplicate for pyrazole and single measurements for formate and glyoxal). All measurements were carried out in presence of *t*-butanol. 10 mM phosphate buffer was used for all measurements but glyoxal. The initial pyrazole concentrations were around 100 μ M for determining pyrazole and formate, and 1 mM for determining glyoxal (Text S3.3).

Benzylpyrazole- O_3 reaction. To facilitate the product identification by LC-HRMS/MS, 1-benzylpyrazole, a substituted pyrazole with a benzyl group, was chosen as an alternative model compound. A similarly inefficient abatement was observed as for the pyrazole-ozone reaction, with an ozone:1-benzylpyrazole molar stoichiometry of 6.5 (Table 3.2 and Figure S3.39). *N*-benzylformamide was detected as a minor product with a yield of 9% per consumed 1-benzylpyrazole. *N*-nitroso compounds were not detected at molar $[O_3]/[1\text{-Benzylpyrazole}]_0$ ratios of 2 and 4. A non-target screening found three masses with $m/z = 191.0813$, 163.0864 , and 151.0864 (as $[M+H]^+$), corresponding to the molecular formulas $C_{10}H_{10}N_2O_2$, $C_9H_{10}N_2O$, and $C_8H_{10}N_2O$, respectively, with a mass deviation of less than 2 ppm (note that the molecular formula of 1-benzylpyrazole is $C_{10}H_{10}N_2$). All masses are characterized by a similar formation trend, increasing in peak intensities for increasing molar ratios of $[O_3]/[1\text{-Benzylpyrazole}]_0$, reaching a maximum at $1 < [O_3]/[1\text{-Benzylpyrazole}]_0 < 2$, and then slightly decreasing at $[O_3]/[1\text{-Benzylpyrazole}]_0 > 2.5$ (Figure S3.40). The evolution of these compounds is quite similar, implying they were formed in parallel and not sequentially.

To elucidate their structures, MS2 spectra of $m/z = 191.0813$, 163.0864 , and 151.0864 were measured (Figures S3.41, S3.42, and S3.43) and compared with simulated fragment ions of candidate structures by an *in silico* fragmenter, MetFrag.⁷² The candidate structures for each mass were found by searching the exact mass (e.g., $m/z = 191.0813$ as $[M+H]^+$) in a compound database, PubChem,⁷³ and were further processed by MetFrag⁷² to generate a list of theoretical fragments based on a bond dissociation approach. More details of procedures and results are described in Text S3.18. The MetFrag analyses proposed two types of transformation products: a ring product with the addition of two oxygens in ketone and enol forms, corresponding to $m/z = 191.0813$ (shown as candidate 191a, Figure 3.8 and Figure S3.41D) and a ring-opened product containing a hydrazide moiety, corresponding to $m/z = 151.0864$ (shown as candidate 151c, Figure 3.8 and Figure S3.43D). For $m/z = 163.0864$, no valid hit was found.

Reaction mechanism. Based on the proposed transformation products, a potential mechanism of the reactions of 1-benzylpyrazole with ozone is proposed in Figure 3.8. The first pathway (H) explains the formation of the ring product (candidate 191a) via a series of oxygen-addition mechanisms. The second pathway (I) describes the formation of the ring-opened product (candidate 151c) or *N*-benzylformamide via a Criegee-type mechanism followed by hydrolysis of the resulting hydrazone. Both pathways are initiated by an ozone attack on the pyrazole moiety rather than on the benzene moiety. This can be substantiated because of the higher ozone reactivity of pyrazole than of benzene ($k_{O_3} = 5.6 \times 10^1 \text{ M}^{-1} \text{ s}^{-1}$ for pyrazole (Table 3.1) and $2 \text{ M}^{-1} \text{ s}^{-1}$ for benzene⁵⁵).

Candidate 191a contains two oxygen atoms added to the C4 and C5 positions of the pyrazole ring. Therefore, it is speculated that a reaction intermediate containing a hydroxypyrazole moiety preceded candidate 191a (e.g., 4-hydroxypyrazole or 5-hydroxypyrazole intermediates, Figure 3.8). The ozone reactivity of 4-hydroxypyrazole was determined as a representative case for hydroxypyrazoles. Its apparent second-order ozone rate constant at pH 7 was estimated to be higher than $9 \times 10^4 \text{ M}^{-1} \text{ s}^{-1}$ (Table 3.1 and Text S3.1), much higher than for that of benzene. Thus, the hydroxypyrazole moiety is significantly more reactive to ozone than the benzene moiety, wherefore, it can further react with ozone to form candidate 191a as a secondary ozonation product. The exact mass of the 4-hydroxypyrazole intermediate was not detected by LC-HRMS/MS for the ozonated benzylpyrazole samples. If the 4-hydroxypyrazole intermediate was formed, it would have been quickly oxidized to the subsequent product and escaped the detection. The fate of the resulting candidate 191a, whether it would be hydrolyzed or further oxidized, is unknown. Candidate 151c formed by the cycloaddition pathway (I) accompanies glyoxal as the other product fragmented from the pyrazole ring (Figure 3.8). Glyoxal was not measured for the benzylpyrazole-ozone reaction, but measured for the pyrazole-ozone reaction (34% glyoxal per consumed pyrazole, Table 3.2). If a similarly high yield of glyoxal is assumed for the benzylpyrazole-ozone reaction, the reaction seems to proceed to a large extent through the cycloaddition pathway.

By extrapolating the findings of the benzylpyrazole-ozone reaction to the pyrazole-ozone reaction, pyrazole would be transformed into 4,5-dihydroxypyrazole and formylhydrazine, equivalent to the candidates 191a and 151c, respectively. However, the corresponding exact masses of the products (101.0346 and 61.0396 as $[M+H]^+$) were not detected by LC-HRMS/MS for any ozonated pyrazole samples. Nevertheless, their formation cannot be entirely ruled out. In addition to the proposed oxygen-addition and cycloaddition pathways, electron transfer pathways seem to be involved in the pyrazole-ozone reaction, based on the particularly high $\bullet\text{OH}$ yield (35% per consumed pyrazole, Table 3.2). The primary ozone attack on pyrazole or secondary ozone reactions of transient reaction intermediates may undergo electron transfer pathways and form excessive $\bullet\text{OH}$. However, the product information is not sufficient to propose a plausible reaction mechanism.

The high molar ozone:azole stoichiometry of the pyrazole and 1-benzylpyrazole is probably attributed to the formation of reaction intermediates at least as reactive with ozone as pyrazole, consuming ozone over-stoichiometrically. Potential ozone consuming products could be hydroxypyrazoles which have been suggested on the basis of the LC-HRMS/MS results. However, their formation upon ozonation still needs to be confirmed by reference standards. Moreover, the formation of hydroxypyrazole alone cannot fully explain the high stoichiometry and more unknown intermediates must have been involved.

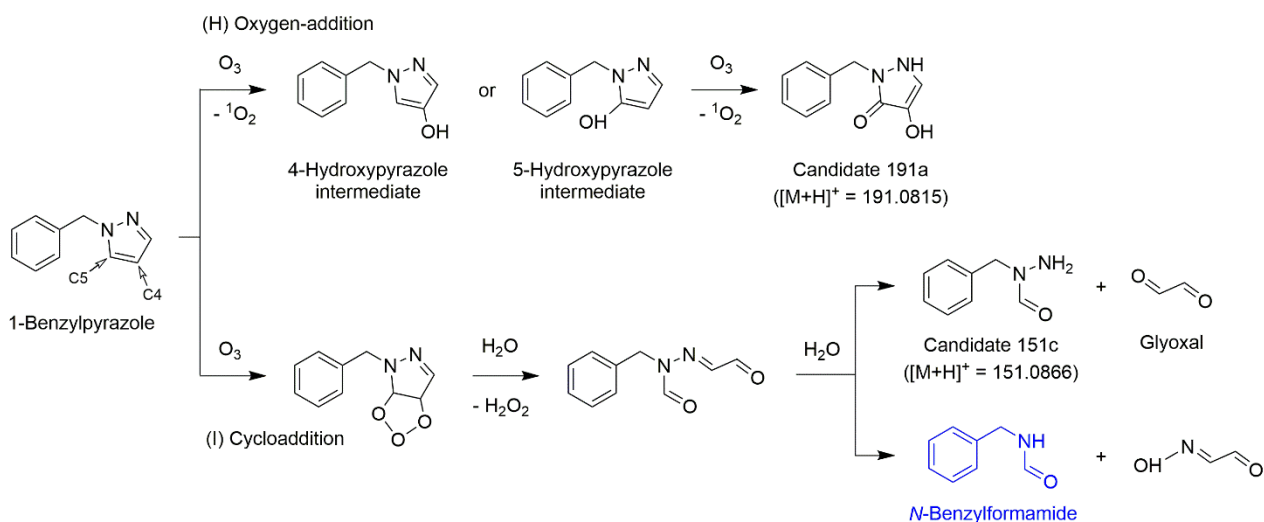


Figure 3.8. Proposed mechanisms for the reaction of 1-benzylpyrazole with ozone based on the identified (highlighted in blue) and the proposed products. Glyoxal was confirmed by a reference standard for the reaction of pyrazole with ozone. Candidates 191a and 151c were proposed based on the exact masses detected by LC-HRMS/MS analyses. Theoretical exact masses are shown in parentheses.

3.3.4 Implications

Pyrrole, imidazole, and pyrazole are present as substructures of biomolecules or micropollutants. Upon ozonation, effective abatement of pyrrole and imidazole is expected according to the high ozone reactivity determined in this study ($k > 10^3 \text{ M}^{-1} \text{ s}^{-1}$). The micropollutants containing pyrrole or imidazole were present in the concentrations below LOQ after ozonation or significantly abated during ozonation (typically > 70% abatement) based on the result reported by a previous study monitoring abatement of micropollutants at a full-scale wastewater treatment plant (Table S3.14).⁷ Pyrrole and imidazole derivatives would be transformed by ozone into the products containing a maleimide, formamide, or cyanate moiety with a moderate to high yield, according to our findings (34% maleimide from the pyrrole-ozone reaction, ~100% formamide and ~100% cyanate from the imidazole-ozone reaction). As single compounds, maleimide, cyanate, and formamide do not appear to be persistent in the aquatic environment, but are rather hydrolyzed^{74,75} or biodegraded.⁷⁶ Since ozonation is typically followed by a biological post-treatment,⁵ they would be readily abated during the post-treatment. However, as substructures of more complex molecules, they may behave differently during the post-treatment and their possible toxic effects may be still relevant. The C-C double bond in maleimide with two neighboring carbonyl groups is highly susceptible to nucleophilic additions. Therefore, maleimide reacts fast and selectively with thiol groups.⁷⁷ Such selectivity may induce toxic effects by converting cysteine residues of proteins, in analogy to α,β -unsaturated enedials and oxoenals produced by oxidation of phenols.⁷⁸ Formamide is polar and biodegradable and is less prone to be bioaccumulated in aquatic organisms.⁷⁶ However, some studies reported toxic effects possibly associated with a formamide moiety in more complex compounds. An increased toxicity observed in phototransformation studies of herbicides was assigned to *N*-formylated products.^{79,80} Similarly, a recent study on phototransformation of ionic liquids containing an imidazole moiety reported an increased toxicity possibly induced by *N*-formyl transformation products.⁸¹ Compared to pyrrole and imidazole, pyrazole reacts slower with ozone ($k_{\text{app}} = 56 \text{ M}^{-1} \text{ s}^{-1}$ at pH 7) and exhibits a much higher ozone:azole molar stoichiometry. Compounds with low ozone reactivity can be still abated during ozonation process by $\cdot\text{OH}$. Examples are irbesartan and acesulfame which are not highly reactive towards ozone ($k_{03} = 23 \text{ M}^{-1} \text{ s}^{-1}$ for irbesartan⁷ and $88 \text{ M}^{-1} \text{ s}^{-1}$ for acesulfame⁸²), but still significantly or reasonably well abated under a conventional ozonation condition (75% for irbesartan and ~50% for

acesulfame).⁷ The $\cdot\text{OH}$ reactivity of pyrazole lies between irbesartan and acesulfame ($k_{\cdot\text{OH}} = \sim 10^{10} \text{ M}^{-1} \text{ s}^{-1}$ for irbesartan,⁷ $4.6 \times 10^9 \text{ M}^{-1} \text{ s}^{-1}$ for acesulfame,⁸² and $\sim 8 \times 10^9 \text{ M}^{-1} \text{ s}^{-1}$ for pyrazole⁸³). Therefore, at least moderate abatement of pyrazole is expected during ozonation process. Ozonation products of pyrazole are still largely unknown. Transformation products, at least as reactive towards ozone as pyrazole (e.g., hydroxypyrazoles), are postulated, but none of them could be confirmed by reference standards, which requires further investigations.

3.4 Conclusion

All azole-ozone reactions investigated in this study were initiated by an ozone attack on the C-C double bond in the ring. From the initial attack, the reactions went through distinct pathways clearly differentiated among pyrrole, imidazole, and pyrazole. Pyrrole reacted with ozone via multiple mechanisms (Criegee and oxygen-addition) to form ring products (5-Hydroxy-1,5-dihydro-2H-pyrrol-2-one and maleimide) as well as a ring-opened product (*N*-(3-oxo-1-propen-1-yl)formamide). The major quantified products from the pyrrole-ozone reaction were maleimide, formamide, and formate with yields of 34%, 14%, and 54%, respectively, per consumed pyrrole. The total yields of all identified products accounted for 48% of the nitrogen mass balance and 54% of the carbon mass balance.

Imidazole reacted with ozone predominantly via a Criegee mechanism with ring cleavage to form three fragments (formamide, cyanate, and formate). The fragmentation was initiated by only a single attack of ozone, and all oxygen atoms ended up in the products, producing almost no reactive oxygen species. The sum of the yields of the three products was $\sim 100\%$ per nitrogen and per carbon, completely closing the mass balance of imidazole.

Pyrazole is the most persistent compound against ozonation among the studied azoles, showing an ozone reactivity at least three orders magnitude lower than those of pyrrole and imidazole. Also, pyrazole requires about five molar equivalents of ozone for a complete abatement. The exceptionally high stoichiometry suggests the formation of primary products, such as hydroxypyrazoles, reacting fast with ozone. Hydroxypyrazoles and hydrazides were postulated, possibly formed via an oxygen-addition and a cycloaddition pathway. Glyoxal and formate were identified as major products, accounting for 65% of the carbon mass balance. No nitrogenous products were identified from the pyrazole-ozone reaction.

All confirmed nitrogenous transformation products (maleimide, formamide, and cyanate) are expected to be readily hydrolyzed and/or biodegraded. Therefore, they are supposed to be well removed by a biological post-treatment typically following ozonation. They do not appear to pose a direct threat to the aquatic environment as single substances, but as subunits of more complex compounds (e.g., micropollutants), they might be persistent during the post-treatment, with unknown (eco)toxicological consequences.

Acknowledgement

The NMR hardware was partially granted by the Swiss National Science Foundation (SNSF, grant no. 206021_150638/1). We thank Elisabeth Salhi for her support with the ozonation experiments and IC-CD measurements, Rebekka Gulde, Jennifer Schollee, and Marc Suter for sharing their expertise on LC-HRMS/MS data analyses, Cornel Niederhauser and Samuel Derrer for the help on the work-up for NMR samples. We would also

like to thank Laura Wiegand and Klaus Kerpen for their support in IC-measurements as well as HPLC-measurements and Natalia Tabler for her help by translation of Russian literature.

3.5 References

- (1) Pal, A.; Gin, K. Y.-H.; Lin, A. Y.-C.; Reinhard, M. Impacts of Emerging Organic Contaminants on Freshwater Resources: Review of Recent Occurrences, Sources, Fate and Effects. *Science of The Total Environment* **2010**, *408* (24), 6062–6069. <https://doi.org/10.1016/j.scitotenv.2010.09.026>.
- (2) Schwarzenbach, R. P.; Escher, B. I.; Fenner, K.; Hofstetter, T. B.; Johnson, C. A.; von Gunten, U.; Wehrli, B. The Challenge of Micropollutants in Aquatic Systems. *Science* **2006**, *313* (5790), 1072–1077. <https://doi.org/10.1126/science.1127291>.
- (3) *Human Pharmaceuticals, Hormones and Fragrances - The Challenge of Micropollutants in Urban Water Management*; Ternes, T., Joss, A., Eds.; IWA Publishing, 2006.
- (4) Ternes, T. A.; Stüber, J.; Herrmann, N.; McDowell, D.; Ried, A.; Kampmann, M.; Teiser, B. Ozonation: A Tool for Removal of Pharmaceuticals, Contrast Media and Musk Fragrances from Wastewater? *Water Research* **2003**, *37* (8), 1976–1982. [https://doi.org/10.1016/S0043-1354\(02\)00570-5](https://doi.org/10.1016/S0043-1354(02)00570-5).
- (5) von Gunten, U. Oxidation Processes in Water Treatment: Are We on Track? *Environmental Science & Technology* **2018**, *52* (9), 5062–5075. <https://doi.org/10.1021/acs.est.8b00586>.
- (6) Eggen, R. I. L.; Hollender, J.; Joss, A.; Schärer, M.; Stamm, C. Reducing the Discharge of Micropollutants in the Aquatic Environment: The Benefits of Upgrading Wastewater Treatment Plants. *Environmental Science & Technology* **2014**, *48* (14), 7683–7689. <https://doi.org/10.1021/es500907n>.
- (7) Bourgin, M.; Beck, B.; Boehler, M.; Borowska, E.; Fleiner, J.; Salhi, E.; Teichler, R.; von Gunten, U.; Siegrist, H.; McArdell, C. S. Evaluation of a Full-Scale Wastewater Treatment Plant Upgraded with Ozonation and Biological Post-Treatments: Abatement of Micropollutants, Formation of Transformation Products and Oxidation by-Products. *Water Research* **2018**, *129*, 486–498. <https://doi.org/10.1016/j.watres.2017.10.036>.
- (8) Dodd, M. C.; Kohler, H.-P. E.; von Gunten, U. Oxidation of Antibacterial Compounds by Ozone and Hydroxyl Radical: Elimination of Biological Activity during Aqueous Ozonation Processes. *Environmental Science & Technology* **2009**, *43* (7), 2498–2504. <https://doi.org/10.1021/es8025424>.
- (9) Huber, M. M.; Ternes, T. A.; von Gunten, U. Removal of Estrogenic Activity and Formation of Oxidation Products during Ozonation of 17 α -Ethinylestradiol. *Environ. Sci. Technol.* **2004**, *38* (19), 5177–5186. <https://doi.org/10.1021/es035205x>.
- (10) Lange, F.; Cornelissen, S.; Kubac, D.; Sein, M. M.; von Sonntag, J.; Hannich, C. B.; Golloch, A.; Heipieper, H. J.; Möder, M.; von Sonntag, C. Degradation of Macrolide Antibiotics by Ozone: A Mechanistic Case Study with Clarithromycin. *Chemosphere* **2006**, *65* (1), 17–23. <https://doi.org/10.1016/j.chemosphere.2006.03.014>.
- (11) Dodd, M. C.; Rentsch, D.; Singer, H. P.; Kohler, H.-P. E.; von Gunten, U. Transformation of β -Lactam Antibacterial Agents during Aqueous Ozonation: Reaction Pathways and Quantitative Bioassay of Biologically-Active Oxidation Products. *Environ. Sci. Technol.* **2010**, *44* (15), 5940–5948. <https://doi.org/10.1021/es101061w>.
- (12) Magdeburg, A.; Stalter, D.; Schlüsener, M.; Ternes, T.; Oehlmann, J. Evaluating the Efficiency of Advanced Wastewater Treatment: Target Analysis of Organic Contaminants and (Geno-)Toxicity Assessment Tell a Different Story. *Water Research* **2014**, *50*, 35–47. <https://doi.org/10.1016/j.watres.2013.11.041>.
- (13) Escher, B. I.; Bramaz, N.; Ort, C. JEM Spotlight: Monitoring the Treatment Efficiency of a Full Scale Ozonation on a Sewage Treatment Plant with a Mode-of-Action Based Test Battery. *Journal of Environmental Monitoring* **2009**, *11* (10), 1836. <https://doi.org/10.1039/b907093a>.
- (14) Stalter, D.; Magdeburg, A.; Oehlmann, J. Comparative Toxicity Assessment of Ozone and Activated Carbon Treated Sewage Effluents Using an in Vivo Test Battery. *Water Research* **2010**, *44* (8), 2610–2620. <https://doi.org/10.1016/j.watres.2010.01.023>.
- (15) von Gunten, U.; Salhi, E.; Schmidt, C. K.; Arnold, W. A. Kinetics and Mechanisms of *N*-Nitrosodimethylamine Formation upon Ozonation of *N*, *N*-Dimethylsulfamide-Containing Waters: Bromide Catalysis. *Environmental Science & Technology* **2010**, *44* (15), 5762–5768. <https://doi.org/10.1021/es1011862>.
- (16) Schmidt, C. K.; Brauch, H.-J. *N,N*-Dimethylsulfamide as Precursor for *N*-Nitrosodimethylamine (NDMA) Formation upon Ozonation and Its Fate During Drinking Water Treatment. *Environ. Sci. Technol.* **2008**, *42* (17), 6340–6346. <https://doi.org/10.1021/es7030467>.
- (17) Lee, Y.; von Gunten, U. Advances in Predicting Organic Contaminant Abatement during Ozonation of Municipal Wastewater Effluent: Reaction Kinetics, Transformation Products, and Changes of Biological Effects. *Environmental Science: Water Research & Technology* **2016**, *2* (3), 421–442. <https://doi.org/10.1039/C6EW00025H>.
- (18) von Sonntag, C.; von Gunten, U. *Chemistry of Ozone in Water and Wastewater Treatment*; IWA Publishing, 2012.
- (19) Lee, M.; Blum, L. C.; Schmid, E.; Fenner, K.; von Gunten, U. A Computer-Based Prediction Platform for the Reaction of Ozone with Organic Compounds in Aqueous Solution: Kinetics and Mechanisms. *Environmental Science: Processes & Impacts* **2017**, *19* (3), 465–476. <https://doi.org/10.1039/C6EM00584E>.
- (20) Lim, S.; McArdell, C. S.; von Gunten, U. Reactions of Aliphatic Amines with Ozone: Kinetics and Mechanisms. *Water Research* **2019**, *157*, 514–528. <https://doi.org/10.1016/j.watres.2019.03.089>.

- (21) Tekle-Röttering, A.; von Sonntag, C.; Reisz, E.; Eyser, C. vom; Lutze, H. V.; Türk, J.; Naumov, S.; Schmidt, W.; Schmidt, T. C. Ozonation of Anilines: Kinetics, Stoichiometry, Product Identification and Elucidation of Pathways. *Water Research* **2016**, *98*, 147–159. <https://doi.org/10.1016/j.watres.2016.04.001>.
- (22) Borowska, E.; Bourgin, M.; Hollender, J.; Kienle, C.; McArdell, C. S.; von Gunten, U. Oxidation of Cetirizine, Fexofenadine and Hydrochlorothiazide during Ozonation: Kinetics and Formation of Transformation Products. *Water Research* **2016**, *94*, 350–362. <https://doi.org/10.1016/j.watres.2016.02.020>.
- (23) Tekle-Röttering, A.; Reisz, E.; Jewell, K. S.; Lutze, H. V.; Ternes, T. A.; Schmidt, W.; Schmidt, T. C. Ozonation of Pyridine and Other N-Heterocyclic Aromatic Compounds: Kinetics, Stoichiometry, Identification of Products and Elucidation of Pathways. *Water Research* **2016**, *102*, 582–593. <https://doi.org/10.1016/j.watres.2016.06.021>.
- (24) Tekle-Röttering, A.; Jewell, K. S.; Reisz, E.; Lutze, H. V.; Ternes, T. A.; Schmidt, W.; Schmidt, T. C. Ozonation of Piperidine, Piperazine and Morpholine: Kinetics, Stoichiometry, Product Formation and Mechanistic Considerations. *Water Research* **2016**, *88*, 960–971. <https://doi.org/10.1016/j.watres.2015.11.027>.
- (25) Joule, J. A.; Mills, K. *Heterocyclic Chemistry At A Glance*, 2nd ed.; Wiley, 2012.
- (26) Ansari, A.; Ali, A.; Asif, M.; Shamsuzzaman, S. Review: Biologically Active Pyrazole Derivatives. *New J. Chem.* **2017**, *41* (1), 16–41. <https://doi.org/10.1039/C6NJ03181A>.
- (27) Bhardwaj, V.; Gumber, D.; Abbot, V.; Dhiman, S.; Sharma, P. Pyrrole: A Resourceful Small Molecule in Key Medicinal Hetero-Aromatics. *RSC Adv.* **2015**, *5* (20), 15233–15266. <https://doi.org/10.1039/C4RA15710A>.
- (28) Narasimhan, B.; Sharma, D.; Kumar, P. Biological Importance of Imidazole Nucleus in the New Millennium. *Med Chem Res* **2011**, *20* (8), 1119–1140. <https://doi.org/10.1007/s00044-010-9472-5>.
- (29) Amde, M.; Liu, J.-F.; Pang, L. Environmental Application, Fate, Effects, and Concerns of Ionic Liquids: A Review. *Environ. Sci. Technol.* **2015**, *49* (21), 12611–12627. <https://doi.org/10.1021/acs.est.5b03123>.
- (30) Richardson, S. D.; Ternes, T. A. Water Analysis: Emerging Contaminants and Current Issues. *Anal. Chem.* **2018**, *90* (1), 398–428. <https://doi.org/10.1021/acs.analchem.7b04577>.
- (31) Baken, K.; Kolkman, A.; van Diepenbeek, P.; Ketelaars, H.; van Wezel, A. Signaleren van ‘overige antropogene stoffen’, en dan? De pyrazool-casus <https://www.h2owaternetwerk.nl/vakartikelen/signaleren-van-overige-antropogene-stoffen-en-dan-de-pyrazool-casus> (accessed Jul 22, 2019).
- (32) Richardson, S. D.; Thruston, A. D.; Rav-Acha, C.; Groisman, L.; Popilevsky, I.; Juraev, O.; Glezer, V.; McKague, A. B.; Plewa, M. J.; Wagner, E. D. Tribromopyrrole, Brominated Acids, and Other Disinfection Byproducts Produced by Disinfection of Drinking Water Rich in Bromide. *Environ. Sci. Technol.* **2003**, *37* (17), 3782–3793. <https://doi.org/10.1021/es030339w>.
- (33) Yang, M.; Zhang, X. Halopyrroles: A New Group of Highly Toxic Disinfection Byproducts Formed in Chlorinated Saline Wastewater. *Environ. Sci. Technol.* **2014**, *48* (20), 11846–11852. <https://doi.org/10.1021/es503312k>.
- (34) Daiber, E. J.; DeMarini, D. M.; Ravuri, S. A.; Liberatore, H. K.; Cuthbertson, A. A.; Thompson-Klemish, A.; Byer, J. D.; Schmid, J. E.; Afifi, M. Z.; Blatchley, E. R.; et al. Progressive Increase in Disinfection Byproducts and Mutagenicity from Source to Tap to Swimming Pool and Spa Water: Impact of Human Inputs. *Environ. Sci. Technol.* **2016**, *50* (13), 6652–6662. <https://doi.org/10.1021/acs.est.6b00808>.
- (35) Bocchi, V.; Chierici, L.; Gardini, G. P.; Mondelli, R. On Pyrrole Oxidation with Hydrogen Peroxide. *Tetrahedron* **1970**, *26* (17), 4073–4082. [https://doi.org/10.1016/S0040-4020\(01\)93048-0](https://doi.org/10.1016/S0040-4020(01)93048-0).
- (36) Wibaut, J. P.; Boon, J. W. P. Über die Einwirkung von Ozon auf Pyrazol sowie einige Homologe und Derivate. *Helvetica Chimica Acta* **1961**, *44* (4), 1171–1190. <https://doi.org/10.1002/hlca.19610440445>.
- (37) Wibaut, J. P. Ozonolysis of Pyrroles, Furans, and γ -Pyrones in Connection with Reactivity of Bonds in Ring System. In *Ozone Chemistry and Technology*; American Chemical Society: 1155 Sixteenth St, N.W. Washington 6, D.C., 1959; Vol. 21, pp 153–161. <https://doi.org/10.1021/ba-1959-0021.ch024>.
- (38) Wasserman, H. H.; Yoo, J. U.; DeSimone, R. W. Singlet Oxygen Reactions from the Adducts of Ozone with Heterocyclic Substrates. *Journal of the American Chemical Society* **1995**, *117* (38), 9772–9773. <https://doi.org/10.1021/ja00143a027>.
- (39) Pryor, W. A.; Giamalva, D. H.; Church, D. F. Kinetics of Ozonation. 2. Amino Acids and Model Compounds in Water and Comparisons to Rates in Nonpolar Solvents. *Journal of the American Chemical Society* **1984**, *106* (23), 7094–7100. <https://doi.org/10.1021/ja00335a038>.
- (40) Ianni, J. C. Kintecus, 2017, Windows Version 6.01, www.kintecus.com.
- (41) Muñoz, F.; von Sonntag, C. Determination of Fast Ozone Reactions in Aqueous Solution by Competition Kinetics. *Journal of the Chemical Society, Perkin Transactions 2* **2000**, No. 4, 661–664. <https://doi.org/10.1039/a909668j>.
- (42) Bader, H.; Hoigné, J. Determination of Ozone in Water by the Indigo Method. *Water Research* **1981**, *15* (4), 449–456.
- (43) Breider, F.; von Gunten, U. Quantification of Total N -Nitrosamine Concentrations in Aqueous Samples via UV-Photolysis and Chemiluminescence Detection of Nitric Oxide. *Analytical Chemistry* **2017**, *89* (3), 1574–1582. <https://doi.org/10.1021/acs.analchem.6b03595>.
- (44) Ohmori, S.; Mori, M.; Kawase, M.; Tsuboi, S. Determination of Methylglyoxal as 2-Methylquinoxaline by High-Performance Liquid Chromatography and Its Application to Biological Samples. *Journal of Chromatography B: Biomedical Sciences and Applications* **1987**, *414*, 149–155. [https://doi.org/10.1016/0378-4347\(87\)80033-6](https://doi.org/10.1016/0378-4347(87)80033-6).
- (45) Flyunt, R.; Leitzke, A.; Mark, G.; Mvula, E.; Reisz, E.; Schick, R.; von Sonntag, C. Determination of $\bullet\text{OH}$, $\text{O}_2\bullet^-$, and Hydroperoxide Yields in Ozone Reactions in Aqueous Solution. *The Journal of Physical Chemistry B* **2003**, *107* (30), 7242–7253. <https://doi.org/10.1021/jp022455b>.
- (46) Nash, T. The Colorimetric Estimation of Formaldehyde by Means of the Hantzsch Reaction. *Biochemical Journal* **1953**, *55* (3), 416.

- (47) Allen, A. O.; Hochanadel, C. J.; Ghormley, J. A.; Davis, T. W. Decomposition of Water and Aqueous Solutions Under Mixed Fast Neutron and Gamma Radiation. **1952**, *56*, 575–586.
- (48) Kitsuka, K.; Mohammad, A. M.; Awad, M. I.; Kaneda, K.; Ikematsu, M.; Iseki, M.; Mushiake, K.; Ohsaka, T. Simultaneous Spectrophotometric Determination of Ozone and Hydrogen Peroxide. *Chem. Lett.* **2007**, *36* (11), 1396–1397. <https://doi.org/10.1246/cl.2007.1396>.
- (49) Frisch, M. J.; Trucks, G. W.; Schlegel, H. B.; Scuseria, G. E.; Robb, M. A.; Cheeseman, J. R.; Scalmani, G.; Barone, V.; Petersson, G. A.; Nakatsuji, H.; et al. *Gaussian 09, Revision D.01*; Gaussian, Inc.: Wallingford CT, 2016.
- (50) Tentscher, P. R.; Lee, M.; von Gunten, U. Micropollutant Oxidation Studied by Quantum Chemical Computations: Methodology and Applications to Thermodynamics, Kinetics, and Reaction Mechanisms. *Acc. Chem. Res.* **2019**, *52* (3), 605–614. <https://doi.org/10.1021/acs.accounts.8b00610>.
- (51) Vydrov, O. A.; Scuseria, G. E. Assessment of a Long-Range Corrected Hybrid Functional. *J. Chem. Phys.* **2006**, *125* (23), 234109. <https://doi.org/10.1063/1.2409292>.
- (52) Trogolo, D.; Arey, J. S.; Tentscher, P. R. Gas-Phase Ozone Reactions with a Structurally Diverse Set of Molecules: Barrier Heights and Reaction Energies Evaluated by Coupled Cluster and Density Functional Theory Calculations. *The Journal of Physical Chemistry A* **2019**. <https://doi.org/10.1021/acs.jpca.8b10323>.
- (53) Marenich, A. V.; Cramer, C. J.; Truhlar, D. G. Universal Solvation Model Based on Solute Electron Density and on a Continuum Model of the Solvent Defined by the Bulk Dielectric Constant and Atomic Surface Tensions. *The Journal of Physical Chemistry B* **2009**, *113* (18), 6378–6396. <https://doi.org/10.1021/jp810292n>.
- (54) Dissociation Constants of Organic Acids and Bases. In *CRC Handbook of Chemistry and Physics, 100th Edition (Internet Version 2019)*; Rumble, J. R., Ed.; CRC Press/Taylor & Francis: Boca Raton, FL, 2019.
- (55) Hoigné, J.; Bader, H. Rate Constants of Reactions of Ozone with Organic and Inorganic Compounds in Water—I: Non-Dissociating Organic Compounds. *Water Research* **1983**, *17* (2), 173–183.
- (56) Muñoz, F.; von Sonntag, C. The Reactions of Ozone with Tertiary Amines Including the Complexing Agents Nitrilotriacetic Acid (NTA) and Ethylenediaminetetraacetic Acid (EDTA) in Aqueous Solution. *Journal of the Chemical Society, Perkin Transactions 2* **2000**, No. 10, 2029–2033. <https://doi.org/10.1039/b004417m>.
- (57) Atkinson, J. H.; Atkinson, R. S.; Johnson, A. W. The Structure and Reactions of Some Pyrrolin-2-Ones. *J. Chem. Soc.* **1964**, 5999–6009.
- (58) Zhang, Y.; Song, R.; Sun, Y.; Sun, J.; Tang, Y.; Wang, R. Mechanistic and Kinetic Study on the Reaction of Pyrrole (C₄H₅N) with O(3P). *Chemical Physics* **2018**, *513*, 50–57. <https://doi.org/10.1016/j.chemphys.2018.06.019>.
- (59) Bailey, P. S.; Colomb, H. O. 1,4-Addition of Ozone to Furans and Pyrroles. *J. Am. Chem. Soc.* **1957**, *79* (15), 4238–4238. <https://doi.org/10.1021/ja01572a068>.
- (60) Boger, D. L.; Baldino, C. M. Singlet Oxygen Mediated Oxidative Decarboxylation of Pyrrole-2-Carboxylic Acids. *J. Org. Chem.* **1991**, *56* (24), 6942–6944. <https://doi.org/10.1021/jo00024a045>.
- (61) Lightner, D. A.; Pak, C.-S. Dye-Sensitized Photooxygenation of Tert-Butylpyrroles. *The Journal of Organic Chemistry* **1975**, *40* (19), 2724–2728. <https://doi.org/10.1021/jo00907a005>.
- (62) Wasserman, H. H.; Frechette, R.; Rotello, V. M.; Schulte, G. Singlet Oxygen Reactions of 2-Carbalkoxy-3-Methoxypyrroles. *Tetrahedron Letters* **1991**, *32* (51), 7571–7574. [https://doi.org/10.1016/0040-4039\(91\)80537-G](https://doi.org/10.1016/0040-4039(91)80537-G).
- (63) Wheeler, S. E.; Ess, D. H.; Houk, K. N. Thinking Out of the Black Box: Accurate Barrier Heights of 1,3-Dipolar Cycloadditions of Ozone with Acetylene and Ethylene. *The Journal of Physical Chemistry A* **2008**, *112* (8), 1798–1807. <https://doi.org/10.1021/jp710104d>.
- (64) Zhao, Y.; Tishchenko, O.; Gour, J. R.; Li, W.; Lutz, J. J.; Piecuch, P.; Truhlar, D. G. Thermochemical Kinetics for Multi-reference Systems: Addition Reactions of Ozone. *The Journal of Physical Chemistry A* **2009**, *113* (19), 5786–5799. <https://doi.org/10.1021/jp811054n>.
- (65) Hoigné, J.; Bader, H.; Haag, W. R.; Staehelin, J. Rate Constants of Reactions of Ozone with Organic and Inorganic Compounds in Water—III. Inorganic Compounds and Radicals. *Water Research* **1985**, *19* (8), 993–1004. [https://doi.org/10.1016/0043-1354\(85\)90368-9](https://doi.org/10.1016/0043-1354(85)90368-9).
- (66) Reisz, E.; Fischbacher, A.; Naumov, S.; von Sonntag, C.; Schmidt, T. C. Hydride Transfer: A Dominating Reaction of Ozone with Tertiary Butanol and Formate Ion in Aqueous Solution. *Ozone: Science & Engineering* **2014**, *36* (6), 532–539. <https://doi.org/10.1080/01919512.2014.891436>.
- (67) Berlett, B. S.; Levine, R. L.; Stadtman, E. R. Comparison of the Effects of Ozone on the Modification of Amino Acid Residues in Glutamine Synthetase and Bovine Serum Albumin. *Journal of Biological Chemistry* **1996**, *271* (8), 4177–4182. <https://doi.org/10.1074/jbc.271.8.4177>.
- (68) Kotiaho, T.; Eberlin, M. N.; Vainiotalo, P.; Kostianen, R. Electrospray Mass and Tandem Mass Spectrometry Identification of Ozone Oxidation Products of Amino Acids and Small Peptides. *Journal of the American Society for Mass Spectrometry* **2000**, *11* (6), 526–535. [https://doi.org/10.1016/S1044-0305\(00\)00116-1](https://doi.org/10.1016/S1044-0305(00)00116-1).
- (69) Schöneich, C. Mechanisms of Metal-Catalyzed Oxidation of Histidine to 2-Oxo-Histidine in Peptides and Proteins. *Journal of Pharmaceutical and Biomedical Analysis* **2000**, *21* (6), 1093–1097. [https://doi.org/10.1016/S0731-7085\(99\)00182-X](https://doi.org/10.1016/S0731-7085(99)00182-X).
- (70) Uchida, K. Histidine and Lysine as Targets of Oxidative Modification. *Amino Acids* **2003**, *25* (3–4), 249–257. <https://doi.org/10.1007/s00726-003-0015-y>.
- (71) Merényi, G.; Lind, J.; Naumov, S.; von Sonntag, C. The Reaction of Ozone with the Hydroxide Ion: Mechanistic Considerations Based on Thermokinetic and Quantum Chemical Calculations and the Role of HO₄[–] in Superoxide Dismutation. *Chemistry – A European Journal* **2010**, *16* (4), 1372–1377. <https://doi.org/10.1002/chem.200802539>.

- (72) Ruttkies, C.; Schymanski, E. L.; Wolf, S.; Hollender, J.; Neumann, S. MetFrag Relaunched: Incorporating Strategies beyond in Silico Fragmentation. *J Cheminform* **2016**, *8* (1), 3. <https://doi.org/10.1186/s13321-016-0115-9>.
- (73) Kim, S.; Chen, J.; Cheng, T.; Gindulyte, A.; He, J.; He, S.; Li, Q.; Shoemaker, B. A.; Thiessen, P. A.; Yu, B.; et al. PubChem 2019 Update: Improved Access to Chemical Data. *Nucleic Acids Res* **2019**, *47* (Database issue), D1102–D1109. <https://doi.org/10.1093/nar/gky1033>.
- (74) National Library of Medicine (US). HSDB: Potassium Cyanate <http://toxnet.nlm.nih.gov/cgi-bin/sis/search2/r?dbs+hsdb:@term+@DOCNO+1757> (accessed Jul 16, 2019).
- (75) Matsui, S.; Aida, H. Hydrolysis of Some N-Alkylmaleimides. *J. Chem. Soc., Perkin Trans. 2* **1978**, No. 12, 1277. <https://doi.org/10.1039/p29780001277>.
- (76) National Library of Medicine (US). HSDB: Formamide <http://toxnet.nlm.nih.gov/cgi-bin/sis/search2/r?dbs+hsdb:@term+@DOCNO+88> (accessed Jul 16, 2019).
- (77) Miyadera, T.; Kosower, E. M. Receptor Site Labeling through Functional Groups. 2. Reactivity of Maleimide Groups. *Journal of Medicinal Chemistry* **1972**, *15* (5), 534–537. <https://doi.org/10.1021/jm00275a024>.
- (78) Prasse, C.; Ford, B.; Nomura, D. K.; Sedlak, D. L. Unexpected Transformation of Dissolved Phenols to Toxic Dicarbonyls by Hydroxyl Radicals and UV Light. *Proceedings of the National Academy of Sciences* **2018**, *115* (10), 2311–2316. <https://doi.org/10.1073/pnas.1715821115>.
- (79) Galichet, F.; Mailhot, G.; Bonnemoy, F.; Bohatier, J.; Bolte, M. Iron(III) Photo-Induced Degradation of Isoproturon: Correlation between Degradation and Toxicity. *Pest. Manag. Sci.* **2002**, *58* (7), 707–712. <https://doi.org/10.1002/ps.505>.
- (80) Tixier, C.; Meunier, L.; Bonnemoy, F.; Boule, P. Phototransformation of Three Herbicides: Chlorbufam, Isoproturon, and Chlorotoluron. Influence of Irradiation on Toxicity. *International Journal of Photoenergy* **2000**, *2* (1), 1–8. <https://doi.org/10.1155/S1110662X00000015>.
- (81) Calza, P.; Vione, D.; Fabbri, D.; Aigotti, R.; Medana, C. Imidazolium-Based Ionic Liquids in Water: Assessment of Photocatalytic and Photochemical Transformation. *Environ. Sci. Technol.* **2015**, *49* (18), 10951–10958. <https://doi.org/10.1021/acs.est.5b02738>.
- (82) Kaiser, H.-P.; Köster, O.; Gresch, M.; Périsset, P. M. J.; Jäggi, P.; Salhi, E.; von Gunten, U. Process Control For Ozonation Systems: A Novel Real-Time Approach. *Ozone: Science & Engineering* **2013**, *35* (3), 168–185. <https://doi.org/10.1080/01919512.2013.772007>.
- (83) Cederbaum, A. I.; Berl, L. Pyrazole and 4-Methylpyrazole Inhibit Oxidation of Ethanol and Dimethyl Sulfoxide by Hydroxyl Radicals Generated from Ascorbate, Xanthine Oxidase, and Rat Liver Microsomes. *Archives of Biochemistry and Biophysics* **1982**, *216* (2), 530–543. [https://doi.org/10.1016/0003-9861\(82\)90242-9](https://doi.org/10.1016/0003-9861(82)90242-9).
- (84) Darnall, K. R.; Townsend, L. B.; Robins, R. K. The Structure of Showdomycin, a Novel Carbon-Linked Nucleoside Antibiotic Related to Uridine. *PNAS* **1967**, *57* (3), 548–553. <https://doi.org/10.1073/pnas.57.3.548>.

Supporting Information for Chapter 3

Reactions of pyrrole, imidazole, and pyrazole with ozone: Kinetics and mechanisms

All reagent solutions (aqueous) were prepared in ultrapurified water obtained from Barnstead™ Nanopure™ (Thermo Scientific) or Direct8/16system (Merck Millipore).

Table S3.1. List of chemicals used.

Chemicals and purity	Suppliers	Product No.
1,5-Dihydro-pyrrol-2-one ≥98%	Chem-Impex	CH6371383198
1-Benzylimidazole 99%	Sigma Aldrich	116416
1-Benzylpyrazole 98%	abcr	AB312011
1H-Pyrazol-4-ol 97%	abcr	AB416886
1H-Pyrazole-3,4,5-d ₃	Toronto Research Chemicals	P842197
6-benzyladenine 98.5%	Dr. Ehrenstorfer	DRE-C10569600
Acetic acid (glacial) 100%	Merck	1370002500
Acetone-d ₆ 99.9%	Cambridge Isotope Laboratories	DLM-9-25
Acetonitrile Optima™ LC/MS Grade	Fisher Chemical	A955-212
Acetylacetone ≥99%	Sigma Aldrich	8000230250
Ammonium acetate ≥98%	Merck	1011160500
Ammonium bicarbonate ≥99.5%	Sigma Aldrich	09830-500G
Ammonium formate ≥99.0%	Sigma-Aldrich	17843
Dimethylsulfoxide 99.9%	J.T. Baker	
di-Sodium hydrogen phosphate dihydrate ≥99.5%	Merck	106580
DMSO-d ₆ 99.9%	Cambridge Isotope Laboratories	DLM-10-100
EPA 8270/Appendix IX Nitrosamines Mix	Sigma Aldrich	502138
Formaldehyde 37%	Merck	
Formic acid 98-100%	Merck	100264
Imidazole anhydrous ≥99%	Sigma Aldrich	792527
Imidazole-d ₄ 98%	Cambridge Isotope Laboratories	DLM-3033-1
Maleimide 99%	Sigma Aldrich	129585-2G
Methanol Optima™ LC/MS Grade	Fisher Chemical	A456-212
N-Benzylformamide 99%	abcr	AB131671
Phosphoric acid ≥85%	Sigma Aldrich	30417
Potassium indigotrisulfonate	Sigma Aldrich	234087
Pyrazole 98%	Sigma Aldrich	P56607-5G
Pyrrole-d ₅ 98%	Cambridge Isotope Laboratories	DLM-3192-1
Sodium cyanate 96%	Sigma Aldrich	185086
Sodium dihydrogen phosphate monohydrate 99-102%	Merck	106346
tert-Butanol ≥ 99.7%	Sigma Aldrich	19460

Text S3.1. Reaction kinetics

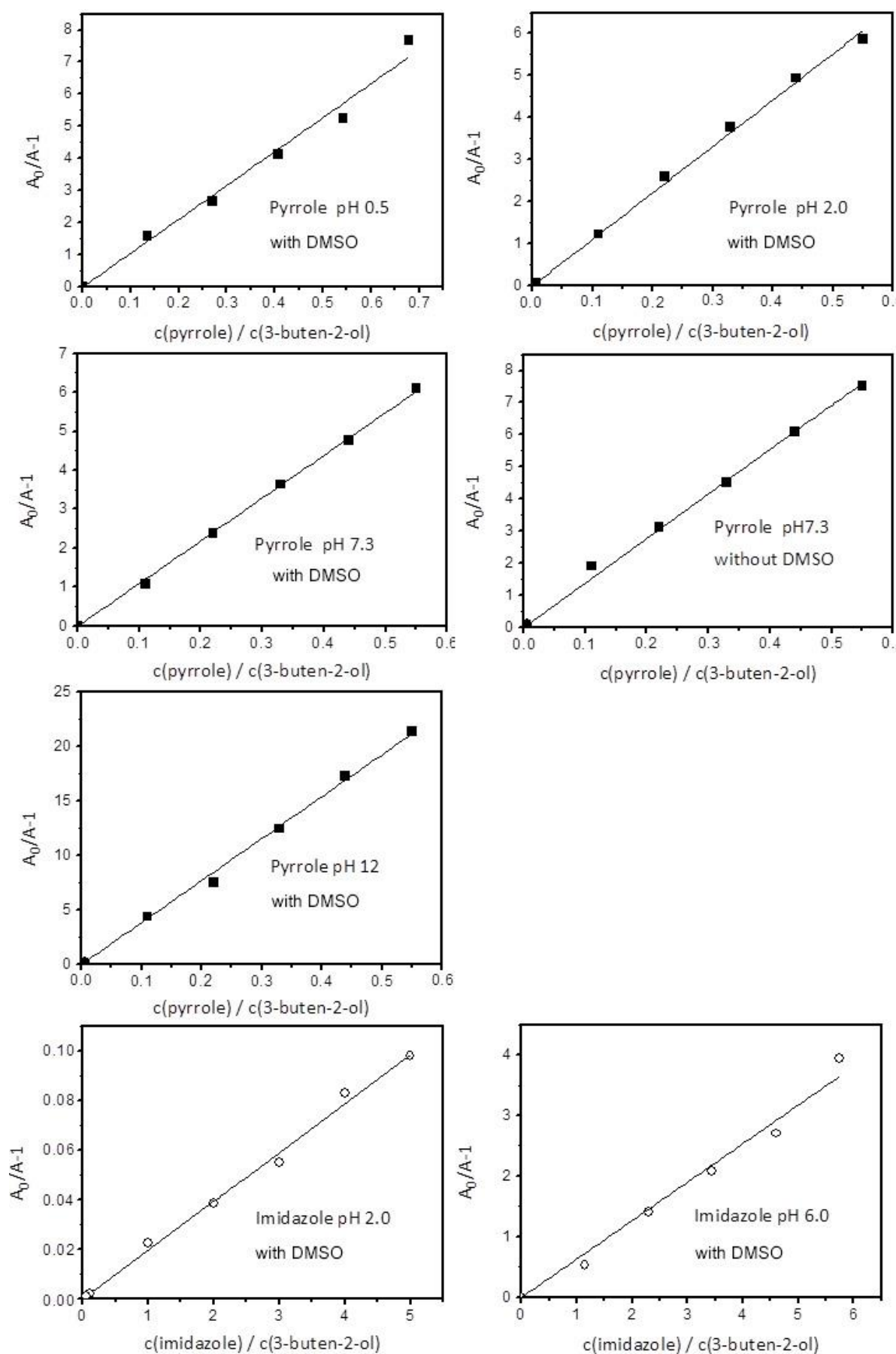
This section describes the methods used for determining the reaction kinetics of the reactions of azoles with ozone and presents the data plots from competition kinetics and pseudo-first-order kinetic experiments (Figure S3.1).

Competition kinetics for determination of k_{O_3} of pyrrole and imidazole. The apparent second-order rate constants for the reactions of pyrrole, imidazole, and pyrazole with ozone (k_{app}) at pH 0.5 to 12 were determined by a competition kinetics method with 3-buten-2-ol as a competitor. Reaction vessels containing an azole (typically 0.1 – 0.6 mM for pyrrole and 1 – 5 mM for imidazole), 3-buten-2-ol (1 mM) at various ratios and dimethylsulfoxide (DMSO, 0.1 M) as a $\cdot OH$ scavenger were prepared and a fixed dosage of an ozone stock solution ($\sim 40 \mu M$) was added under rapid mixing. DMSO was used to quench $\cdot OH$ instead of *t*-butanol, because the reaction of *t*-butanol with $\cdot OH$ produces formaldehyde, the same product as expected for the reaction of 3-buten-2-ol with ozone. The second-order rate constants are $8.2 M^{-1} s^{-1}$ for the reaction of DMSO with ozone¹ and $6.6 \times 10^9 M^{-1} s^{-1}$ for the reaction of DMSO with $\cdot OH$.² After the reaction, formaldehyde, a product of the reaction of 3-buten-2-ol with ozone, was quantified by the Hantzsch method.³ The second-order rate constant of an azole was deduced based on the following equation with $7.9 \times 10^4 M^{-1} s^{-1}$ as $k_{O_3,3\text{-buten-2-ol}}$.⁴

$$\frac{[\text{formaldehyde}]_0}{[\text{formaldehyde}]} = 1 + \frac{k_{O_3,azole}[\text{azole}]}{k_{O_3,3\text{-buten-2-ol}}[3\text{-buten-2-ol}]}$$

Direct measurement of pyrazole decrease for determination of k_{O_3} of pyrazole. The apparent second-order rate constant for the reaction of pyrazole with ozone at pH 7 was determined by a direct method following pyrazole decrease over time under conditions with ozone in excess. Using the ozone-excess condition was necessary, because otherwise the ozone-reactive transformation products formed during the pyrazole-ozone reaction (see the section 3.3.3.3 of the main text) would lead to an overestimation of the second-order ozone rate constant. A solution containing 5 μM of pyrazole and 0.3 mM of *t*-butanol as a $\cdot OH$ scavenger was prepared at pH 7 (10 mM phosphate buffer). An aliquot of the primary ozone stock solution (typically 1.3 – 1.5 mM) was added to the pyrazole solution to yield 100 μM ozone. Samples were taken by a laboratory dispenser at pre-determined reaction times (starting from 15 s) at which the residual ozone concentrations in the samples were quenched by approximately 200 μM cinnamic acid. The pyrazole concentrations were determined by HPLC-UV.

Direct measurement of ozone decrease by a quench-flow apparatus for determination of k_{O_3} of maleimide and 4-hydroxypyrazole. A solution containing 1.9 mM of maleimide or 4-hydroxypyrazole and 0.5 M of *t*-butanol was prepared at pH 7 (10 mM phosphate buffer). An ozone stock solution (0.275 mM) was prepared by diluting the primary ozone stock solution (typically 1.3 – 1.5 mM) with 1 mM hydrochlorous acid solution and kept in ice packs. The reaction was initiated by mixing the substrate and the ozone solutions at a ratio of 10:1 (1.7 mM substrate and 0.025 mM ozone as the concentrations after mixing) and an indigotrisulfonate solution (0.038 mM) was added at pre-determined reaction times to quench the remaining ozone. The experiments were conducted by a quench-flow apparatus (BioLogic, SFM-400/Q) which allows quenching the reactions within a ms range. The ozone concentrations were determined by the decolorization of the indigo solution measured spectrophotometrically at 600 nm ($\epsilon_{600nm} = 20,000 M^{-1} cm^{-1}$).⁵ For 4-hydroxypyrazole, ozone was completely consumed within the shortest reaction time (22 ms). Assuming 98% of ozone is consumed at 22 ms, the second-order rate constant for the reaction of 4-hydroxypyrazole with ozone was estimated to be higher than $9 \times 10^4 M^{-1} s^{-1}$.



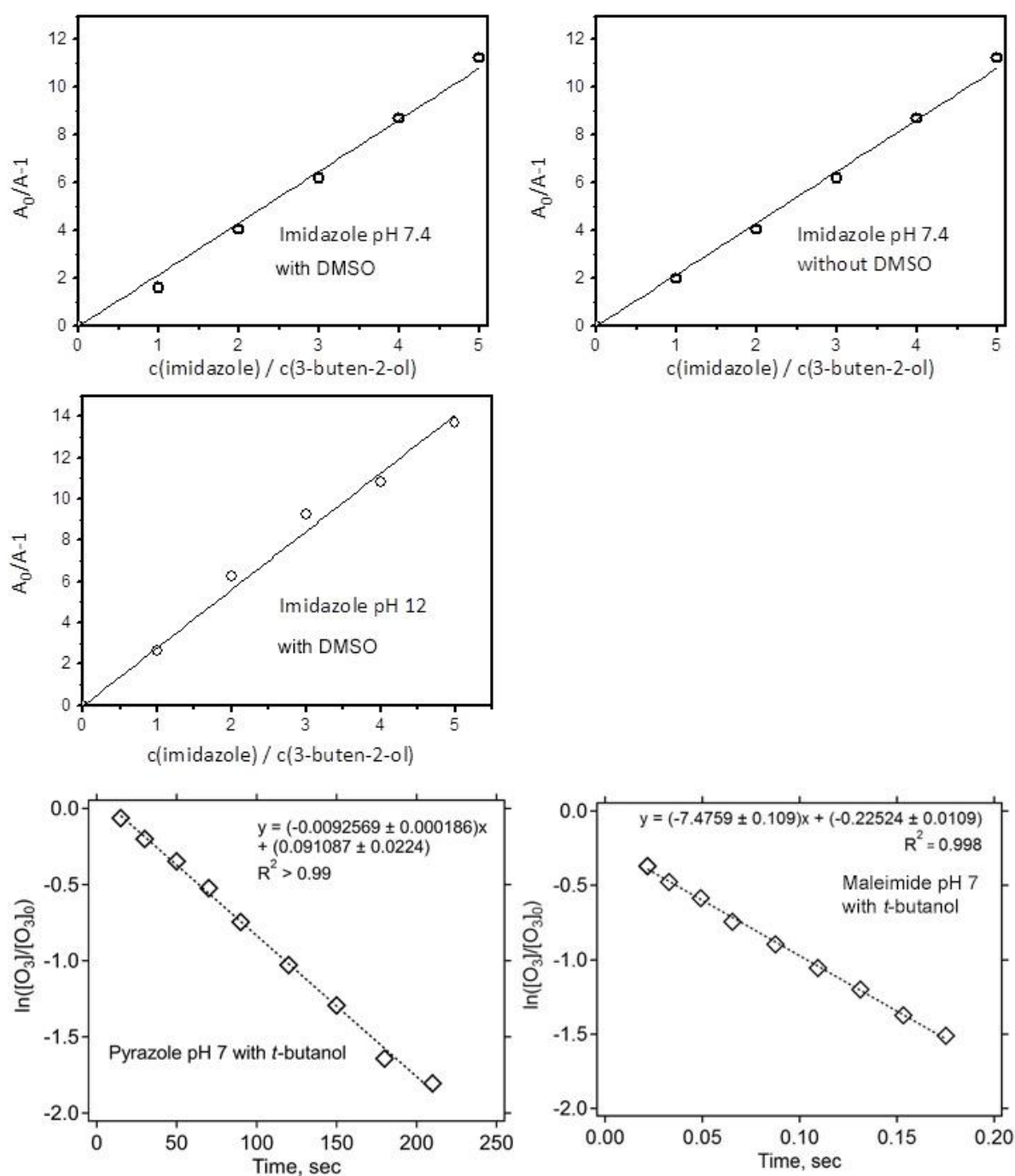


Figure S3.1. Competition kinetics plots for the reactions of ozone with pyrrole, imidazole, and pyrazole under varying pH conditions corresponding to the results presented in Table S3.2. A pseudo-first-order kinetic plot for the reaction of maleimide with ozone at pH 7 is also shown. Data points shown in each plot are from single measurements.

Table S3.2. Compilation of the apparent second-order rate constants (k_{app}) for the reactions of pyrrole, imidazole, pyrazole, and maleimide with ozone for the pH range 0.5 – 12.

Compound	pH	$\cdot\text{OH}$ scavenger	$k_{app}, \text{M}^{-1} \text{s}^{-1}$
Pyrrole	0.5	DMSO	$(8.3 \pm 0.6) \times 10^5$
	2.0	DMSO	$(8.7 \pm 0.6) \times 10^5$
	7.3	DMSO	$(8.6 \pm 0.7) \times 10^5$
	7.3	None	$(1.1 \pm 0.2) \times 10^6$
	12.0	DMSO	$(3.1 \pm 0.4) \times 10^6$
Imidazole	2.0	DMSO	$(1.5 \pm 0.1) \times 10^3$
	6.0	DMSO	$(5.0 \pm 0.5) \times 10^4$
	7.4	DMSO	$(1.7 \pm 0.2) \times 10^5$
	7.4	None	$(1.5 \pm 0.1) \times 10^5$
	12.0	DMSO	$(2.2 \pm 0.2) \times 10^5$
Pyrazole	7.0	<i>t</i> -butanol	$(5.6 \pm 0.9) \times 10^1$
Maleimide	7.1	<i>t</i> -butanol	$(4.2 \pm 0.2) \times 10^3$

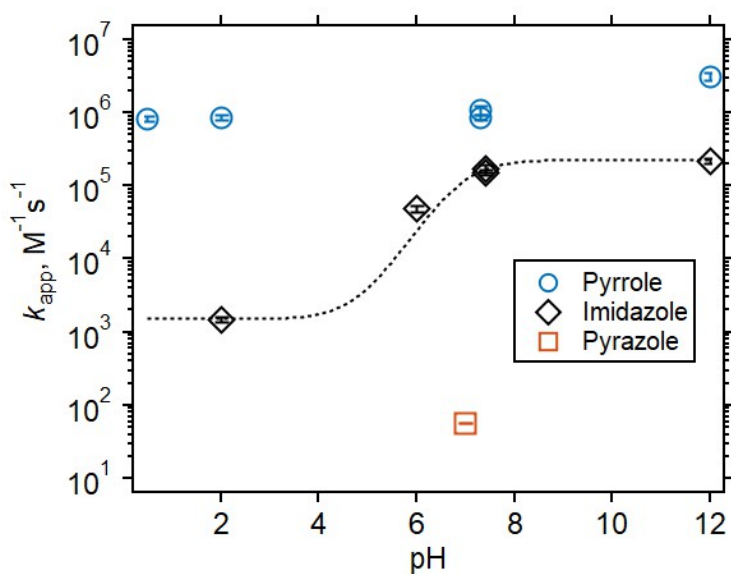


Figure S3.2. Logarithmic apparent second-order rate constants (k_{app}) for the reactions of pyrrole, imidazole, and pyrazole with ozone as a function of the pH in the range 0 to 12. The k_{app} values of imidazole were fitted to the expression: $k_{app} = k_{NH^+}(1-\alpha) + k_N\alpha$ and $\alpha = 1/(1 + 10^{pK_a - pH})$, where k_{NH^+} and k_N are the species-specific second-order rate constants for the protonated and the neutral imidazole, respectively, α is the fraction of the neutral imidazole, and a pK_a value of imidazole is 7.0.⁶ The following species-specific second-order rate constants were obtained: $(2.3 \pm 0.1) \times 10^5 \text{ M}^{-1} \text{ s}^{-1}$ for neutral imidazole (k_N) and $(1.5 \pm 0.1) \times 10^3 \text{ M}^{-1} \text{ s}^{-1}$ for protonated imidazole (k_{NH^+}). The species-specific second-order rate constant for the reaction of pyrrole with ozone was obtained to be $(1.4 \pm 1.1) \times 10^6 \text{ M}^{-1} \text{ s}^{-1}$ by averaging k_{app} for the pH range 0.5 – 12.

Text S3.2. Kinetic simulations

The evolution of pyrrole and its transformation products as a function of the molar ratio of $[O_3]/[Pyrrole]_0$ was simulated by a kinetic simulation with the Kintecus software⁷ based on a model described in Table 3.3. The simulated concentrations are shown as lines in Figure 3.2 in the main text. The imidazole-ozone reaction was also simulated based on a model described in Table 3.4 and the results are shown as lines in Figure 3.5 in the main text. Only the consumption of ozone by pyrrole, imidazole, and their transformation products were considered.

Table S3.3. Kinetic model for the pyrrole-ozone reactions performed by Kintecus.⁷ The initial concentrations of pyrrole and ozone were set as $[pyrrole] = 115 \mu M$ and $[O_3] = 0 - 250 \mu M$ (in $2 \mu M$ increments). Simulated reaction time was set as 4 h.

No.	Reaction	$k_{app,pH7}, M^{-1} s^{-1}$	Reference
1	Pyrrole + $O_3 \rightarrow 0.34 \cdot \text{maleimide}$	8.6×10^5	Table 3.1 of main text
2	Maleimide + $O_3 \rightarrow \text{Products}$	4.2×10^3	Table 3.1 of main text

Table S3.4. Kinetic model for the imidazole-ozone reaction performed by Kintecus.⁷ The initial concentrations of imidazole and ozone were set as $[pyrrole] = 94.5 \mu M$ and $[O_3] = 0 - 250 \mu M$ (in $2 \mu M$ increments). Simulated reaction time was set as 4 h.

No.	Reaction	$k_{app,pH7}, M^{-1} s^{-1}$	Reference
1	Imidazole + $O_3 \rightarrow \text{Cyanate} + \text{Formamide} + \text{Formate}$	1.7×10^5	Table 3.1 of main text
2	Cyanate + $O_3 \rightarrow \text{Products}$	1.0×10^{-2}	Hoigné et al. (1985) ⁸
3	Formamide + $O_3 \rightarrow \text{Products}$	1.0×10^{-2}	assumed as a slow reaction, considering the similar evolution as for cyanate (see Figure 3.5 in the main text)
4	Formate + $O_3 \rightarrow \text{Products}$	46	Reisz et al. (2014) ⁹

Text S3.3. Ozonation experiments

The required initial concentrations of azoles and ozone doses varied depending on the applied analytical methods for product identification. For example, NMR analyses require at least a few milligrams of isolated solids, whereas LC-HRMS is capable of detecting submicromolar concentrations. Accordingly, various ozonation conditions were applied in this study and are described below.

- a) *Ozonation experiment for quantifying pyrrole, imidazole, pyrazole, 1-benzylimidazole, 1-benzylpyrazole, maleimide, urea, N-benzylformamide, cyanate, formate, and total N-nitrosamines by LC-HRMS/MS, IC-CD, and total N-nitrosamine analyses.* Ozonation experiments were conducted under the condition as described in the section 3.2 of the main text: $[azole] \sim 100 \mu M$, $[t\text{-butanol}] = 50 \text{ mM}$, $[ozone] = 0 - 200 \mu M$, and 10 mM phosphate buffer (pH 7). Ozone stock solutions were prepared by an ozone generator (BMT MESSTECHNIK GMBH, BMT 803 BT). The oxygen gas flow rate was set as 0.15 NL min^{-1} (N stands for normal conditions being 0°C and 1 atm) and the power of ozone generator was 100%. Based on the instrument manual (Rev. 05/2014), this condition yielded approximately 2.4 g h^{-1} of ozone production rate. Additionally for quantifying maleimide, $100 \mu M$ of pyrrole and 50 mM of *t*-butanol were prepared at pH 2 (10 mM phosphate buffer) to investigate the pH effect on maleimide formation.

- b) *Ozonation experiment for quantifying formamide by HPLC-UV.* Because of the high dilution factor (100-fold) required for quantification of formamide by HPLC-UV (see Text S3.4 for detailed method), a millimolar range of formamide should be formed during the azole-ozone reactions for the detection. Millimolar concentrations of azole and ozone were required accordingly. To this end, the primary ozone stock solution (1.59 ± 0.05 mM) was prepared as described above and 9 mL of the ozone stock solution were transferred to a 10 mL reaction vessels containing 1 – 2 mL of the mixture of azole, 1 M *t*-butanol, and 10 mM phosphate buffer solution at pH 7 under rapid stirring. The concentrations of azole in the mixtures were 0.8 mM – 2 mM of pyrrole, 1 mM – 4 mM of imidazole, and 0.3 mM – 1.5 mM of pyrazole, to produce varying molar $[O_3]/[azole]_0$ ratios of 0.8 – 2.0 for pyrrole, 0.4 – 1.5 for imidazole, and 1.0 – 5.6 for pyrazole. The ozonated solutions were left at room temperature for 4 hours and stored at 4 °C prior to HPLC-UV analysis carried out within 3 days.
- c) *Ozonation experiment for quantifying glyoxal by derivatization followed by HPLC-UV and for quantifying formate by IC-CD.* 1 mM of azoles were prepared in ultrapurified water without buffering agents in a volume of 20 – 25 mL in presence (0.1 – 0.5 M) or absence of *t*-butanol. Additionally, 1 mM of azoles in presence (0.1 – 0.5 M) or absence of *t*-butanol were prepared at pH 2 (by adding sulfuric acid) or pH 11 (by adding sodium hydroxide) to investigate the pH effect on glyoxal and formate formation. Ozone stock solutions were prepared by another ozone generator (Erwin Sander Elektroapparatebau GmbH, Laboratory Ozonizer 300.5), yielding the maximum concentration of the stock solution of 1 mM. An aliquot of the ozone stock solution was added to the azole solution to initiate ozonation with ozone doses ranging from 40 μ M to 200 μ M. The pH of the azole solution without buffering agents was in the range of pH 6.5 – 7.4 prior to ozonation, which decreased to pH 4.3 – 6.1 after ozonation. The pH of the acidified (pH 2) and basified (pH 11) solutions remained the same after ozonation. The complete consumption of ozone was verified regularly with indigotrisulfonate.
- d) *Ozonation experiments for identifying TP1, TP2, and maleimide by NMR.* Solutions containing 1 mM of pyrrole and 1 M of *t*-butanol were prepared in ultrapurified water without buffering agents with a total volume of 1 L. Buffering agents could not be used because they would remain in too large quantities after work-ups for NMR (Text S3.4), which makes it difficult to isolate ozonation products. A decrease in pH was observed from pH 5.8 before ozonation to pH 4.5 after ozonation. Ozonation was initiated by directly sparging an ozone-containing oxygen gas flow produced by an ozone generator (BMT MESSTECHNIK GMBH, BMT 803 BT) to the pyrrole solution, which was kept at room temperature under constant stirring. The oxygen gas flow rate was set as 0.02 NL min⁻¹ and the power of ozone generator was 30 %. Under this condition, the ozone production rate would be roughly 0.1 g h⁻¹. During ozonation, 100 μ L of samples were withdrawn at pre-defined reaction times, to analyze the remaining pyrrole concentrations in the solution by HPLC-UV. As a result, a 30 min ozonation time was selected for NMR analyses, for which more than 80% pyrrole was abated. A control experiment by sparging oxygen gas with the same flow rate but without generating ozone was performed in parallel to confirm the effect of the gas flow on evaporation or abatement of pyrrole. The HPLC-UV result of the control experiment confirmed that the pyrrole concentrations remained unchanged over 90 min under the oxygen gas flow.

Text S3.4. Analytical methods for azoles and their transformation products

This section describes the analytical methods used for quantifying abatement of azoles upon ozonation and for identifying/quantifying transformation products formed during the azole-ozone reactions.

NMR analyses for TP1, TP2, and maleimide. Prior to NMR analyses, *t*-butanol and water in ozonated solutions were removed by (1) rotary evaporation (Hei-VAP, Heidolph) at 40 °C to dryness, or (2) rotary evaporation at 25 °C to 20 % removal in weight, followed by lyophilization (LYOVAC GT 2-E, STERIS) to dryness. The work-up procedure (2) was employed to minimize the increase of temperature in the solution, which appeared to promote polymerization of ozonated products. The isolated solids were dissolved in acetone- d_6 or DMSO- d_6 . ^1H and ^{13}C NMR data were measured at 400.2 MHz and 100.6 MHz using a 5 mm CryoProbe™ Prodigy probe equipped with z-gradient on a Bruker Avance III 400 NMR spectrometer (Bruker Biospin AG, Fällanden, Switzerland). The 1D ^1H , ^{13}C and ^1H 1D-NOESY NMR experiments and the 2D correlated ^1H - ^{13}C HSQC, ^1H - ^{13}C HMBC, ^1H - ^1H DQF-COSY, and ^1H - ^1H NOESY experiments were performed at 298 K using the Bruker standard pulse programs and parameter sets applying 90° pulse lengths of 11.4 μs (^1H) and 10.0 μs (^{13}C). Chemical shifts (δ) in ppm are calibrated to residual solvent peaks (DMSO- d_6 : δ = 2.49 and 38.5 ppm; acetone- d_6 : δ = 2.05 and 29.8 ppm). Details of product identification by the NMR analyses are provided in Text S3.7.

LC-HRMS for pyrrole, imidazole, pyrazole, 1-benzylimidazole, 1-benzylpyrazole, maleimide, urea, and N-benzylformamide. Non-ozonated (ozone dose = 0 μM , azole concentration 100 μM) and ozonated samples were diluted 10-fold (for imidazole, pyrazole, 1-benzylimidazole, urea, and *N*-benzylformamide) or 20-fold (for pyrrole and 1-benzylpyrazole) in ultrapurified water or in acetonitrile depending on the applied LC column. For quantifying maleimide, ozonated samples were analyzed without dilution, because of the relatively poor sensitivity of detecting maleimide by LC-HRMS/MS (see the limits of quantification of maleimide and other compounds summarized in Table S3.6). Pyrrole- d_5 (5 μM as final concentration), imidazole- d_5 (10 μM), pyrazole (1 μM), or 6-benzyladenine (1 μM) prepared in acetonitrile or in ultrapurified water were used as internal standards for all analytes except urea (Text S3.16). Pyrrole, pyrazole, 1-benzylimidazole, 1-benzylpyrazole, and *N*-benzylformamide in the samples diluted in ultrapurified water were separated on a C18 reversed-phase (RP) column (Atlantis® T3, 3 μm particle size, 3.0 \times 150 mm, Waters) at 30 °C with a flow of 300 $\mu\text{L}/\text{min}$ and ultrapurified water and methanol as eluents. 0.1% formic acid was added to both eluents. The gradient started with 98% of ultrapurified water during the first 1.5 min, which linearly decreased to 2% between 1.5 min and 17.5 min, maintained at 2% until 25 min, returned to the initial condition of 98% ultrapurified water at 25.1 min, and maintained at 98% until 29.5 min for column re-equilibration. Imidazole and urea in the samples diluted in acetonitrile were separated on a hydrophilic interaction liquid chromatography (HILIC) column (XBridge™ BEH HILIC XP, 2.5 μm particle size, 3.0 \times 150 mm, Waters) at 30 °C with a flow of 400 $\mu\text{L min}^{-1}$ and ultrapurified water and an acetonitrile:methanol:ultrapurified water mixture (95:3:2) as eluents. 1mM ammonium formate and 0.1% formic acid was added to both eluents. The gradient started with 100% of the acetonitrile mixture during the first 2 min, which linearly decreased to 5% between 2 min and 12 min, maintained at 5% until 17 min, returned to the initial condition of 100% acetonitrile mixture at 17.1 min, and maintained at 100% until 37 min for column re-equilibration. After separation on the RP or HILIC column, compounds were detected by a Thermo Scientific Q-Exactive high-resolution mass spectrometer (R = 70,000) with electrospray ionization (ESI) in positive full scan mode with a spray voltage of 4000 V, a capillary temperature of 350 °C, a sheath gas flow rate of 40 (arbitrary units), and an auxiliary gas flow rate of 10 (arbitrary units). Detected and theoretical exact masses deviated typically within 5 ppm (Table S3.5), except urea which showed high mass deviation of ~50 ppm for both ozonated samples and standards (Text S3.16).

Table S3.5. Theoretical and detected exact masses as $[M+H]^+$ of the compounds (parent compounds (azoles) and identified or suspected transformation products) measured by LC-HRMS/MS.

Compound	Type	Molecular formula	Theoretical mass	Detected mass
Pyrrole	Parent	C ₄ H ₅ N	68.0495	68.0495
Maleimide	TP	C ₄ H ₃ NO ₂	98.0237	98.0236
N-(3-oxo-1-propen-1-yl)formamide (TP1)	TP	C ₄ H ₅ NO ₂	100.0393	100.0391
5-Hydroxy-1,5-dihydro-2H-pyrrol-2-one (TP2)	TP	C ₄ H ₅ NO ₂	100.0393	100.0391
1,5-dihydro-pyrrole-one	TP	C ₄ H ₅ NO	84.0444	84.0443
Imidazole	Parent	C ₃ H ₄ N ₂	69.0447	69.0448
Urea	TP	CH ₄ N ₂ O	61.0396	61.0368
1-Benzylimidazole	Parent	C ₁₀ H ₁₀ N ₂	159.0917	159.0915
N-Benzylformamide	TP	C ₈ H ₉ NO	136.0757	136.0755
Pyrazole	Parent	C ₃ H ₄ N ₂	69.0447	69.0448
Formylhydrazine	TP	CH ₄ N ₂ O	61.0396	ND
4,5-dihydroxypyrazole	TP	C ₃ H ₄ N ₂ O ₂	101.0346	ND
1-Benzylpyrazole	Parent	C ₁₀ H ₁₀ N ₂	159.0917	159.0919
Candidate 191	TP	C ₁₀ H ₁₀ N ₂ O ₂	191.0815	191.0813
Candidate 151	TP	C ₈ H ₁₀ N ₂ O	151.0866	151.0864

Table S3.6. Limits of quantification (LOQ) of azoles and identified or suspected transformation products.

Compound	Method	LC column	LOQ, μM^a	Calibration	R ² of calibration curve	Retention time
Pyrrole	LC-HRMS/MS	RP	1.1	0.5 μM – 5 μM	> 0.99	9.2
Imidazole	LC-HRMS/MS	HILIC	0.8	1 μM – 10 μM	> 0.99	6.8
Pyrazole	LC-HRMS/MS	RP	2.5	1 μM – 10 μM	> 0.99	6.4
1-Benzylimidazole	LC-HRMS/MS	RP	3.0	1 μM – 10 μM	> 0.99	8.6
1-Benzylpyrazole	LC-HRMS/MS	RP	2.7	0.5 μM – 5 μM	0.97	15.8
Maleimide	LC-HRMS/MS	RP	12.9	10 μM – 100 μM	> 0.99	4.9
N-(3-oxo-1-propen-1-yl)formamide (TP1)	LC-HRMS/MS	RP	ND	ND	ND	6.3 ^b
5-Hydroxy-1,5-dihydro-2H-pyrrol-2-one (TP2)	LC-HRMS/MS	RP	ND	ND	ND	4.2 ^b
1,5-Dihydro-pyrrole-one	LC-HRMS/MS	RP	ND	ND	ND	Unconfirmed ^c
Urea ^d	LC-HRMS/MS	HILIC	2.1	1 μM – 10 μM	> 0.99	4.0
N-benzylformamide	LC-HRMS/MS	RP	2.9	1 μM – 10 μM	> 0.99	12.6
Candidate 191	LC-HRMS/MS	RP	ND	ND	ND	12.0
Candidate 151	LC-HRMS/MS	RP	ND	ND	ND	11.7
Cyanate	IC-CD	AS19	0.5	1 μM – 20 μM	> 0.99	10.0
Formate	IC-CD	AS19	1.0	1 μM – 20 μM	> 0.99	6.2
Formamide	HPLC-UV	HILIC	1.6	1 μM – 10 μM	> 0.99	2.9
Total N-nitrosamines	UV-Photolysis and Chemiluminescence ¹²	NA	0.7 ^e	0.4 μM – 4 μM	0.94	NA
Glyoxal	Deriv-HPLC-UV ^f	RP	0.8	1 μM – 20 μM	-	9.3

^aLOQs were estimated based on the slope of the calibration curve (s) and the standard deviation of the y-intercept of the calibration curve (σ) with the following equation, $\text{LOQ} = 10 \times \sigma/s$,¹¹ for all compounds except total N-nitrosamines. ^bInconclusive but suggested based on structural characteristics and distinct MS2 fragmentation patterns (see main text). ^cBecause of too many peaks (Figure S3.23b). ^dUrea quantification

was performed without internal standard. e LOQ of total *N*-nitrosamine analysis was determined based on a signal-to-noise ratio of 10.¹² *o*-phenylenediamine derivatization followed by HPLC-UV analysis.¹³

IC-CD for cyanate and formate and IC-MS for cyanate. Ozonated samples in the pH 7 buffered system (parent concentration 100 μ M) were diluted 4-fold in ultrapure water to reduce column overloading from phosphate buffer. Cyanate and formate in the diluted samples were then separated on a capillary anion-exchange IC column (Ion-Pac AS19-4 μ M, 0.4 \times 250 mm, Dionex) with a gradient of KOH as eluent with a flow rate of 0.01 mL min⁻¹. The eluent concentration was initially at 10 mM for 10 min, increased to 28.5 mM between 10 min and 15 min, increased to 120 mM between 15 min and 15.1 min, was maintained at 120 mM until 23 min, went back to the initial concentration of 10 mM between 23 min and 23.1 min, and held at 10 mM until 32 min. The anions were detected by suppressed conductivity (ACES 300 Capillary Electrolytic Suppressor, Dionex). Examples of chromatograms of an ozonated sample and standards are shown in Figure S3.3. For cyanate, additional confirmation was carried out once by using a mass spectrometer (TSQ-Vantage, Thermo Scientific) by following a fragmentation reaction: $m/z = 42.0 \rightarrow 26.0$ (36 V collision energy). The MS measurements were performed in negative mode, HESI at 150°C. The peak corresponding to cyanate was observed at a retention time of 11.0 min. Formate in the ozonated samples without buffering agents or under pH 2 and 11 conditions (parent concentration 1 mM) was analyzed by IC-CD (883 Basic IC plus, Metrohm) equipped with a Metrosep Organic Acids column (Metrohm). The eluent was 0.5 mM sulphuric acid with a flow rate of 0.5 mL min⁻¹. The suppressor was regenerated with a 30 mM lithium chloride solution.

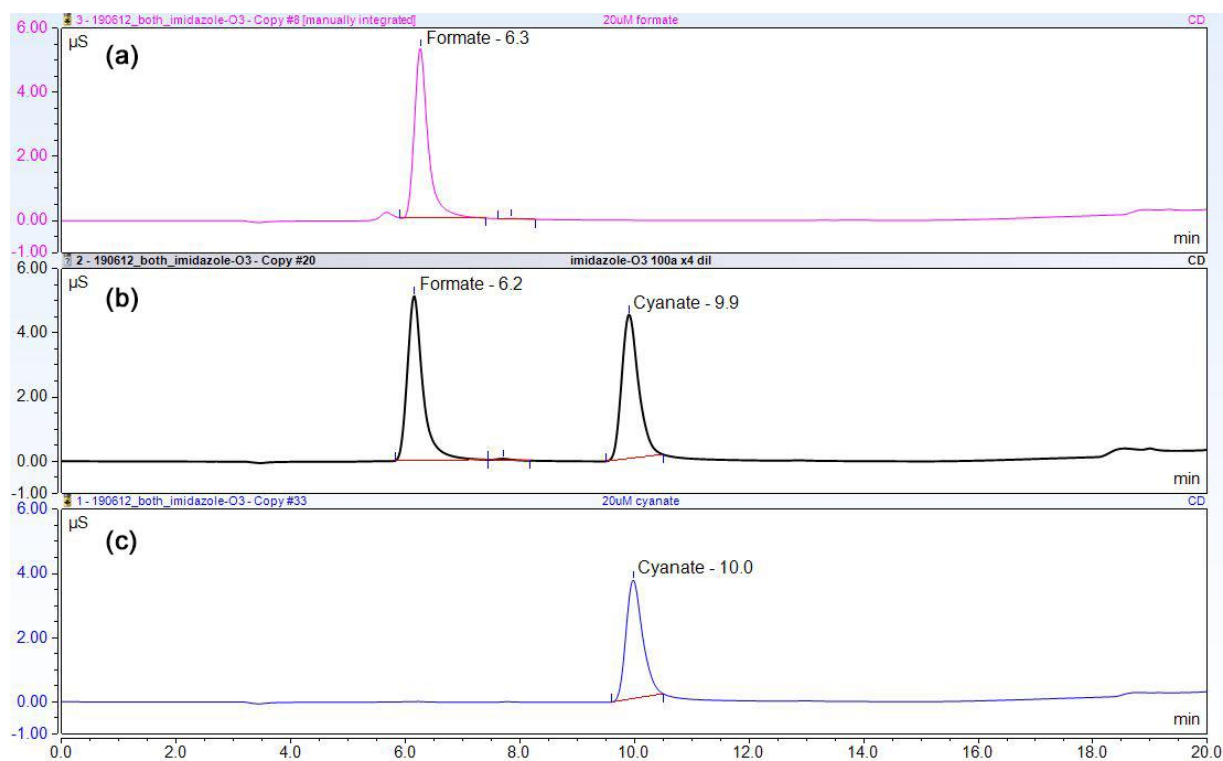


Figure S3.3. Stacked IC-CD chromatograms of (a) a 20 μ M formate standard, (b) an ozonated imidazole solution at $[O_3]/[imidazole]_0 \sim 1$ diluted 4-fold in ultrapurified water, and (c) 20 μ M cyanate standard.

HPLC-UV for pyrrole, imidazole, and pyrazole. Pyrrole and imidazole which were ozonated by sparging ozone directly into the azole solution for NMR and GC-MS analyses were analyzed by HPLC-UV to quantify the abatement. 100 μL of samples were withdrawn during ozonation at pre-determined time points and diluted 10-fold with ultrapurified water. Pyrazole of which ozone reactivity was determined by following the pyrazole decrease over time, was also analyzed by HPLC-UV without dilution. The samples for analyzing pyrrole and imidazole were separated on a Cosmosil C18 column (5C18-MS-II, 3.0×100 mm, NACALAI TESQUE, INC.) with a gradient (0.5 mL min^{-1}) of acetonitrile as eluent A and ultrapurified water (for pyrrole) or 10 mM phosphate buffer at pH 7.5 (for imidazole) as eluent B. The gradient started at 5% acetonitrile (eluent A) during 1.5 min, which linearly increased to 95% between 1.5 min and 17.5 min, maintained at 95% to 22.5 min, decreased back to the initial condition of 5% acetonitrile until 23 min, and maintained at the initial conditions until 28 min. The samples for analyzing pyrazole were separated on the same column with an isocratic method (0.5 mL min^{-1}) with 5% acetonitrile and 95% 10 mM phosphate buffer (pH 7). All azoles were analyzed by UV detection at 210 nm.

HPLC-UV for formamide. The ozonated samples containing formamide (parent concentrations 0.3 mM – 4 mM) were diluted 100-fold in acetonitrile and were separated on the HILIC column (XBridge™ BEH HILIC XP, $2.5 \mu\text{m}$ particle size, 3.0×150 mm, Waters) at 30°C with a flow of $400 \mu\text{L min}^{-1}$ via isocratic eluents of 3% ultrapurified water and 97% acetonitrile. The high dilution factor (100-fold) was required to achieve the ideal sample composition of 99% acetonitrile and 1% aqueous solution for the HILIC column. Because of the low molecular weight (m/z 45) below the MS scan range ($m/z \geq 50$), formamide could not be detected by MS. Instead, it was analyzed by UV detection at 210 nm. Known concentrations of formamide standards (5 μM and 10 μM) were added to the ozonated samples containing formamide to additionally confirm the peak retention time and the quantified results. The peak retention times remained the same (2.94 min) before and after the addition of standard solutions (Figure S3.4). The averages of the relative difference between the measured increase in formamide concentration of the spiked sample and the concentration of the spiked formamide standard were $(9 \pm 7)\%$ for 5 μM addition and $(11 \pm 1)\%$ for 10 μM addition.

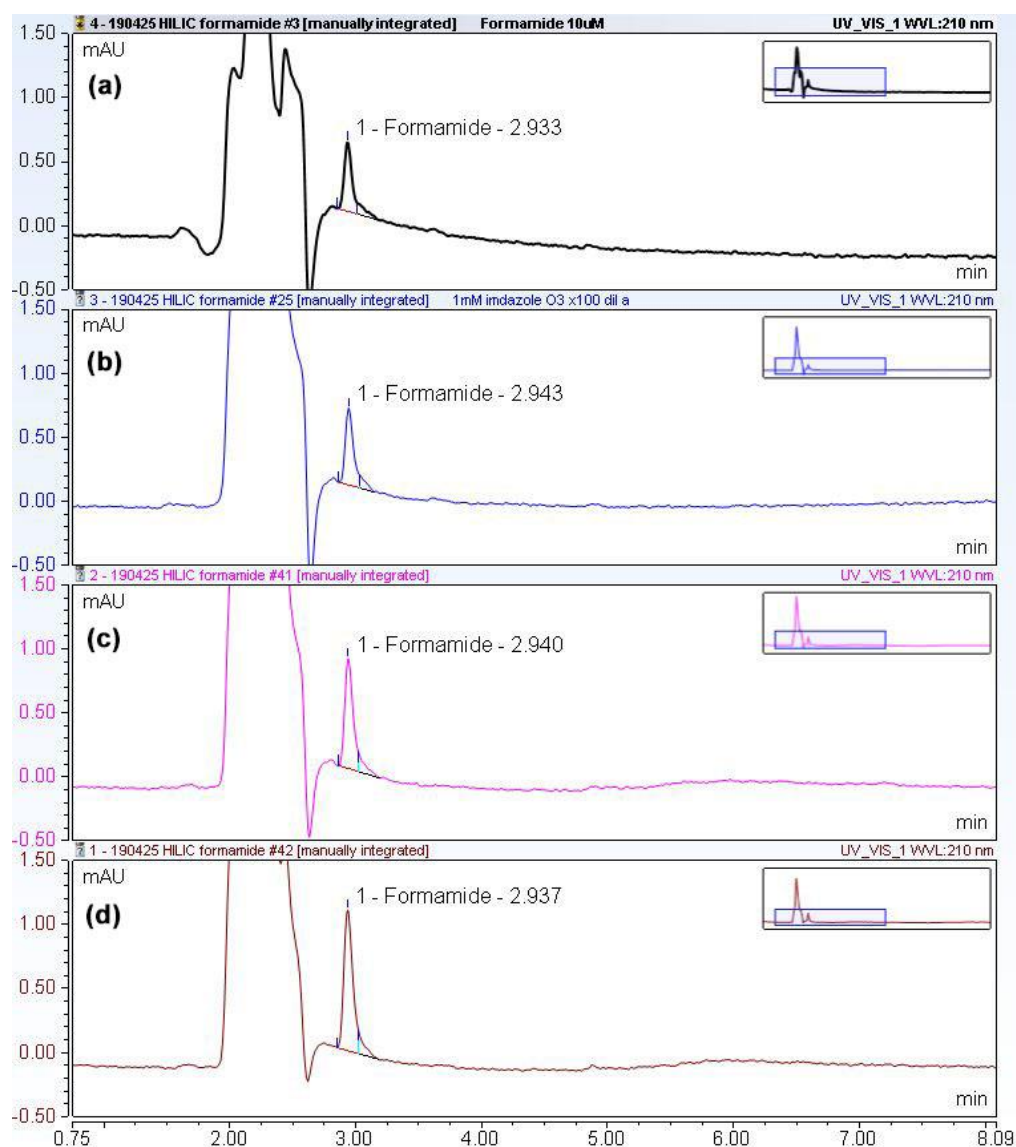


Figure S3.4. Stacked HPLC-UV chromatograms for (a) a 10 μM formamide standard, (b) an ozonated imidazole solution at $[\text{O}_3]/[\text{imidazole}]_0 \sim 1$, (c) the ozonated imidazole solution after the addition of a 5 μM formamide standard, and (d) the ozonated imidazole solution after the addition of a 10 μM formamide standard. The dead volume time of the column was 2.65 min and the retention time of formamide was at 2.94 min.

GC-MS for formamide. The formation of formamide from the imidazole-ozone reaction was additionally confirmed by GC-MS. Because of very low sensitivity of formamide by the GC-MS method ($\text{LOQ} = 3.3 \text{ mM}$) and lack of extraction methods for formamide, the method was applied only once and thereafter no longer applied for further quantifications. To yield high production of formamide suitable for the GC-MS method, an ozonation experiment was carried out by using high initial concentrations of imidazole (1 mM) and *t*-butanol (1 M) prepared in 1 L of ultrapurified water by directly sparging ozone-containing gas to the imidazole solution with an oxygen gas flow of 0.02 NL min^{-1} and ozone generator power of 30 % (BMT MESSTECHNIK GMBH, BMT 803 BT). After 90 min of ozonation, when a complete abatement of imidazole was confirmed by HPLC-UV, the resulting solution was further processed by an evaporator (Büchi Syncore® Analyst) with preset operating parameters (heating temperature of 40°C , cooling temperature of 15°C , target pressure of 45 mbar over 3 hours, and 230 RPM) to remove *t*-butanol and subsequently by a lyophilizer (STERIS, LYOVAC GT 2-E) to remove the remaining water in

the ozonated solution. The resulting particles were dissolved in 0.7 mL dimethylformamide and analyzed by GC-MS equipped with a Restek-Stabilwax column (60m, 0.32mm I.D., 1 μ m d_f, Restek) by injecting 1 μ L in the splitless mode with an inlet temperature of 220 °C. The column oven was initially at 100 °C for 1 min, ramped to 180 °C between 1 min and 9 min, held at 180 °C between 9 min and 24 min, ramped to 220 °C between 24 min and 25 min, and held at 220 °C until 30 min. After separation, formamide was detected by a Thermo Scientific DSQ II mass spectrometer with positive SIM mode. A quantification ion for formamide was m/z = 45. No internal standards were applied. The GC-MS chromatograms of the formamide standard solutions and the ozonated imidazole solution further treated by evaporation and lyophilization are shown in Figure S3.5. The concentration of formamide present in the ozonated sample was determined to be 2.4 mM based on the calibration of peak areas (R^2 = 0.98). This corresponds to 0.0017 mmol of formamide (by multiplying the volume of added dimethylformamide, 0.7 mL), which is 0.17 % of the initial amount of imidazole of 1 mmol (1 mM imidazole prepared in 1 L of ultrapurified water). The determined yield may underestimate the actual amount of formamide formed during the ozonation, because formamide could be degraded or evaporated during evaporation and lyophilization.

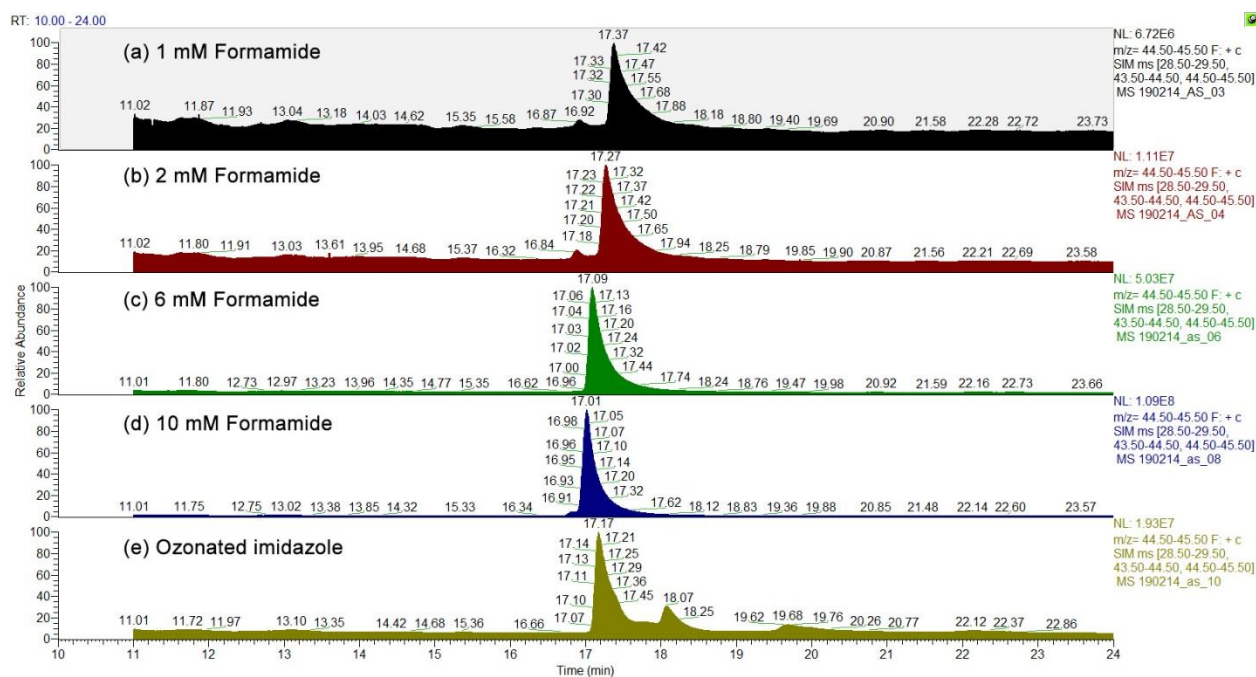


Figure S3.5. Stacked GC-MS chromatograms of (a) – (d) formamide standard solutions and (e) an ozonated imidazole solution treated by evaporation and lyophilization. The intensities of the highest peaks of (a) – (e) are 6.72×10^6 , 1.11×10^7 , 5.03×10^7 , 1.09×10^8 , and 1.93×10^7 .

UV-photolysis-chemiluminescence for total N-nitrosamines. Ozonated pyrazole and 1-benzylpyrazole samples (parent concentration 100 μ M) were analyzed by a UV-photolysis-chemiluminescence system¹⁰ to determine total *N*-nitrosamines (TONO). The total *N*-nitrosamine standards were prepared from a mix comprising *N*-nitrosodimethylamine (NDMA), *N*-nitrosodiethylamine (NDEA), *N*-nitrosodipropylamine (NDPA), *N*-nitrosodibutylamine (NDBA), *N*-nitrosodiphenylamine (NDPhA), *N*-nitrosopiperidine (NPiP), *N*-nitrosopyrrolidine (NPYR), and *N*-nitrosomorpholine (NMOR). A signal of the lowest concentration of the standard (0.4 μ M) is shown in Figure S3.6.

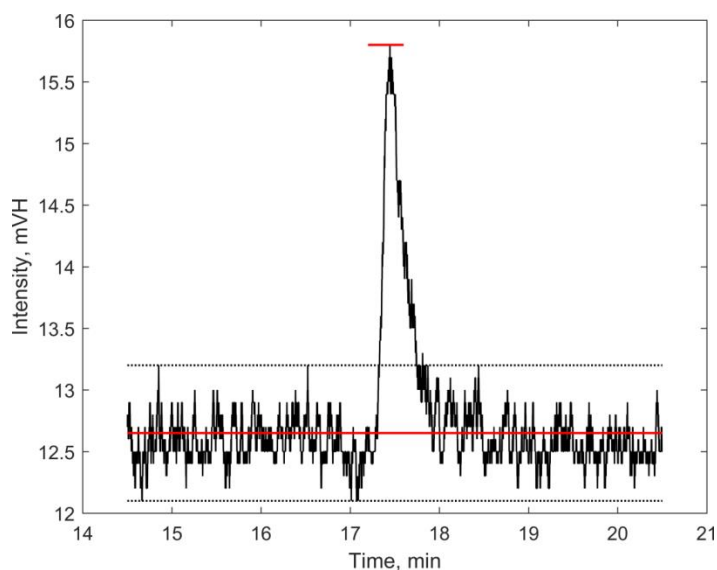


Figure S3.6. Example of a chemiluminescence signal of a $0.4\ \mu\text{M}$ total *N*-nitrosamine standard in ultrapurified water. The signal-to-noise was 5.7. LOQ calculated based on the signal-to-noise was $0.7\ \mu\text{M}$ by the equation of $\text{LOQ} = [\text{concentration of standard}]/[\text{signal-to-noise}] \times 10$.

OPD derivatization followed by HPLC-DAD for glyoxal. Glyoxal in the ozonated samples (parent concentration $1\ \text{mM}$) was analyzed by a derivatization method using *o*-phenylendiamine (OPD).¹³ Derivatization was performed by adding sodium hydroxide to $10\ \text{mL}$ of the ozonated sample to make the solution alkaline and then by mixing it with $1\ \text{mL}$ of the OPD solution prepared by dissolving $0.5\ \text{g}$ of OPD in $100\ \text{mL}$ of ultrapurified water. The mixture was heated at $60\ ^\circ\text{C}$ for $3\ \text{h}$. After cooling, the derivatized product, quinoxaline, was determined by HPLC-DAD (LC 20, Shimadzu). The instrument was equipped with a C18 column (Prontosil, NC-04, $250\ \text{mm} \times 4.0\ \text{mm}$ I.D., $5.0\ \mu\text{m}$, Bischoff). $50\ \mu\text{L}$ of the derivatized solution was separated by a water/acetonitrile gradient system (35% ACN/ $5\ \text{min}$, 45% ACN/ $10\ \text{min}$, 100% ACN) with a flow rate of $0.5\ \text{mL min}^{-1}$ for the ozonated imidazole and pyrazole samples. For the ozonated pyrrole samples, a water/methanol gradient system was used (20% MeOH/ $2\ \text{min}$, 80% MeOH/ $5\ \text{min}$). Quinoxaline was quantified by UV detection at $380\ \text{nm}$.

Text S3.5. Analytical methods for reactive oxygen species

This section describes the analytical methods used for quantifying reactive oxygen species (singlet oxygen, hydroxyl radical, and hydrogen peroxide) formed during the azole-ozone reactions.

Singlet oxygen. The formation of $^1\text{O}_2$ formed during the azole-ozone reactions was quantified by detecting the phosphorescence emitted by $^1\text{O}_2$ at $1270\ \text{nm}$ by a near-infrared photomultiplier tube (NIR-PMT, H10330B-45, Hamamatsu). The setup is described in detail in a previous study.¹⁴ The $^1\text{O}_2$ signals were calibrated by the reaction of triethylamine with ozone ($[\text{triethylamine}] = 2\ \text{mM}$ and $[\text{ozone}] = 5 - 50\ \mu\text{M}$, as initial concentrations), which forms $^1\text{O}_2$ with a 70% yield.¹⁴ The calibration reaction needs similar reaction kinetics to the azole-ozone reactions, because the shape of $^1\text{O}_2$ signals strongly depends on the kinetics of $^1\text{O}_2$ formation and could affect the peak integration and quantification.¹⁴ Therefore, the calibration was performed at pH 10 (achieved by $20\ \text{mM}$ carbonate buffer) where the triethylamine reacts with ozone with a second-order rate constant $> 10^5\ \text{M}^{-1}\text{s}^{-1}$, similar to the apparent second-order rate constants of the azole-ozone reactions at pH 7. The calibration reaction by hydrogen peroxide and hypochlorous acid, applied in previous studies,^{14,15} could not be used, because of its

lower reactivity (maximum $k \sim 3 \times 10^3 \text{ M}^{-1} \text{ s}^{-1}$ at around pH 10).¹⁶ The calibration curve is shown in Figure S3.7. The azole-ozone reactions were carried out under azole-excess conditions where [azole] = 2 mM or 3 mM and [ozone] = 90 – 100 μM as initial concentrations. 1 M *t*-butanol was added and the pH was maintained at pH 7 – 8 by 20 mM phosphate buffer. The results are summarized in Table S3.7 and examples of $^1\text{O}_2$ signals are shown in Figure S3.8.

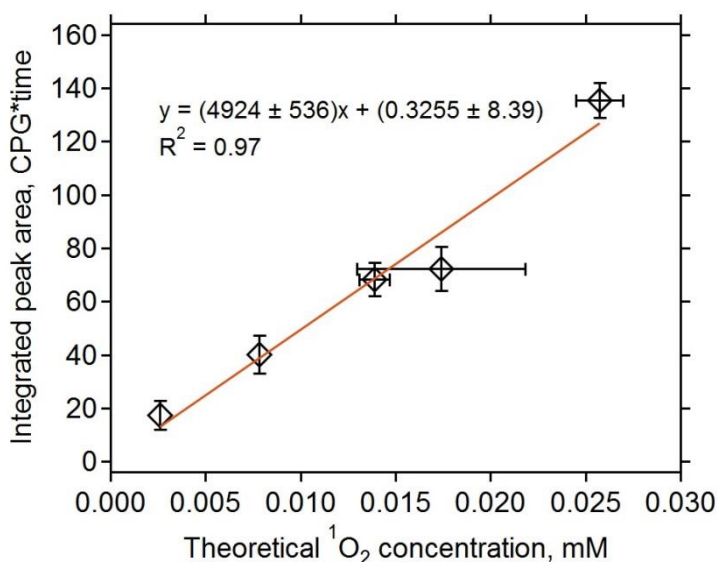


Figure S3.7. Integrated $^1\text{O}_2$ signals as a function of the theoretical concentrations of $^1\text{O}_2$ formed during the reaction of triethylamine with ozone, producing a 70% yield of $^1\text{O}_2$ at pH 10. Data points are average values of five individual measurements. Conditions: [triethylamine]₀ = 2 mM, [ozone]₀ = 5 μM – 50 μM , and pH 10 (20 mM carbonate buffer).

Table S3.7. Measuring conditions and $^1\text{O}_2$ yields of the azole-ozone reactions. All reactions were performed in presence of 1 M *t*-butanol. Each condition was repeated at least five times and the average values \pm standard deviations are shown in bold at the last row for each condition.

Compound	$^1\text{O}_2$ Measuring conditions			Results		
	C, mM ^a	O ₃ , mM ^a	pH	Peak area	$^1\text{O}_2$, mM	$^1\text{O}_2/\text{O}_3$
Pyrrole	3	0.101	7.3	63.27	0.0128	13%
		0.094		42.96	0.0087	9%
		0.098		65.51	0.0132	14%
		0.101		49.58	0.0100	10%
		0.096		50.34	0.0102	11%
		0.098			0.0110 \pm 0.0020	(11 \pm 2)%
Imidazole	2	0.096	7.6	0.70	0.00008	0.08%
		0.089		1.08	0.00015	0.17%
		0.086		0.70	0.00008	0.09%
		0.087		0.77	0.00009	0.10%
		0.089 ^b		0.88	0.00011	0.13%
		0.089 ^b		0.86	0.00011	0.12%
		0.089			0.00010 \pm 0.00003	(0.12 \pm 0.03)%
Pyrazole	3	0.096	7.5	8.56	0.00167	1.7%
		0.096		8.64	0.00169	1.8%
		0.088		8.49	0.00166	1.9%
		0.091		8.98	0.00176	1.9%
		0.093 ^b		8.19	0.00160	1.7%
		0.093			0.00167 \pm 0.00006	(1.8 \pm 0.1)%

^aconcentration in the mixture, ^bthe original measured concentration was missing and therefore replaced by the average value of the other ozone concentrations measured for the same condition.

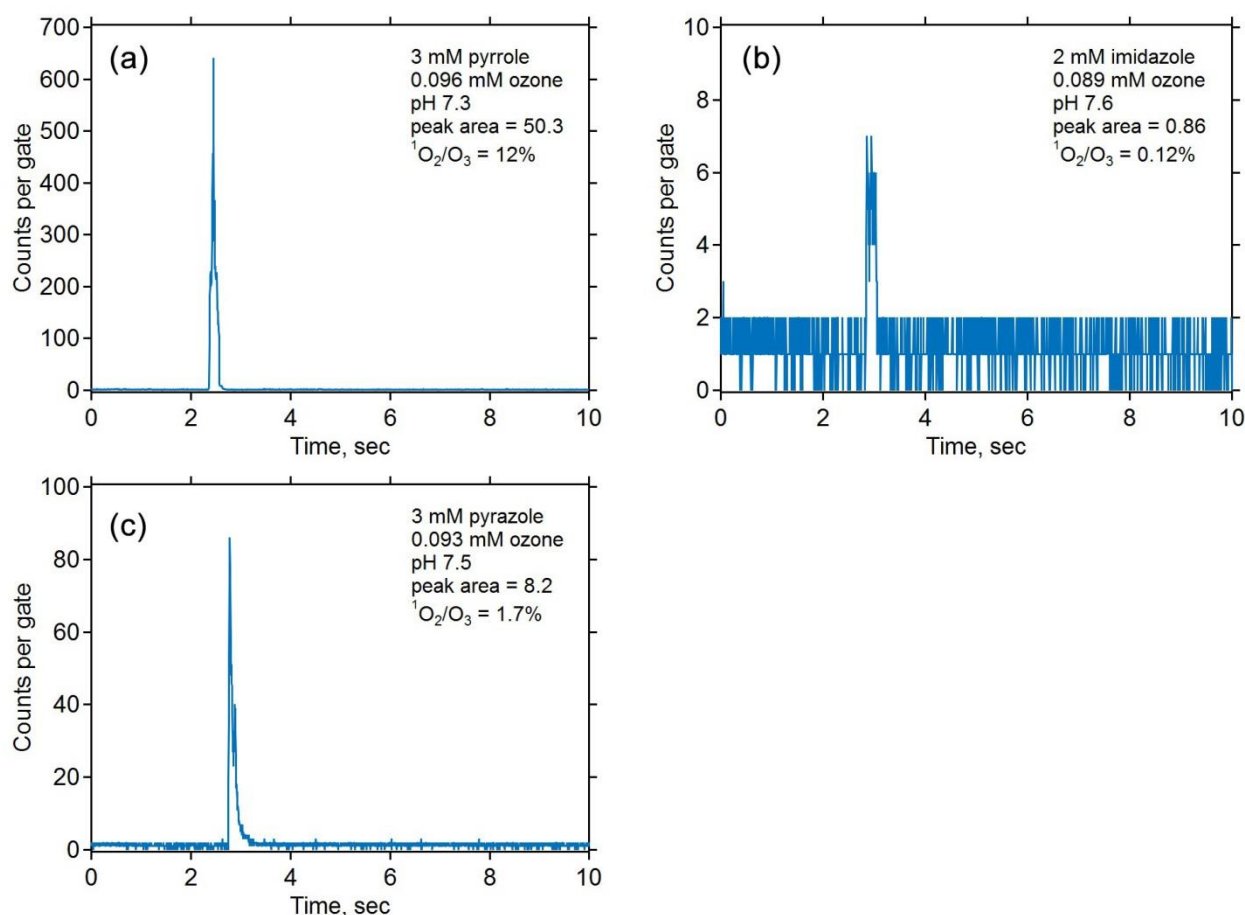


Figure S3.8. Examples of $^1\text{O}_2$ signals for the reactions of (a) pyrrole, (b) imidazole, and (c) pyrazole with ozone.

Hydroxyl radical. The concentrations of $\cdot\text{OH}$ formed during the reactions of pyrrole, imidazole, and pyrazole with ozone were quantified by using the $\cdot\text{OH}$ scavenger *t*-butanol. An azole solution containing 1 mM azole and 0.5 M *t*-butanol was prepared at pH 7 (5 mM phosphate buffer). Additionally, an azole solution containing 1 mM azole and 0.1 M *t*-butanol was prepared at pH 2 (by adding sulfuric acid) or at pH 11 (by adding sodium hydroxide) to investigate the pH effect on $\cdot\text{OH}$ formation. Varying doses of ozone (30 μM – 300 μM) were applied to the solution. After the reaction, formaldehyde, a product of the reaction of *t*-butanol with $\cdot\text{OH}$, was quantified by the Hantzsch method³ which derivatizes formaldehyde with acetylacetone and ammonium acetate and measures the absorbance of the derivatized product (diacetyldihydrolutine) at the wavelength of 412 nm ($\epsilon = 7700 \text{ M}^{-1} \text{ cm}^{-1}$). The $\cdot\text{OH}$ concentrations were estimated by doubling the formaldehyde concentrations based on the previously reported formaldehyde yield of $\sim 50\%$.¹⁷ The determined $\cdot\text{OH}$ concentrations as a function of the ozone doses for the azole-ozone reactions are shown in Figure S3.9.

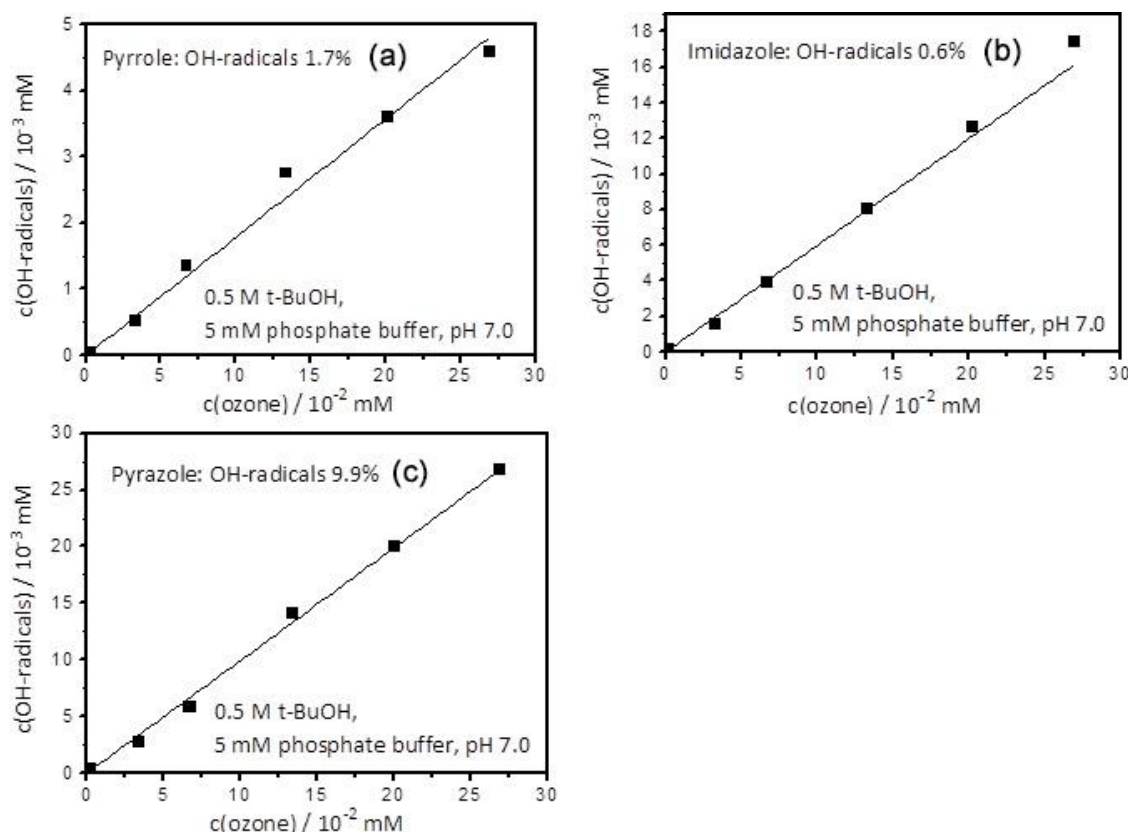
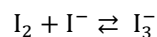
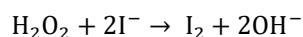


Figure S3.9. $\cdot\text{OH}$ formation during the reactions of (a) pyrrole, (b) imidazole, and (c) pyrazole with ozone (initial azole concentration = 1 mM). Symbols indicate the determined $\cdot\text{OH}$ concentrations and lines are the linear regression of the data for ozone doses ranging from 30 μM to 300 μM . Numbers in percentage are $\cdot\text{OH}$ yields obtained by the slopes of the linear regression.

Hydrogen peroxide. An azole solution containing 1 mM azole and 0.5 M *t*-butanol was prepared at pH 7 (5 mM phosphate buffer). Additionally, an azole solution containing 1 mM azole in absence of a $\cdot\text{OH}$ scavenger was prepared at pH 2 (by adding sulfuric acid) or at pH 11 (by adding sodium hydroxide) to investigate the pH effect on H_2O_2 formation. Varying doses of ozone (30 μM – 300 μM) were applied to the solution. After the reaction, H_2O_2 was quantified spectrophotometrically with Allen's reagent (molybdate-activated iodide).^{18,19} H_2O_2 oxidizes molybdate activated iodide ions to iodine, which can be detected as I_3^- according to the following equations:



The quantitative determination of H_2O_2 was achieved by adding the following solutions to UV-cells (1 cm path length): 1 mL of Allen's reagent A (1 g NaOH + 33 g KI + 0.1 g $(\text{NH}_4)_6\text{Mo}_7\text{O}_{24} \cdot \text{H}_2\text{O}$ filled up to 500 mL ultrapurified water), 1 mL of Allen's reagent B (10 g potassium hydrogen phthalate (KHP) dissolved in 500 mL ultrapurified water), and 1 mL of sample. After rapid mixing, the H_2O_2 concentrations were derived by spectrophotometrically measuring the absorbance at 350 nm ($\epsilon_{350\text{nm}} = 25,500 \text{ M}^{-1} \text{ cm}^{-1}$). The H_2O_2 measurements were carried out in presence and absence of *t*-butanol, both of which show similar results (Figure S3.10). It has to be noted that oxidation of iodide may also be induced by other peroxides. Organic peroxides can be formed *via* recombination of oxyl radicals. These oxyl radicals can either be formed by $\text{HO}_2\cdot$ cleavage of an ozone adduct after insertion, or from tetroxide decay. These reactions have rarely been reported, indicating that they may be of minor im-

portance. Yet, such interferences can also not be fully excluded by other methods for H_2O_2 determination such as peroxidase catalyzed oxidation of *N,N*-diethyl-*p*-phenylenediamine (DPD).²⁰

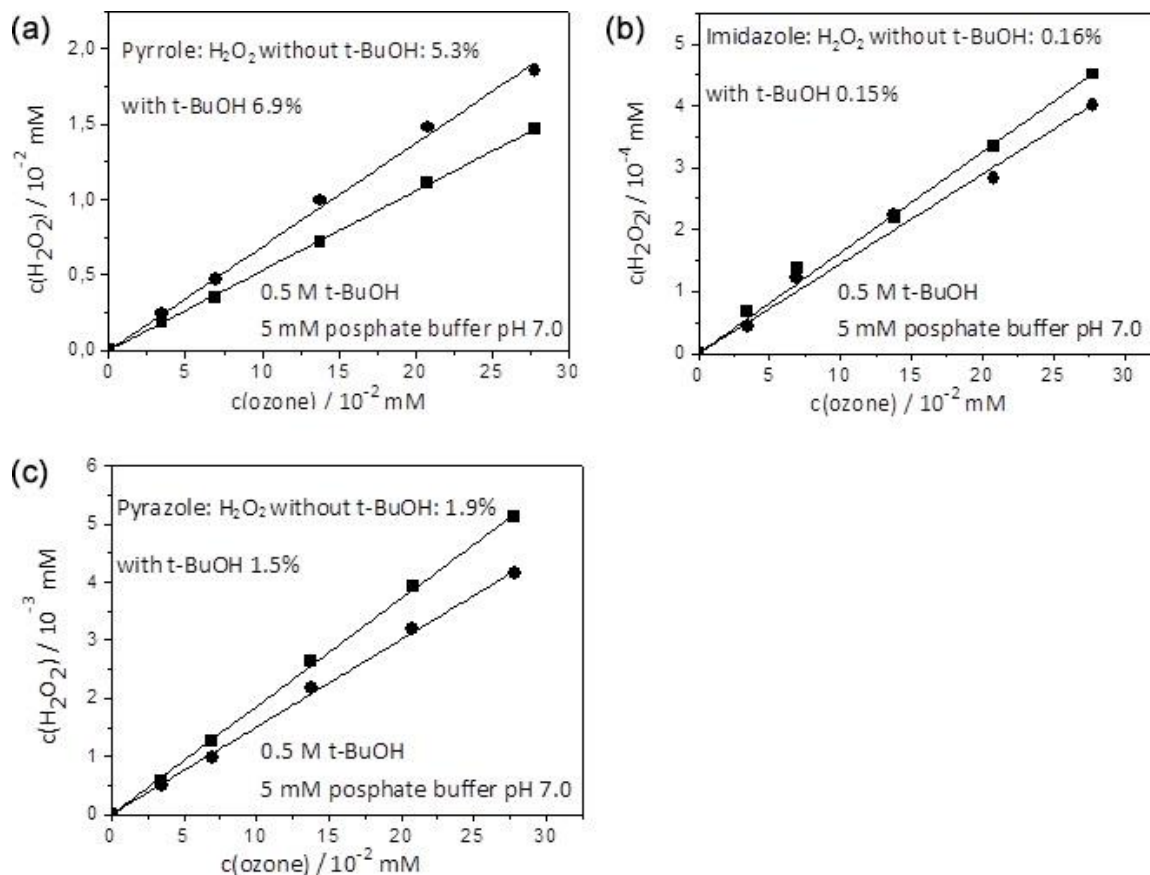


Figure S3.10. H_2O_2 formation during the reactions of (a) pyrrole, (b) imidazole, and (c) pyrazole with ozone (initial azole concentration = 1 mM). Symbols indicate the determined H_2O_2 concentrations with *t*-butanol (circle) and without *t*-butanol (square) and lines are the linear regression of the data for ozone doses ranging from 30 μM to 300 μM . Numbers in percentage are H_2O_2 yields obtained by the slopes of the linear regression.

Text S3.6. Detailed methods of quantum chemical computations

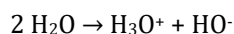
All computations were performed with Gaussian09 vD.01.²¹ Geometry optimizations used the LC- ω PBE/6-31+G(d,p)²² method together with the implicit SMD²³ model to account for aqueous solvation. The nature of all stationary structures was verified by normal mode analysis. Internal Reaction Coordinate²⁴ (IRC) calculations were performed to verify the connectivity of transition structures on the potential energy surface (PES). Energy differences are reported with respect to separate reactants ozone and pyrrole as follows: Electronic energy differences were evaluated with the LC- ω PBE/def2-tzvppd^{22,25} model chemistry in combination with the SMD solvation model, using the structures described above. Additional electronic energy calculations were performed with the M06-2X/tzvppd model chemistry,²⁶ also using the LC- ω PBE-optimized geometries. All calculations used the restricted Kohn-Sham approach for singlet systems, unless mentioned otherwise. For doublet systems, unrestricted Kohn-Sham was used for geometry optimization and frequency calculations, and unrestricted open shell Kohn-Sham for single point energy calculations with the tvzppd basis set. For doublet species, the energetic dif-

ference between unrestricted and restricted open shell calculations was 4 kcal mol⁻¹ in the most pronounced case, and did not affect the mechanistic interpretation.

Rotational, vibrational, and translational contribution to the Gibbs free energy were estimated with the harmonic oscillator/rigid rotor models at the LC- ω PBE/6-31+G(d,p) level at 1 atm and 298.15 K, and were modified with the GoodVibes software package using standard options. All vibrational frequencies were scaled by a factor of 0.9367,²⁷ and vibrational frequencies below 100 cm⁻¹ were treated with the free rotor approach.

The accuracy of the free energy differences can be expected to be somewhere in a 5-10 kcal mol⁻¹ range, owing to cumulative errors of the electronic structure methods and the solvation models. The absolute error in the free energy difference is expected to be larger, since describing ozone additions is challenging for density functional theory methods.^{28,29} However, this is the result of an error in the description of ozone, and this systematic error will propagate through all results. Conversely, when comparing molecules with similar charge distribution and bonding pattern, or comparing reactions of the same type, the error should be < 5 kcal mol⁻¹. Three types of energies are reported: LC- ω PBE energies at 0 K that include zero-point vibrational energies, LC- ω PBE Gibbs free energies at 298 K, and M06-2X Gibbs free energies at 298 K. Throughout the reaction schemes presented from Figure S3.27 to Figure S3.32, and presented in Figure S3.36, these highlight that the results especially for charged species strongly depend on the choice of density functional and on the inclusion of temperature effects. For evaluating the feasibility of each step, it should be most instructive to compare all three types of energy to the preceding molecule. In the main text, the LC- ω PBE Gibbs free energies at 298 K were used for discussion.

The explored reaction pathways involve the addition of HO⁻, deprotonation by HO⁻, or protonation. To treat this in an energetically consistent fashion, the given energies refer to a reference energy corresponding to the addition of two H₂O molecules to the system. These have to undergo proton transfer to form H₃O⁺ and HO⁻, which are the species used in actual reactions. In the presented schemes, every time a reaction with HO⁻ is involved, it is preceded by the reaction:



It should be noted that the SMD implicit solvation model underestimates the free energies of solvation of H₃O⁺ and HO⁻ by 6 kcal mol⁻¹ and 10 kcal mol⁻¹, respectively, owing to the strong specific interaction of these species with solvent molecules. This leads to a miss-estimation of the free energy differences associated with these reactions.

Figures S3.27 to S3.32 and Figure S3.36 depict mechanisms that are based on these quantum chemical computations. These are annotated with reaction energies, where the energetic references are always isolated molecules of ozone and pyrrole or imidazole. For each species, the three energies given are: LC- ω PBE/def2-tzvppd//LC- ω PBE/6-31+G(d,p), including (1) zero-point vibrational energy, (2) thermal corrections to Gibbs free energy, and (3) M06-2X/def2-tzvppd//LC- ω PBE/6-31+G(d,p) including thermal corrections to the Gibbs free energy. Transition structures (first order saddle points on the potential energy surface) are marked with square brackets and a double dagger. Usually, chemical species should be connected by a transition structure. If this is not drawn, then calculations were not carried out. If arrows connecting stable species and transition structures are dotted, then internal reaction coordinate (IRC) calculations did not succeed for technical reasons. The connectivity was then concluded from visualizing the imaginary vibrational mode of the transition structure, and from “relaxed scan” calculations that were used to locate the transition structure in the first place. Relaxed scans vary a selected bond distance between two atoms systematically and keep it fixed in each step, while the geometry of the remainder of the system is optimized with respect to the potential energy. Thus, if the chosen bond distances

closely correspond to the reaction coordinate, these calculations give an indication of the connectivity on the PES and possible product structures.

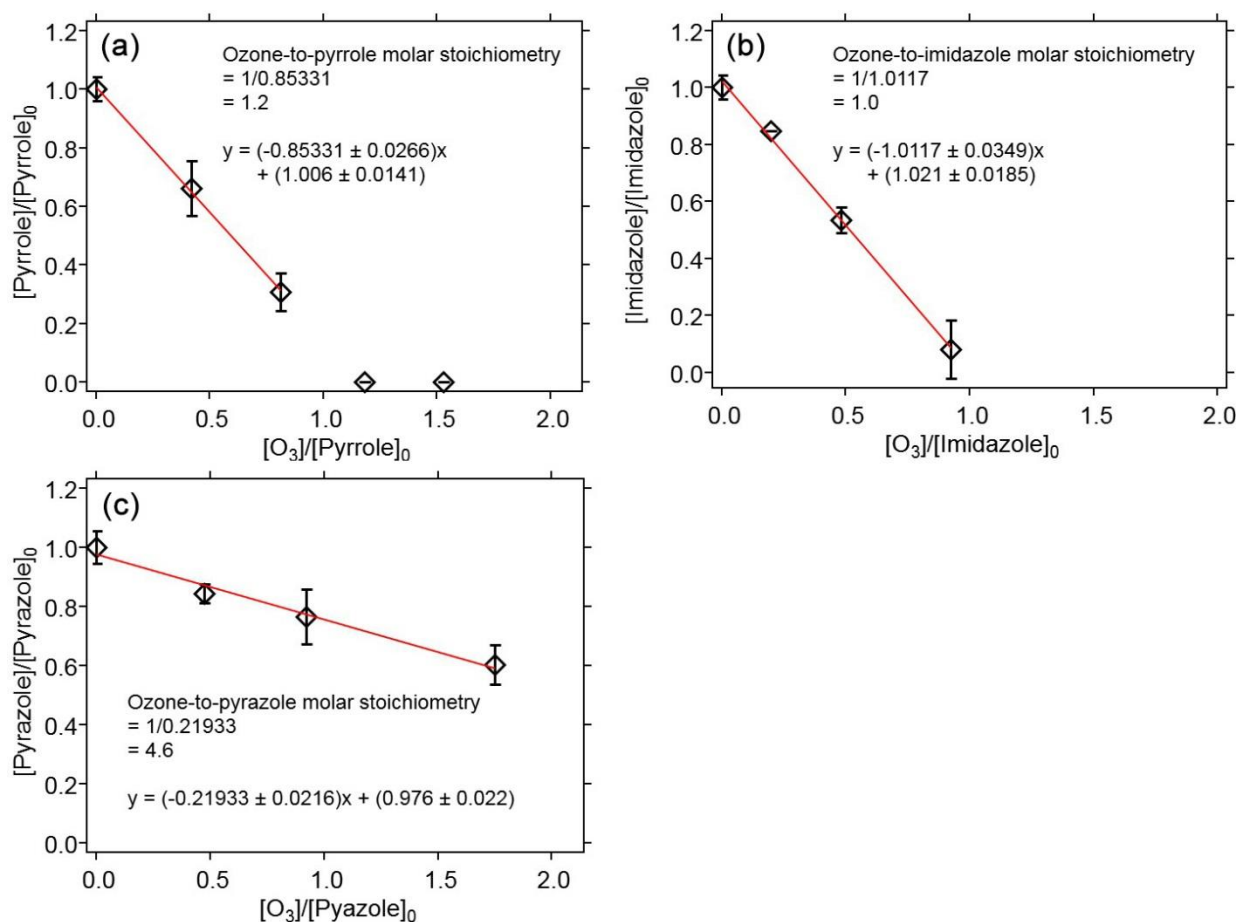


Figure S3.11. Ozone:azole molar stoichiometry calculated by inverting the slopes from linear regressions of the measured azole concentrations as a function of the molar ratio of $[O_3]/[azole]_0$: (a) Pyrrole, (b) imidazole, (c) pyrazole. All measurements were carried out in presence of 50 mM *t*-butanol at pH 7 (10 mM phosphate buffer). The initial azole concentrations were 100 – 110 μ M.

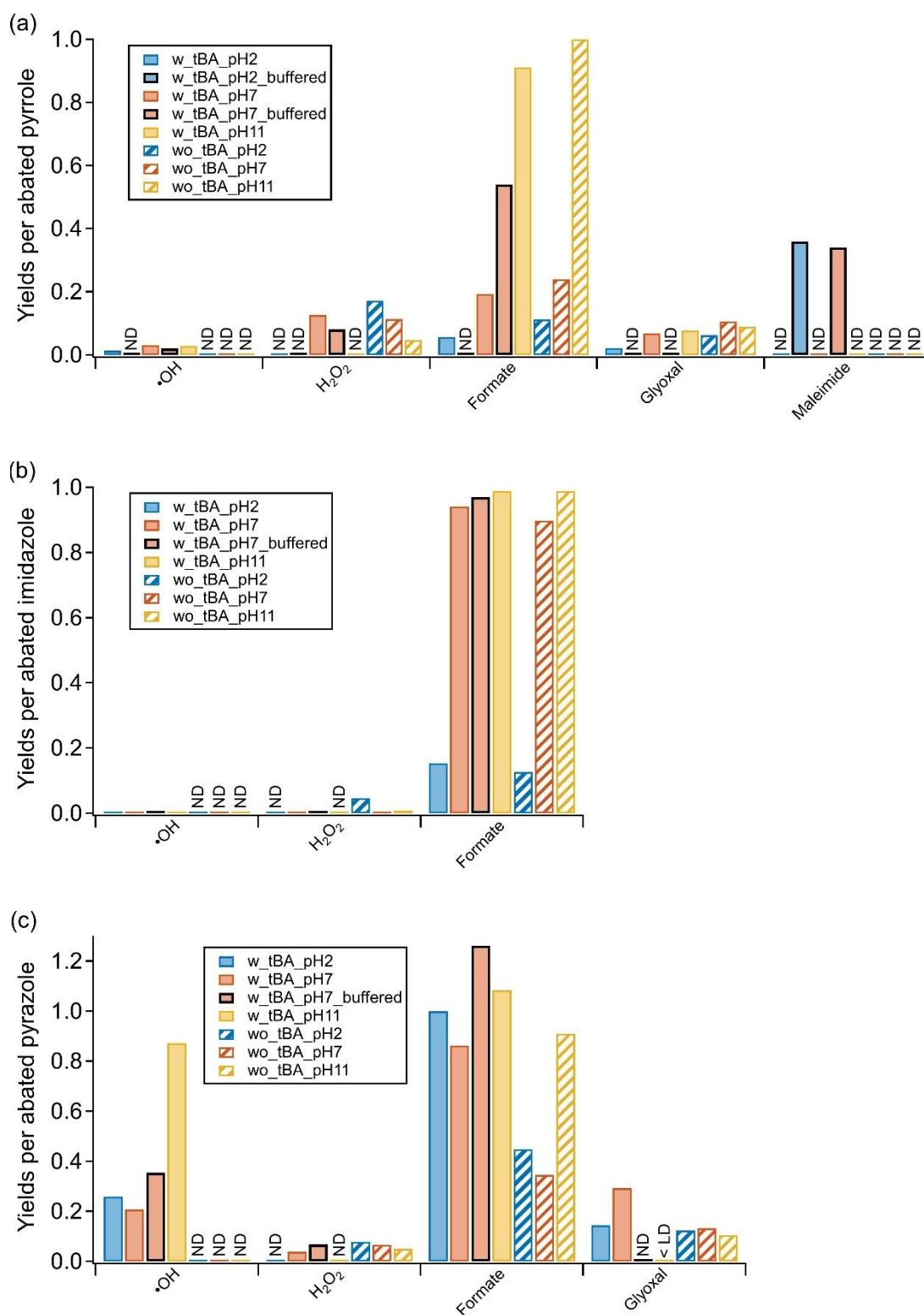


Figure S3.12. Product yields measured under various pH and $\cdot\text{OH}$ scavenging conditions for the reactions of (a) pyrrole, (b) imidazole, and (c) pyrazole with ozone. The yields are expressed with regard to the abatement of azole under the corresponding reaction condition as shown in Table S3.8. Blue, red, and yellow bars indicate pH 2, 7, and 11, respectively. Solid and hashed patterns indicate the presence and absence of $\cdot\text{OH}$ scavenger, respectively. Experiments were carried out with or without buffering agents and the results obtained under the buffered condition (10 mM phosphate buffer for pH 2 and 7) are shown as bars with black edges.

Table S3.8. Reaction stoichiometry and product yields for the reactions of pyrrole, imidazole, and pyrazole with ozone at pH 2, 7, and 11 in presence and absence of *t*-butanol. The yields are expressed as the specific ozone consumption ($\Delta[X]/\Delta[O_3]$) or relative to the abatement of azole ($\Delta[X]/\Delta[Azole]$).

azole	product (X)	X type	pH	Buffer	t-butanol	O3:azole stoichiometry	$\Delta[X]/\Delta[O_3]$	$\Delta[X]/\Delta[azole]$
pyrrole	•OH	ROS	2.0	none	presence	1.9	0.013	0.025
	•OH	ROS	7.3	none	presence	1.8	0.017	0.030
	•OH	ROS	11.0	none	presence	1.8	0.016	0.029
	•OH	ROS	7.0	PBS 5mM	presence	1.2	0.017	0.020
	H ₂ O ₂	ROS	2.0	none	absence	1.7	0.10	0.172
	H ₂ O ₂	ROS	7.3	none	absence	2.0	0.057	0.114
	H ₂ O ₂	ROS	11.0	none	absence	1.9	0.025	0.047
	H ₂ O ₂	ROS	7.3	none	presence	1.8	0.072	0.126
	H ₂ O ₂	ROS	7.0	PBS 5mM	presence	1.2	0.069	0.081
	formate	TP_C	2.0	none	absence	1.7	0.065	0.112
	formate	TP_C	7.3	none	absence	2.0	0.12	0.240
	formate	TP_C	11.0	none	absence	1.9	0.53	1.000
	formate	TP_C	2.0	none	presence	1.9	0.056	0.108
	formate	TP_C	7.3	none	presence	1.8	0.11	0.193
	formate	TP_C	11.0	none	presence	1.8	0.51	0.911
	fomate	TP_C	7	PBS 10mM	presence	1.2	0.46	0.539
	glyoxal	TP_C	2.0	none	absence	1.7	0.036	0.062
	glyoxal	TP_C	7.3	none	absence	2.0	0.053	0.106
	glyoxal	TP_C	11.0	none	absence	1.9	0.047	0.089
	glyoxal	TP_C	2.0	none	presence	1.9	0.021	0.040
	glyoxal	TP_C	7.3	none	presence	1.8	0.039	0.068
	glyoxal	TP_C	11.0	none	presence	1.8	0.043	0.077
imidazole	•OH	ROS	2	none	presence	1.4	0.0007	0.001
	•OH	ROS	7.4	none	presence	1.2	0.0009	0.001
	•OH	ROS	11	none	presence	1.1	0.0009	0.001
	•OH	ROS	7	PBS 5mM	presence	1.0	0.006	0.006
	H ₂ O ₂	ROS	2	none	absence	1.3	0.037	0.047
	H ₂ O ₂	ROS	7.4	none	absence	1.1	0.0019	0.002
	H ₂ O ₂	ROS	11	none	absence	1.1	0.0075	0.008
	H ₂ O ₂	ROS	7.4	none	presence	1.2	0.0017	0.002
	H ₂ O ₂	ROS	7	PBS 5mM	presence	1.0	0.0015	0.001
	formate	TP_C	2	none	absence	1.3	0.099	0.127
	formate	TP_C	7.4	none	absence	1.1	0.78	0.897
	formate	TP_C	11	none	absence	1.1	0.91	0.989
	formate	TP_C	2	none	presence	1.4	0.11	0.153
	formate	TP_C	7.4	none	presence	1.2	0.8	0.941
	formate	TP_C	11	none	presence	1.1	0.94	0.989
	formate	TP_C	7	PBS 10mM	presence	1.0	0.98	0.968
pyrazole	•OH	ROS	2	none	presence	3.7	0.070	0.259
	•OH	ROS	6.5	none	presence	3.4	0.061	0.207
	•OH	ROS	11.0	none	presence	8.3	0.105	0.872
	•OH	ROS	7.0	PBS 5mM	presence	4.6	0.077	0.354
	H ₂ O ₂	ROS	2	none	absence	3.4	0.023	0.079
	H ₂ O ₂	ROS	6.5	none	absence	4.2	0.016	0.067
	H ₂ O ₂	ROS	11.0	none	absence	4.5	0.011	0.050
	H ₂ O ₂	ROS	6.5	none	presence	3.4	0.011	0.038
	H ₂ O ₂	ROS	7.0	PBS 5mM	presence	4.6	0.015	0.068
	formate	TP_C	2	none	absence	3.4	0.13	0.448
	formate	TP_C	6.5	none	absence	4.2	0.083	0.346
	formate	TP_C	11	none	absence	4.5	0.2	0.909
	formate	TP_C	2.0	none	presence	3.7	0.27	1.000
	formate	TP_C	6.5	none	presence	3.4	0.25	0.862
	formate	TP_C	11	none	presence	8.3	0.13	1.083
	formate	TP_C	7	PBS 10mM	presence	4.6	0.28	1.262
	glyoxal	TP_C	2	none	absence	3.4	0.04	0.124
	glyoxal	TP_C	6.5	none	absence	4.2	0.032	0.133

glyoxal	TP_C	11	none	absence	4.5	0.023	0.105
glyoxal	TP_C	2	none	presence	3.7	0.039	0.144
glyoxal	TP_C	6.5	none	presence	3.4	0.085	0.293
glyoxal	TP_C	11	none	presence	8.3	< LD	< LD

Text S3.7. NMR results – Identification of TP2, maleimide, and TP1 formed upon ozonation of pyrrole.

This section presents assignments of ^1H and ^{13}C NMR data and NMR spectra overviews and expanded parts of the 1D ^1H , ^1H -NOESY, and ^{13}C , as well as the 2D, ^1H - ^{13}C HSQC, ^1H - ^{13}C HMBC, and ^1H - ^1H DQF-COSY NMR spectra, analyzed to identify TP1, TP2, and maleimide, formed during the reaction of pyrrole with ozone.

The ^1H and ^{13}C NMR spectra of isolated products from ozonated pyrrole samples show many resonances from unknown products (indicated as “by-products” in Figure S3.14a, Figure S3.14b, Figure S3.15a, Figure S3.17a, and Figure S3.17b). Moreover, it seems that the broad resonances observed in the base of the ^1H NMR spectra originate from polymerized substances which had been formed during ozonation or during the sample work-up. Despite the large number of the unidentifiable signals in the NMR spectra, some characteristic ^1H and ^{13}C NMR chemical resonances were observed and successfully assigned to specific chemical structures (TP2, maleimide, and TP1, Figure S3.13). Two different sample work-up procedures were applied after ozonation: (1) only rotary evaporation until dryness, and (2) rotary evaporation followed by lyophilization (Text S3.4). Depending on the applied work-up (1) or (2), different product compositions were detected by the NMR analysis for the samples prepared under the same ozonation condition. Isolated solids by the work-up (1) contained TP2 and maleimide, whereas isolated solids by the work-up (2) mainly contained TP2 and TP1. TP2 could be identified as a main product regardless of the work-up procedures. The following sections discuss the assignments of ^1H and ^{13}C NMR chemical shifts to the identified products for NMR samples.

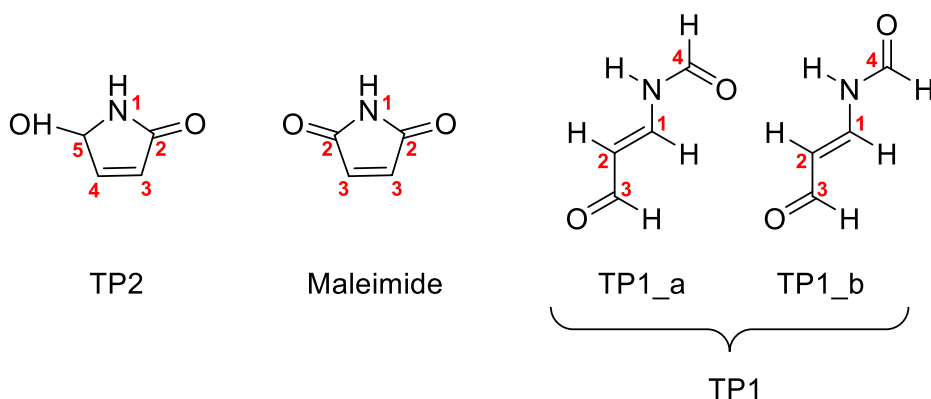


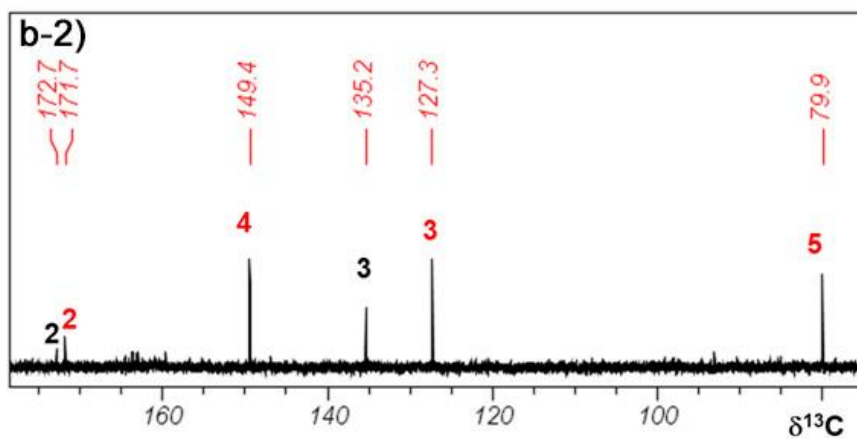
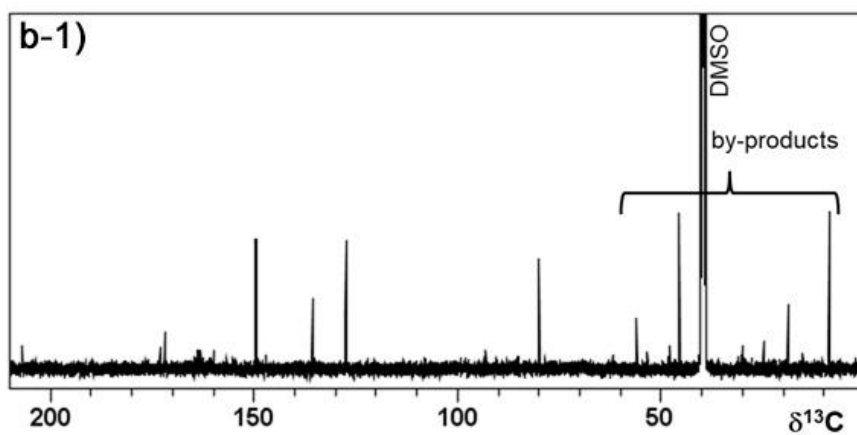
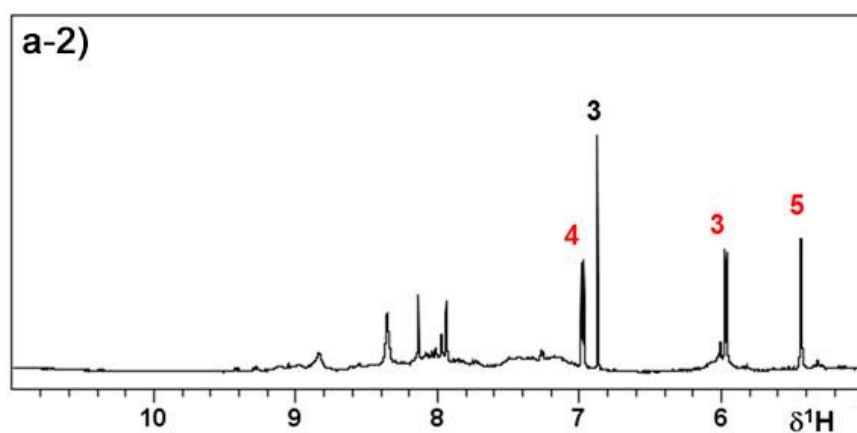
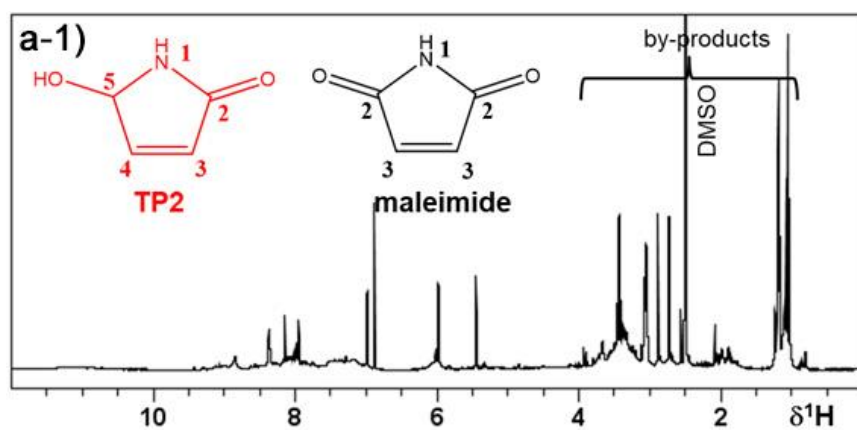
Figure S3.13. Chemical structures of TP2 (5-Hydroxy-1,5-dihydro-2H-pyrrol-2-one), maleimide, and TP1 (*N*-(3-oxo-1-propen-1-yl)formamide), isolated from the reaction of pyrrole with ozone. TP1_a and TP1_b are two stereoisomers of TP1 present in equilibrium. Positions used for NMR resonance assignments are indicated as red numbers.

- 1) *NMR identification of TP2 isolated by the work-up (1).* The NMR data recorded in DMSO- d_6 for the NMR sample processed by the work-up (1) show one set of resonances that could be assigned to TP2. The full assignment of ^1H and ^{13}C NMR data to TP2 is shown in Table S3.9 and Figure S3.14. In the ^1H - ^1H DQF-COSY NMR spectrum (Figure S3.14e), the cross signals observed between H-3, H-4, and H-5 prove that the three protons belong to the same spin system. Additionally, weak correlations of H-3, H-4, and H-5 to H-1 were detected (spectral region not shown in Figure S3.14e). From chemical shift reasons and from the ^1H - ^{13}C HSQC correlation (Figure S3.14c), it is clear that position 5 of TP2 can be assigned to a R-**CH**(OH)-R group. From the NOESY NMR data (Figure S3.14f), it is clear that the NH group must be next to position 5 and subsequently H-4 (NOE to H-5) and H-3 (NOE to H-4 and coupling $J_{34} = 5.7$ Hz) could be assigned. All observed ^1H - ^{13}C HMBC long-range correlations (Figure S3.14d and Table S3.9) support the proposed chemical structure. The NMR data of the same sample recorded in acetone- d_6 (Figure S3.15) shows considerably reduced amounts of resonances and is consistent with the assignments discussed above. The isolate was only partially soluble in acetone- d_6 and therefore the sample composition was different from the isolated dissolved in DMSO- d_6 (see Text S3.8).

Table S3.9 Assignments of ¹H and ¹³C NMR data of extracted products from the reaction of pyrrole with ozone (TP2, maleimide, TP1_a, and TP1_b as shown in Figure S3.13) and the reference standard of maleimide.

Compound ^a	Solvent ^b	Position ^a	¹ H NMR ^c				¹³ C NMR ^d		Correlations observed: HMBC, DQF-COSY, NOESY (w = weak) ^e
			δ ¹ H	Cp	J [Hz]	no. H	δ ¹³ C	mult.	
TP2	acetone-d ₆	1	n.d.						HMBC (Figure S3.15c): H-3 → C-(2, 4, 5); H-4 → C-(2, 3, 5); H-5 → C-(2, 3, 4)
TP2	acetone-d ₆	2					172.3	s	
TP2	acetone-d ₆	3	5.95	d(br)	5.8	1	128.4	d	
TP2	acetone-d ₆	4	6.99	d(br)	5.8	1	149.4	d	
TP2	acetone-d ₆	5	5.61	m		1	81	d	
TP2	DMSO-d ₆	1	8.36	s(br)		1			HMBC (Figure S3.14d): H-1 → C-(4w) (not shown); H-3 → C-(2, 4, 5); H-4 → C-(2, 3, 5); H-5 → C-(2, 3, 4) DQF-COSY (Figure S3.14e): H-1 → H-(3w, 4w, 5w) (not shown); H-3 → H-(1w, 4, 5); H-4 → H-(1w, 3, 5); H-5 → H-(1w, 3, 4) NOESY (Figure S3.14f): H-1 → H-(5); H-3 → H-(4); H-4 → H-(3, 5); H-5 → H-(1, 4)
TP2	DMSO-d ₆	2					171.7	s	
TP2	DMSO-d ₆	3	5.97	d(br)	5.7	1	127.3	d	
TP2	DMSO-d ₆	4	6.98	d(br)	5.7	1	149.4	d	
TP2	DMSO-d ₆	5	5.44	m		1	79.9	d	
Maleimide	acetone-d ₆	1	n.d.						HMBC (Figure S3.15c): H-3 → C-(2, 3w)
Maleimide	acetone-d ₆	2					172.4	s	
Maleimide	acetone-d ₆	3	6.79	s		2	136.0	d	HMBC (Figure S3.14d): H-3 → C-(2, 3w)
Maleimide	DMSO-d ₆	1	n.d.						
Maleimide	DMSO-d ₆	2					172.7	s	HMBC (Figure S3.16d): H-3 → C-(2, 3w)
Maleimide	DMSO-d ₆	3	6.87	s		2	135.2	d	
Maleimide ^f	DMSO-d ₆	1	10.9	s(br)		1			
Maleimide ^f	DMSO-d ₆	2					172.7	s	
Maleimide ^f	DMSO-d ₆	3	6.87	s		2	135.2	d	
TP1_a	acetone-d ₆	NH	10.3	s(br)		1			HMBC (Figure S3.17d-1): H-1 → C-(3, 4); H-3 → C-(2); H-4 → C-(1) DQF-COSY (Figure S3.14e): H-1 → H-(2); H-2 → H-(1, 3); H-3 → H-(2)
TP1_a	acetone-d ₆	1	7.89	dd	14.2/11.4	1	144.5	d	
TP1_a	acetone-d ₆	2	5.91	dd	14.2/8.1	1	115	d	
TP1_a	acetone-d ₆	3	9.48	dd	8.1	1	192.9	d	
TP1_a	acetone-d ₆	4	8.40	s		1	160.7	d	
TP1_b	acetone-d ₆	NH	10.2	s(br)		1			HMBC (Figure S3.17d-1): H-1 → C-(3, 4); H-3 → C-(2) DQF-COSY (Figure S3.17e): H-1 → H-(2); H-2 → H-(1, 3); H-3 → H-(2)
TP1_b	acetone-d ₆	1	7.89	dd	n.d.	1	150.6	d	
TP1_b	acetone-d ₆	2	5.79	dd	13.7/8.0	1	113.2	d	
TP1_b	acetone-d ₆	3	9.38	dd	8.0	1	191.6	d	
TP1_b	acetone-d ₆	4	8.64	d(br)	8.7	1	164.9	d	

^a Compound structures and numbering of positions are shown in Figure S3.13; ^b NMR solvent used, ^c "Cp" indicates coupling patterns described as s = singlet, d = doublet, dd = doublet of doublets, m = multiplet, br = broad; "no. H" indicates the number of hydrogens, ^d "mult." Indicates multiplicities of carbons described as s = quaternary and d = doublet (= CH group). ^e numbers next to H- or C- indicate the positions as described in Figure S3.13. ^f a commercially available reference standard of maleimide.



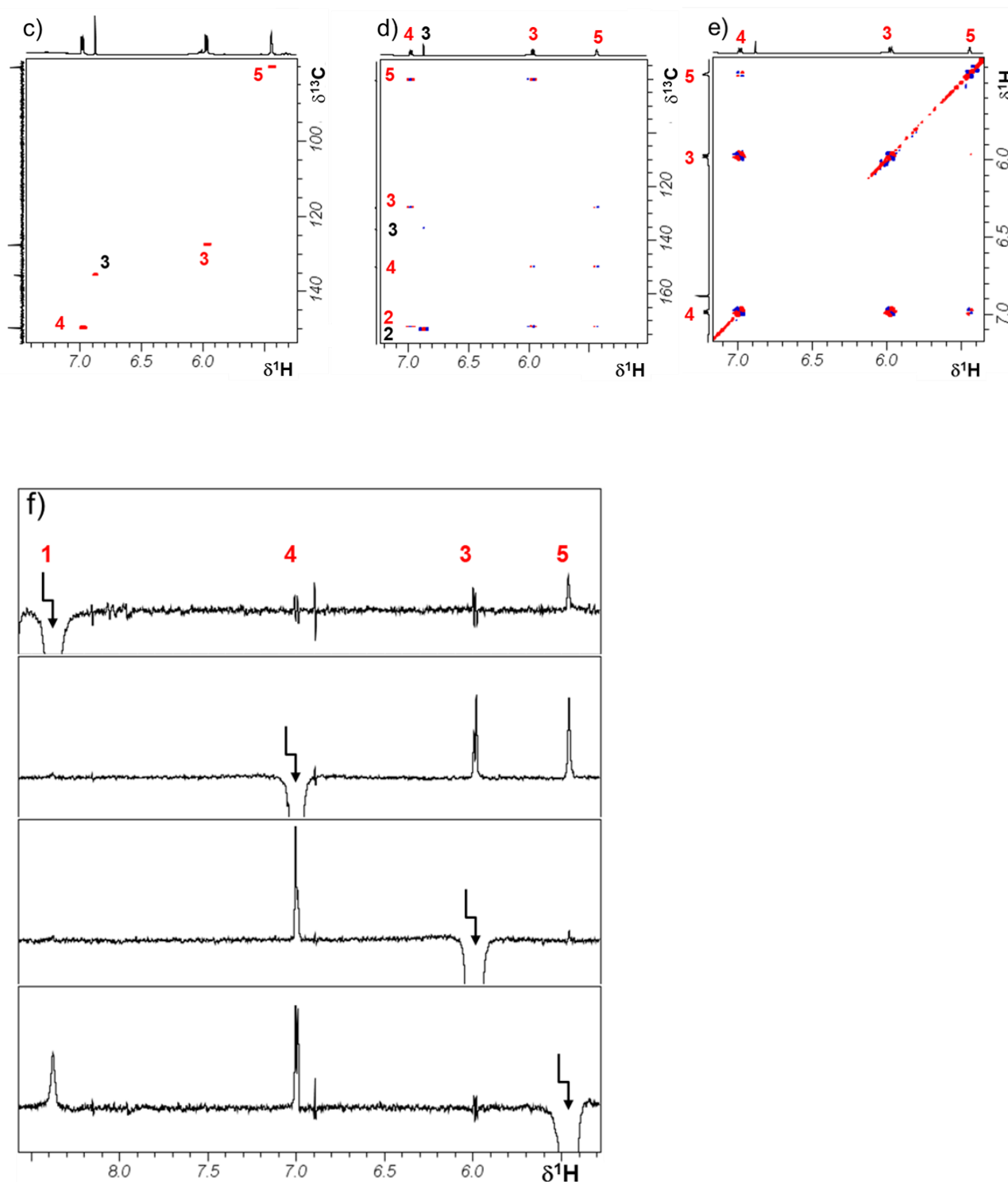


Figure S3.14. NMR data of ozonated pyrrole sample prepared by the work-up (1) (Text S3.7) recorded in DMSO-d_6 : (a-1 and a-2) ^1H with chemical structures of TP2 and maleimide, (b-1 and b-2) ^{13}C , (c) ^1H - ^{13}C HSQC, (d) ^1H - ^{13}C HMBC, (e) ^1H - ^1H DQF-COSY, and (f) 1D-NOESY with arrows indicating the selectively excited resonances. ^1H and ^{13}C NMR spectra of the full spectral regions (a-1 and b-1) and of the regions of interest (a-2 and b-2) are shown. The numbers assigned across the NMR spectra correspond to the positions of the structures of TP2 (in red) and maleimide (in black).

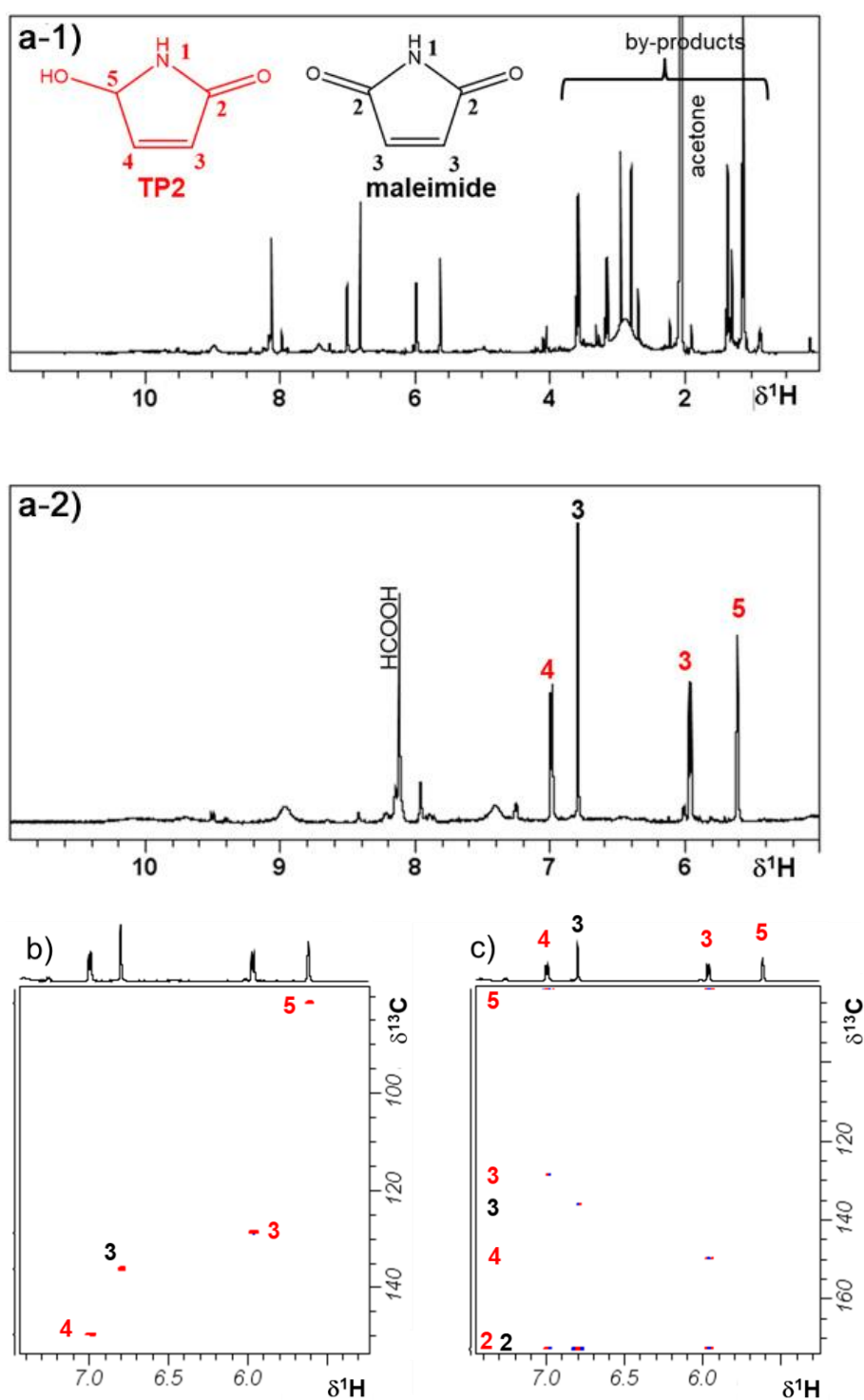
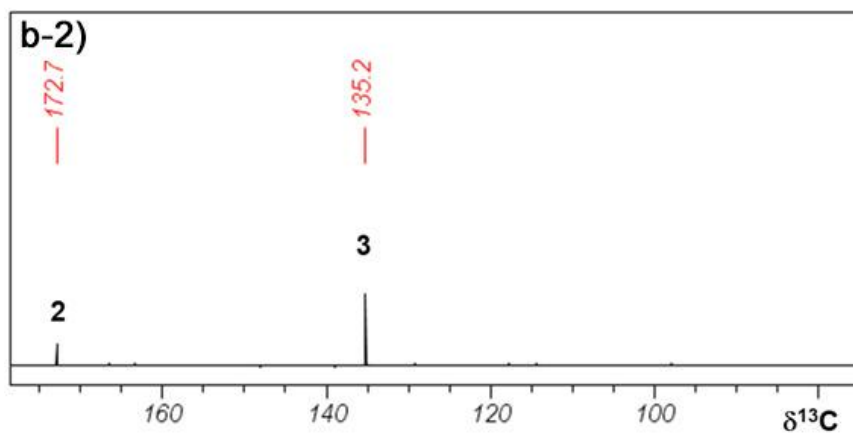
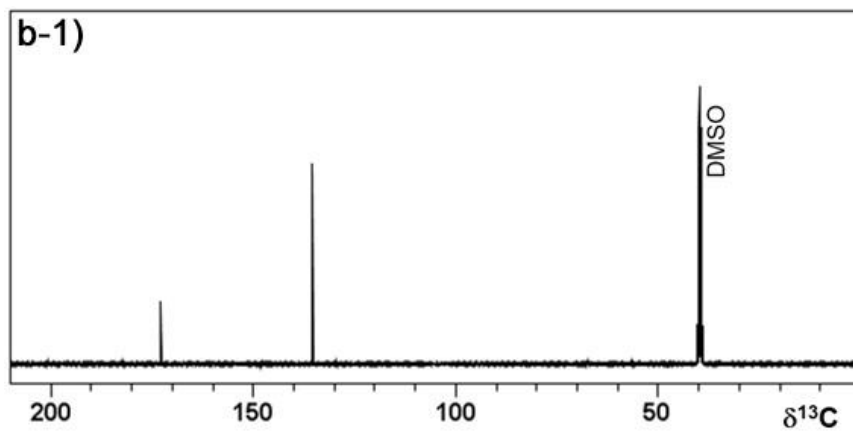
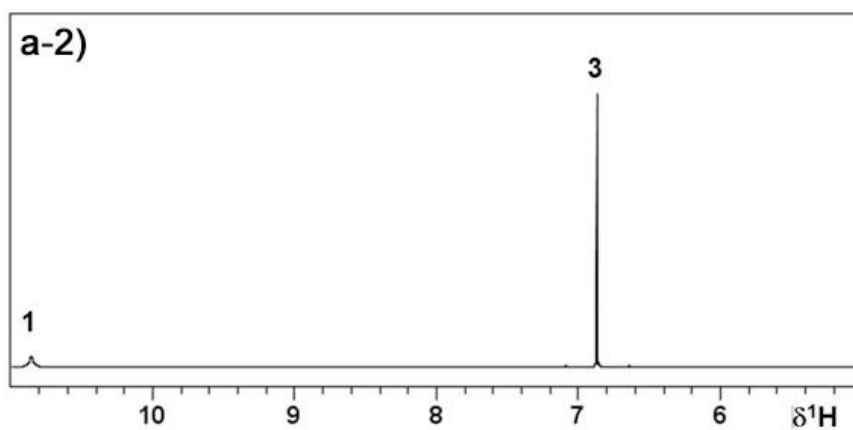
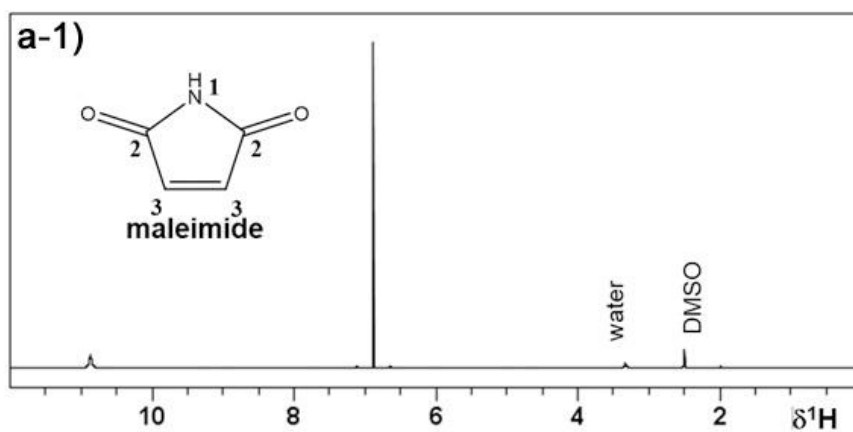


Figure S3.15. NMR data of ozonated pyrrole sample prepared by the work-up (1) (Text S3.7) recorded in acetone-d₆: (a-1 and a-2) ¹H with chemical structures of TP2 and maleimide, (b) ¹H-¹³C HSQC, and (c) ¹H-¹³C HMBC. ¹H NMR spectra of the full spectral region (a-1) and of the region of interest (a-2) are shown. The numbers assigned across the NMR spectra correspond to the positions of the structures of TP2 (in red) and maleimide (in black).

- 2) *NMR identification of maleimide isolated by the work-up (1).* The singlet signal observed at 6.87 ppm in the ^1H NMR spectrum shows a direct attachment to carbon at 135.2 ppm, in the olefinic region of chemical shifts (Figure S3.14c). It also shows long-range correlations to carbons at 172.7 ppm (Figure S3.14d) as well as a weak correlation to 135.2 ppm (correlation to “itself”) (Figure S3.14d). Therefore, we concluded that this chemical species must be symmetrical and maleimide was suggested as a potential candidate. The ^1H and ^{13}C NMR data of a commercially available reference standard of maleimide recorded in DMSO-d_6 solution (Figure S3.16 and Table S3.9) show exactly the same chemical shifts as obtained from the isolated species, unambiguously confirming the presence of maleimide in the NMR sample of the ozonated pyrrole solution.



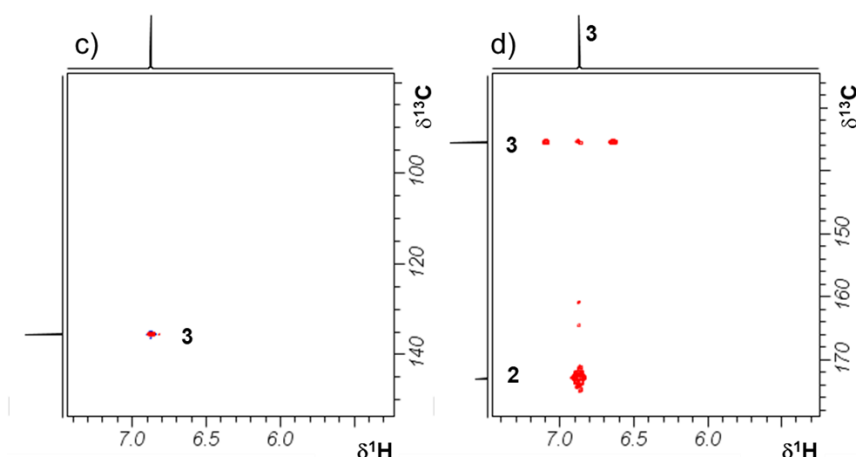
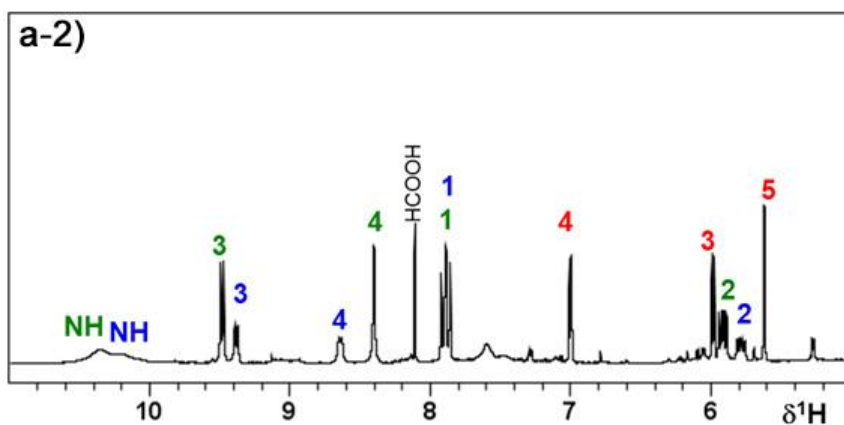
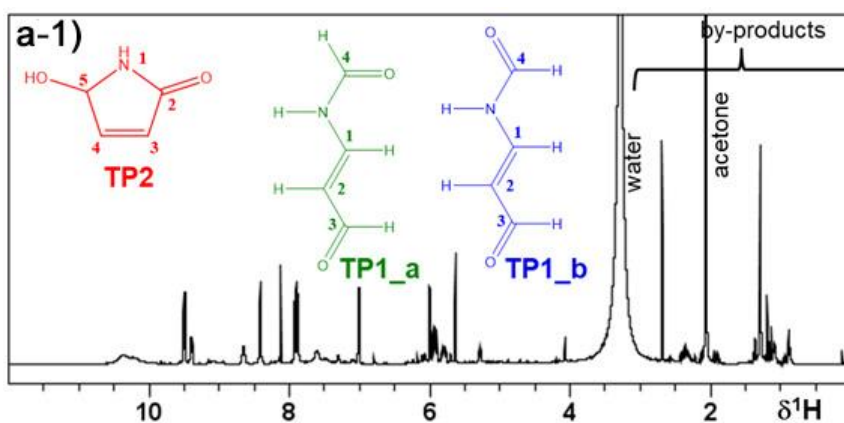
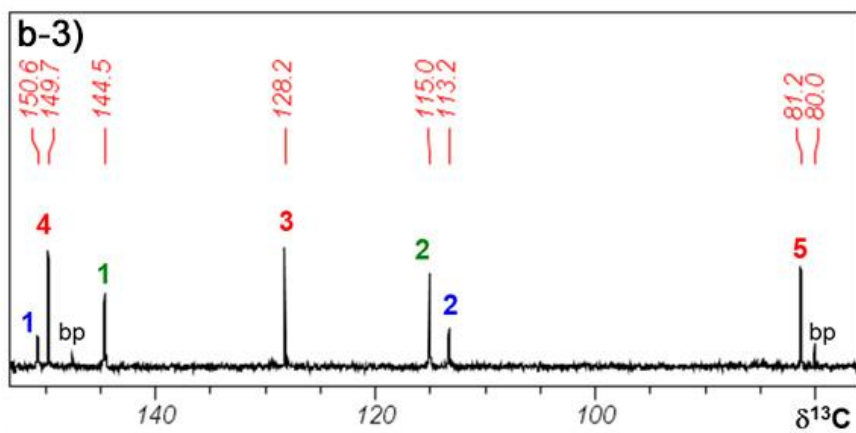
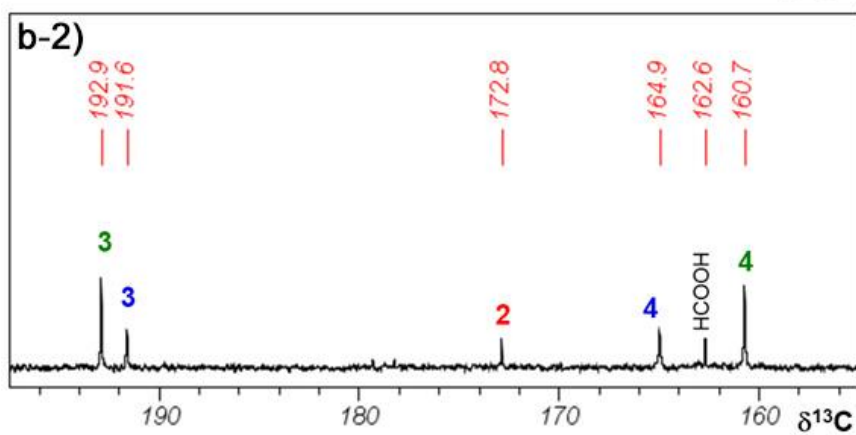
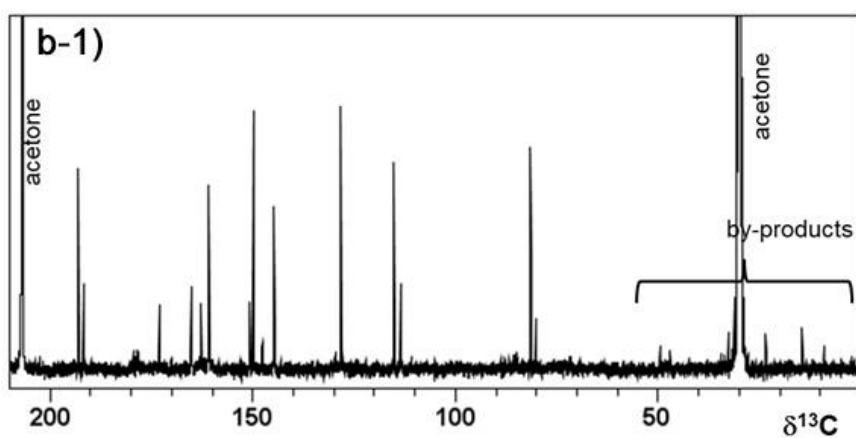


Figure S3.16. NMR data of a commercially available reference standard of maleimide recorded in DMSO- d_6 : (a-1 and a-2) ^1H with chemical structure of maleimide, (b-1 and b-2) ^{13}C , (c) ^1H - ^{13}C HSQC, and (d) ^1H - ^{13}C HMBC. ^1H and ^{13}C NMR spectra of the full spectral regions (a-1 and b-1) and of the regions of interest (a-2 and b-2) are shown. The numbers assigned across the NMR spectra correspond to the positions of the structures of maleimide.

- 3) *NMR identification of TP2, TP1_a, and TP1_b isolated by the work-up (2).* The presence of TP2 in the isolate prepared by the work-up (2) was confirmed by the ^1H and ^{13}C NMR chemical shifts and 2D NMR correlation signals (Figure S3.17) based on the assignments as discussed above in “1) *NMR identification of TP2 isolated by the work-up (1)*”. Unlike the isolate prepared by work-up (1), the isolate prepared by the work-up (2) did not seem to contain much maleimide. The low intensity signal at 6.9 ppm (singlet) in the ^1H NMR spectrum can be attributed to traces of maleimide (resonance assignments not shown in Figure S3.17). In addition to TP2 and traces of maleimide, resonances of two additional chemical species were found. The ^1H - ^{13}C HSQC experiment resulted in prominent correlations between 9.48 ppm and 192.9 ppm and between 9.38 ppm and 191.6 ppm, respectively (Figure S3.17c-1 and Table S3.9), indicating the presence of aldehyde groups. Furthermore, formamide-type correlations were found between protons and carbons at 8.40 ppm and 160.7 ppm and between 8.64 ppm and 164.9 ppm, respectively (Figure S3.17c-2 and Table S3.9). As a result of the ^1H - ^1H DQF-COSY experiment (Figure S3.17e) and ^1H - ^{13}C long-range correlations (Figure S3.17d), the chemical structure of TP1 (with no specific stereochemistry yet) was presumed with the skeleton structure of $\text{C}(=\text{O})\text{H}-\text{NH}-\text{CH}=\text{CH}-\text{C}(=\text{O})\text{H}$. For small molecules, typically the opposite sign is expected for 2D NOESY interactions with respect to the diagonal peaks: e.g., the cross signal of H-3 to H-4 of TP2 in Figure S3.17f. However, all other observable 2D NOESY NMR cross peaks have the same sign as the diagonal peaks (Figure S3.17f), wherefore, a chemical exchange process between two stereoisomers must be postulated. For the isomers TP1_a and TP1_b, $J(\text{H}-1, \text{H}-2)$ of 14.2 Hz and 13.7 Hz were determined, respectively (Table S3.9). Therefore, H-1 and H-2 must be in *trans* configuration to each other at the double bond. For both isomers, $J(\text{H}-2, \text{H}-3)$ of 8.0 Hz was found. This indicates a *trans* configuration of H-2 and H-3. Because of the presence of the aldehyde group, the coupling constants between H-2 and H-4 are considerably smaller than $J(\text{H}-1, \text{H}-2)$. Finally, $J(\text{H}-4, \text{NH}) = 8.7$ Hz for TP1_b proved that H-4 and NH of the TP1_b must be *trans* to each other. In contrast, for TP1_a, $J(\text{H}-4, \text{NH})$ was small and not resolved, indicating *cis* configuration of H-4 and NH. Such isomer specific J values can be found in literature, e.g., for formamide as reference compound.³⁰





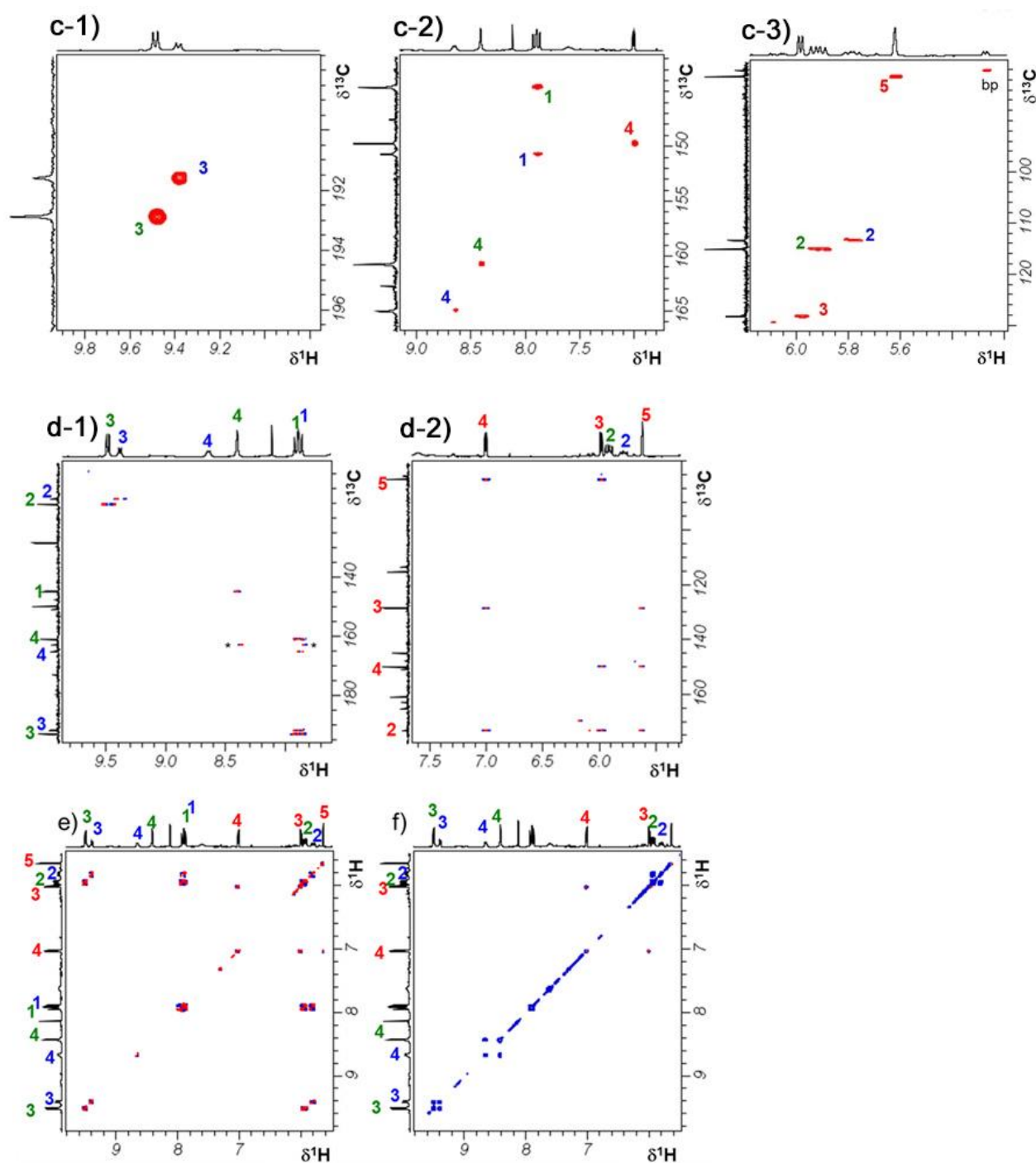


Figure S3.17. NMR data of an ozonated pyrrole sample prepared by the work-up (2) (Text S3.7) recorded in acetone- d_6 : (a-1 and a-2) ^1H with chemical structures of TP2, TP1_a and TP1_b, (b-1, b-2, and b-3) ^{13}C , (c-1, c-2, and c-3) ^1H - ^{13}C HSQC, (d-1 and d-2) ^1H - ^{13}C HMBC, (e) ^1H - ^1H DQF-COSY, and (f) ^1H - ^1H NOESY. ^1H and ^{13}C NMR spectra of the full spectral regions (a-1 and b-1) and of the regions of interest (a-2, b-2, and b-3) are shown. The numbers assigned across the NMR spectra correspond to the positions of the structures of TP2 (in red), TP1_a (in green), and TP1_b (in blue).

Text S3.8. NMR results – ^1H peak integration for TP1, TP2, and maleimide

The relative amounts of TP1, TP2, and maleimide in the NMR samples can be determined by integrating substance-specific ^1H NMR resonances. However, the isolated solids from the ozonated pyrrole solution were only partially soluble in acetone- d_6 , making a reproducible estimate of the isolated products impossible. Moreover, the ^1H NMR signal intensities varied significantly depending on the applied work-up procedures for removal of water after ozonation (Text S3.4). Specifically, the ratio of the integrated peak areas of TP2:TP1:maleimide was 1:0.1:0.5 for the sample isolated by work-up (1) treated by rotary evaporation with an elevated temperature (Table S3.10), whereas the ratio was 1:1.8:0.02 for the sample isolated by work-up (2) treated by rotary evaporation and lyophilization (Table S3.11). The isolated solids were almost completely soluble in DMSO- d_6 but with the disadvantage that broad background resonances of polymerized material made reliable integration of the signals of interest difficult. Therefore, a different sample composition of 1:0.08:0.3 for TP2:TP1:maleimide was obtained compared to those in acetone d_6 solutions (Table S3.10 and Table S3.12).

Table S3.10. Peak integration of ^1H NMR spectra recorded in acetone- d_6 for TP1, TP2, and maleimide detected in the ozonated pyrrole sample treated by the work-up (1) (only rotary evaporation to dryness).

Compound	$\delta^1\text{H}$	No. of H	Peak integration	Peak integration per H
TP2	7.0/6.0/5.4	3	3.000	1.000
TP1_a	9.5	1	0.076	0.076
TP1_b	9.4	1	0.032	0.032
Maleimide	6.8	2	0.948	0.474

Table S3.11. Peak integration of ^1H NMR spectra recorded in acetone- d_6 for TP1, TP2, and maleimide detected in the ozonated pyrrole sample treated by work-up (2) (rotary evaporation followed by lyophilization).

Compound	$\delta^1\text{H}$	No. of H	Peak integration	Peak integration per H
TP2	7.0/6.0/5.4	3	3.004	1.001
TP1_a	9.5/8.4/5.9	3	3.518	1.173
TP1_b	9.4/8.7/5.7	3	1.846	0.615
Maleimide	6.8	2	0.041	0.021

Table S3.12. Peak integration of ^1H NMR spectra recorded in DMSO- d_6 for TP1, TP2, and maleimide detected in the ozonated pyrrole sample treated by the work-up (1) (only rotary evaporation to dryness).

Compound	$\delta^1\text{H}$	No. of H	Peak integration	Peak integration per H
TP2	7.0/6.0/5.4	3	2.976	0.992
TP1_a	9.4	1	0.045	0.045
TP1_b	9.3	1	0.038	0.038
Maleimide	6.9	2	0.506	0.253

Text S3.9. LC-HRMS/MS results – detection of $C_4H_5NO_2$ and C_4H_5NO upon ozonation of pyrrole.

This section presents LC-HRMS/MS chromatograms, MS2 spectra, and integrated LC-MS peak areas as a function of the molar ratio of $[O_3]/[Pyrrole]_0$ for $C_4H_5NO_2$ and C_4H_5NO formed during the reaction of pyrrole with ozone.

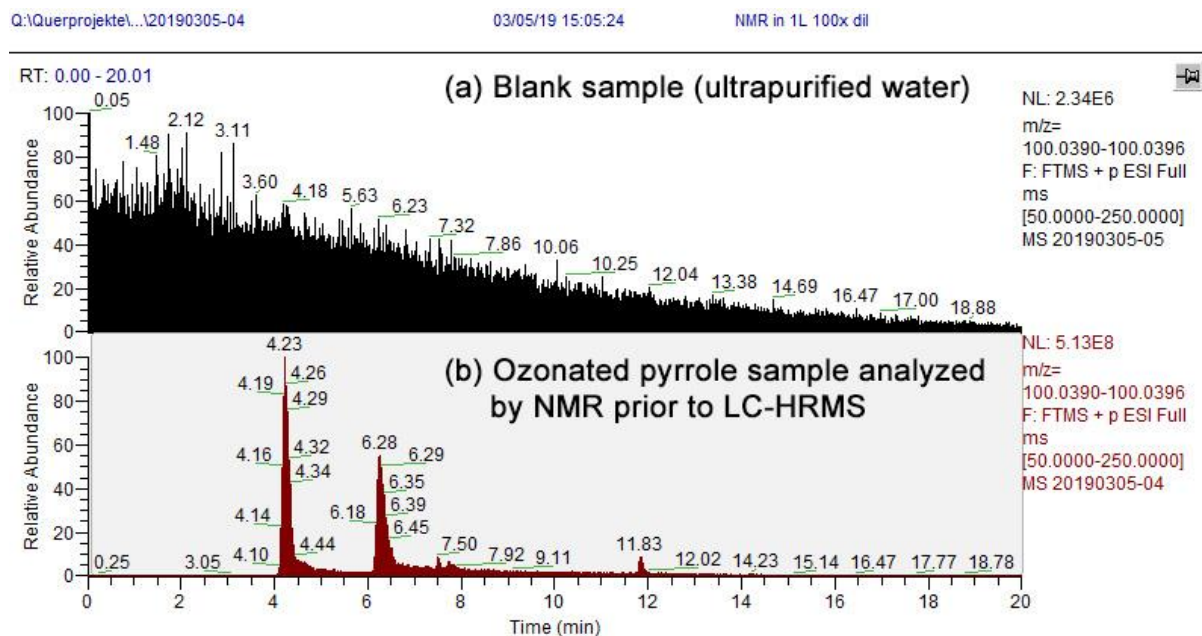


Figure S3.18. LC-HRMS/MS total ion chromatogram filtered by 100.0393, the exact mass of $C_4H_5NO_2$ as $[M+H]^+$ for (a) a blank sample with ultrapurified water and (b) a sample containing pyrrole ozonated and analyzed by NMR.

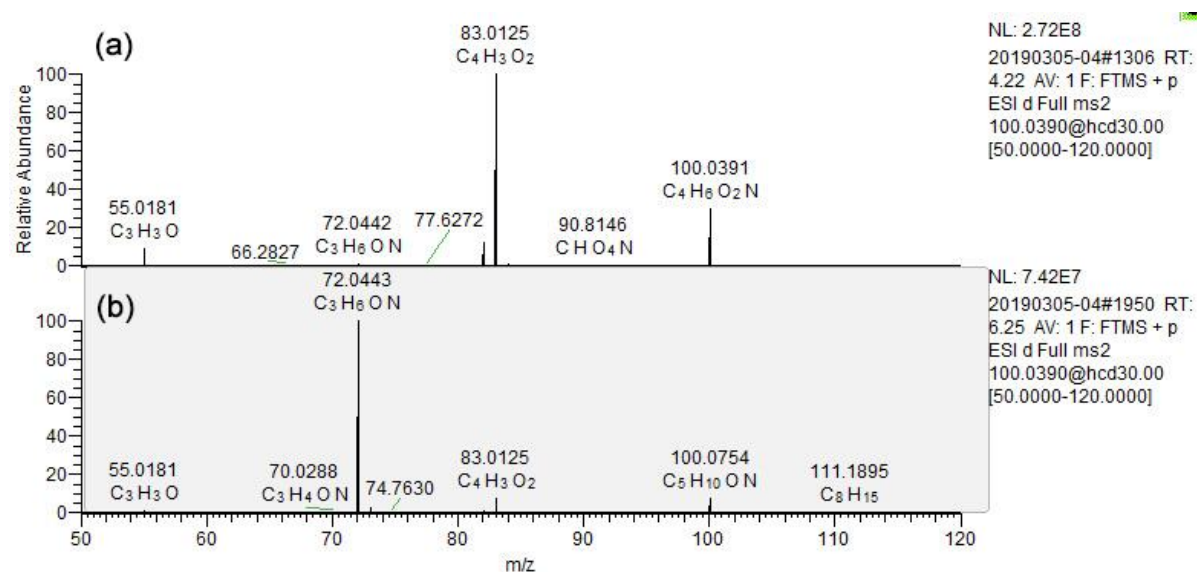


Figure S3.19. MS2 fragmentation patterns for the peaks at retention times of (a) 4.2 min and (b) 6.3 min for $m/z = 100.0393$ as shown in Figure S3.18.

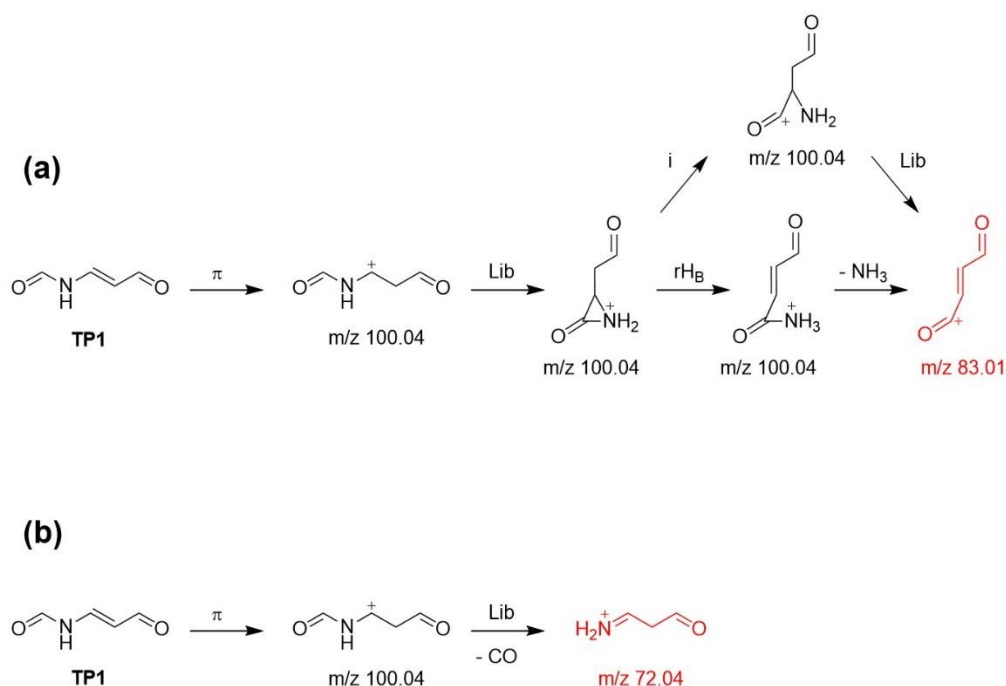


Figure S3.20. Fragmentation pathways predicted by a mass spectra interpretation software (Mass Frontier™, Thermo Scientific) from TP1 (a) to a fragment ion of $m/z = 83.0125$ and (b) to a fragment ion of $m/z = 72.0443$. Only selected patterns with the shortest pathway are shown. The codes used to describe the pathways are π : pi-electron ionization, Lib: fragmentation library mechanism, rHB : charge site rearrangement (γ), i : inductive cleavage.

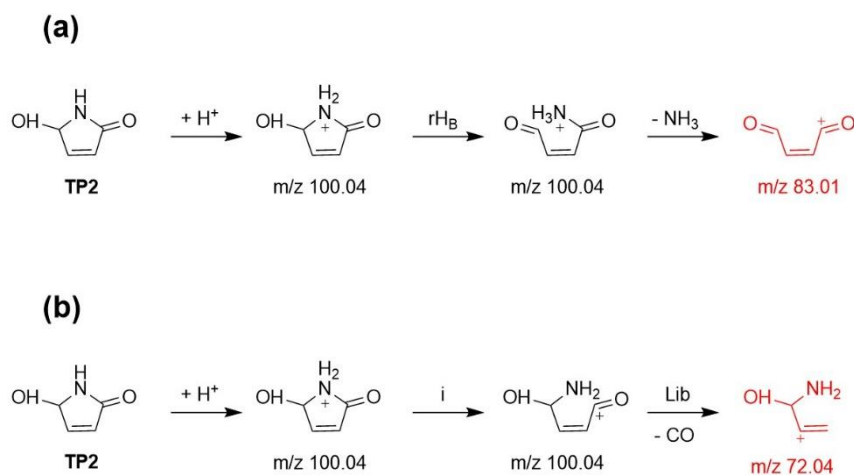


Figure S3.21. Fragmentation pathways predicted by a mass spectra interpretation software (Mass Frontier™, Thermo Scientific) from TP2 (a) to a fragment ion of $m/z = 83.0125$ and (b) to a fragment ion of $m/z = 72.0443$. Only selected patterns with the shortest pathway are shown. The codes used to describe the pathways are $+\text{H}^+$: protonation, i : inductive cleavage, Lib: fragmentation library mechanism, rHB : charge site rearrangement (γ).

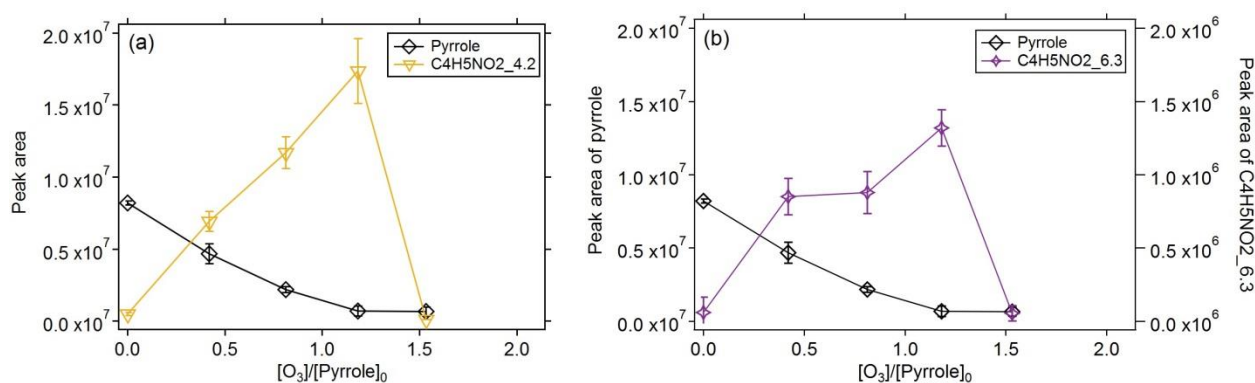


Figure S3.22. Integrated peak areas of (a and b) pyrrole, (a) $C_4H_5NO_2_{4.2}$, and (b) $C_4H_5NO_2_{6.3}$ as a function of the molar ratio of $[O_3]/[Pyrrole]_0$. $C_4H_5NO_2_{4.2}$ and $C_4H_5NO_2_{6.3}$ are peaks with $m/z = 100.0393$ (as $[M+H]^+$) as shown in Figure S3.18. All measurements were carried out in presence of 50 mM *t*-butanol at pH 7 (10 mM phosphate buffer). The initial pyrrole concentration was around 110 μ M.

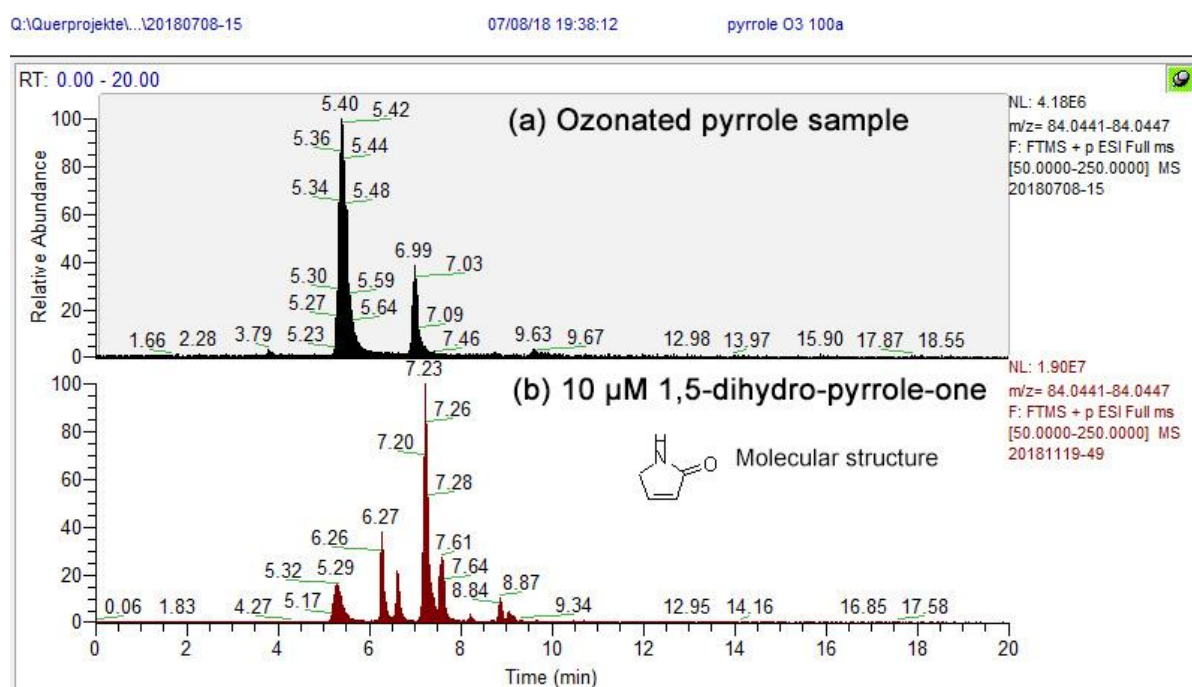


Figure S3.23. LC-HRMS/MS total ion chromatogram filtered by $m/z = 84.0444$, the exact mass of C_4H_5NO as $[M+H]^+$ ($\Delta mass = 3$ ppm) for an ozonated sample with (a) a molar $[O_3]/[Pyrrole]_0$ ratio of ~ 1 and (b) for 10 μ M of 1,5-dihydro-pyrrole-one.

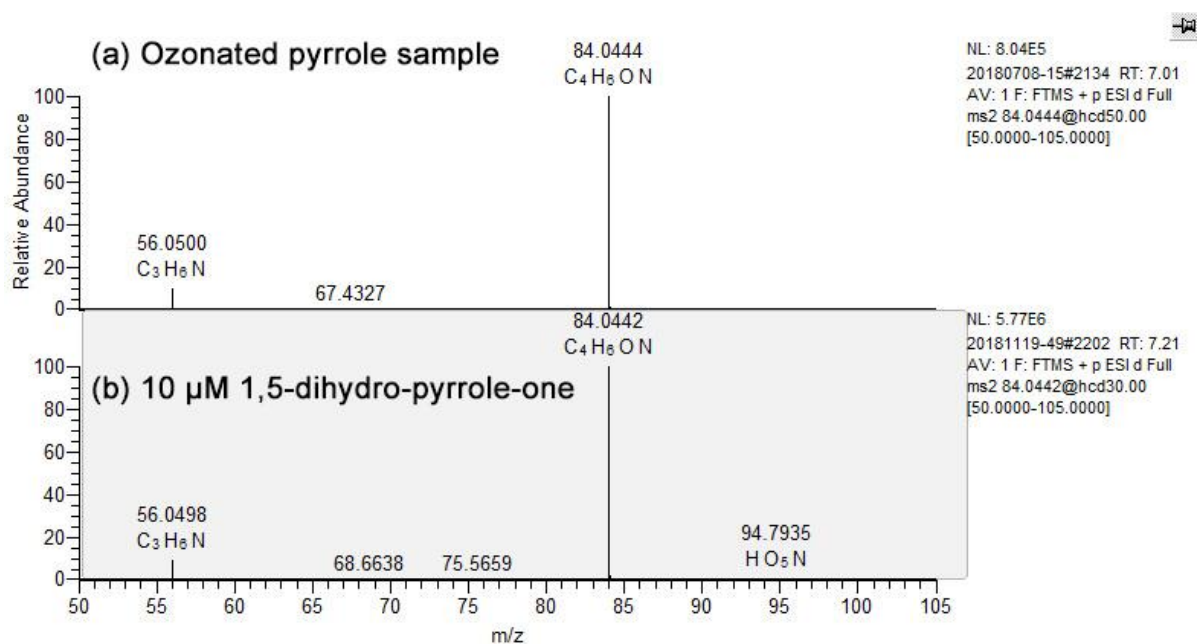


Figure S3.24. MS2 fragmentation patterns for the peaks (a) at a retention time of 7.0 min for an ozonated sample with a molar $[O_3]/[Pyrrole]_0$ ratio of ~ 1 and (b) at a retention time of 7.2 min for 10 μ M 1,5-dihydro-pyrrole-one, as shown in Figure S3.23.

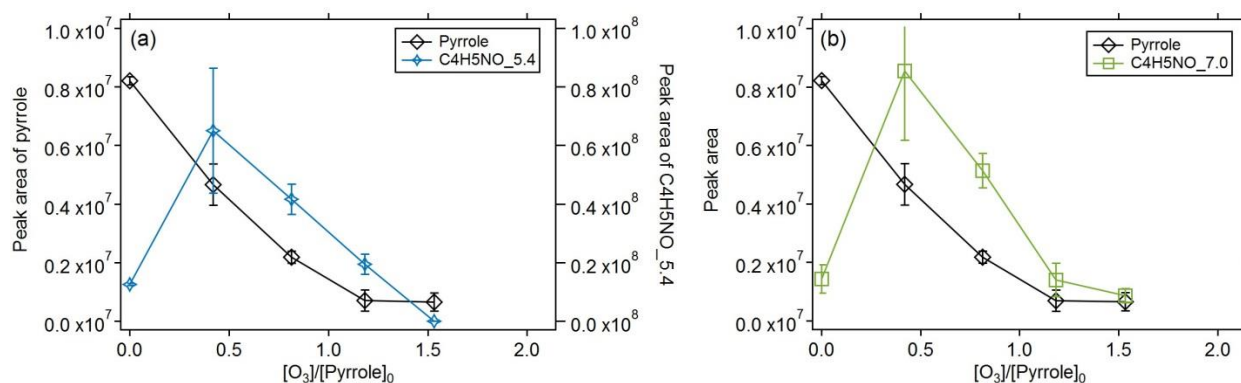


Figure S3.25. Integrated peak areas of (a and b) pyrrole, (a) $C_4H_5NO_{5.4}$, and (b) $C_4H_5NO_{7.0}$ as a function of the molar ratio of $[O_3]/[Pyrrole]_0$. $C_4H_5NO_{5.4}$ and $C_4H_5NO_{7.0}$ are unknown peaks with $m/z = 84.0444$ (as $[M+H]^+$) as shown in Figure S3.23. All measurements were carried out in presence of 50 mM *t*-butanol at pH 7 (10 mM phosphate buffer). The initial pyrrole concentration was around 110 μ M.

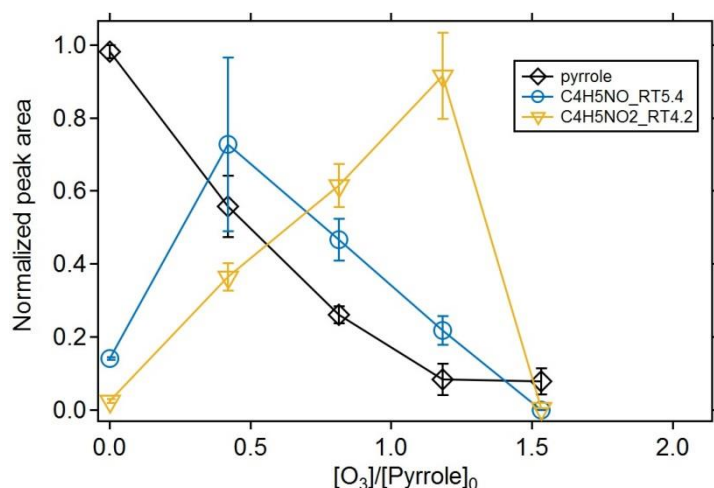


Figure S3.26. Integrated peak areas of pyrrole, C₄H₅NO₂_5.4, and C₄H₅NO₂_4.2 as a function of the molar ratio of [O₃]/[Pyrrole]₀. The areas were normalized by the largest area detected for each compound. C₄H₅NO₂_5.4, and C₄H₅NO₂_4.2 are the same as shown in Figure S3.25 and Figure S3.22, respectively. All measurements were carried out in presence of 50 mM *t*-butanol at pH 7 (10 mM phosphate buffer). The initial pyrrole concentration was around 110 μM.

Text S3.10. Quantum chemical computation results: initial pathways (A – C) of the pyrrole-ozone reaction

Based on the methods described in Text S3.6, the proposed reaction mechanisms of the pyrrole-ozone reaction were further investigated by quantum chemical computations. For the initial attack of ozone on pyrrole, different mechanisms are imaginable (Figure 3.3 in the main text and Figure S3.27). Following the formation of a pre-reactive complex, ozone could undergo concerted, bidentate cycloadditions at C2 and C3, or at C2 and C5. The other possibility is a monodentate addition at position C2. Transition structures for the monodentate attack were found using restricted as well as unrestricted calculations. We searched for transition structures for the bidentate attack by first optimizing the system keeping the C2-O and C3-O (or C2-O and C5-O) distances fixed at the same value (different values were tried), and optimizing the rest of the system. Starting from these partially optimized structures, a conventional transition structure optimization was performed. Neither for restricted nor for unrestricted (preceded by a wavefunction stability analysis) calculations were we able to obtain a transition structure for a concerted cycloaddition. Instead, the optimizations yielded transition structures for monodentate additions.

We note that the LC- ω PBE density functional was chosen as it performed best in reproducing gas phase barrier heights for ozone reactions with different substrates, including bidentate cycloaddition to ethane/ethyne, and monodentate attack on trimethylamine and bromide.²⁸ This suggests that if a bidentate cycloaddition to pyrrole in implicit water solvation is possible, LC- ω PBE should have been the most suitable density functional to find such transition structures. In contrast, a polar solvent can be expected to somewhat favor ionic reaction mechanisms, such as the monodentate attack that yields a zwitterion as an unstable intermediate. Lastly, as ozone is considered a multireference system, results obtained with single-reference methods have to be interpreted with caution, and the possibility of a bidentate attack cannot be entirely ruled out.

If a bidentate attack was possible, we would expect the barrier for formation of the C2,C5-cycloadduct to be higher than that for the formation of the C2,C3-cycloadduct. We reason that the strain in the C2,C5-cycloadduct that is responsible for its inferior stability compared to the C2,C3-cycloadduct is also partly present in the transi-

tion structure, and will destabilize the latter. We thus think that the formation of the C2,C5-cycloadduct is rather unlikely (see also Text S3.12).

The zwitterion that results from monodentate attack can exist in at least two stable conformations, which are separated by a low energetic barrier. Despite failing IRC calculations, the imaginary frequency of the transition structure is clearly associated with the torsion that would interconvert these conformers. From these, the C2,C3-cycloadduct can be reached also by a low barrier, whereas the C2,C5-cycloadduct can be reached only passing a higher barrier.

It is discussed in Text S3.11 to Text S3.15 that pathways (A) and (C) (including the subsequent pathways (D – G)) could be competitive, at least within the margin of error of the simulations, whereas pathway (B) is predicted to be rather unlikely.

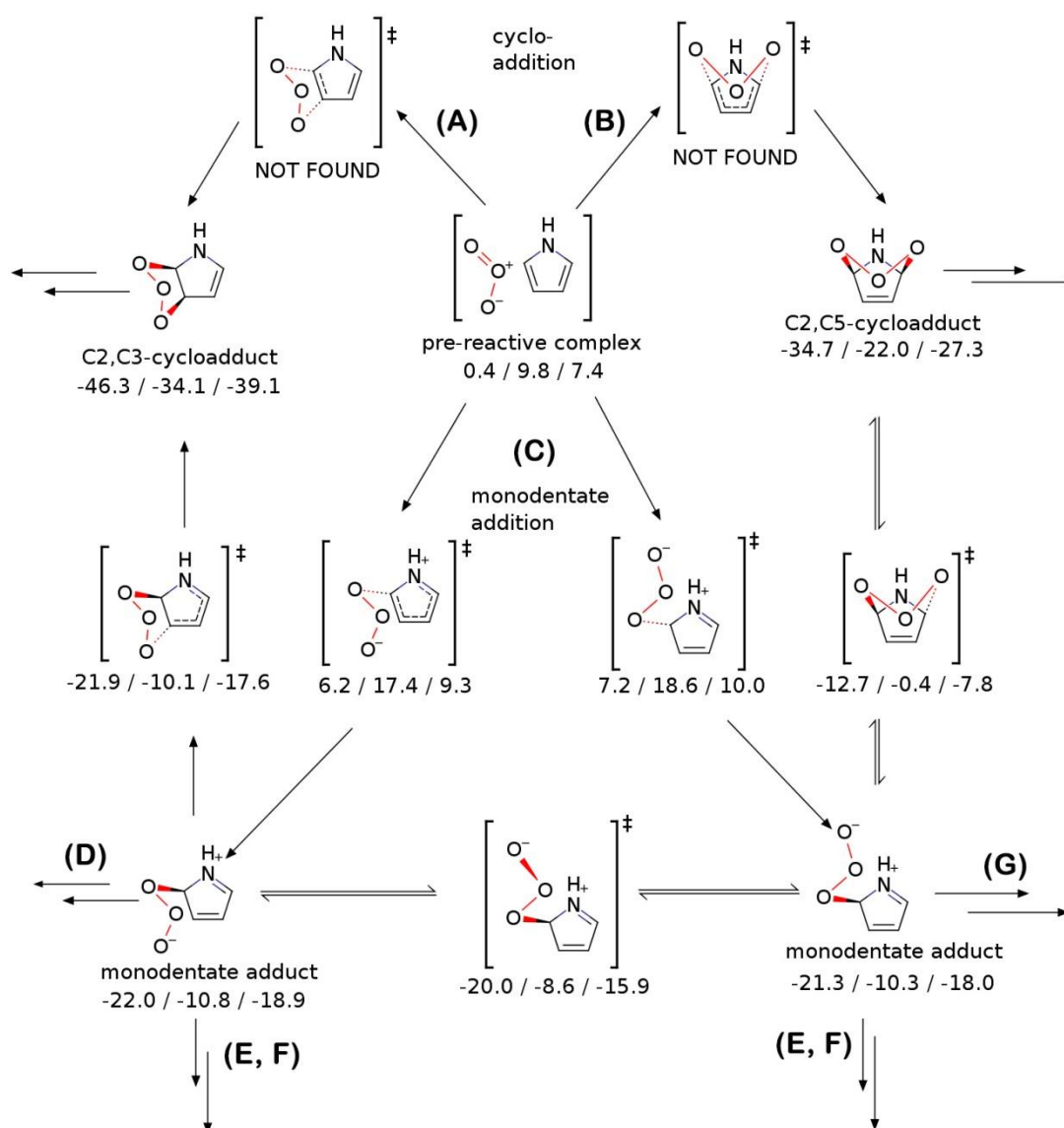


Figure S3.27. Computational depiction of the initial pathways (A – C) of the pyrrole-ozone reactions. The three numbers below each reaction species indicate LC- ω PBE energies at 0 K including zero-point vibrational energies, LC- ω PBE Gibbs free energies at 298 K, and M06-2X Gibbs free energies at 298 K (from left to right).

Text S3.11. Quantum chemical computation results: pathway (A) of the pyrrole-ozone reaction

Figure S3.28 shows how the double bond can be cleaved from the C2,C3-cycloadduct, leading eventually to the observed product TP1 and H₂O₂ in an exothermic/exergonic reaction. However, in the Gibbs free energy picture, the barrier for breaking the remaining C-C single bond is rather high, and the energy rises back to -10/-18 kcal mol⁻¹. This free energy of the transition structure is comparable to that of transition structures that connect the monodentate adduct to products, suggesting possible competition between different pathways.

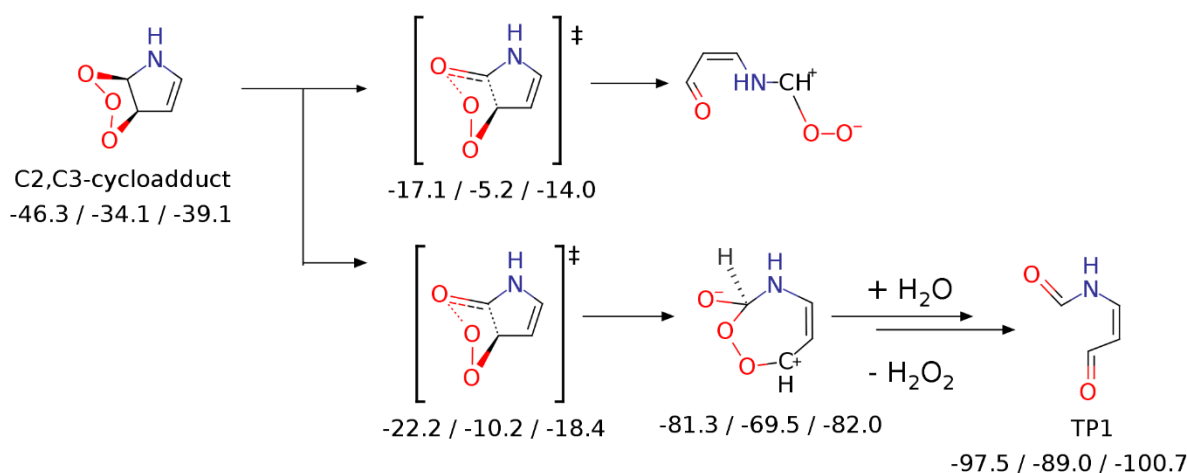
(A) C2,C3-cycloaddition and Criegee pathway

Figure S3.28. Computational depiction of the pathway (A), the cleavage of the double bond, following the formation of a cyclic adduct during the pyrrole-ozone reaction. The three numbers below each reaction species indicate LC- ω PBE energies at 0 K including zero-point vibrational energies, LC- ω PBE Gibbs free energies at 298 K, and M06-2X Gibbs free energies at 298 K (from left to right).

Text S3.12. Quantum chemical computation results: pathway (B) of the pyrrole-ozone reaction

The first step of the reaction refers to the autoprotolysis of two water molecules, which formally consumes ~51 kcal mol⁻¹. Hydroxide can abstract a proton from the cycloadduct with a relatively high barrier ($\Delta G^\ddagger = 27/23$ kcal mol⁻¹, Figure S3.29). This leads immediately to the cleavage of an O-O bond, a planarization, and formation of a C=O double bond. The resulting peroxo-anion can be protonated to yield a stable intermediate. The intermediate can be reacted to the observed product maleimide, cleaving one water molecule. This reaction needs to be catalyzed by another HO⁻, but seems kinetically feasible ($\Delta G^\ddagger = 17/14$ kcal mol⁻¹), and leads to an unstable intermediate that cleaves HO⁻ to yield maleimide.

The overall feasibility of this route depends on (a) if the C2,C5-cycloadduct can be formed and (b) if the initial deprotonation of the cycloadduct is not outcompeted by the back-reaction from the cycloadduct. Since in the real system, hydroxide originates from the (fast) autoprotolysis of water, it will be present at a steady state concentration of 10⁻⁷ M at pH 7, which should be multiplied with the rate constant to yield an apparent first order rate constant. If an underestimation of the barrier by 5 kcal mol⁻¹ is assumed, the Eyring equation will still predict a second order rate constant of 4 × 10⁻¹ M⁻¹s⁻¹, and an apparent rate constant of 4 × 10⁻⁸ s⁻¹. The barrier for the reaction of the cycloadduct back to the monodentate adduct is predicted to be ~20 kcal mol⁻¹, corresponding to a rate constant of 1 × 10⁻² s⁻¹. To proceed with pathway (B), the barrier of this back-reaction would need to be underestimated by ~5 kcal mol⁻¹. Conversely, it can be argued that the implicit solvation model should underes-

timate the solvation energy of hydroxide, and to a lesser extent also the solvation energy of the trioxoanion substituent. This should lead to the opposite effect: an underestimation of the barrier connected to the attack of hydroxide, and an overestimation of the barrier of the back-reaction. Thus, pathway (B) seems rather unlikely, even if the C2,C5-cycloadduct can be formed in some way.

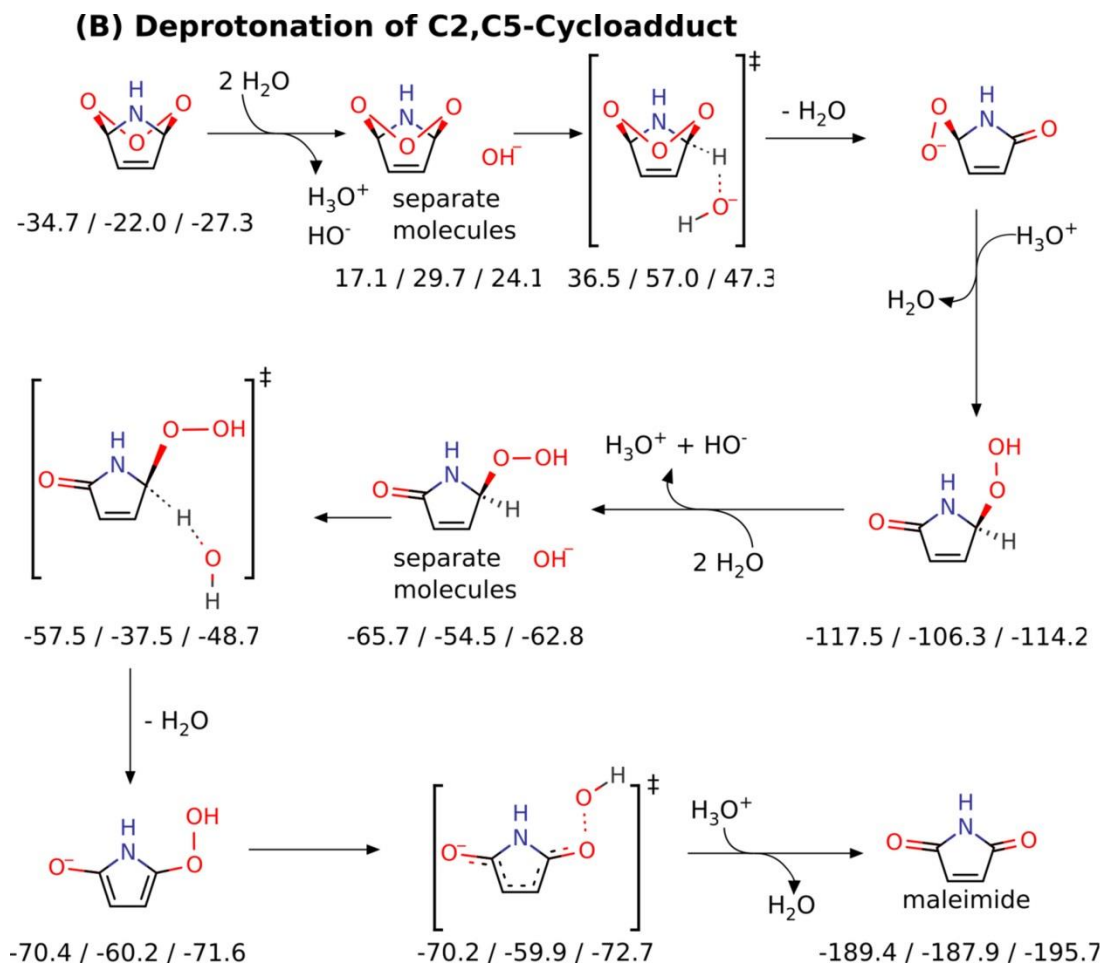


Figure S3.29. Computational depiction of the pathway (B), the deprotonation of the C2,C5-cycloadduct during the pyrrole-ozone reaction. The three numbers below each reaction species indicate LC- ω PBE energies at 0 K including zero-point vibrational energies, LC- ω PBE Gibbs free energies at 298 K, and M06-2X Gibbs free energies at 298 K (from left to right).

Text S3.13. Quantum chemical computation results: pathway (D) of the pyrrole-ozone reaction

All energies in Figure S3.30 depict a low barrier (2-3 kcal mol⁻¹) for cleaving singlet oxygen from the monodentate adduct. Although IRC calculations did not succeed, the imaginary frequency of the transition structure clearly corresponds to the relevant O-O stretch. This reaction is depicted as exergonic by free energy calculations, but as endothermic when neglecting temperature effects. Either way, the energy is drastically lowered when the resulting singlet oxygen converts to its triplet ground state in an irreversible reaction. Cleaving oxygen yields a zwitterion, from which different rearrangements are imaginable, of which we only report final energies. One of the products, 2-hydropyrrole, would be fast-reacting with ozone, and could form secondary products.

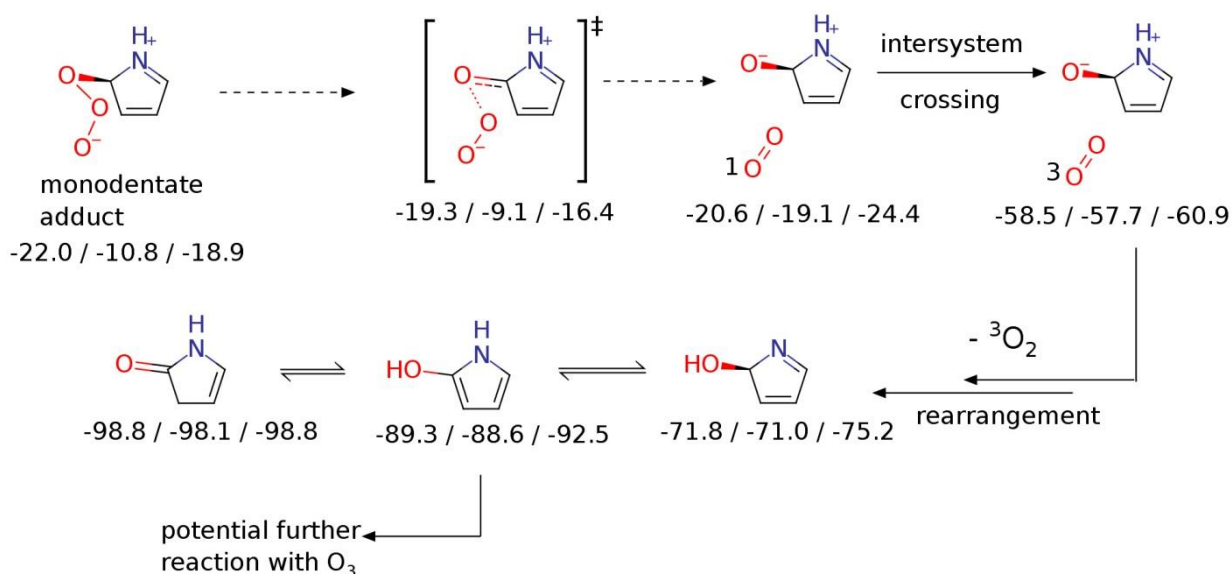
(D) Cleavage of singlet oxygen ($^1\text{O}_2$)

Figure S3.30. Computational depiction of the pathway (D), the deprotonation of singlet oxygen cleavage from a monodentate adduct. The three numbers below each reaction species indicate LC- ω PBE energies at 0 K including zero-point vibrational energies, LC- ω PBE Gibbs free energies at 298 K, and M06-2X Gibbs free energies at 298 K (from left to right).

Text S3.14. Quantum chemical computation results: pathways (E) and (F) of the pyrrole-ozone reaction

The zwitterionic adduct can undergo a rearrangement reaction, in which the negatively charged oxygen attacks the C-H position (Figure S3.31). Calculations could locate a closed-shell transition structure for this reaction, but IRC calculations failed, probably owing to a relatively flat PES around the transition structure. Relaxed scans along H-O distance would yield a zwitterionic, closed shell complex, which is highly unstable. Two possible cage reactions are N-H proton transfer to HOO^- or addition of HOO^- to the ring, both with negligible barriers. These could lead either to the observed product maleimide, or to pyrrole-2-one. Pyrrole-2-one can potentially hydrolyze, which would lead to the observed TP2. If this reaction is kinetically feasible is not easily answered, as the barrier for reactions with hydroxide could be severely underestimated.

In contrast, a radicalic mechanism should also be possible from the beginning. Owing to limitations of the used methods, complexed radical pairs cannot be simulated. However, the energy of isolated radicals is much lower than that of the zwitterionic complex. A transition structure for radical recombination could be found, though, and this pathway should be kinetically feasible.

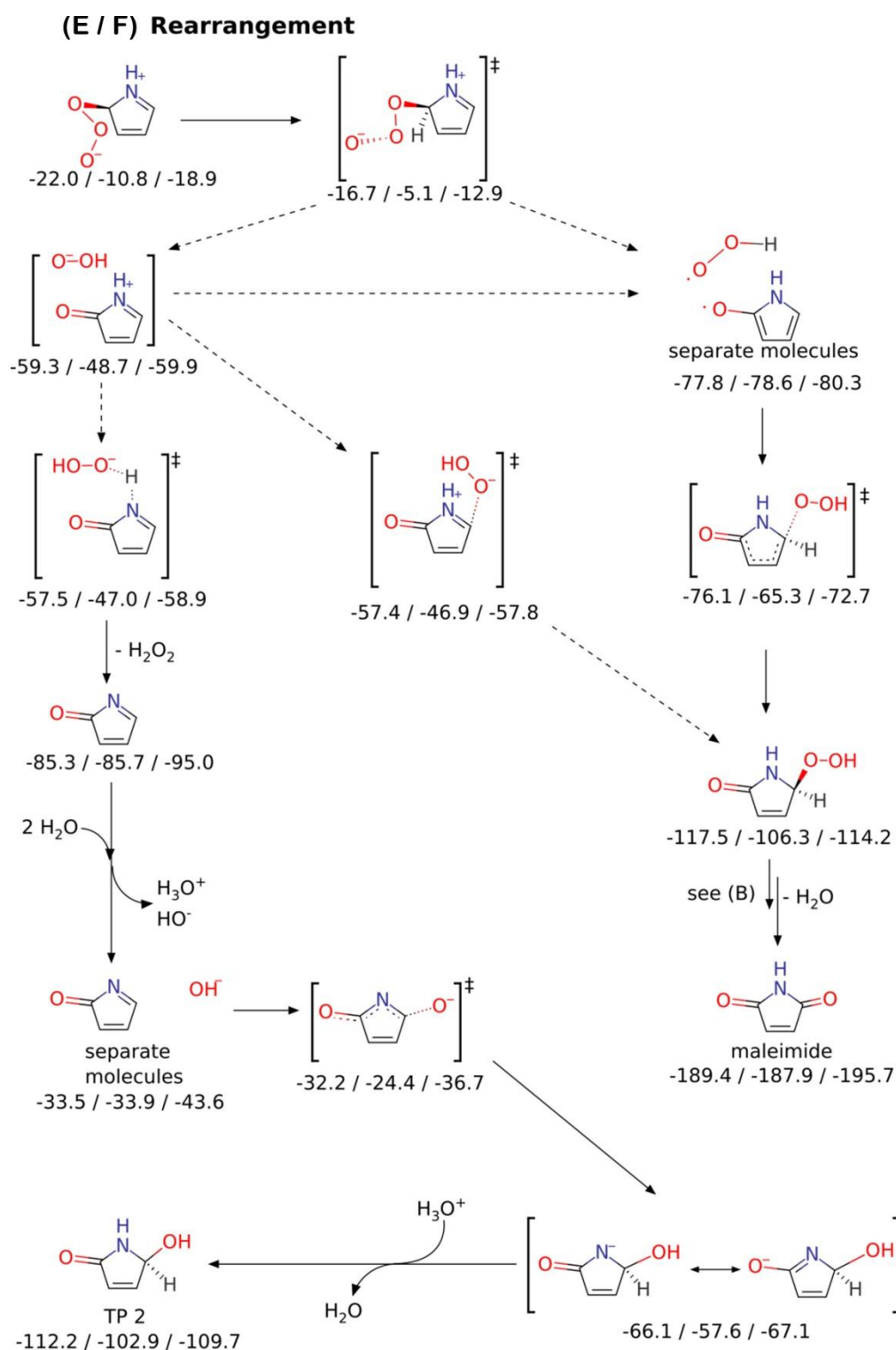


Figure S3.31. Computational depiction of the pathways (E) and (F), the rearrangement reactions of the zwitterionic adduct. The three numbers below each reaction species indicate LC- ω PBE energies at 0 K including zero-point vibrational energies, LC- ω PBE Gibbs free energies at 298 K, and M06-2X Gibbs free energies at 298 K (from left to right).

Text S3.15. Quantum chemical computation results: pathway (G) of the pyrrole-ozone reaction

Computations predict that the monodentate adduct can undergo another proton transfer reaction, in which the N-H proton is transferred to the trioxoanion moiety (Figure S3.32). This reaction is depicted as exergonic. A further exergonic rearrangement is catalyzed by water in the form of hydroxide and hydronium cation, and yields pyrrole with a -OOOH substituent. This molecule should dissociate rather easily into a hydroperoxyl radical and an organic radical, in which the unpaired electron can be stabilized by delocalization in the ring. This reaction is analogous to pathway (E/F) (see above), with the same limitation that the radical pair cannot be simulated.

The initial proton transfer is clearly kinetically feasible, but leads to an only slightly more stable product. From this product, the back-reaction (and subsequent reaction through other pathways) may be in competition with deprotonation by HO⁻. The free energy barrier of the reaction with hydroxide is predicted at 6-10 kcal mol⁻¹, but may be underestimated because of shortcomings in the solvation model. In a “back of the envelope” estimation with the Eyring equation, a barrier of 6 kcal mol⁻¹ would yield a rate constant of $2 \times 10^8 \text{ M}^{-1} \text{ s}^{-1}$, and an apparent first order rate constant of $2 \times 10^1 \text{ s}^{-1}$. In comparison, the barrier for the back-reaction is predicted as 16-17 kcal mol⁻¹, formally corresponding to a rate constant of $1 \times 10^1 \text{ s}^{-1}$. Thus, an equilibrium between the proton-transferred structure and the monodentate adduct cannot be excluded, and the forward reaction eventually leading to the observed product maleimide may compete with the back-reaction to the monodentate adduct.

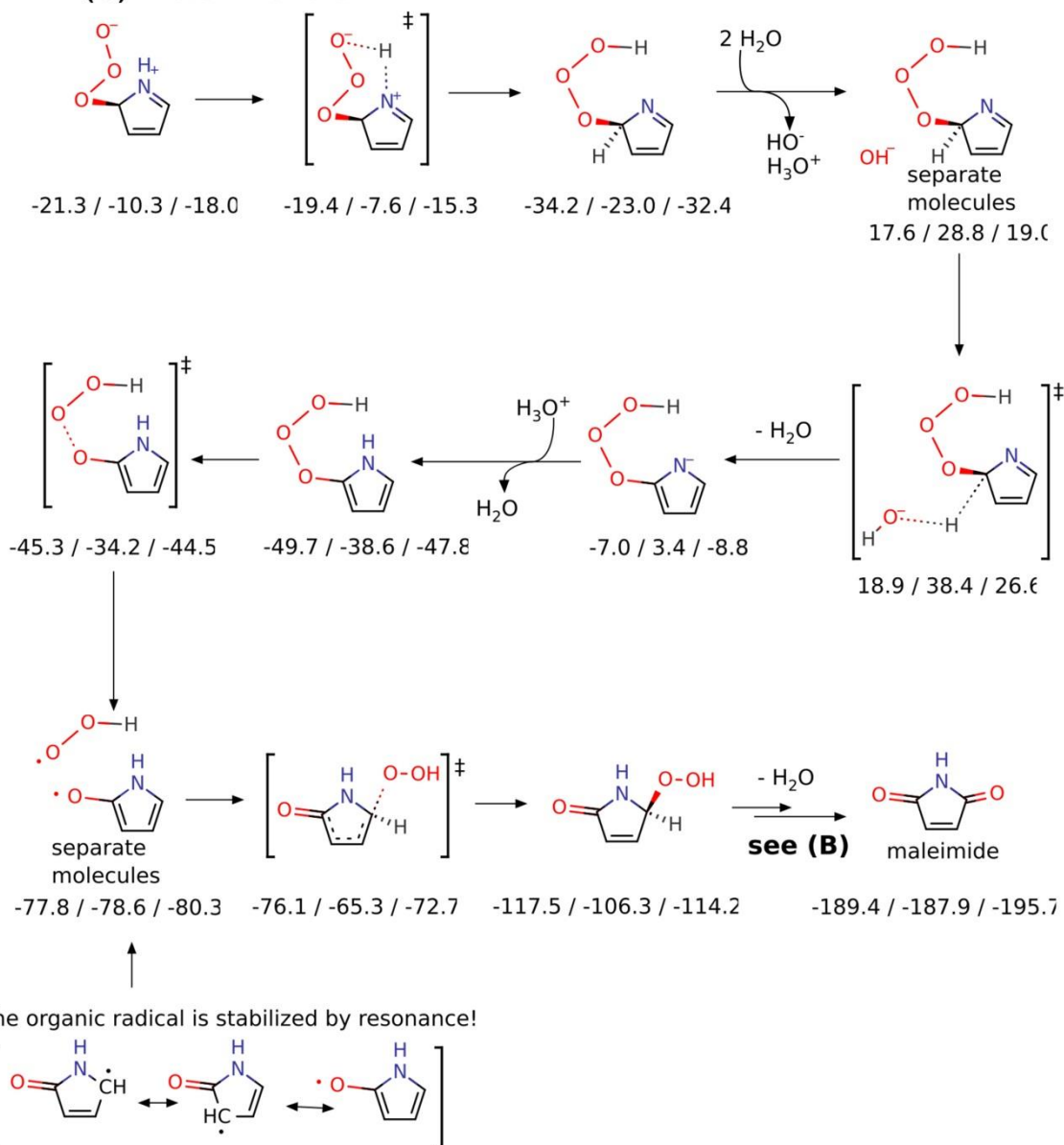
(G) Proton transfer

Figure S3.32. Computational depiction of the pathway (G), the proton transfer pathway starting from the zwitterionic adduct. The three numbers below each reaction species indicate LC- ω PBE energies at 0 K including zero-point vibrational energies, LC- ω PBE Gibbs free energies at 298 K, and M06-2X Gibbs free energies at 298 K (from left to right).

Text S3.16. Semi-quantification of urea during the imidazole- O_3 reaction.

A minor formation of urea during the reaction of imidazole with ozone was suggested by LC-HRMS/MS with the corresponding reference standard by matching the retention time. The formation of urea as a function of the molar ratio of $[\text{O}_3]/[\text{Imidazole}]_0$ is shown in Figure S3.33. Accordingly the yield of urea per consumed imidazole was determined to be 8%. However, the urea concentrations should be considered as only semi-quantitative, since they were determined without any internal standards. Moreover, for this analysis, a high mass deviation of ~ 50 ppm was observed for both ozonated samples and standards (the detected exact mass = 61.0368 in comparison to the theoretical exact mass = 61.0396 for urea as $[\text{M}+\text{H}]^+$), probably caused by an inadequate mass calibration. This was much higher than the usual mass deviations within 2 ppm for all other analytes (Table S3.5). Therefore, additional tests with a more careful mass calibration and with an internal standard are required to confirm the formation of urea and its yield for certain.

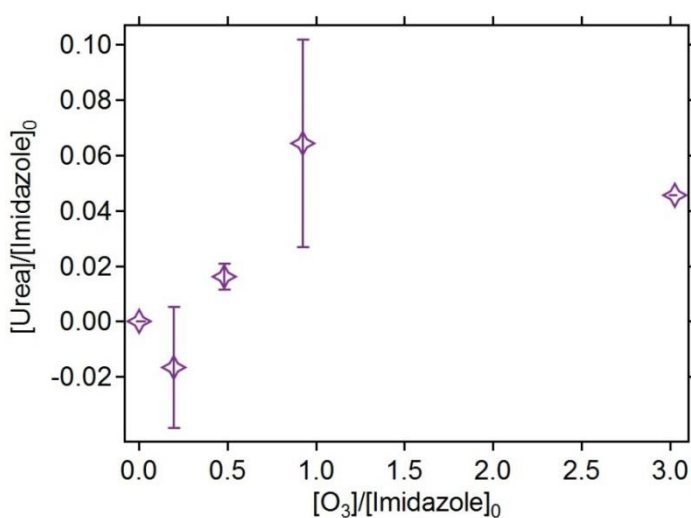


Figure S3.33. Formation of urea as a function of the molar ratio of $[\text{O}_3]/[\text{Imidazole}]_0$ determined by LC-HRMS/MS without internal standards. All measurements were carried out in presence of 50 mM *t*-butanol at pH 7 (20 mM bicarbonate buffer). The initial imidazole concentrations were around 100 μM .

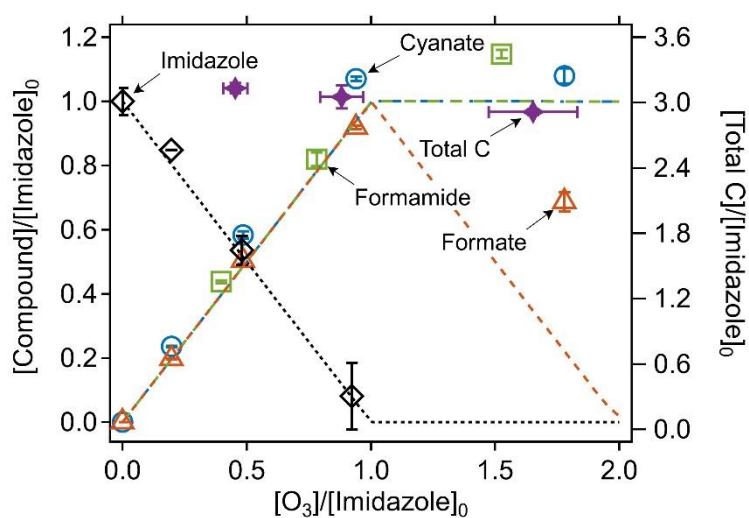


Figure S3.34. Relative abatement of imidazole and the formation of transformation products as a function of the molar ratio of $[O_3]/[Imidazole]_0$, as shown in Figure 3.5 in the main text. The symbols indicate the measured concentrations (duplicate or triplicate) and the lines indicate simulated concentrations based on the kinetic models described in Table S3.4. Total C indicates the sum of the concentrations of all carbons in the remaining imidazole and the carbon-containing transformation products.

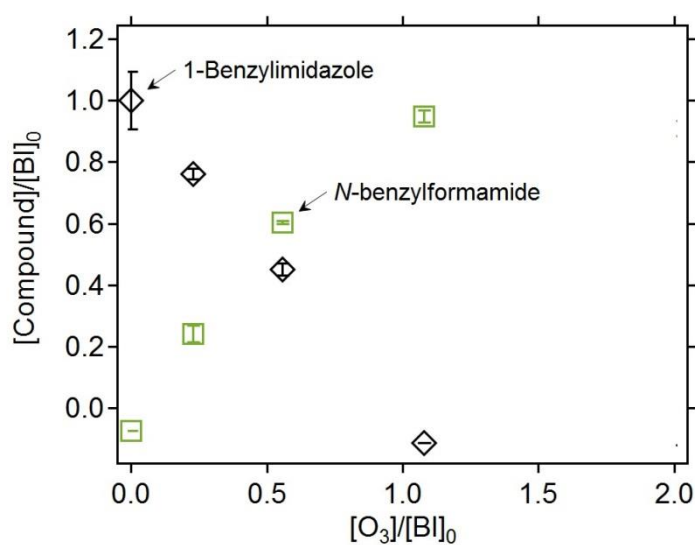


Figure S3.35. Relative abatement of 1-benzylimidazole (BI) and formation of *N*-benzylformamide as a function of the molar ratio of $[O_3]/[BI]_0$. All measurements were carried out in presence of 50 mM *t*-butanol at pH 7 (10 mM phosphate buffer). The initial BI concentrations were around 90 μ M.

Text S3.17. Quantum chemical computation results: the imidazole-ozone reaction

The fate of the cyclic ozonide formed by addition to imidazole was investigated (Figure S3.36). This reaction can initially follow the Criegee pathway to cleave the double bond. In the resulting acyclic molecules with a zwitterion form, mesomeric effects delocalize the positive charge that is formally assigned to a carbon atom. A ring formation seems then possible with the anionic peroxy substituent of the zwitterion acting as a nucleophile. Two cyclic intermediates containing a dioxazole moiety can be formed in these exergonic reactions. From both structures, rearrangement reactions to formamide and formylisocyanate are imaginable, but were not investigated in more detail. However, this reaction would be strongly exergonic. Reactions of possible monodentate adducts that may be in competition with the shown Criegee mechanism were not investigated.

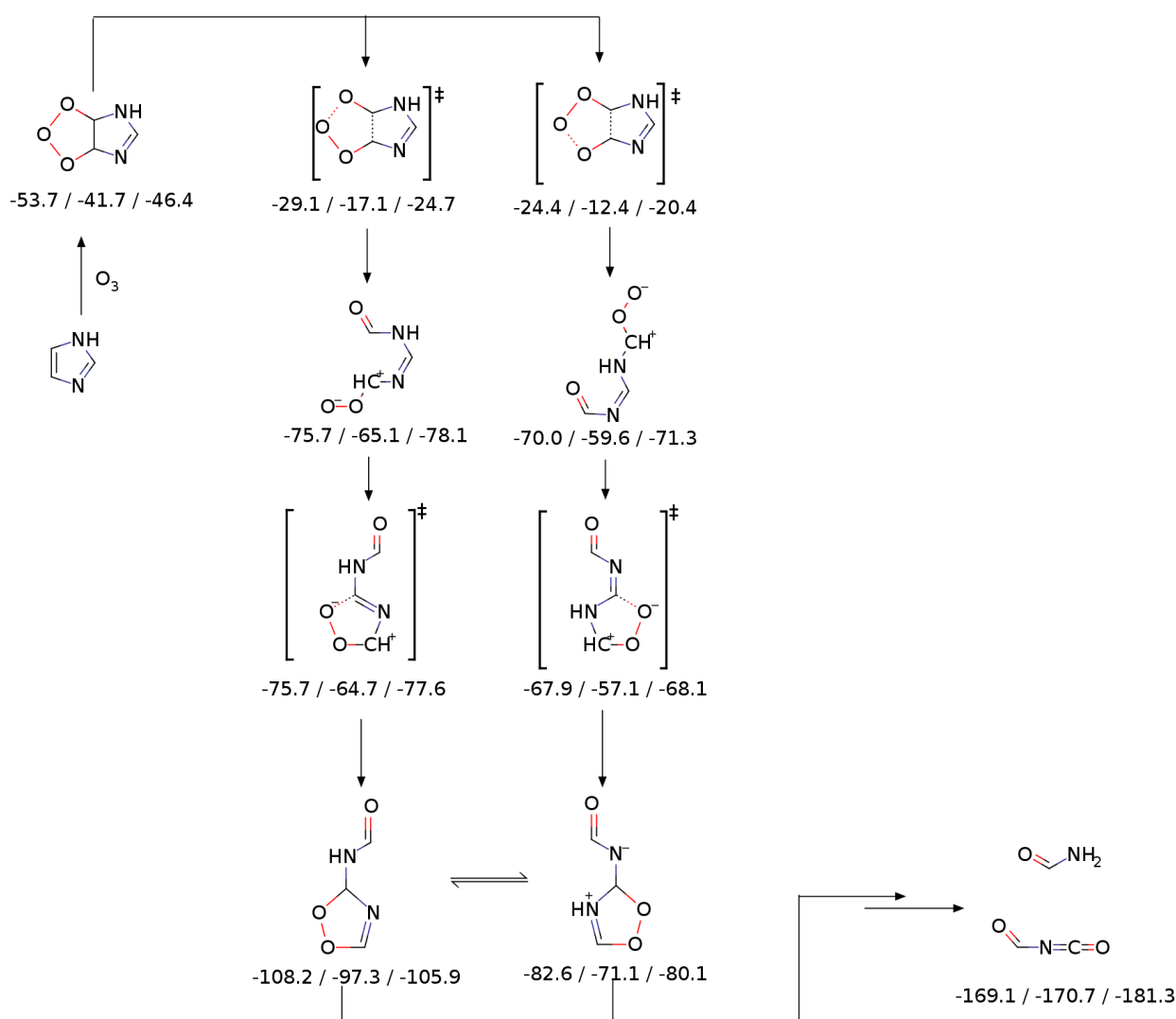


Figure S3.36. Computational depiction of the reaction of imidazole with ozone. The three numbers below each reaction species indicate LC- ω PBE energies at 0 K including zero-point vibrational energies, LC- ω PBE Gibbs free energies at 298 K, and M06-2X Gibbs free energies at 298 K (from left to right).

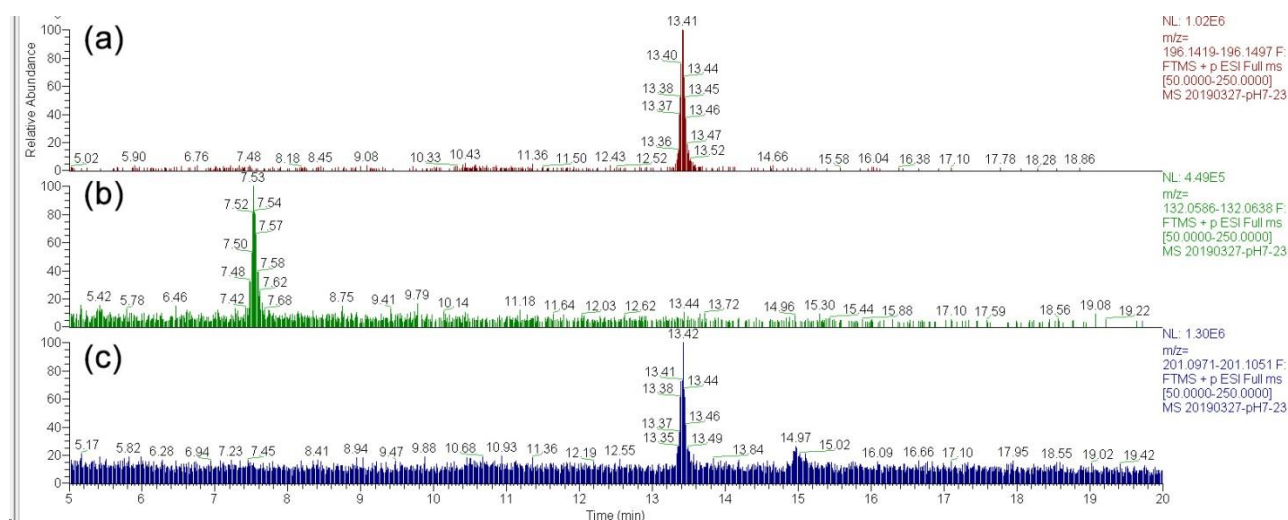


Figure S3.37. LC-HRMS/MS chromatogram filtered by m/z = (a) 196.1458, (b) 132.0612, and (c) 201.1009 for an ozonated pyrazole sample with a molar $[O_3]/[Pyrazole]_0$ ratio of ~ 3 . All measurements were carried out in presence of 50 mM *t*-butanol at pH 7 (10 mM phosphate buffer). The initial pyrazole concentration was around 100 μ M.

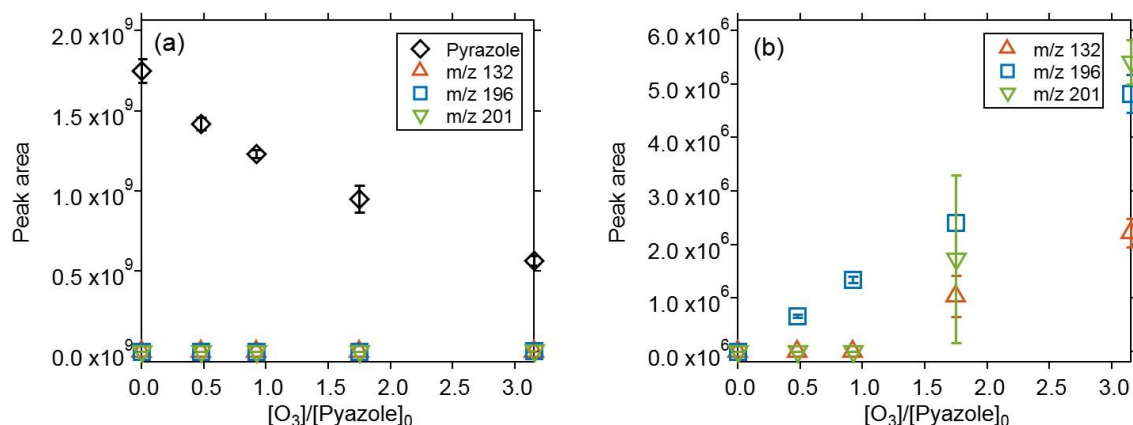


Figure S3.38. Integrated peak areas of (a) pyrazole and (b) m/z = 132.0612, 196.1458, and 201.1009 as a function of the molar ratio of $[O_3]/[Pyrazole]_0$. All measurements were carried out in presence of 50 mM *t*-butanol at pH 7 (10 mM phosphate buffer). The initial pyrazole concentration was around 100 μ M.

Table S3.13. Possible molecular formulas for the exact masses of m/z = 132.0612, 196.1458, and 201.1009 by assuming the maximum numbers of occurrences of the isotopes ^{12}C , ^{14}N , ^{16}O , 1H , and ^{23}Na to be 10, 10, 10, 20, and 1, respectively. Only the formulas with mass deviations of less than 20 ppm are shown.

Exact mass	Possible molecular formula	Mass deviation, ppm
132.0612	$CH_9O_2N_4Na$	-4.3
	CH_6ON_7	-12.4
196.1458	$C_{10}H_{18}ON_3$	6.9
	$C_8H_{16}N_6$	13.8
	$C_8H_{19}ON_3Na$	19.2
201.1009	$C_{10}H_{11}N_5$	0.03
	$C_{10}H_{14}ON_2Na$	5.3
	$C_9H_{15}O_4N$	6.7
	$C_8H_{12}N_5Na$	12.0
	$C_7H_{13}O_3N_4$	13.3
	$C_7H_{16}O_4Nna$	18.6

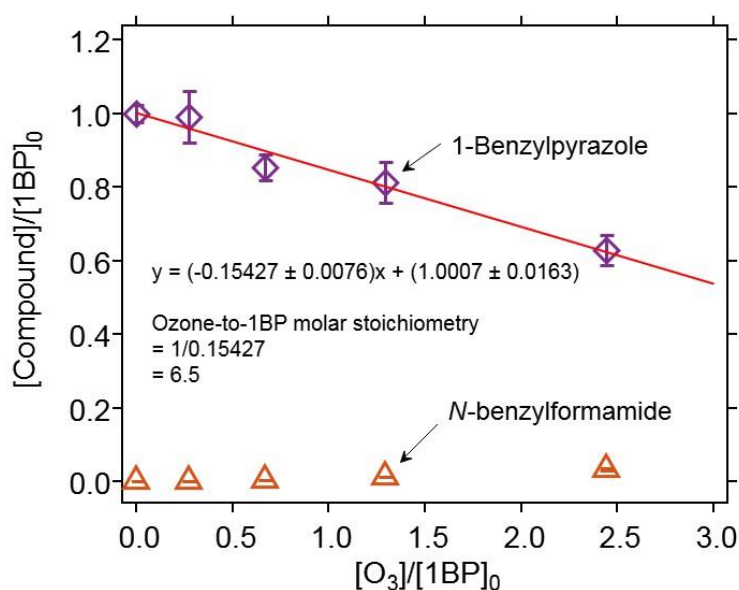


Figure S3.39. Relative abatement of 1-benzylpyrazole (1BP) and the formation of *N*-benzylformamide as a function of the molar ratio of $[O_3]/[1BP]_0$. The ozone:1BP molar stoichiometry was calculated by inverting the slopes from a linear regression of the measured 1BP concentrations. All measurements were carried out in presence of 50 mM *t*-butanol at pH 7 (10 mM phosphate buffer). The initial 1BP concentration was around 70 μ M.

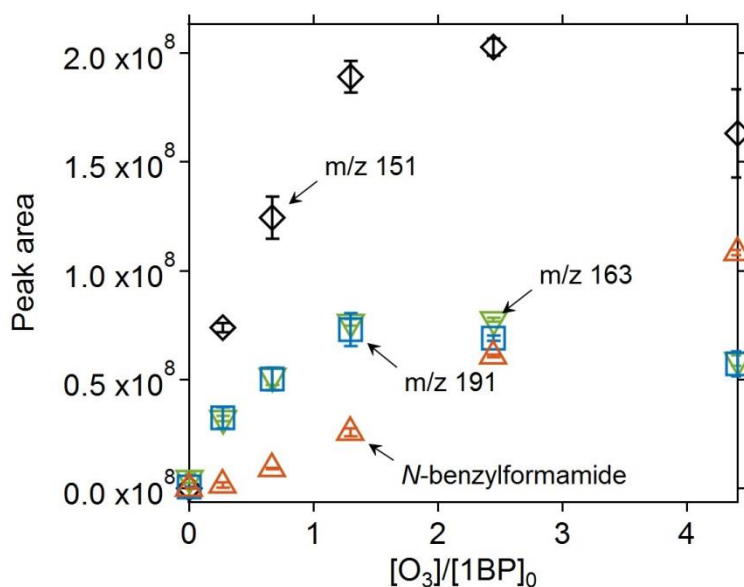
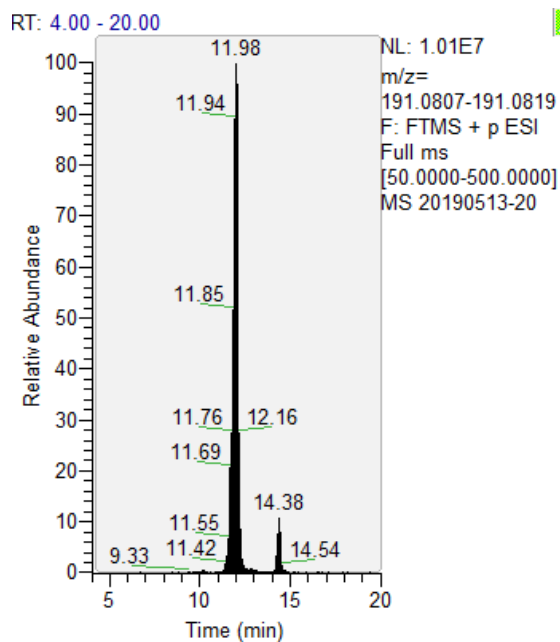


Figure S3.40. Integrated peak areas of *N*-benzylformamide (triangle), $m/z = 151.0864$ (diamond), 163.0864 (inversed triangle), and 191.0813 (square) as a function of the molar ratio of $[O_3]/[1BP]_0$ for ozonated 1-benzylpyrazole samples. All measurements were carried out in presence of 50 mM *t*-butanol at pH 7 (10 mM phosphate buffer). The initial 1BP concentration was around 70 μ M.

A. Chromatogram

- Peak retention time: 12.0 min
- Peak intensity: 1.0×10^7

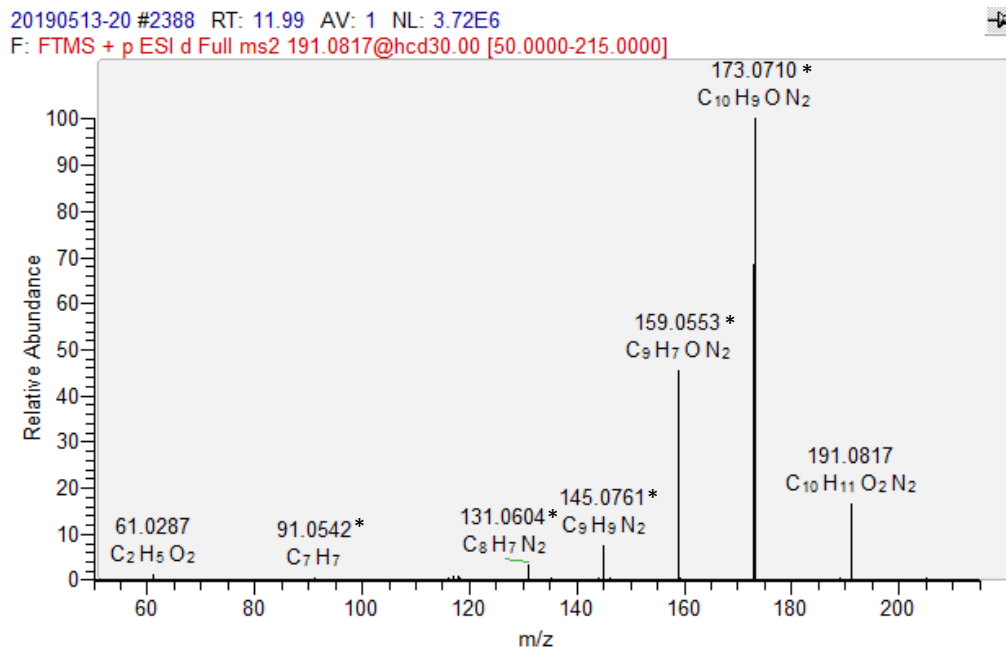
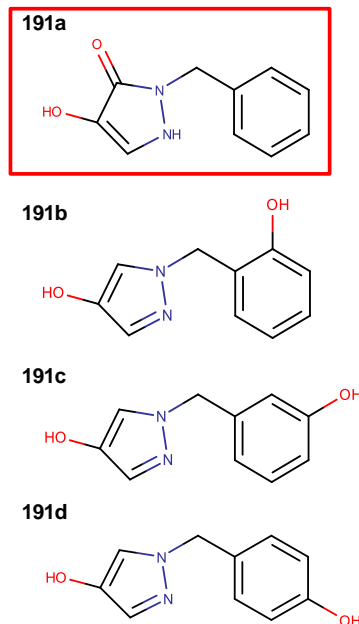
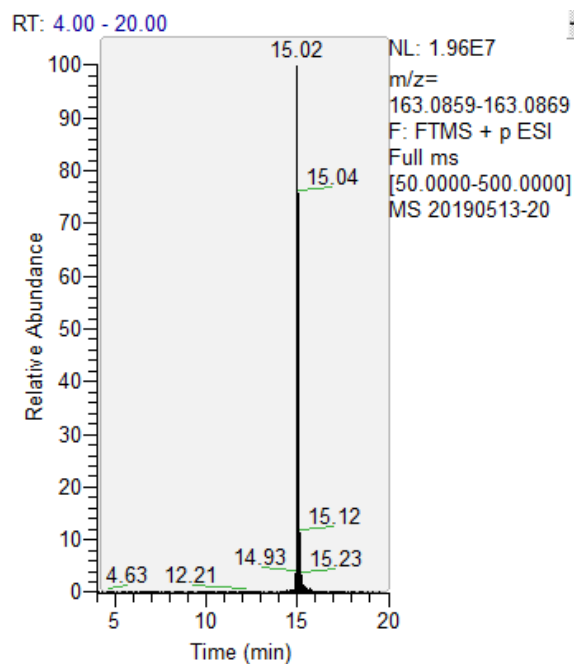
B. MS2 spectra**C. Proposed molecular formula**C₁₀H₁₀N₂O₂**D. Candidate structures**

Figure S3.41. (A) LC-HRMS/MS total ion chromatogram filtered by $m/z = 191.0813$, (B) the corresponding MS2 spectrum, (C) a proposed molecular formula, and (D) candidate structures of $m/z = 191.0813$ found by MetFrag analyses for an ozonated 1-benzylpyrazole sample with a molar ratio of $[O_3]/[1BP]_0 \sim 1$. The fragment ions denoted with asterisks (*) match those simulated by MetFrag as shown in Figure S3.44 and Figure S3.45. The candidate structure highlighted by a red square indicates the most plausible structure (Text S3.18).

A. Chromatogram

- Peak retention time: 15.0 min
- Peak intensity: 2.0×10^7

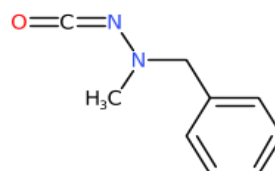
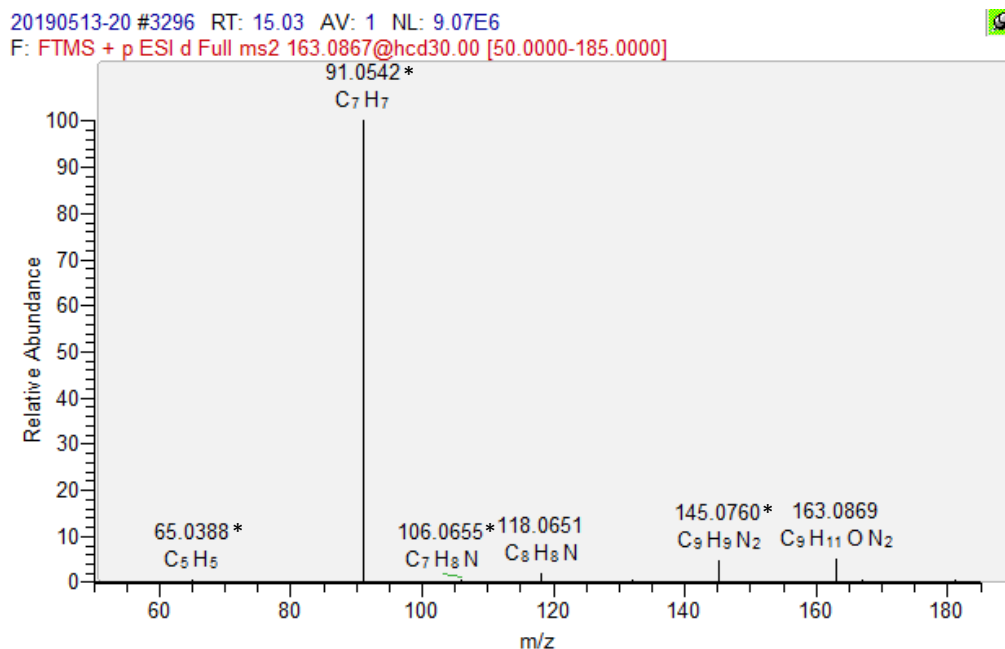
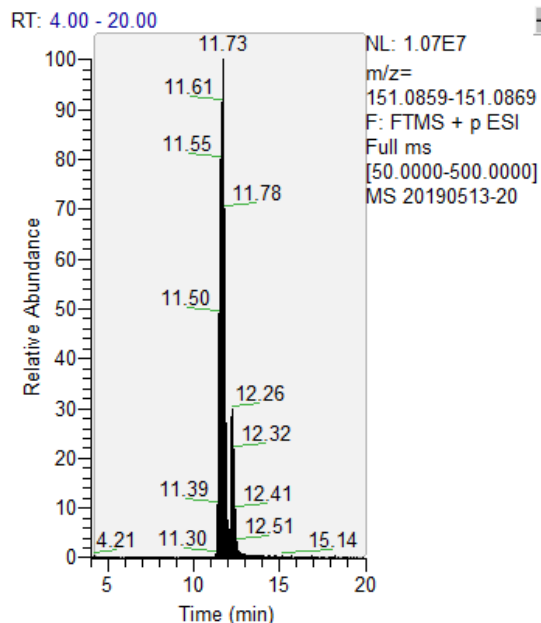
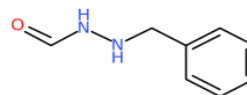
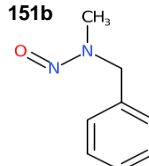
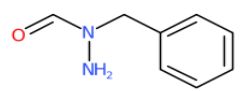
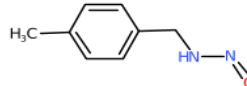
C. Proposed molecular formula**D. Candidate structures****B. MS2 spectra**

Figure S3.42. (A) LC-HRMS/MS total ion chromatogram filtered by $m/z = 163.0864$, (B) the corresponding MS2 spectrum, (C) a proposed molecular formula, and (D) a candidate structure of $m/z = 163.0864$ found by MetFrag analyses for an ozonated 1-benzylpyrazole sample with a molar ratio of $[O_3]/[1BP]_0 \sim 1$. The fragment ions denoted with asterisks (*) match those simulated by MetFrag as shown in Figure S3.46.

A. Chromatogram

- Peak retention time: 11.7 min
- Peak intensity: 1.1×10^7

C. Proposed molecular formulaC₈H₁₀N₂O**D. Candidate structures****151a****151b****151c****151d****B. MS2 spectra**

20190513-20 #2284 RT: 11.64 AV: 1 NL: 5.98E6
 F: FTMS + p ESI d Full ms2 151.0868@hcd30.00 [50.0000-170.0000]

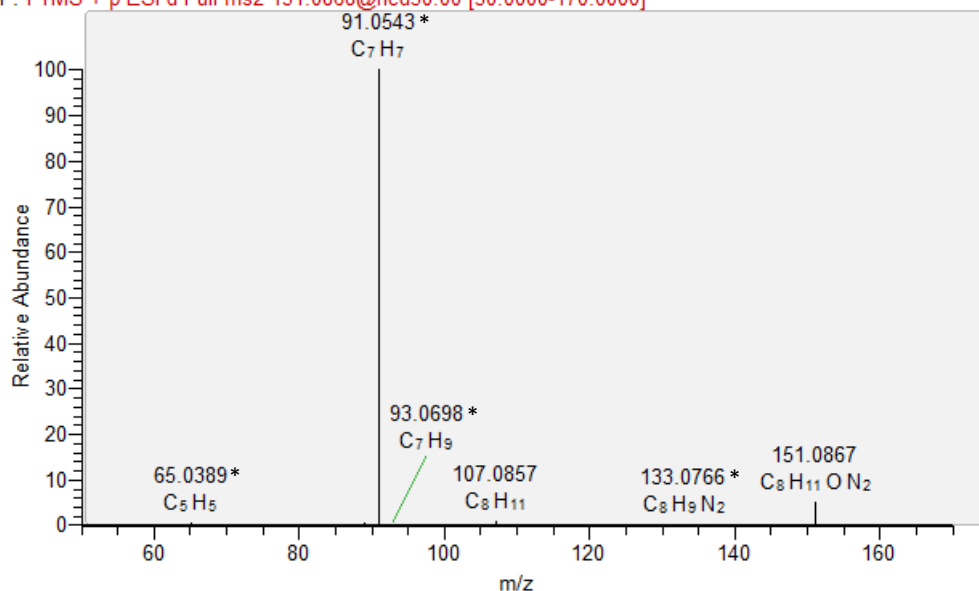


Figure S3.43. (A) LC-HRMS/MS total ion chromatogram filtered by $m/z = 151.0864$, (B) the corresponding MS2 spectrum, (C) a proposed molecular formula, and (D) candidate structures of $m/z = 151.0864$ found by MetFrag analyses for an ozonated 1-benzylpyrazole sample with a molar ratio of $[O_3]/[1BP]_0 \sim 1$. The fragment ions denoted with asterisks (*) match those simulated by MetFrag as shown in Figures S3.47 to S3.50. The candidate structure highlighted by a red square indicates the most plausible structure (Text S3.18).

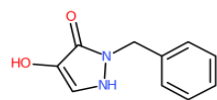
Text S3.18. MetFrag procedure and results for m/z 151.0864, 163.0864, and 191.0813 found in the reaction of 1-benzylpyrazole with ozone

To elucidate structures of unknown LC-MS peaks with the exact masses of m/z = 151.0864, 163.0864, and 191.0813 (as $[M+H]^+$) detected in ozonated 1-benzylpyrazole samples, their MS2 spectra were recorded (Figures S3.41 to S3.43) and compared with simulated fragment ions of candidate structures obtained by a compound database, PubChem³¹ and an *in silico* fragmenter, MetFrag.³² The database search is incorporated into the web-based MetFrag workflow, available at <https://msbi.ipb-halle.de/MetFragBeta/>. It should be noted that this approach has the limitation that it only covers the candidate structures available in the applied database, PubChem.³¹ Moreover, in some cases, the recorded MS2 spectra contained only a few distinguishing fragment ions, providing only limited structural information (see the cases of m/z = 151.0864 and 163.0864 as examples).

Preliminary candidate structures were obtained by searching PubChem for the exact mass (e.g., 151.0864 as $[M+H]^+$) with mass deviation of 5 ppm. The resulting candidates (total 2993 entries for 151.0864) were further narrowed down (to 4 entries) by filtering their structures with a specific substructure, selecting only the candidates containing a *N*-benzylhydrazine moiety (or “c1ccc(cc1)[CH2]NN” as an input for the structural identifier, SMILES arbitrary target specification), based on the assumption that the moiety should be less reactive towards ozone and thus still be seen as a transformation product. The final candidate structures were then fragmented by MetFrag, using a bond dissociation approach. The resulting fragments were compared with the measured fragment ions by submitting a list of m/z (of fragments) and the corresponding intensities recorded by LC-HRMS/MS measurements. The results are presented below for m/z = 191.0813, 163.0864, and 151.0864, respectively.

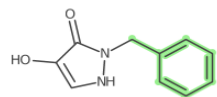
- a) m/z = 191.0813 corresponding to $C_{10}H_{10}N_2O_2$ with a mass deviation of -1.1 ppm. A total of four candidate structures (candidates 191a – 191d as shown in Figure S3.41D) resulted from the PubChem search. Candidate 191a forms benzylpyrazole with two oxygens added to the pyrazole ring. The other three candidates, candidates 191b – 191d, form benzylpyrazole with two oxygens added to the pyrazole and the benzene rings, respectively. The only difference among candidates 191b – 191d is the location of the hydroxyl group on the benzene ring and thus only candidate 191b is discussed as a representative case hereafter. The candidate structures processed by MetFrag are shown in Figures S3.44 and S3.45. The MS2 fragments simulated by MetFrag and matched to the detected fragments are also compiled. The substructure of the candidate structure, forming an individual fragment is highlighted in green. Candidates 191a and 191b share all fragments in common. Thus, it is difficult to conclude which is more plausible than the other based on this analysis. Based on the ozone reactivity, 4-hydroxypyrazole (a possible precursor of both candidates 191a and 191b) is more reactive towards ozone than benzene (Table 3.1 in the main text). Accordingly, the 4-hydroxypyrazole moiety is more susceptible to the ozone attack than the benzene ring, and therefore, candidate 191a is more plausible than candidate 191b.

Candidate 191a



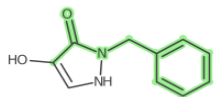
Name: 2-benzyl-4-hydroxy-1H-pyrazol-3-one
Molecular formula: C₁₀H₁₀N₂O₂
Monoisotopic mass: 190.074
[M+H]⁺ = 191.081

Fragments



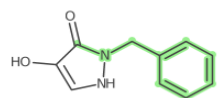
Fragment 1

Formula [C₇H₇]⁺
Mass 91.0543
Peak m/z 91.0542



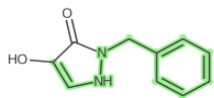
Fragment 7

Formula [C₉H₇NO]⁺
Mass 145.0522
Peak m/z 145.0520



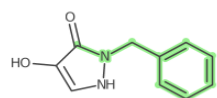
Fragment 2

Formula [C₈H₇N-H]⁺
Mass 116.0495
Peak m/z 116.0492



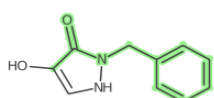
Fragment 8

Formula [C₉H₉N₂]⁺
Mass 145.0761
Peak m/z 145.0761



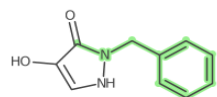
Fragment 3

Formula [C₈H₇N]⁺
Mass 117.0573
Peak m/z 117.0573



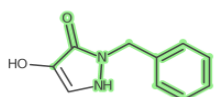
Fragment 9

Formula [C₉H₇NO]⁺+H⁺
Mass 146.0601
Peak m/z 146.0601



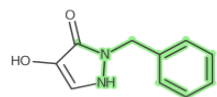
Fragment 4

Formula [C₈H₇N]⁺+H⁺
Mass 118.0652
Peak m/z 118.0650



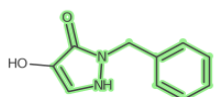
Fragment 10

Formula [C₉H₈N₂O-H]⁺
Mass 159.0553
Peak m/z 159.0553



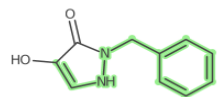
Fragment 5

Formula [C₈H₈N₂-H]⁺
Mass 131.0604
Peak m/z 131.0604



Fragment 11

Formula [C₁₀H₉N₂O]⁺
Mass 173.0710
Peak m/z 173.0710

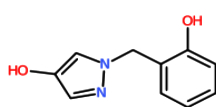


Fragment 6

Formula [C₉H₉N₂-H]⁺
Mass 144.0682
Peak m/z 144.0683

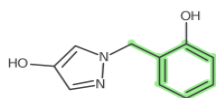
Figure S3.44. MetFrag results of the candidate 191a. Eleven fragments of 191a obtained by *in silico* fragmentation of MetFrag are shown under “Fragments”. The substructure of 191a forming an individual fragment is highlighted in green. “Mass” indicates the theoretical exact mass of the fragment and “Peak m/z” indicates the exact mass detected by LC-HRMS/MS measurement as shown in Figure S3.41B.

Candidate 191b



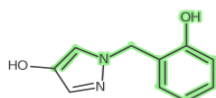
Name: 1-[(2-hydroxyphenyl)methyl]pyrazol-4-ol
 Molecular formula: C₁₀H₁₀N₂O₂
 Monoisotopic mass: 190.074
 [M+H]⁺ = 191.081

Fragments



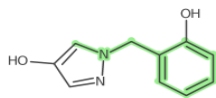
Fragment 1

Formula [C₇H₆]+H⁺
 Mass 91.05426
 Peak m/z 91.0542



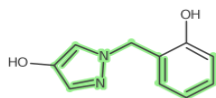
Fragment 7

Formula [C₉H₈NO-H]⁺
 Mass 145.0522
 Peak m/z 145.052



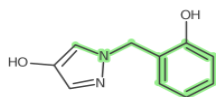
Fragment 2

Formula [C₈H₇N-H]⁺
 Mass 116.0495
 Peak m/z 116.0492



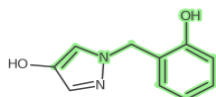
Fragment 8

Formula [C₉H₈N₂]+H⁺
 Mass 145.0761
 Peak m/z 145.0761



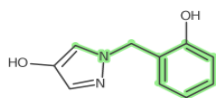
Fragment 3

Formula [C₈H₇N]⁺
 Mass 117.0573
 Peak m/z 117.0573



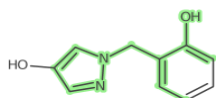
Fragment 9

Formula [C₉H₈NO]⁺
 Mass 146.0601
 Peak m/z 146.0601



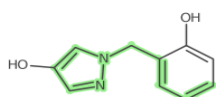
Fragment 4

Formula [C₈H₇N]+H⁺
 Mass 118.0652
 Peak m/z 118.065



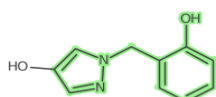
Fragment 10

Formula [C₉H₈N₂O-H]⁺
 Mass 159.0553
 Peak m/z 159.0553



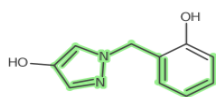
Fragment 5

Formula [C₈H₇N₂]⁺
 Mass 131.0604
 Peak m/z 131.0604



Fragment 11

Formula [C₁₀H₉N₂O]⁺
 Mass 173.071
 Peak m/z 173.071

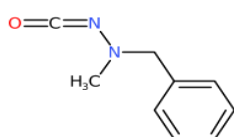


Fragment 6

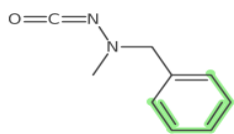
Formula [C₉H₈N₂]⁺
 Mass 144.0682
 Peak m/z 144.0683

Figure S3.45. MetFrag results of the candidate 191b. Eleven fragments of 191b obtained by *in silico* fragmentation of MetFrag are shown under “Fragments”. The substructure of 191b forming an individual fragment is highlighted in green. “Mass” indicates the theoretical exact mass of the fragment and “Peak m/z” indicates the exact mass detected by LC-HRMS/MS measurement as shown in Figure S3.41B.

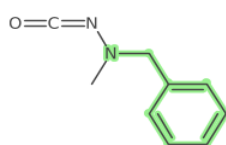
- b) $m/z = 163.0864$ corresponding to $C_9H_{10}N_2O$ with a mass deviation of -1.2 ppm. The MetFrag analysis resulted in only one candidate structure characterized by an aminoisocyanate moiety (Figure S3.46). It can form by the prior ozone attack on the pyrazole ring, followed by ring cleavage via a Criegee mechanism. However, it is unlikely that the ring cleavage reaction leaves the methyl substituent on the nitrogen. Instead, carbonyl compounds are often produced as a result of the Criegee mechanism. Therefore, another compound, probably not included in the PubChem database, seems responsible for $m/z = 163.0864$.

Candidate 163

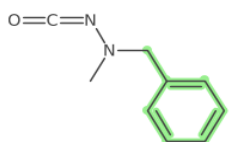
Name: N-isocyanato-N-methyl-1-phenyl-methanamine
Molecular formula: $C_9H_{10}N_2O$
Monoisotopic mass: 162.079
 $[M+H]^+$ = 163.086

Fragments**Fragment 1**

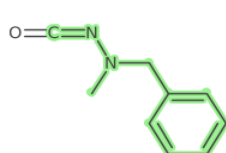
Formula $[C_5H_5]^+$
Mass 65.0386
Peak m/z 65.0388

**Fragment 4**

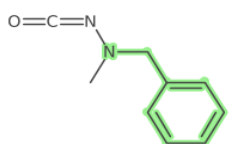
Formula $[C_7H_7N]^+H^+$
Mass 106.065
Peak m/z 106.066

**Fragment 2**

Formula $[C_7H_7]^+$
Mass 91.0543
Peak m/z 91.0542

**Fragment 5**

Formula $[C_9H_{10}N_2-H]^+$
Mass 145.0761
Peak m/z 145.076

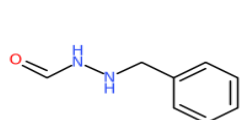
**Fragment 3**

Formula $[C_7H_7N-H]^+$
Mass 104.05
Peak m/z 104.05

Figure S3.46. MetFrag results of the candidate 163. Five fragments of 163 obtained by *in silico* fragmentation of MetFrag are shown under "Fragments". The substructure of 163 forming an individual fragment is highlighted in green. "Mass" indicates the theoretical exact mass of the fragment and "Peak m/z " indicates the exact mass detected by LC-HRMS/MS analysis as shown in Figure S3.42B.

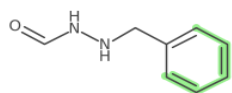
- c) $m/z = 151.0864$ corresponding to $C_8H_{10}N_2O$ with a mass deviation of -1.3 ppm. The MetFrag analysis resulted in four candidate structures, candidates 151a – 151d (Figures S3.47 to S3.50). Candidates 151b and 151d contain an *N*-nitroso moiety of which presence was rejected by the total *N*-nitrosamine analysis that detected no nitrosamines. The remaining candidates 151a and 151c contain a hydrazide moiety and candidate 151c is more likely to form via a Criegee mechanism as shown in Figure S3.8 in the main text.

Candidate 151a



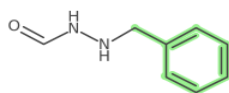
Name: N-(benzylamino)formamide
Molecular formula: $C_8H_{10}N_2O$
Monoisotopic mass: 150.079
 $[M+H]^+$ = 151.086

Fragments



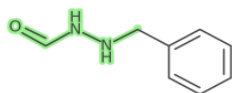
Fragment 1

Formula $[C_5H_5]^+$
Mass 65.0386
Peak m/z 65.0389



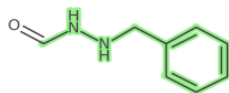
Fragment 4

Formula $[C_7H_7+H]^+ + H^+$
Mass 93.0699
Peak m/z 93.0698



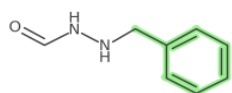
Fragment 2

Formula $[C_2H_5N_2O]^+$
Mass 73.0397
Peak m/z 73.0397



Fragment 5

Formula $[C_8H_{10}N_2-H]^+$
Mass 133.076
Peak m/z 133.077

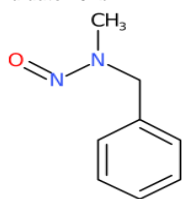


Fragment 3

Formula $[C_7H_7]^+$
Mass 91.0543
Peak m/z 91.0543

Figure S3.47. MetFrag results of the candidate 151a. Five fragments of 151a obtained by *in silico* fragmentation of MetFrag are shown under "Fragments". The substructure of 151a forming an individual fragment is highlighted in green. "Mass" indicates the theoretical exact mass of the fragment and "Peak m/z" indicates the exact mass detected by LC-HRMS/MS analysis as shown in Figure S3.43B.

Candidate 151b



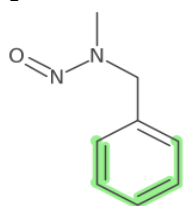
Name: N-benzyl-N-methyl-nitrous amide

Molecular formula: C₈H₁₀N₂O

Monoisotopic mass: 150.079

[M+H]⁺ = 151.086

Fragments

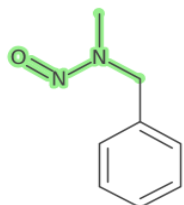


Fragment 1

Formula [C₅H₅]⁺

Mass 65.0386

Peak m/z 65.0389

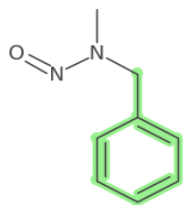


Fragment 2

Formula [C₂H₅N₂O]⁺

Mass 73.0397

Peak m/z 73.0397

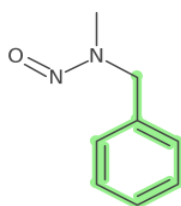


Fragment 3

Formula [C₇H₇]⁺

Mass 91.0543

Peak m/z 91.0543

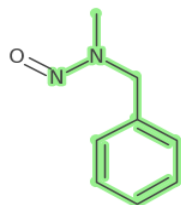


Fragment 4

Formula [C₇H₇+H]⁺+H⁺

Mass 93.0699

Peak m/z 93.0698



Fragment 5

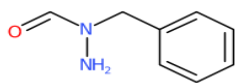
Formula [C₈H₁₀N₂-H]⁺

Mass 133.076

Peak m/z 133.077

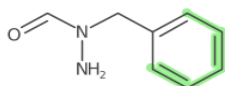
Figure S3.48. MetFrag results of the candidate 151b. Five fragments of 151b obtained by *in silico* fragmentation of MetFrag are shown under "Fragments". The substructure of 151b forming an individual fragment is highlighted in green. "Mass" indicates the theoretical exact mass of the fragment and "Peak m/z" indicates the exact mass detected by LC-HRMS/MS analysis as shown in Figure S3.43B.

Candidate 151c



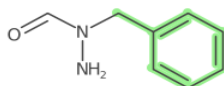
Name: N-amino-N-benzyl-formamide
Molecular formula: C₈H₁₀N₂O
Monoisotopic mass: 150.079
[M+H]⁺ = 151.086

Fragments



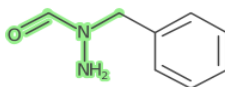
Fragment 1

Formula [C₅H₅]⁺
Mass 65.0386
Peak m/z 65.0389



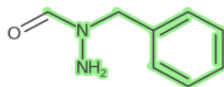
Fragment 4

Formula [C₇H₇+H]⁺+H⁺
Mass 93.0699
Peak m/z 93.0698



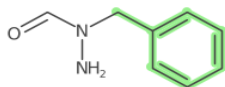
Fragment 2

Formula [C₂H₅N₂O]⁺
Mass 73.0397
Peak m/z 73.0397



Fragment 5

Formula [C₈H₁₀N₂-H]⁺
Mass 133.076
Peak m/z 133.077

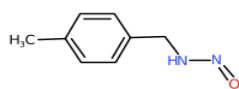


Fragment 3

Formula [C₇H₇]⁺
Mass 91.0543
Peak m/z 91.0543

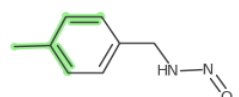
Figure S3.49. MetFrag results of the candidate 151c. Five fragments of 151c obtained by *in silico* fragmentation of MetFrag are shown under "Fragments". The substructure of 151c forming an individual fragment is highlighted in green. "Mass" indicates the theoretical exact mass of the fragment and "Peak m/z" indicates the exact mass detected by LC-HRMS/MS analysis as shown in Figure S3.43B.

Candidate 151d



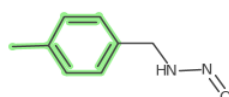
Name: N-(p-tolylmethyl)nitrous amide
Molecular formula: C₈H₁₀N₂O
Monoisotopic mass: 150.079
[M+H]⁺ = 151.086

Fragments



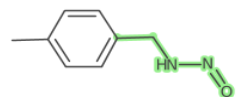
Fragment 1

Formula [C₅H₆-H]⁺
Mass 65.0386
Peak m/z 65.0389



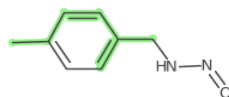
Fragment 5

Formula [C₇H₇+H]⁺
Mass 93.0699
Peak m/z 93.0698



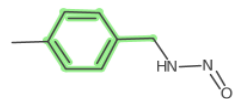
Fragment 2

Formula [C₂H₃N₂O+H]⁺
Mass 73.0397
Peak m/z 73.0397



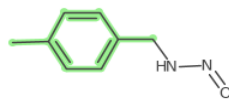
Fragment 6

Formula [C₇H₈+2H]⁺
Mass 95.0856
Peak m/z 95.0854



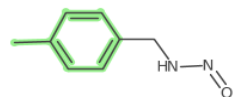
Fragment 3

Formula [C₇H₆-H]⁺
Mass 89.0386
Peak m/z 89.0386



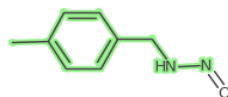
Fragment 7

Formula [C₈H₉+H]⁺
Mass 107.086
Peak m/z 107.086



Fragment 4

Formula [C₇H₇]⁺
Mass 91.0543
Peak m/z 91.0543



Fragment 8

Formula [C₈H₁₀N₂-H]⁺
Mass 133.076
Peak m/z 133.077

Figure S3.50. MetFrag results of the candidate 151d. Eight fragments of 151d obtained by *in silico* fragmentation of MetFrag are shown under “Fragments”. The substructure of 151d forming an individual fragment is highlighted in green. “Mass” indicates the theoretical exact mass of the fragment and “Peak m/z” indicates the exact mass detected by LC-HRMS/MS analysis as shown in Figure S3.43B.

Table S3.14. Average abatement of the micropollutants containing a pyrrole, imidazole, or pyrazole moiety during ozonation at a full-scale wastewater treatment plant, based on the Table S7 in Bourgin et al. (2018).³³ The abatements were calculated by comparing the average concentrations after biological treatment with after ozonation. For the substrates of which concentrations were below LOQ after ozonation, their abatements were calculated by using the LOQs and presented as the minimum abatements with ">" signs.³³

Substance	Substructure	Use	LOQ, ng L ⁻¹	Average concentration after biological treatment, ng L ⁻¹	Average concentration after ozonation, ng L ⁻¹	Average abatement during ozonation, %
Fluvastatin	Pyrrole	Pharmaceuticals	1.3	4	< LOQ	> 67
Fludioxonil	Pyrrole	Pesticides	1	3	< LOQ	> 64
Atorvastatin	Pyrrole	Pharmaceuticals	35	60	< LOQ	> 41
Etodolac	Pyrrole	Pharmaceuticals	0.8	110	< LOQ	> 99
Indomethacin	Pyrrole	Pharmaceuticals	2	91	< LOQ	> 98
Thiabendazol	Imidazole	Pesticides	1.6	6	1	> 65
Candesartan	Imidazole	Pharmaceuticals	5	330	91	72
Eprosartan	Imidazole	Pharmaceuticals	3	45	< LOQ	> 93
2-Aminobenzimidazol	Imidazole	Biocides	5	10	< LOQ	> 50
Metronidazol	Imidazole	Pharmaceuticals	8	112	47	58
Carbendazim	Imidazole	Biocides	3	28	< LOQ	> 89
Climbazol	Imidazole	Personal Care Products	1	66	2	98
Losartan	Imidazole	Pharmaceuticals	4	260	3	> 98
Ketoconazol	Imidazole	Pharmaceuticals	10	65	< LOQ	> 84
Telmisartan	Imidazole	Pharmaceuticals	1	93	22	76
Fipronil	Pyrazole	Pesticides	0.9	5	2	58
Fipronil-sulfon	Pyrazole	Pesticides	0.5	2	1	58

References

- (1) Pryor, W. A.; Giamalva, D. H.; Church, D. F. Kinetics of Ozonation. 2. Amino Acids and Model Compounds in Water and Comparisons to Rates in Nonpolar Solvents. *Journal of the American Chemical Society* **1984**, *106* (23), 7094–7100. <https://doi.org/10.1021/ja00335a038>.
- (2) Buxton, G. V.; Greenstock, C. L.; Helman, W. P.; Ross, A. B. Critical Review of Rate Constants for Reactions of Hydrated Electrons, Hydrogen Atoms and Hydroxyl Radicals ($\cdot\text{OH}/\cdot\text{O}^-$ in Aqueous Solution. *Journal of Physical and Chemical Reference Data* **1988**, *17* (2), 513–886. <https://doi.org/10.1063/1.555805>.
- (3) Nash, T. The Colorimetric Estimation of Formaldehyde by Means of the Hantzsch Reaction. *Biochemical Journal* **1953**, *55* (3), 416.
- (4) Dowideit, P.; von Sonntag, C. Reaction of Ozone with Ethene and Its Methyl- and Chlorine-Substituted Derivatives in Aqueous Solution. *Environmental Science & Technology* **1998**, *32* (8), 1112–1119.
- (5) Bader, H.; Hoigné, J. Determination of Ozone In Water By The Indigo Method: A Submitted Standard Method. *Ozone: Science & Engineering* **1982**, *4* (4), 169–176. <https://doi.org/10.1080/01919518208550955>.
- (6) Dissociation Constants of Organic Acids and Bases. In *CRC Handbook of Chemistry and Physics, 100th Edition (Internet Version 2019)*; Rumble, J. R., Ed.; CRC Press/Taylor & Francis: Boca Raton, FL, 2019.
- (7) Ianni, J. C. Kintecus, 2017, Windows Version 6.01, www.kintecus.com.
- (8) Hoigné, J.; Bader, H.; Haag, W. R.; Staehelin, J. Rate Constants of Reactions of Ozone with Organic and Inorganic Compounds in Water—III. Inorganic Compounds and Radicals. *Water Research* **1985**, *19* (8), 993–1004. [https://doi.org/10.1016/0043-1354\(85\)90368-9](https://doi.org/10.1016/0043-1354(85)90368-9).
- (9) Reisz, E.; Fischbacher, A.; Naumov, S.; von Sonntag, C.; Schmidt, T. C. Hydride Transfer: A Dominating Reaction of Ozone with Tertiary Butanol and Formate Ion in Aqueous Solution. *Ozone: Science & Engineering* **2014**, *36* (6), 532–539. <https://doi.org/10.1080/01919512.2014.891436>.
- (10) Breider, F.; von Gunten, U. Quantification of Total *N*-Nitrosamine Concentrations in Aqueous Samples via UV-Photolysis and Chemiluminescence Detection of Nitric Oxide. *Analytical Chemistry* **2017**, *89* (3), 1574–1582. <https://doi.org/10.1021/acs.analchem.6b03595>.
- (11) Shrivastava, A.; Gupta, B., V. Methods for the Determination of Limit of Detection and Limit of Quantitation of the Analytical Methods. *Chronicles of Young Scientists* **2011**, *2* (1), 21. <https://doi.org/10.4103/2229-5186.79345>.
- (12) McArdell, C. S.; Alder, A. C.; Göbel, A.; Löffler, D.; Suter, M. J.-F.; Ternes, T. A. Analytical Methods. In *Human pharmaceuticals, hormones and fragrances. The challenge of micropollutants in urban water management*; 2006; pp 55–105.
- (13) Ohmori, S.; Mori, M.; Kawase, M.; Tsuboi, S. Determination of Methylglyoxal as 2-Methylquinoxaline by High-Performance Liquid Chromatography and Its Application to Biological Samples. *Journal of Chromatography B: Bio-medical Sciences and Applications* **1987**, *414*, 149–155. [https://doi.org/10.1016/0378-4347\(87\)80033-6](https://doi.org/10.1016/0378-4347(87)80033-6).
- (14) Lim, S.; McArdell, C. S.; von Gunten, U. Reactions of Aliphatic Amines with Ozone: Kinetics and Mechanisms. *Water Research* **2019**, *157*, 514–528. <https://doi.org/10.1016/j.watres.2019.03.089>.
- (15) Muñoz, F.; Mvula, E.; Braslavsky, S. E.; von Sonntag, C. Singlet Dioxygen Formation in Ozone Reactions in Aqueous Solution. *Journal of the Chemical Society, Perkin Transactions 2* **2001**, No. 7, 1109–1116. <https://doi.org/10.1039/b101230o>.
- (16) Held, A. M.; Halko, D. J.; Hurst, J. K. Mechanisms of Chlorine Oxidation of Hydrogen Peroxide. *Journal of the American Chemical Society* **1978**, *100* (18), 5732–5740.
- (17) Flyunt, R.; Leitzke, A.; Mark, G.; Mvula, E.; Reisz, E.; Schick, R.; von Sonntag, C. Determination of $\cdot\text{OH}$, $\text{O}_2\cdot^-$, and Hydroperoxide Yields in Ozone Reactions in Aqueous Solution. *The Journal of Physical Chemistry B* **2003**, *107* (30), 7242–7253. <https://doi.org/10.1021/jp022455b>.
- (18) Allen, A. O.; Hochanadel, C. J.; Ghormley, J. A.; Davis, T. W. Decomposition of Water and Aqueous Solutions Under Mixed Fast Neutron and Gamma Radiation. **1952**, *56*, 575–586.
- (19) Kitsuka, K.; Mohammad, A. M.; Awad, M. I.; Kaneda, K.; Ikematsu, M.; Iseki, M.; Mushiaki, K.; Ohsaka, T. Simultaneous Spectrophotometric Determination of Ozone and Hydrogen Peroxide. *Chem. Lett.* **2007**, *36* (11), 1396–1397. <https://doi.org/10.1246/cl.2007.1396>.
- (20) Bader, H.; Sturzenegger, V.; Hoigne, J. Photometric Method for the Determination of Low Concentrations of Hydrogen Peroxide by the Peroxidase Catalyzed Oxidation of *N,N*-Diethyl-*p*-Phenylenediamine (DPD). *Water Research* **1988**, *22* (9), 1109–1115.
- (21) Frisch, M. J.; Trucks, G. W.; Schlegel, H. B.; Scuseria, G. E.; Robb, M. A.; Cheeseman, J. R.; Scalmani, G.; Barone, V.; Petersson, G. A.; Nakatsuji, H.; et al. *Gaussian 09, Revision D.01*; Gaussian, Inc.: Wallingford CT, 2016.
- (22) Vydrov, O. A.; Scuseria, G. E. Assessment of a Long-Range Corrected Hybrid Functional. *J. Chem. Phys.* **2006**, *125* (23), 234109. <https://doi.org/10.1063/1.2409292>.
- (23) Marenich, A. V.; Cramer, C. J.; Truhlar, D. G. Universal Solvation Model Based on Solute Electron Density and on a Continuum Model of the Solvent Defined by the Bulk Dielectric Constant and Atomic Surface Tensions. *The Journal of Physical Chemistry B* **2009**, *113* (18), 6378–6396. <https://doi.org/10.1021/jp810292n>.
- (24) Fukui, K. The Path of Chemical Reactions - the IRC Approach. *Acc. Chem. Res.* **1981**, *14* (12), 363–368. <https://doi.org/10.1021/ar00072a001>.
- (25) Rappoport, D.; Furche, F. Property-Optimized Gaussian Basis Sets for Molecular Response Calculations. *J. Chem. Phys.* **2010**, *133* (13), 134105. <https://doi.org/10.1063/1.3484283>.

- (26) Zhao, Y.; Truhlar, D. G. The M06 Suite of Density Functionals for Main Group Thermochemistry, Thermochemical Kinetics, Noncovalent Interactions, Excited States, and Transition Elements: Two New Functionals and Systematic Testing of Four M06-Class Functionals and 12 Other Functionals. *Theoretical Chemistry Accounts* **2008**, *120* (1), 215–241. <https://doi.org/10.1007/s00214-007-0310-x>.
- (27) Jiménez-Hoyos, C. A.; Janesko, B. G.; Scuseria, G. E. Evaluation of Range-Separated Hybrid Density Functionals for the Prediction of Vibrational Frequencies, Infrared Intensities, and Raman Activities. *Physical Chemistry Chemical Physics* **2008**, *10* (44), 6621–6629. <https://doi.org/10.1039/B810877C>.
- (28) Trogolo, D.; Arey, J. S.; Tentscher, P. R. Gas-Phase Ozone Reactions with a Structurally Diverse Set of Molecules: Barrier Heights and Reaction Energies Evaluated by Coupled Cluster and Density Functional Theory Calculations. *The Journal of Physical Chemistry A* **2019**. <https://doi.org/10.1021/acs.jpca.8b10323>.
- (29) Zhao, Y.; Tishchenko, O.; Gour, J. R.; Li, W.; Lutz, J. J.; Piecuch, P.; Truhlar, D. G. Thermochemical Kinetics for Multi-reference Systems: Addition Reactions of Ozone. *The Journal of Physical Chemistry A* **2009**, *113* (19), 5786–5799. <https://doi.org/10.1021/jp811054n>.
- (30) Quintanilla-Licea, R.; Colunga-Valladares, J.; Caballero-Quintero, A.; Rodríguez-Padilla, C.; Tamez-Guerra, R.; Gómez-Flores, R.; Waksman, N. NMR Detection of Isomers Arising from Restricted Rotation of the C-N Amide Bond of N-Formyl-o-Toluidine and N,N'-Bis-Formyl-o-Tolidine. *Molecules* **2002**, *7* (8), 662–673. <https://doi.org/10.3390/70800662>.
- (31) Kim, S.; Chen, J.; Cheng, T.; Gindulyte, A.; He, J.; He, S.; Li, Q.; Shoemaker, B. A.; Thiessen, P. A.; Yu, B.; et al. PubChem 2019 Update: Improved Access to Chemical Data. *Nucleic Acids Res* **2019**, *47* (Database issue), D1102–D1109. <https://doi.org/10.1093/nar/gky1033>.
- (32) Ruttkies, C.; Schymanski, E. L.; Wolf, S.; Hollender, J.; Neumann, S. MetFrag Relaunched: Incorporating Strategies beyond in Silico Fragmentation. *J Cheminform* **2016**, *8* (1), 3. <https://doi.org/10.1186/s13321-016-0115-9>.
- (33) Bourgin, M.; Beck, B.; Boehler, M.; Borowska, E.; Fleiner, J.; Salhi, E.; Teichler, R.; von Gunten, U.; Siegrist, H.; Mc Ardell, C. S. Evaluation of a Full-Scale Wastewater Treatment Plant Upgraded with Ozonation and Biological Post-Treatments: Abatement of Micropollutants, Formation of Transformation Products and Oxidation by-Products. *Water Research* **2018**, *129*, 486–498. <https://doi.org/10.1016/j.watres.2017.10.036>.

Chapter 4 Conclusions and Outlook

Nitrogen-containing compounds in water and wastewater treatment where ozonation is applied for disinfection or oxidation are of significance in terms of three aspects: (1) they are commonly found in natural waters in dissolved organic nitrogen and micropollutants; (2) they are often susceptible to an electrophilic attack by ozone because of the electron-rich nature of the neutral form of nitrogen in organic compounds; (3) they have potential to form nitrogenous disinfection byproducts or harmful transformation products upon ozonation (e.g., NDMA).

A considerable number of studies had been conducted about the fate and behavior of nitrogenous compounds during ozonation. However, the reactivity of some common nitrogen-containing functional groups towards ozone is only poorly understood. This thesis summarizes the up-to-date information available for the reactions of nitrogen-containing compounds with ozone (Chapter 1) and provides novel information on experimental investigations of the reactions of ozone with aliphatic amines (Chapter 2) and azoles (Chapter 3). The investigations were carried out according to the main objectives of (1) determining the second-order rate constants (k_{03}) of the reactions of nitrogen-containing compounds with ozone, (2) identifying/quantifying transformation products and reactive oxygen species, (3) performing kinetic simulations and quantum chemical computations to supplement or corroborate empirical evidences. Reaction mechanisms were proposed by compiling the results from all aspects, providing a better understanding of the reactions of nitrogen-containing compounds with ozone.

The first nitrogen-containing functional groups investigated were the simple aliphatic amines, triethylamine, diethylamine, and ethylamine (Chapter 2), with an emphasis on diethylamine and ethylamine (a secondary and a primary amine, respectively). For these compounds, mass balances and transformation products upon ozonation have only been investigated scarcely compared to triethylamine (a tertiary amine). Species-specific k_{03} of the neutral forms of amines ranged from $9.3 \times 10^4 \text{ M}^{-1} \text{ s}^{-1}$ to $2.2 \times 10^6 \text{ M}^{-1} \text{ s}^{-1}$. The apparent k_{03} at pH 7 for potential or identified transformation products were $6.8 \times 10^5 \text{ M}^{-1} \text{ s}^{-1}$ for *N,N*-diethylhydroxylamine, $\sim 10^5 \text{ M}^{-1} \text{ s}^{-1}$ for *N*-ethylhydroxylamine, $1.9 \times 10^3 \text{ M}^{-1} \text{ s}^{-1}$ for *N*-ethylethanamine oxide, and $3.4 \text{ M}^{-1} \text{ s}^{-1}$ for nitroethane. Product analyses revealed that all amines predominantly underwent oxygen-transfer pathways to form major transformation products containing nitrogen-oxygen bonds: triethylamine *N*-oxide (88% per abated triethylamine) and nitroethane (69% per abated diethylamine and 100% per abate ethylamine). *N*-dealkylated products were found as minor products for triethylamine and diethylamine (< 10% per abated amines). Diethylamine and ethylamine exhibited high ozone molar stoichiometry (ozone:amine ≥ 4), which resulted from the formation of primary transformation products highly reactive towards ozone. *N,N*-diethylhydroxylamine was a potential primary transformation product during the diethylamine-ozone reaction. Its formation was not confirmed due to its high ozone reactivity, but supported by measurements of reactive oxygen species, kinetic simulations, and quantum chemical computations.

The second target groups were the five-membered heterocyclic compounds (azoles) pyrrole, imidazole, and pyrazole (Chapter 3). They are widespread in nature as substructures of biomolecules and micropollutants, but the kinetics and mechanisms of their reactions with ozone had not been well known. Pyrrole and imidazole reacted fast with ozone for a wide pH range ($k_{03} > 10^3 \text{ M}^{-1} \text{ s}^{-1}$ at pH 1 – 12). Pyrazole reacted moderately fast with ozone ($k_{03} = 56 \text{ M}^{-1} \text{ s}^{-1}$ at pH 7). All azoles underwent an addition of ozone to the C-C double bond in the ring. Subsequent pathways after the initial ozone addition varied considerably among the azoles. Pyrrole reacted with ozone via multiple mechanisms (Criegee-type and oxygen-addition) to form ring products (5-Hydroxy-1,5-dihydro-2H-pyrrol-2-one and maleimide) as well as a ring opened-product (*N*-(3-oxo-1-propen-1-yl)formamide). The major identified products (yield per abated pyrrole) from the pyrrole-ozone reaction were maleimide (34%), formamide (14%) and formate (54%). Imidazole predominantly reacted via a Criegee-type mechanism with ring cleavage and formation of three fragments, formamide, cyanate, and formate. The fragmen-

tation required only a single attack of ozone and all oxygen atoms ended up in the products. The yields of the three products were ~100 % respectively, completely closing the mass balance of imidazole. Among the azoles, pyrazole is the most persistent compound towards ozone, showing an exceptionally high ozone molar stoichiometry (ozone:pyrazole ≥ 4). Only carbonous products were identified (126% formate and 34% glyoxal per abated pyrazole). Products containing hydroxypyrazole and hydrazide moieties were postulated, possibly formed via an oxygen addition and a Criegee-type mechanism, respectively.

Various nitrogenous transformation products were identified during the studies presented in Chapters 2 and 3, which may have different implications for the aquatic environment. The high yields of nitroethane determined during the diethylamine- and ethylamine-ozone reactions implies significant formation of nitroalkanes upon ozonation especially for waters with high dissolved organic nitrogen contents. Toxic effects of nitroalkanes seem to be compound specific: nitroethane considered rather a tolerable substance in mammalian systems, whereas nitromethane and 2-nitropropane are considered suspect human carcinogens. Thus, further efforts are needed to understand occurrences of nitroalkanes and their impact on the aquatic environment and human health. In contrast, the nitrogenous products identified during the azole-ozone reactions (maleimide, formamide, and cyanate) are readily hydrolyzed or biodegraded and thus are expected to be well abated by biological post-treatment after ozonation. However, maleimide may induce toxic effects attributed to its high selectivity to thiol groups which can cause protein damage. Additionally, a formamide moiety developed by oxidation of imidazole derivatives was reported as possibly responsible for an observed increased toxicity. This indicates different toxic effects may be induced when the identified products are present as substructures in more complex compounds (e.g., micropollutants).

The results obtained in this work provide new insights into the reactions of ozone with common nitrogen-containing functional groups such as primary amines, secondary amines, hydroxylamines (as ozonation products of primary/secondary amines), and azoles. However, these functional groups can branch into numerous subcategories that may react with ozone differently and certainly worth future investigation. Examples are azoles containing more than two nitrogen atoms in the ring such as triazoles and tetrazole. Triazoles exist in two isomers, 1,2,3-triazole and 1,2,4-triazole. Kinetics and reaction mechanisms of 1,2,3-triazole upon ozonation can be supposed by previous studies on the reaction of benzotriazole with ozone. However, information on the reaction of ozone with 1,2,4-triazole, a common moiety of antifungal drugs, is not available. 1,2,4-triazole contain a N-N single bond in the five-membered ring like pyrazole, and therefore, understanding the 1,2,4-triazole-ozone reaction also may shed light on the pyrazole-ozone reaction of which nitrogenous transformation products still remain unidentified.

Besides the azole functional groups, there are still many heterocyclic moieties with diverse structures present in micropollutants. To predict kinetics and product formation of the reactions of the heterocycles with ozone, understanding their chemical properties seems important. For example, different π -electron distributions of the five- and six-membered heterocyclic amines (e.g., π -excessive pyrrole vs. π -deficient pyridine) result in distinct ozone reaction pathways (ozone attack on the C=C double bond vs. on the nitrogen) and consequently different transformation products (ring-opened products vs. *N*-oxides). Such chemical properties of the aromatic systems have been extensively studied for simple heterocyclic compounds and also can be simulated by quantum chemical computations. Therefore, a future study to identify which properties are responsible for deciding dominant ozone reaction pathways would be helpful for a better prediction of the fate of micropollutants containing complex heterocyclic moieties upon ozonation.

Curriculum Vitae

Sungeun Lim

Born 23rd April 1988 in Gyeonggi-do, South Korea

Education

- 2015 – present **PhD** (Supervision: Prof Urs von Gunten, Drinking Water Chemistry, Eawag)
Eawag and EPFL, Switzerland
- 2012 – 2013 **MSc** *Water and Wastewater Engineering*
Cranfield University, UK
- 2010 **Exchange student**
UCLA, USA
- 2007 – 2012 **BSc** *Chemistry*
Yonsei University, South Korea

Employment history

- 2014 – 2015 Research assistant at Gwangju Institute of Science and Technology (South Korea)
in the group of Prof Yunho Lee